

Dynamics and Control of Tethered Satellite Formations for the Purpose of Space-Based Remote Sensing

DISSERTATION

Kurt A. Vogel, Lt Col, USAF

AFIT/DS/ENY/06-04

DEPARTMENT OF THE AIR FORCE
AIR UNIVERSITY

AIR FORCE INSTITUTE OF TECHNOLOGY

Wright-Patterson Air Force Base, Ohio

APPROVED FOR PUBLIC RELEASE; DISTRIBUTION UNLIMITED.

The views expressed in this dissertation are those of the author and do not reflect the official policy or position of the Department of Defense or the United States Government.

AFIT/DS/ENY/06-04

Dynamics and Control of Tethered Satellite Formations for the Purpose of Space-Based Remote Sensing

DISSERTATION

Presented to the Faculty

Department of Aeronautical and Astronautical Engineering

Graduate School of Engineering and Management

Air Force Institute of Technology

Air University

Air Education and Training Command

In Partial Fulfillment of the Requirements for the

Degree of Doctor of Philosophy in Astronautical Engineering

Kurt A. Vogel, B.S., M.S.

Lt Col, USAF

August 2006

APPROVED FOR PUBLIC RELEASE; DISTRIBUTION UNLIMITED.

AFIT/DS/ENY/06-04

Dynamics and Control of Tethered Satellite Formations for the Purpose of Space-Based Remote Sensing

Kurt A. Vogel, B.S., M.S.

Lt Col, USAF

Approved:

Dr. Richard G. Cobb Dissertation Advisor	11 Aug 06 date
Dr. William P. Baker Committee Member	11 Aug 06 date
Lt Col Nathan A. Titus, PhD Committee Member	11 Aug 06 date
Dr. Stephen G. Tragesser Committee Member	15 Aug 06 date
Col Michael J. Caylor, PhD Dean's Representative	11 Aug 06 date

Accepted:

Marlin U. Thomas Dean, Graduate School of Engineering and Management	29 Aug 06 Date

AFIT/DS/ENY/06-04

Abstract

In recent years, much thought has been given to the use of small satellite clusters with distributed sensors to provide large virtual apertures, which have significant weight and packaging efficiencies. One proposed method to maintain the formation shape is with the use of tethers. This dissertation assesses the utility of tethered satellite formations for the space-based remote sensing mission. The research objectives are to determine the effects of energy dissipation on the foundational rigid body dynamics, find equilibrium conditions, apply controls, and assess the relative utility of tethers for formation control on continuously earth-facing aperture clusters.

Energy dissipation is found to have a long-term destabilizing effect on prolate bodies that start in certain (Likins-Pringle) equilibria, while oblate bodies in the same equilibria suffer only short-term destabilization from energy dissipation before settling into a near-limit cycle. Consequently, oblate ring formations are exclusively chosen for the multi-body system.

It is shown that a continuously earth-facing equilibrium condition for a fixed-length tethered system does not exist since the spin rate required for the proper precession would not be high enough to maintain tether tension. The range of required spin rates for steady-spin motion is numerically defined here, but none of these conditions can meet the continuously earth-facing criteria. Of particular note is the discovery that applying certain rigid body conditions to a free-flying formation creates the desired equilibrium condition.

Control methods applied to the tethered system fail to maintain formation orientation or are cost prohibitive. The overall assessment is that tethers have great value for general formations, however, by themselves tethers cannot conduct formation control for *continuously* earth-facing aperture clusters. Even with additional controls, the utility of tethers for this mission is limited.

Acknowledgements

I must first give heartfelt thanks to my advisor, Dr. Rich Cobb, for his empathetic support over the last 3 years. Throughout the setbacks and successes, he always offered encouragement and sound advice. His willingness to help on any level was second to none.

Another great deal of appreciation is owed to the rest of my committee (Lt Col Nate Titus, Dr. Steve Tragesser, and Dr. Bill Baker) for offering their office time in order to educate a guy who was probably too old to be pursuing a PhD. Dr. Titus agreed to do the heavy lifting on the dynamics front and did a fantastic job of keeping me focused. Dr. Tragesser was not only the inspiration for this research, but he lent a great deal of enthusiastic, positive feedback. I am humbled by Dr. Baker's sincere interest in this topic and grateful for his patience with my less-than-blinding math skills. Also from the faculty, I would be remiss if I didn't thank Dr. William Wiesel for his continued wise counsel and kind words, and Col Mike Caylor for presiding over two landmark events in my life over the last year.

To my friends – Brian, Vinnie, Jeff, Shawna, Shad, Paul, and multiple Scotts, Steves, and Johns – I owe tremendous thanks for lending me their ears and shoulders. I would not have persevered if it had not been for their thoughtful help.

My parents have been at every major milestone in my life, but their presence was felt long before each event arrived. They deserve the lion's share of the credit for the successes I have enjoyed. Dad is the reason I wear the uniform and the foundation upon which I have built my life. Mom is ever the optimist, always encouraging, and mindful that "things will always work out in the end" – so true.

On the home front, my beautiful wife deserves special recognition for the effort she put forth in raising our children, managing our family, providing encouragement to an occasionally grumpy doctoral student, bringing balance to my life, and riding this roller coaster with me hand-in-hand. Thank you for commiserating with me

during the lows and celebrating with me during the highs... what a ride! I'm also grateful and proud that you found your voice again.

Finally, I owe a distinctive kind of gratitude to my son and daughter. Unlike previous school experiences, this time I was blessed with their ability to recharge my batteries by making me a proud Dad and carefree playmate. My kids made sure I took time out to have some fun along the way – which helped immeasurably! Whether we were having lightsaber duels or exchanging butterfly kisses, they kept me grounded on what is really important. For that, I dedicate this work, with all of my love, to my pal and my princess.

Kurt A. Vogel

Table of Contents

Page

Abstract iv

Acknowledgements v

List of Figures xii

List of Tables xix

List of Symbols xx

List of Abbreviations xxiii

I. Introduction 1
- 1.1 Spaced-Based Formations 1
- 1.2 Tethered Systems 2
- 1.3 Remote Sensing Mission 3
- 1.4 Research Goals 3
- 1.5 Chapter Outline 4

II. Historical Development for Research in Tethered Formations . . . 5
- 2.1 Tethered System Dynamics 6
  - 2.1.1 General Tethered Systems 6
  - 2.1.2 Inertially-Fixed Systems 8
  - 2.1.3 Earth-Facing Systems 11
- 2.2 Semi-Rigid Body Dynamics 17
  - 2.2.1 Rigid Body Equilibrium Conditions (with Torques Present) 18
  - 2.2.2 Energy Dissipation (Torque Free) 19
  - 2.2.3 Energy Dissipation (with Torques Present) . . . 20
  - 2.2.4 Energy Dissipation (with Specific Gravity Gradient Torques) 20
- 2.3 Tether Modeling 20
- 2.4 Formation Control Using Tethers 23
- 2.5 Formation Control Using Thrusters Only 25
- 2.6 Tethered Spaceflights To Date 27
- 2.7 Summary 28

Page

III. Roadmap for Present Research 29
3.1 Research Methodology Roadmap 30
3.2 Dissertation Overview 32
3.3 Summary 33

IV. Rigid and Semi-Rigid Body Dynamics 34
4.1 Rigid Body Development 34
4.1.1 Reference Frames 35
4.1.2 Euler's Equations-of-Motion 38
4.1.3 Orientation Equations-of-Motion 42
4.1.4 Likins-Pringle Equilibria 44
4.1.5 Euler Angle Initial Conditions 44
4.1.6 Angular Velocity Initial Conditions for Likins-Pringle 45
4.2 Rigid Body Simulations 46
4.2.1 Results for the Torque-Free Rigid Body 48
4.2.2 Results for the Likins-Pringle Rigid Body 50
4.3 Semi-Rigid Body Development 54
4.3.1 Total System Angular Momentum 55
4.3.2 3-Rotor Equations-of-Motion 57
4.3.3 Kinetic Energy 59
4.4 Semi-Rigid Body Simulations 59
4.4.1 Torque-Free Energy Dissipation Effects 60
4.4.2 Energy Dissipation Effects on Likins-Pringle . . 67
4.4.3 Equilibrium Condition for Semi-Rigid Bodies . . 72
4.5 Summary 74

V. Multi-body Formation Dynamics 76
5.1 Two-Body Model Development 76
5.1.1 Reference Frames and Generalized Coordinates 77
5.1.2 Initializing States from Generalized Coordinates 78
5.1.3 Equations-of-Motion 80
5.1.4 Converting States to Generalized Coordinates . 82
5.1.5 Initial Conditions for Likins-Pringle 82
5.2 Three-Body Model Development 86
5.2.1 Reference Frames 86
5.2.2 Initializing States from Generalized Coordinates 88
5.2.3 Initial Conditions for Likins-Pringle 89
5.2.4 Equations-of-Motion 91

Page

5.2.5 Converting States to Variables of Interest (VOI) 94
5.3 Initial Three-Body Simulations 96
5.3.1 L-P Free Flight 100
5.3.2 Strategy for Adding Springs and Tethers 108
5.3.3 Method 1: L-P Massless Springs 109
5.3.4 Method 2: L-P Massless, Elastic Tethers 113
5.3.5 Summary 117
5.4 Strategy: Non-Linear Spring in Tether Model 119
5.5 Strategy: Modify Tether and Formation Parameters . . . 121
5.5.1 Tether Stiffness 121
5.5.2 Damping Coefficient 123
5.5.3 System Altitude 125
5.5.4 Tether Length 126
5.5.5 Combining the Best 127
5.6 Strategy: Four-Body Hub-and-Spoke 131
5.6.1 Rationale for Radial Configurations 131
5.6.2 Model Development 131
5.6.3 4-Body H-A-S Results 133
5.7 Strategy: Six-Body Ring 139
5.7.1 Rationale for Additional Ring Satellites 139
5.7.2 Model Development 141
5.7.3 6-Body Ring Results 141
5.8 Strategy: Seven-Body Closed-Hub-and-Spoke 147
5.8.1 Rationale for a C-H-A-S 147
5.8.2 Model Development 147
5.8.3 7-Body C-H-A-S Results 148
5.9 Strategy: Select Prograde Likins-Pringle Conditions . . . 154
5.9.1 Torque Required to Precess 154
5.9.2 Torque Generated by Gravity Gradient 155
5.9.3 Graphical Explanation of Likins-Pringle 157
5.9.4 Prograde Likins-Pringle Conditions 159
5.9.5 How the "Kumar Range" Changes 161
5.10 Summary 164

VI. Applying Controls to the Tethered System 167
6.1 Control Method 1: Using Thrust to Mimic Spring Compression 167
6.1.1 Model Modifications 168
6.1.2 Baseline Case Results 169

Page

6.1.3 Sensitivity to Thrust Levels and Delay Times . 172
6.1.4 Adding Perturbations 176
6.1.5 "Optimized" Formation Parameters Case 178
6.2 Control Method 2: Programmed Reels 180
6.2.1 Baseline "Single Satellite Ellipse" Equilibrium Condition 180
6.2.2 Programming the Reels 183
6.2.3 Baseline Case Results 183
6.2.4 Circular Formation Case 185
6.3 Control Method 3: Thrust to Precess High Spin Rate . . 188
6.3.1 Required Torques for a Rigid Body 189
6.3.2 Rigid Body Model Modifications 191
6.3.3 Determining ΔV Required 193
6.3.4 Rigid Body Results as a Multi-Body System Estimate 195
6.4 Control Method 4: Constant Tension Reels 197
6.4.1 Model Modifications 197
6.4.2 Initial Constant Tension Results 199
6.4.3 Changing the Constant Tension Parameters . . 201
6.4.4 Bottom Line 202
6.5 Summary 203

VII. Assessing Utility 205
7.1 Assumptions and Foundational Rigid Body Motion . . . 205
7.2 Tethered-Only System Dynamics 206
7.3 Thruster Assistance 206
7.3.1 Thrust for Spring Compression 206
7.3.2 Thrust to Precess High Spin Rate 208
7.3.3 Bottom Line 208
7.4 Breathing Effects 208
7.5 Overall Assessment 209

VIII. Conclusions 211
8.1 Review of Research Objectives 211
8.2 Recommendations for Future Research 213
8.3 Contributions 214

Appendix A. Likins-Pringle Equilibria Development 216
A.1 Equilibrium Condition Development 216
A.2 Stability Analysis 221

Appendix B. Transverse Moment-of-Inertia Development 226

Page

Appendix C. Calculations for Period Matching 231

Appendix D. Period Difference Between Free-Flying Bodies in Likins-Pringle Equilibria 233

Appendix E. Back-of-Envelope Calculations for Kumar Range 241

Appendix F. MATLAB Code 244
F.1 Semi-Rigid Body Codes 244
F.2 Multi-Body System Codes 250

Bibliography 265

Vita 271

List of Figures

Figure		Page
1.1.	Space Tether Example from TSS-1R Mission [1]	2
2.1.	Research Area Flowchart	5
2.2.	Double Pendulum Equilibrium Configurations	7
2.3.	SPECS-HEX Configuration	9
2.4.	SPECS-Tetra-Star Configuration	9
2.5.	Relative Equilibrium for an Axisymmetric Spinning Satellite	13
2.6.	Lumped Mass Tether Bowing	14
2.7.	Double Pyramid Configuration	15
2.8.	Double Tetrahedron Configuration	16
2.9.	Double Tetrahedron Simulation	17
2.10.	Existing Research on Stability Dynamics of Axisymmetric Bodies	18
2.11.	Tether Modeling Factors	21
2.12.	Decou's Static Tether Shape Cases	21
2.13.	Tragesser's Tether Model	22
3.1.	Research Area Flowchart	29
3.2.	Dissertation Overview	32
4.1.	Axisymmetric Rigid Bodies of Interest	34
4.2.	Coordinate Reference Frames and Rotations	35
4.3.	$\hat{e_r}$ axis relative to $\hat{i}$ and $\hat{a}$ frames	41
4.4.	Conical Equilibrium Conditions	46
4.5.	$\vec{H}$, $\vec{\omega}$, and $\hat{b_3}$-axis (Inertial, Prolate Rigid Body, Gravity Off)	48
4.6.	Angles-over-time (Prolate Rigid Body, Gravity Off)	49
4.7.	Dynamic Cones of Torque-Free Rigid Bodies	49
4.8.	$\vec{H}$ and $\vec{\omega}$ in the body frame (Prolate Rigid Body, L-P)	50
4.9.	Angles-over-time (Prolate Rigid Body, L-P)	51

Figure Page

4.10. $\vec{H}$, $\vec{\omega}$, and $\hat{b_3}$-axis (Inertial, Prolate Rigid Body, L-P) 51

4.11. $\vec{H}$, $\vec{\omega}$, and $\hat{b_3}$-axis (Inertial, Oblate Rigid Body, L-P) 52

4.12. $\hat{b_3}$-axis in the orbit frame (Oblate Rigid Body, L-P) 53

4.13. States (Prolate Rigid Body, L-P) 53

4.14. States (Oblate Rigid Body, L-P) 53

4.15. 3-Rotor Set Added to the System 54

4.16. $\vec{H}$ (Body Frame, Prolate Semi-Rigid Body, Gravity Off) 61

4.17. $\vec{H}$, $\vec{\omega}$, and $\hat{b_3}$-axis (Inertial, Prolate Semi-Rigid Body, Gravity Off) 61

4.18. Polhodes of Different Constant Energy Levels 62

4.19. Polhodes with Energy Dissipation 62

4.20. Angles-over-time (Prolate Semi-Rigid Body, Gravity Off) . . . 63

4.21. States and Kinetic Energy (Prolate Semi-Rigid Body, Gravity Off) 64

4.22. $\vec{H}$ and $\vec{\omega}$ (Body Frame, Oblate Semi-Rigid Body, Gravity Off) . 65

4.23. $\vec{\omega}$ and $\hat{b_3}$-axis (Inertial, Oblate Semi-Rigid Body, Gravity Off) . 66

4.24. Angles-over-time (Oblate Semi-Rigid Body, Gravity Off) 66

4.25. States and Kinetic Energy (Oblate Semi-Rigid Body, Gravity Off) 67

4.26. $\vec{H}$, $\vec{\omega}$, and $\hat{b_3}$-axis (Inertial, Prolate Semi-Rigid Body, L-P, 1-Orbit) 68

4.27. $\vec{H}$, $\vec{\omega}$, and $\hat{b_3}$-axis (Inertial, Prolate Semi-Rigid Body, L-P, 10-Orbits) 69

4.28. $\hat{b_3}$-axis in the Rotating Orbit Frame (Prolate Semi-Rigid Body, L-P, 10-Orbit) 69

4.29. $\vec{H}$, $\vec{\omega}$, and the $\hat{b_3}$-axis in the inertial frame (Oblate Semi-Rigid Body, L-P, 1-Orbit) 70

4.30. $\vec{H}$, $\vec{\omega}$, and the $\hat{b_3}$-axis in the inertial frame (Oblate Semi-Rigid Body, L-P, 10-Orbits) 71

4.31. $\hat{b_3}$-axis in the Rotating Orbit Frame (Oblate Semi-Rigid Body, L-P, 10-Orbit) 71

4.32. $\hat{b_3}$-axis in the Rotating Orbit Frame (Oblate Semi-Rigid Body, L-P, Orbits 140-150) 73

Figure Page

5.1. Block Diagram for System Model 76
5.2. Two-Body Reference Frames 77
5.3. Two-Body Likins-Pringle Set-up 83
5.4. Likins-Pringle $\dot{\psi}$ Iteration Loop 84
5.5. Two-body Transverse MOI 85
5.6. Three-Body Ring Formation 86
5.7. Three-Body Reference Frames (Set-up) 87
5.8. Stroboscopic Frame (for Observation) 87
5.9. Three-Body Likins-Pringle Set-up 90
5.10. Three-Body Model Vectors 91
5.11. Body Positions, Verification Example 98
5.12. Tether Length, Verification Example 98
5.13. Initial Body Positions, β=40° 100
5.14. Body Positions, Free Flight, β=40° – Orbit Frame 101
5.15. Body Positions, Free Flight, β=40° – Stroboscopic Frame . . . 101
5.16. Tether Length, Free Flight, β=40° 102
5.17. L-P Free Flight Ellipses – True Anomaly Shift 103
5.18. Body Positions, Free Flight, β=25° 104
5.19. Body Positions, Free Flight, β=70° 104
5.20. Body Positions, Free Flight, β=60° 106
5.21. Relationship of C-W vs L-P parameters 107
5.22. Body Positions, Full Springs, β=40° 110
5.23. "Spring" Length, Full Springs, β=40° 110
5.24. Radial Distance, Full Springs, β=40° 111
5.25. Body Positions Relative, Full Springs, β=60° 112
5.26. "Spring" Length, Full Springs, β=60° 113
5.27. Body Positions, Massless Tethers, β=40° – Baseline 114
5.28. Tether Length, Massless Tethers, β=40° – Baseline 114

Figure Page

5.29. Why Tethers Initially Go Slack 115
5.30. Summary of Initial Three-body Results 118
5.31. Tether Length over Time (3 Body, Non-Linear Tethers, β=40°) 120
5.32. Body Positions, Non-Linear Tethers, β=40° 120
5.33. Tether Length, K_s=2.0) 121
5.34. Tether Length, K_s=0.2 122
5.35. Tether Length, K_s=0.002 122
5.36. Tether Length, K_s=200 123
5.37. Tether Length, μ_d=0.5 124
5.38. Tether Length, μ_d=0.9 124
5.39. Tether Length, $X_\oplus$=6.6 DU 125
5.40. Body Positions, $X_\oplus$=6.6 DU 126
5.41. Tether Length, ρ_o=$\rho(0)$=1 km 127
5.42. Tether Length, Optimized Parameters 128
5.43. Body Positions, Optimized Parameters 128
5.44. Body Positions, Optimized Parameters, t=460K s 129
5.45. Body Positions, Optimized Parameters, t=1M s 130
5.46. Tether Length, Optimized Parameters, 1M secs 130
5.47. 4-Body Hub-and-Spoke Formation 131
5.48. 4-Body Hub-and-Spoke Vectors of Interest 132
5.49. Body Positions, 4-Body H-A-S, β=0°, SR=8.123 134
5.50. Tether Length, 4-Body H-A-S, β=0°, SR=8.123 135
5.51. Tether Length, 4-Body H-A-S, β=0°, SR=8.123, 100K secs . . 135
5.52. Tether Length, 4-Body H-A-S, β=0°, SR=0.812 136
5.53. Body Positions, 4-Body H-A-S, β=0°, SR=0.812 137
5.54. Tether Length, 4-Body H-A-S, β=40°, SR=-1.532, L-P 137
5.55. Body Positions, 4-Body H-A-S, β=40°, SR=-1.532, L-P 138
5.56. Tether Interaction – Subtended Angles < 90° 139

Figure Page

5.57. Tether Interaction – Subtended Angles > 90° 140
5.58. Six Body Ring Formation 140
5.59. Tether Length, 6-Body Ring, β=0°, SR=8.123 142
5.60. Body Positions, 6-Body, β=0°, SR=8.123 142
5.61. Body Positions, 6-Body, Tethers, β=0°, SR=0.812 143
5.62. Body Positions, 6-Body, β=0°, SR=0.812, Snapshots 144
5.63. Initial Motion of 6-Body Formation 144
5.64. Body Positions, 6-Body Ring, β=40°, SR=-1.532, L-P 145
5.65. Body Positions, 6-Body Ring, β=40°, SR=-1.532, L-P, Snapshots 146
5.66. Tether Length, 6-Body Ring, β=40°, SR=-1.532, L-P 146
5.67. 7-Body Closed-Hub-and-Spoke System 147
5.68. Tether Lengths, 7-Body C-H-A-S, β=0°, SR=8.123 148
5.69. Body Positions, 7-Body C-H-A-S, β=0°, SR=8.123 149
5.70. Tether Lengths, 7-Body C-H-A-S, β=0°, SR=0.812 149
5.71. Body Positions, 7-Body C-H-A-S, β=0°, SR=0.812 150
5.72. Tether Lengths, 7-Body C-H-A-S, β=40°, SR=-1.532, L-P . . . 152
5.73. Body Positions, 7-Body C-H-A-S, β=40°, L-P, Snapshots . . . 152
5.74. Body Positions, 7-Body C-H-A-S, Full Springs, β=40°, L-P . . 153
5.75. Torque Required to Precess Spinning Disk 155
5.76. Gravity Gradient Forces Acting on Disks 156
5.77. Gravity Gradient Torque vs Cone Angle 157
5.78. Torque Required and Gravity Gradient Torques Generated . . 157
5.79. Spin Rate Plot with Kumar Range 158
5.80. Tether Length, β=140°, Prolate L-P 160
5.81. Body Positions, β=140°, Prolate L-P 160
5.82. Spin Rate Plot with Updated SR Range 163
5.83. Summary of Simulation Results 164
5.84. Spin Rate Plot with Possible Operating Regions 165

Figure Page

6.1. Tether Lengths, Thrusters as Half-Springs, F_t=2.0, Q_d=0.1 – Baseline 170

6.2. Body Positions, Thrusters as Half-Springs, F_t=2.0, Q_d=0.1 – Baseline 171

6.3. Tether Lengths, Thrusters as Half-Springs, F_t=20.0, Q_d=1.0 – Case 1 173

6.4. Tether Lengths, Thrusters as Half-Springs, F_t=200.0, Q_d=10.0 – Case 2 173

6.5. Tether Lengths, Thrusters as Half-Springs, F_t=0.2, Q_d=0.1 – Case 3 174

6.6. Body Positions, Thrusters as Half-Springs, F_t=0.2, Q_d=0.1 – Case 3 174

6.7. Tether Lengths, Thrusters as Half-Springs, F_t=2.0, Q_d=0.5 – Case 4 175

6.8. Tether Lengths, Thrusters as Half-Springs, F_t=2.0, Q_d=0.1, w/ Perturbations 177

6.9. Body Positions, Thrusters as Half-Springs, F_t=2.0, Q_d=0.1, w/ Perturbations 177

6.10. Body Positions, Thrusters as Half-Springs, F_t=2.0, Q_d=0.1, Optimized Parameters, w/ Perturbations 179

6.11. Tether Lengths, Thrusters as Half-Springs, F_t=2.0, Q_d=0.1, Optimized Parameters, w/ Perturbations 179

6.12. Body Positions, Free Flight, β=40° 180

6.13. Body Positions, Free Flight, "Single Satellite Ellipse", β=40° . 181

6.14. Tether Lengths, Free Flight, "Single Satellite Ellipse", β=40° . 182

6.15. Tether Lengths, Full Springs, Programmed Reels, w/ Perturbations 184

6.16. Body Positions, Full Springs, Programmed Reels w/ Perturbations 184

6.17. Body Positions, Free Flight, β=60° – Circular Formation . . . 185

6.18. Tether Lengths, Free Flight, β=60° – Circular Formation . . . 186

Figure Page

6.19. Tether Lengths, Full Springs, Programmed Reels – "Circular Formation" w/ Perturbations 187

6.20. Body Positions, Full Springs, Programmed Reels – "Circular Formation" w/ Perturbations 187

6.21. Spin Rate Plot with Possible Operating Regions 188

6.22. Desired Precession and Required Torque for an Oblate Rigid Body 189

6.23. $\vec{H}$, $\vec{\omega}$, and $\hat{b_3}$-axis (Inertial, Oblate Rigid Body, Calculated Torques Required) 192

6.24. $\hat{b_3}$-axis (Orbit Frame, Oblate Rigid Body, Calculated Torques) . 193

6.25. Constant Tension Pseudocode 198

6.26. Tension Control Response 198

6.27. Body Positions, Constant Tension, L-P, β=40°, $rr = 1$, $T_{thd} = 0.2$, Δt=1 199

6.28. Tether Lengths, Constant Tension, L-P, β=40°, $rr = 1$, $T_{thd} = 0.2$, Δt=1) 200

6.29. ether Lengths, Constant Tension, L-P, β=40°, $rr = 1$, $T_{thd} = 0.2$, Δt=0.1 201

6.30. Body Positions, Constant Tension, L-P, β=40°, $rr = 1$, $T_{thd} = 0.2$, Δt=0.1 202

7.1. Utility Assessment Indicator Areas 209

8.1. High Spin Rate Constellation Concept 214

A.1. Coordinate Reference Frames and Rotations 216

A.2. Instability Conditions for Oblate Likins-Pringle Equilibria . . . 225

B.1. Transverse Moment-of-Inertia 226

E.1. Centrifugal vs Gravity Gradient Restoring Forces 241

List of Tables

Table		Page
2.1.	Previous Tethered Spaceflights	28
4.1.	Rigid Body Constant Values.	47
5.1.	Baseline 3-body Constant Values	96
5.2.	Baseline Initial Condition Variables for L-P.	99
5.3.	"Optimized" Formation Parameters.	127
6.1.	Case List for Thrust Levels and Delay Times.	172
6.2.	"Optimized" and Baseline Formation Parameters.	178
6.3.	Example Torques and ΔV's (SR=-2.6, θ=40°, r_{disk}=5.7km, m_{disk}=600kg, Δt=10s, Alt=1.1 DU).	194
6.4.	Example Torques and ΔV's (SR=-2.6, θ=90°, r_{disk}=5.7km, m_{disk}=600kg, Δt=10s, Alt=1.1 DU).	194
6.5.	Rigid Body Simulating System – Torques and ΔV's Required for "Perfect" Precession (SR=-2.4, θ=45°, r_{disk}=5.774km, m_{disk}=600kg, Δt=10s, Alt=1.1 DU).	195
6.6.	Rigid Body Simulating System – Torques and ΔV's Required for "Perfect" Precession (SR=-2.4, θ=45°, r_{disk}=5.774km, m_{disk}=600kg, Δt=10s, Alt=6.6 DU).	196
7.1.	Free Flying ΔV Requirements for a Circular Formation [54]. .	207

List of Symbols

Symbol		Page
$\hat{i}$, $\hat{j}$, $\hat{k}$	inertial frame axes	35
ϕ, θ, and ψ	Euler angles	35
A	transverse moment of inertia	36
C	axial moment of inertia	36
I	Moment of Inertia	36
$\oplus$	Center of Mass	36
R_i	elementary rotation matrix	36
C^{bi}	rotation matrix from inertial frame to body frame	36
C^{ab}	rotation matrix from body frame to orbit frame	37
$\vec{M}$	external torque	38
$\vec{H}$	angular momentum	38
$\vec{\omega}^{bi}$	inertial angular velocity of the body	39
$\vec{R}$	position vector from inertial frame origin to rigid body	41
R	distance from inertial frame origin to rigid body	41
X, Y, Z	components of R in body frame	41
$\mu_\oplus$	gravitational constant for the Earth	42
G	universal gravitational constant	42
$M_\oplus$	mass of the Earth	42
$\vec{\varepsilon}$	Euler angle vector	43
X	state vector	43
D_i, E_i, and F_i	moments of inertia of the rotors	55
σ_i	relative spin velocity of the i^{th} rotor	55
J	common minor moment of inertia for the rotors	56
D	common major moment of inertia for the rotors	56
$\vec{H}_{sys}$	total angular momentum of the system	56

Symbol		Page
μ_d	damping coefficient	58
m_i	satellite (or body) masses	76
ν	orbit angle	77
α	right ascension of m_1	77
β	declination of m_1 (ultimately equates to cone angle)	77
ρ	distance between two bodies (or tether length)	78
${}^{\hat{i}}\vec{R}_{\oplus}$	position from inertial frame origin to system CoM	78
r_i	relative position vectors with respect to CoM	78
l_i	tether length from CoM for m_i	78
${}^{\hat{i}}\vec{R}_i$	inertial position vectors	79
${}^{\hat{i}}\vec{V}_i$	inertial velocity vectors	79
$\dot{\nu}$	angular orbit rate	79
h	specific angular momentum	79
$\dot{\psi}$	system spin rate	80
ρ_o	unstretched tether length	81
K_s	tether stiffness (or coefficient of elasticity)	81
ρ_{ss}	steady state tether length	84
n	number of bodies	85
σ	aspect angle	85
$\vec{r}_{ij}$	vector from mass i to mass j	91
E_Y	Young's modulus	96
ΔE	change in total energy	105
ΔP	orbital period difference	105
F_c	centrifugal force	115
F_r	gravity gradient restoring force	115
SR	spin rate ratio	116
F_{gg}	gravity gradient force	155
F_t	thruster force	169

Symbol		Page
Q_d	thruster firing delay threshold	169
ΔV	speed change provided by thruster	169
J_2	second zonal harmonic of the geopotential	176
H_r	$\hat{e}_r$ component of the angular momentum	189
H_3	$\hat{e}_3$ component of the angular momentum	189
Ω_p	angular velocity of the precession	189
ρ_{io}	individual unstretched tether lengths	197
T_{thd}	tension threshold	199
rr_{in}	reel-in rate	199
rr_{out}	reel-out rate	199

List of Abbreviations

Abbreviation		Page
EC	equilibrium condition	4
H-A-S	Hub-and-Spoke	8
C-H-A-S	Closed-Hub-and-Spoke	8
FLT	Feedback Linearization Technique	23
CW	Clohessy and Wiltshire	25
LQR	Linear Quadratic Regulator	26
TSS	Tethered Satellite System	27
SEDS	Small Expendable Deployer System	27
PMG	Plasma Motor Generator	27
NRO	National Reconnaissance Office	27
TiPS	Tether Physics and Survivability Spacecraft	27
OEDIPUS	Observation of Electric-Field Distribution in the Ionospheric Plasma - a Unique Strategy	27
EOM	Equations-of-Motion	34
MOI	moment of inertia	36
L-P	Likins-Pringle	50
KE	Kinetic Energy	59
CoM	Center of Mass	77
RK4	fourth order Runge-Kutte numerical integrator	80
VOI	Variables of Interest	94
ito	in terms of	97
ICs	initial conditions	108

Dynamics and Control of Tethered Satellite Formations for the Purpose of Space-Based Remote Sensing

I. Introduction

Surveillance and imaging of earth objects from space is of particular interest to the U.S. Air Force and the Department of Defense. In an effort to develop and operate unique and innovative space systems the U.S. military has given consideration to the concept of satellite formations, whose shape can be managed by thrusters, tethers, and/or natural dynamic forces. This research is intended to investigate the dynamics and explore methods of control for tethered satellite formations in order to assess the utility of such formations for the particular mission of space-based remote sensing.

1.1 Spaced-Based Formations

Because the mission of interest is space-based, program managers want to increase the aperture of the sensor platform yet decrease launch costs. To decrease launch costs, the spacecraft needs to be small and lightweight. Unfortunately, a single small and lightweight spacecraft is inconsistent with the objective of a large aperture sensor. However, using a formation of these smaller satellites operating in relatively close proximity, space-based remote sensing can be enhanced. A cluster of small satellites with distributed sensors can provide a large overall virtual aperture while also decreasing overall system size and weight. The bulk of this present research presumes that the portion of the satellite cluster that forms the virtual aperture is distributed in a "ring" or circular formation to most closely simulate a single large aperture, and therefore create the best observation plane for the mission.

Satellite formations in general have been of particular interest in recent years [7, 11, 54, 57, 61]. The general problem for free-flying satellite clusters is that each spacecraft in the cluster is in a slightly different orbit about the parent body (such

as the earth), therefore the satellites have a natural relative motion with respect to each other. This natural relative motion is further complicated by the presence of perturbations. The challenge then becomes stationkeeping to maintain the relative shape of the cluster.

1.2 Tethered Systems

Many research efforts have investigated the use of thrusters to maintain guidance and control of such clusters, however thruster propulsion is a non-renewable resource, and as such limits mission lifetime. Alternatively, some research has investigated the feasibility of using tethers under tension to maintain the shape of the satellite formation [26,77]. A tether is simply a length of high-strength fibers or wires (typically only a couple of millimeters in diameter) that can be used to couple spacecraft together (see Figure 1.1). The basic idea is that positive tether tension can be maintained from the centrifugal forces caused by system rotation. Additionally, one could control the tension in the tethers by reeling in or paying out tether length between the various bodies. Using tethers could minimize or eliminate the dependence on reaction thrusters for stationkeeping, thus extending mission life.

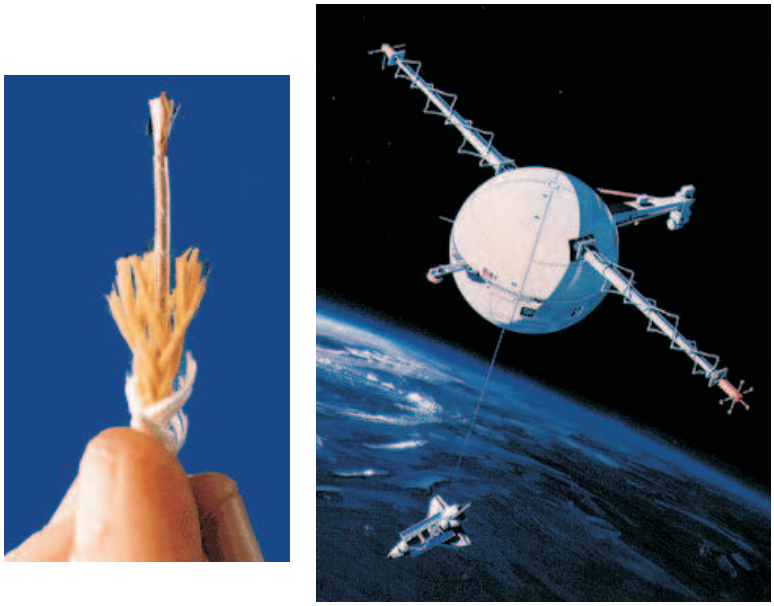


Figure 1.1: Space Tether Example from TSS-1R Mission [1]

1.3 Remote Sensing Mission

To perform the mission of remote sensing of earth objects, the satellite formation would optimally have a continuous earth-facing component. That is, a projection onto the earth of the virtual aperture created by the "ring" formation must remain fairly constant. Limited research has been accomplished for this particular application of tethered satellite formations, but one of the key contributions was Tragesser [66]. He noted a stability condition for axisymmetrc rigid bodies called the conical Likins-Pringle equilibrium [20] behaves precisely as described above: a component of its spin axis is always "facing" the earth (nadir) from a circular orbit. Tragesser proposed that one might find a tethered system equilibrium condition that is comparable to a conical Likins-Pringle equilibrium. This concept was applied for both oblate [66] and prolate [67, 69, 78] formations, but the majority (and most recent) work has been focused on prolate, double-tetrahedron formations. To date, no one has found a conclusively long-term stable condition for an earth-facing tethered system.

1.4 Research Goals

The hypothesis of this research is that tethers can reduce or eliminate the cost of formation control and combat perturbing forces for the space-based remote sensing mission by passively maintaining semi-rigid behavior through tension. The overarching goal of this research is to evaluate the relative utility of tethered satellite systems for continuously earth-facing aperture clusters. To perform this evaluation, several specific research objectives are undertaken in a build-up fashion. As mentioned above, no one has found a conclusively long-term stable condition for an earth-facing tethered system. It is possible that long-term stability in Likins-Pringle is not feasible due to the equivalent dynamic effects akin to energy dissipation on a rigid body. Hence, the starting point of this research is to assess the effects of energy dissipation on the Likins-Pringle equilibria for rigid bodies. The remaining rationale behind each of the five objectives is detailed in the next chapter.

Objective 1: Determine Effects of Energy Dissipation: Determine the effects of energy dissipation on semi-rigid bodies that are in/near Likins-Pringle dynamic equilibria.

Objective 2: Find an Equilibrium Condition – Semi-Rigid Body: Define and/or determine the existence of an equilibrium condition (EC) for a semi-rigid body with a continuous earth-facing component in the presence of energy dissipation.

Objective 3: Find an Equilibrium Condition – Tethered System: Define and/or determine the existence of an equilibrium condition for a flexible tethered satellite system with a continuous earth-facing component.

Objective 4: Apply Controls: Apply control schemes to the tethered system to combat perturbations and maintain desired motion.

Objective 5: Assess Utility: Assess the relative utility of using tethered systems for formation control on continuously earth-facing aperture clusters.

1.5 Chapter Outline

The historical development and rationale for these specific objectives is covered in more detail in Chapter II. The methodology roadmap and overview for the current research is discussed in Chapter III. With Chapter III serving as a research outline, Chapters IV-VII delve into the specifics of each phase. Chapter IV is a presentation of the rigid body work, while Chapter V covers the tethered systems dynamics. The application of various control schemes to the tethered systems is discussed in Chapter VI. Chapter VII serves as an assessment on the utility of tethered systems for conducting space-based remote sensing. Finally, Chapter VIII reviews the objectives, discusses recommendations, and highlights the contributions of this research to academia, the remote sensing mission, and the Department of Defense.

II. Historical Development for Research in Tethered Formations

The study of tethered satellite systems spans multiple decades and hundreds of authors. This chapter presents an overview of previous work from the pertinent areas of this research, such as tethered system dynamics and tether modeling. Each area of research is broken out into a separate section. Figure 2.1 shows a flow diagram of how each research area ties to the next. The arrows denote what research areas are required at each level to accomplish the previous level. The numbered research objectives for this work are shown next to their corresponding areas and will be highlighted throughout this chapter, although they do not appear in sequential order.

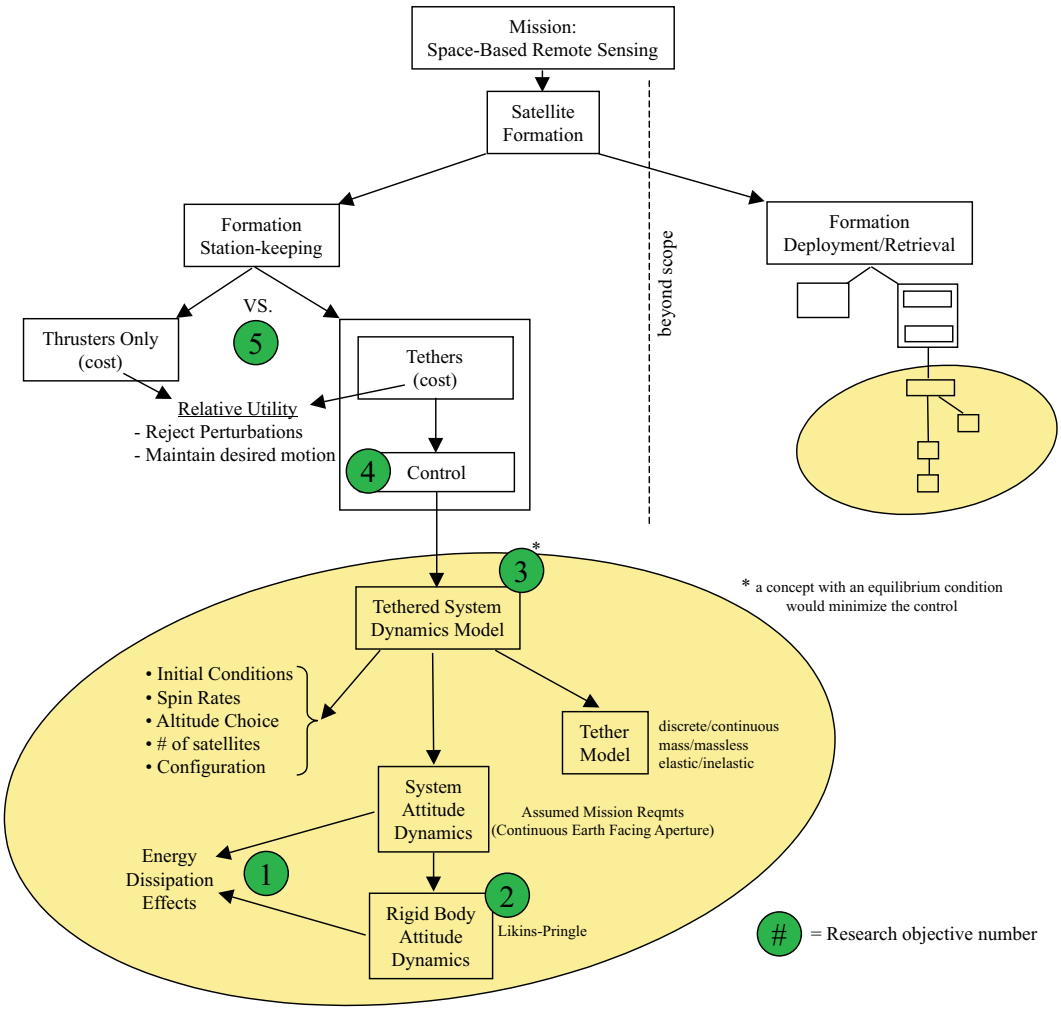


Figure 2.1: Research Area Flowchart

2.1 Tethered System Dynamics

2.1.1 General Tethered Systems.

As early as the 1960's, researchers have investigated the dynamics of tethered systems [2, 4, 9, 27, 49]. Over the years, the concepts and configurations have ranged from single satellites with flexible appendages to constellations of small satellites with multiple tethers connecting each object [5, 12]. Examples of the various applications and benefits of tethered systems include: momentum/orbit transfer, attitude control, artificial gravity, atmospheric measurements, electrodynamics, and space interferometry.

The most common research in tethered system dynamics and control, especially in the 1980's, involved 2-body/1-tether systems, where gravity-gradient forces create a nadir pointing system equilibrium [14, 35, 38, 39]. By comparison, a relatively small amount of research has been accomplished for multiple body/multiple tether formations, as summarized in Williams [77] and Kumar [26].

In 1987, Misra, Amier, and Modi [33] studied the dynamics of tether-connected three-body systems in a circular orbit for both constant and variable length tethers. Their study was confined to a double pendulum arrangement with motion limited to the orbit plane. They found four equilibrium conditions, where the in-plane orientation with respect to an orbiting reference frame is fixed, but they assumed massless tethers. The four equilibrium configurations are shown in Figure 2.2. Two are collinear while two lie in a triangular formation.

Several years later, Misra and Modi [36] expanded their study to three dimensions and considered N-bodies connected by N-1 tethers in a "string-of-pearls" fashion. They noted quantifiable relationships between in-plane librations, out-of-plane librations, and orbital frequency for one of the equilibrium conditions they had found earlier. This work was broadened further by Keshmiri, Misra, and Modi [23] in 1996. They considered the same N-bodies/N-1 tethers for both in-plane and out-of-plane librations but generalized the formulation to include tether mass and elasticity to

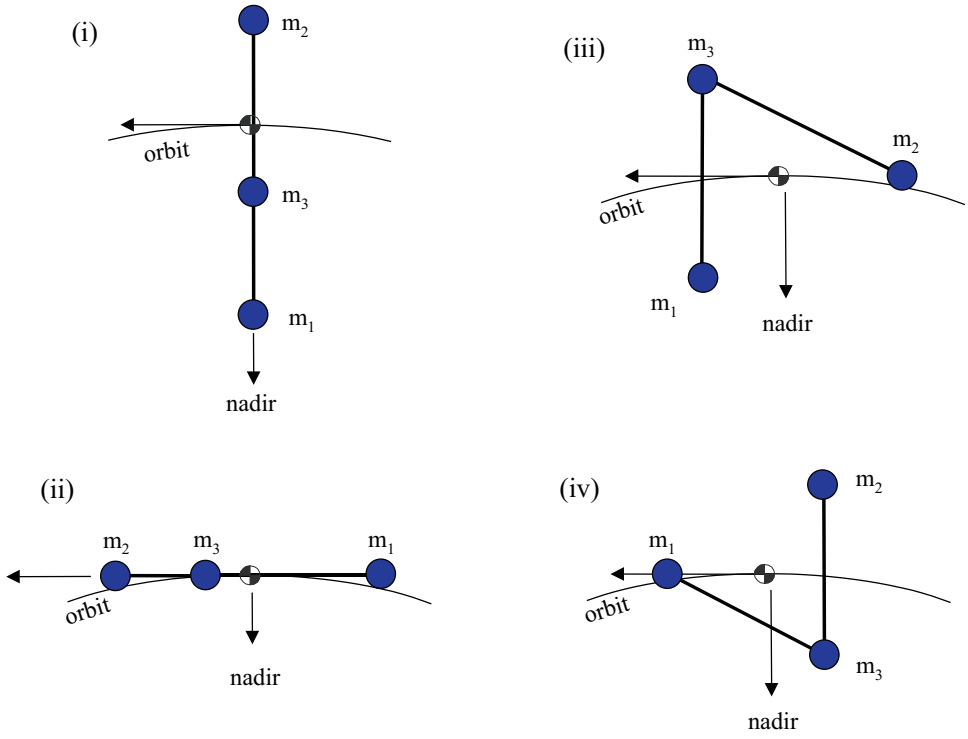


Figure 2.2: Equilibrium Configurations of Misra et al. [33]

account for upper atmospheric perturbations. Furthermore, they found that while damping had little effect on transverse tether oscillations, it had a significant effect on longitudinal oscillations of the tethers. Kalantzis et al. [22] continued working with this generalized formulation, but expanded the research by adding emphasis on attitude and vibrational control schemes. Discussion of this work will be included in the *tether controls* section of this chapter. In 2001, Misra [37] once again investigated the four planar equilibrium configurations of the three-body tethered system in circular orbit. While the previous studies were numerical in nature, Misra took a more analytical approach in this work and examined the stability of the four equilibrium configurations. The vertical configuration was found to be Lyapunov (marginally) stable while the triangular configurations were found to be unstable. Lyapunov stable meant that small perturbations from the equilibrium condition would result in oscillatory behavior in the neighborhood of the equilibrium. Asymptotic stability was not found for these equilibria.

Pizarro-Chong and Misra [47] studied the dynamics and stability of spinning N-body tethered systems in low earth orbit, but they looked at two new kinds of configurations: 1) hub-and-spoke (H-A-S); and 2) closed hub-and-spoke (C-H-A-S). The hub-and-spoke formation involved a central body with individual satellites tethered independently to it. The closed hub-and-spoke formation included the same system as the normal hub-and-spoke but each of the peripheral satellites were also connected to each other in a "ring" using outer tethers. They found that for up to four bodies, the hub-and-spoke configurations were stable (asymptotic or Lyapunov) assuming an initial spin rate and massless, yet elastic tethers. Above four bodies, outer tethers (C-H-A-S) were required for stability. Their work was limited, however, to very high spin rates (10-30 times the orbit rate) and two specific system orientations (orbit plane and normal to orbit plane), neither of which can remain earth facing.

2.1.2 Inertially-Fixed Systems.

One of the emerging concepts for tethered constellations is interferometry. Generally speaking, a spinning constellation of tethered satellites will tend to keep its spin axis inertially fixed, lending itself nicely to astronomical observation missions. With this in mind, Quinn and Folta [52] proposed a mission concept called the Submillimeter Probe of the Evolution of Cosmic Structure (SPECS), which would be a tethered constellation located at the Sun-Earth L_2 Lagrange point. Their proposed hub-and-spoke configuration, called SPECS HEX, employed three 600 meter long tethers, each with a mirrored subaperture on one end, and a ballast on the other (see Fig. 2.3). The ballasts reel-in and reel-out in the opposite direction of the subapertures to keep a constant system spin rate should the subapertures need to be moved in or out.

Farley and Quinn [18] performed further operational evaluations of the SPECS HEX concept as well as an additional configuration they called the SPECS Tetra-Star. The Tetra-Star configuration also uses three subapertures and three ballasts,

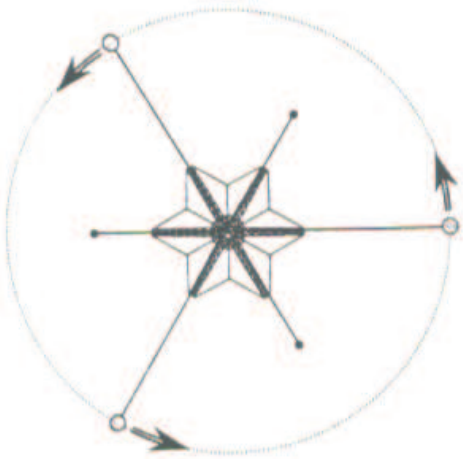


Figure 2.3: SPECS-HEX Configuration [52]

but makes use of nine tethers in triangular formations to give the system more in-plane shape rigidity (see Fig. 2.4).

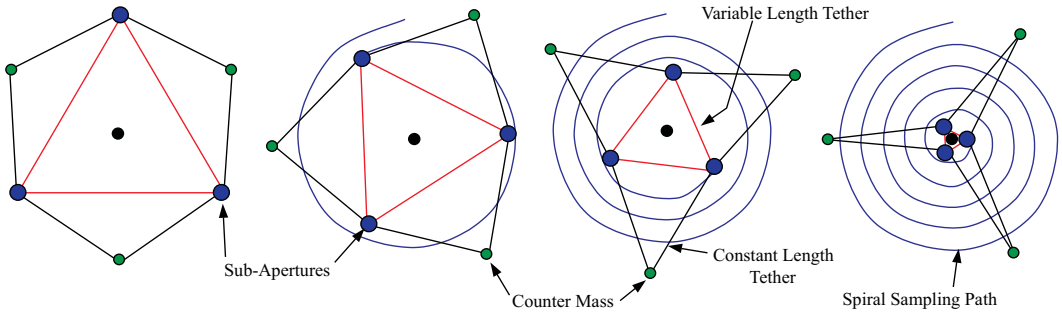


Figure 2.4: SPECS-Tetra-Star Configuration [18]

Recently, Kim and Hall studied the dynamics and control of multiple point masses interconnected by multiple idealized tethers as applied to the SPECS mission. Particular attention was paid to the symmetrical triangular scenario of three masses and three tethers. They evaluated relative equilibria and designed controllers to meet specific SPECS mission scenarios [25]. Similarly, they evaluated the Tetra-Star configuration and compared the utility of Tetra-Star to the triangular formation. They found that the complexity of Tetra-Star made it less controllable and less stabilizable than the basic triangle, especially for plane changes [24].

In 2001, Marco Quadrelli built a numerical simulation environment for studying the dynamics and control of tethered formations. His model was capable of including N spacecraft, three-dimensional elastic tethers, and thermal perturbations. Using his model, Quadrelli developed simulations for three different tethered configurations: a two-spacecraft system; a three-spacecraft/two-tether "string of pearls" system; and a four-spacecraft/three-tether "hub-and-spoke" system [50]. Quadrelli's work supported both the heliocentric astronomical observation missions as well as the low earth orbit (LEO) interferometry missions.

Misra et al. [34] considered the planar motion of a two-satellite tethered system in the vicinity of the Earth-Moon Lagrangian points. They found that the librational frequencies of the tether are approximately $4n$ at L_1, $3n$ at L_2, and $\sqrt{3}n$ at all other Lagrangian points, where n is the lunar mean motion.

Around the same time as the previous two works, Bombardelli et al. [6] took a closer look at a specific tethered space interferometer concept. They analyzed the pointing dynamics of a three-body "string-of-pearls" in an earth-following, heliocentric orbit. Particular attention was paid to the influence of environmental perturbations. Solar radiation pressure and thermal variations were found to the dominant perturbations. The former affect causes lateral oscillations of the system, while the latter causes cyclic variations in tether length. They also made recommendations regarding tether material properties.

In 1989, Decou [16] performed a detailed analysis of the static shape of finite mass tethers in a rotating triangular system of three-spacecraft/three-tethers. This work is detailed further in the *Tether Modeling* section, and provides the initial look at calculating the dynamic response of the same system in the presence of perturbing dynamic forces, such as gravity gradient, solar radiation pressure, and atmospheric drag. Decou also studied the specific effects of gravity gradient forces on the rotation rate and out-of-plane motion for three-body, triangular, spinning tethered systems [15] and applied this to a geocentric astronomical observation mission [13]. He assumed

massless, fixed-length tethers and assumed the rotation rate of the tethered system would be significantly higher than the orbital rate of the system. The result was an inertially fixed spin axis for the triangular system.

2.1.3 Earth-Facing Systems.

The study of inertially-fixed, astronomical systems above leads to another natural application of spaced-based interferometry: remote sensing, or earth observation, from geocentric orbit. However, to perform earth observations from a nearby orbit, different attitude dynamics of the system must be created. Keeping a system's spin axis inertially fixed works well for the interferometry missions that observe long distant astronomical phenomenon, but in the case of remote sensing, the tethered system would need to continuously change its orientation such that the formation of sensors would constantly "face" the earth.

The most inexpensive way to accomplish this constant geocentric attitude maneuver is to find a stable relative equilibrium condition that balances all the dynamic forces in the orbit's rotating reference frame such that the system's attitude changes at approximately the same rate as the orbital rate. This is defined in one of the research objectives, which is restated below:

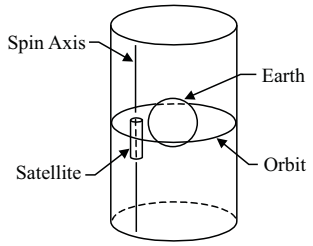
Research Objective 3 (and 2): *Define and/or determine the existence of an equilibrium condition for a flexible tethered satellite system (and semi-rigid body) with a continuous earth-facing component.*

Obviously, finding the equilibrium condition is dependent on the specific tethered formation geometry that is chosen. For example, some researchers tackled this problem by letting gravity gradient forces stabilize a single tether in a nadir direction [14, 38, 39]. The equilibrium condition for this relatively simple geometry is easy to see. Unfortunately, single tether geometries will presumably not create the desired apertures required for many earth observation missions.

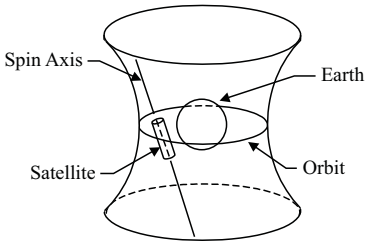
Rotating ring formations, on the other hand, are assumed to create better observation planes, but an equilibrium condition needs to be found such that the spin axis of the formation rotates with the system's orbit, ensuring the relative spin axis always has a component along the nadir direction. A comparitively small amount of research has been dedicated to this particular kind of tethered dynamics problem [26, 66, 67, 69, 78], however it is the foundation of this present work, so it is detailed in the remainder of this section.

In 2000, Tragesser [66] investigated the motion of a three-body, planar, tethered ring formation, much like Decou. Tragesser's primary differences from Decou were: 1) Tragesser also considered the more general N-body ring formation; and 2) the spin rate of the Tragesser's ring formation was much slower than Decou's, allowing the spin axis to vary in inertial space. Tragesser advanced the idea of finding a relative equilibrium condition for an N-body ring formation by first looking at the stable equilibria of an axially-symmetric spinning rigid body in a circular orbit. These rigid body equilibria are divided into three classes: cylindrical, hyperbolic, and conical [20]. Each was named for the relative three-dimensional shape created by the motion of the spin axis during the orbit (shown in Figure 2.5). The cylindrical case is also known as the Thomson equilibrium [65], where the spin axis is perpendicular to the orbit plane and the gravitational torque disappears. The latter two are called Likins-Pringle equilibria where the gravitational torques cause the rigid body to precess at the same rate as the orbital rate.

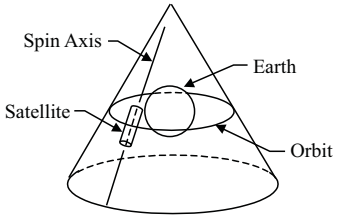
Tragesser modeled his three-body ring formation with the assumption that the spin tension would "rigidize" the system, thus closely emulate the rigid body and obey the same relative equilibria. He performed numerical simulations for both the cylindrical and conical cases, but the conical case is the only one that offers a component of the spin axis in the nadir direction. That is, the conical case is the only one that allows the ring formation to project an ellipsoid on the earth's surface for the application of remote sensing.



(a) Thomson Equilibrium -- Cylindrical Case



(b) Likins-Pringle Equilibrium -- Hyperbolic Case



(c) Likins-Pringle Equilibrium -- Conical Case

Figure 2.5: Types of Relative Equilibrium for an Axisymmetric Spinning Satellite in Circular Orbit [20]

He modeled the flexible tethers as discrete masses, and started each simulation with the tethers perfectly straight on each side of the triangular formation, letting them bow out over the course of the simulation as shown in Figure 2.6.

Tragesser concluded that tether flexibility introduces unstable modes in the rigid-body equilibria. For the cylindrical case, two relative spin rates were used: $0.5n$ and $5n$, where n is the orbital rate. When the spin rate was $0.5n$, the system was not stable. When spun at the higher rate, however, the system behaved similarly to a rigid body. For the conical case, none of the attempted spin rates produced stable results, unless tether flexibility was removed.

Most recently, Kumar and Yasaka [26] investigated the cylindrical case of the three-body/three-tether triangular system and found that the spin rate required for

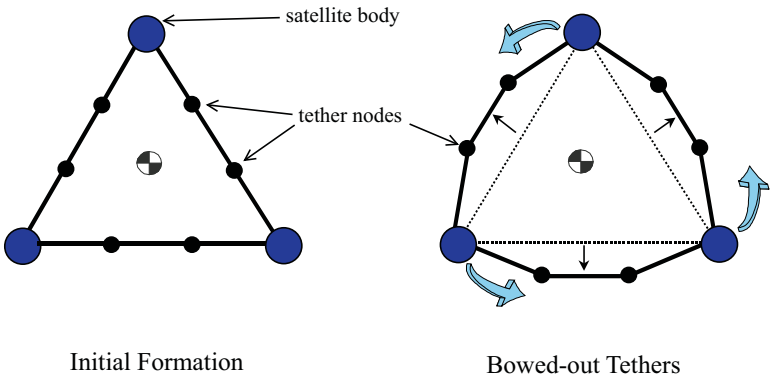


Figure 2.6: Lumped Mass Tether Bowing

system steady-spin motion in the orbital plane was greater than $0.58n$ or less than $-2.58n$. In later chapters, this range of values ($-2.58n$ to $0.58n$) is referred to as the "Kumar Range". Their analysis included massless, elastic tethers and considered elliptical orbits as well.

In 2002, Williams and Moore [78] investigated two different tethered configurations, each with a different technique for producing the necessary, non-propulsive torque required to keep the formation earth-facing. They assumed massless tethers that remain straight for both configurations. The first configuration was a planar ring similar to Decou and Tragesser, with the added notion of using conductive tethers and geomagnetic interaction to produce the required torque. They concluded that the current and power requirements for such electromagnetic torquing would likely be too prohibitive for large scale tethered systems. The second configuration considered by Williams and Moore was a three-dimensional double-pyramid geometry of four ring satellites, two anchor masses, four ring tethers, eight diagonal tethers and a single "spine" tether as shown in Figure 2.7.

The idea for this double-pyramid configuration was to use gravity gradient forces acting on the anchor masses to stabilize the spin axis along nadir. Williams and Moore explored various combinations of values for spin rate and fraction of gravity gradient tension carried by the spine and proposed a stability region with those parameters as variables. They found that tether tension, while growing over two system rotations,

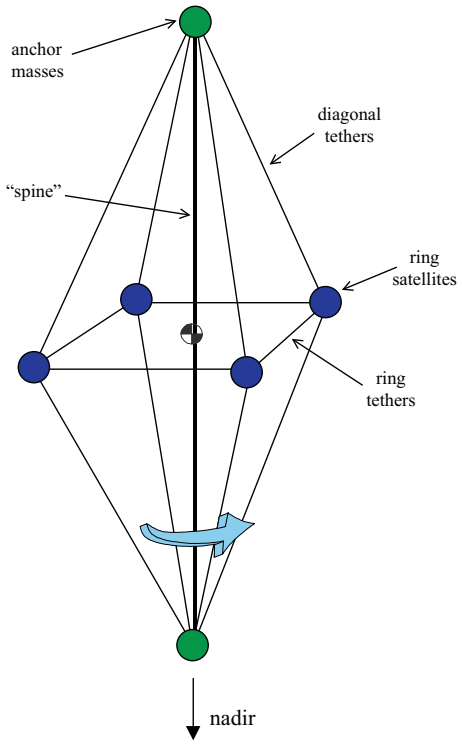


Figure 2.7: Double Pyramid Configuration

stayed small and positive. They also observed that spin rates less than $1.33n$ produced unstable results, and they reported that spin rates higher than $4.36n$ would produce stable behavior without a spine tether. In addition, they determined that stablility was also tied to geometric parameters of the formation, such as height-to-width and mass ratios.

A short time later, Tragesser and Tuncay [67, 69] applied the double-pyramid idea to Tragesser's original concept of using the Likins-Pringle equilibria. Their new configuration was a double tetrahedron with three ring satellites, two anchor masses, three ring tethers, and six diagonal tethers – basically, the double-pyramid with one less ring satellite and no central spine tether (see Figure 2.8). As with Tragesser's first study, they investigated the stability of such a formation when placed in the off-nadir, earth-facing orientation created by the Likins-Pringle conical equilibria. They included flexibility of the tethers in their model using discrete, lumped masses.

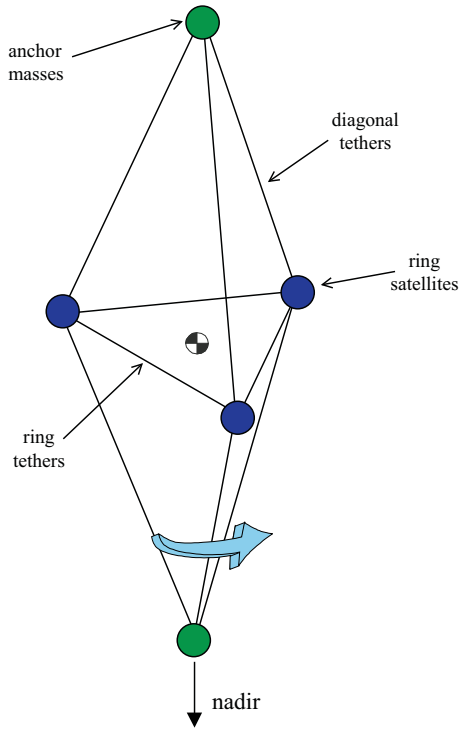


Figure 2.8: Double Tetrahedron Configuration

The main design parameters for the formation were: height, diameter, spin rate, and mass ratio. They ran simulations for ten orbits and plotted the positions of the masses and tether elements with respect to a rotating orbital frame, $\widehat{o}$. Figure 2.9 shows typical results of their simulations. The oscillations in the tether elements are due to the tethers starting perfectly straight yet bowing outward during system rotation [16].

The numerical results of Tragesser and Tuncay demonstrated that such a formation could hold a 'stable' orientation toward the earth in the short term (i.e. for a number of orbits) before controls would need to be applied. However, all of the configurations they analyzed eventually diverged, meaning they had not yet found an equilibrium condition that was Lyupanov stable. Even so, they did recognize that some configurations were more stable than others and they illustrated stability regions of their main formation parameters, namely formation dimensions, mass ratios and spin rates.

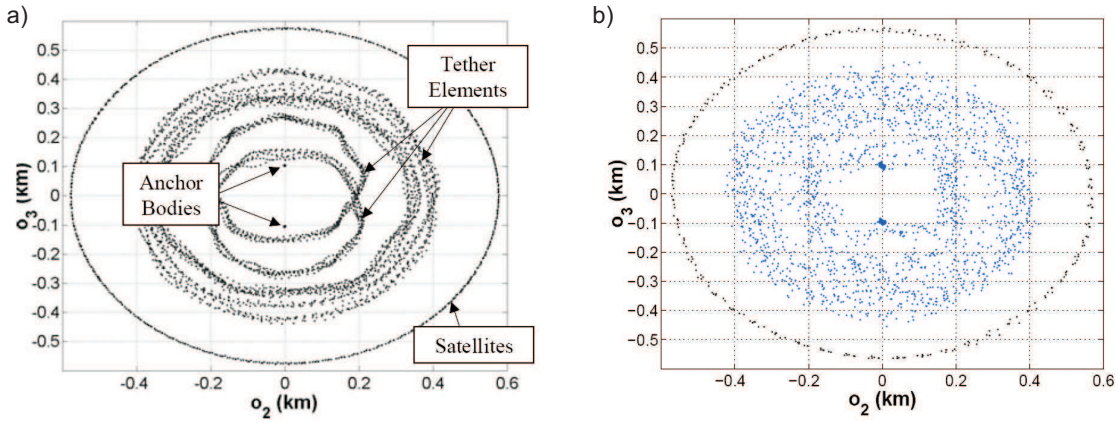


Figure 2.9: Double Tetrahedron Simulation: a)after 1 orbit b)after 10 orbits [67]

One of the hypotheses of this present research is that the "prolated-ness" of the above three-dimensional configurations creates a double-edge sword. For example, in rigid body dynamics, a prolate object takes advantage of gravity gradient torques to keep the long axis pointed earth-ward, but a prolate object also has a tendency to migrate away from spin about its minor axis when subjected to energy dissipation [75]. The presumption is that flexible/elastic tethers introduce energy dissipation on the system and might therefore explain why Tragesser and Tuncay were unable to find long term stability for their prolate formation. It is important then, to try and understand the effects of energy dissipation on the Likins-Pringle dynamic equilibria when attempting to find a new equilibrium condition. This is formulated in the first research objective, repeated below:

Research Objective 1: *Determine the effects of energy dissipation on semi-rigid bodies that are in/near Likins-Pringle dynamic equilibria.*

2.2 Semi-Rigid Body Dynamics

As mentioned in the last section, the study of rigid and semi-rigid body dynamics could give great insight into finding a dynamic equilibrium condition for a tethered system. To that end, this section highlights what has been accomplished in the pertinent areas of stability dynamics of axisymmetric (semi-)rigid bodies. A Venn

diagram is included in Figure 2.10 to help illustrate how the different areas of research interconnect.

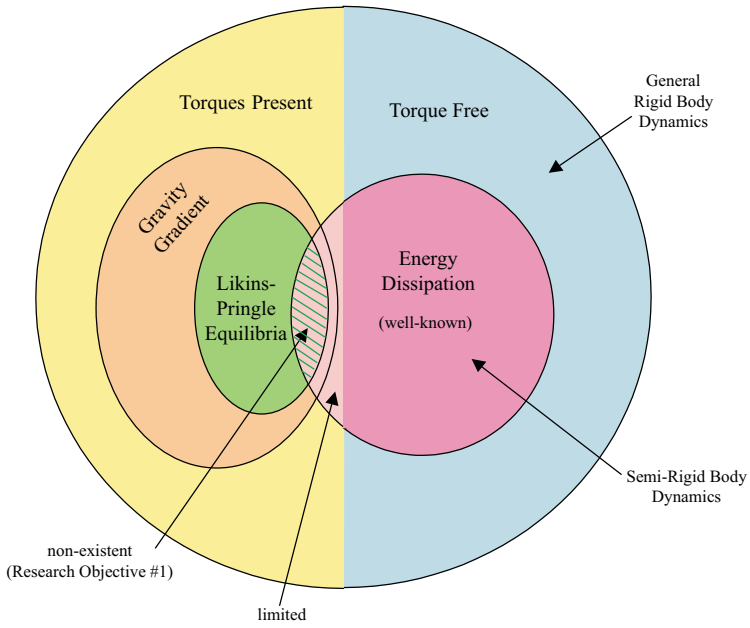


Figure 2.10: Existing Research on Stability Dynamics of Axisymmetric Bodies

In effect, this research couples two formerly independent areas of study: torque-free energy dissipation effects and dynamic equilibria in the presence of particular torques. There has been plenty of research done in both areas independently but virtually nothing that combines the two (that is, energy dissipation effects on a torque-induced equilibrium condition).

2.2.1 Rigid Body Equilibrium Conditions (with Torques Present).

A large body of work exists that discusses the stability dynamics of axisymmetric bodies in the presence of gravity gradient torques. This area is represented by the orange section of the Venn diagram in Figure 2.10. These works date back as far as the 1960's [29, 40, 53, 63, 64] and were expanded on by various authors over the next several decades [45, 59, 72], but Hughes [20] was the one key piece of literature that outlined and summarized the three classes of relative equilibria of a spinning, axially-symmetric, rigid body under the influence of gravity gradient torques in a circular

orbit. As noted in the previous section, these three classes of relative equilibria are: cylindrical, hyperbolic, and conical. Of these, the conical case is the only one that is useful to the earth-facing application of remote sensing, so it will of primary interest in this present research.

2.2.2 Energy Dissipation (Torque Free).

A discussion of the effects of energy dissipation on a semi-rigid body in a torque-free environment can be found in almost any text on rigid body dynamics [20, 60, 74, 75]. The two key concepts involved are the Energy Sink Hypothesis and the Major Axis Rule.

The Energy Sink Hypothesis states that "during the motion of any real body the kinetic energy will tend to be converted – slowly – to heat energy [20]." In the case of truly semi-rigid bodies, like those with flexible booms or sloshing fuel tanks, the loss of kinetic energy due to internal motion is easily understood.

The Major Axis Rule as surmised by Sidi [60] says that "in the presence of energy dissipation, a spinning body is in stable angular motion only if the spin is about the major axis." Wiesel [75] further states that for the axisymmetric case, "pure spin about the symmetry axis is stable only if the symmetry axis is the major axis. Prolate semi-rigid bodies will eventually achieve an end-over-end tumble state." This could be an important point in the context of the prolate three-dimensional tethered formations that were previously considered.

Multiple authors have investigated the attitude stability of semi-rigid bodies and have derived stability criteria using Liapunov's second method [21] as well as the method of averaging [68]. Along the way, it has been noted that semi-rigid bodies carry with them certain caveats to conventional theory. For example, Hughes and Fung [21] found that for spinning satellites with long flexible appendages, the Major Axis Rule is a necessary, but not sufficient condition for stability. However, they went on to derive the necessary conditions and showed that flexible booms could be used to stabilize an unstable central body.

2.2.3 Energy Dissipation (with Torques Present).

By comparison, very little study has been devoted to energy dissipation effects in the presence of external torques (represented by the left side of the pink section of the Venn diagram on Figure 2.10).

One of these few pieces of work was done by Livneh and Wie [31], who studied the effects of energy dissipation on a rigid body under the influence of constant body-fixed torques about either the major, intermediate, or minor axis. Their conclusions, based on numerical simulations, were: "(i) torque about the major resulted in a spin up maneuver in the torque direction, (ii) for torque about either the minor or the intermediate axis the spacecraft ended up rotating about an equilibrium point with large angular velocity component about the major axis, (iii) the polarity of the final equilibrium point is sensitive to initial conditions and also tends to converge to the nearest branch of the corresponding hyperbola of equilibrium points, and (iv) a constant minor axis torque might result in a flare up in angular velocity about this axis before converging to an equilibrium point with large angular velocity component about the major axis [31]." Their research differs from this present work since our external torques of interest (gravity gradient) are not body-fixed.

2.2.4 Energy Dissipation (with Specific Gravity Gradient Torques).

As of this writing, no research has been found on the study of energy dissipation effects on a semi-rigid body under the influence of gravity gradient torques when placed in one of the Likins-Pringle stability equilibria. This is the green hashed area of the Venn diagram in Figure 2.10 (Research Objective 1).

2.3 Tether Modeling

A major consideration in the development of a tethered system model is how to model the tethers themselves. Figure 2.11 shows three main factors to consider when deciding how to represent the behavior of the tethers: elastic vs inelastic (assume they

stretch?), massless vs flexible (assume they bow out?), discrete mass vs continuous mass (simplifying solution).

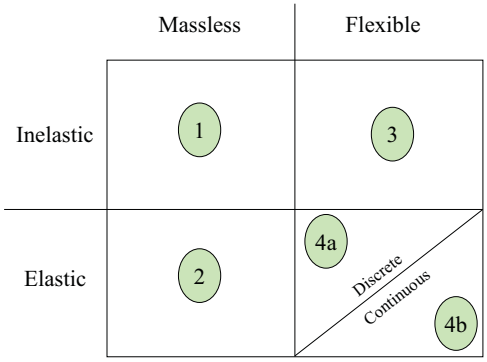


Figure 2.11: Tether Modeling Factors

The body of work in tethered systems to date covers all combinations of these factors (i.e. all areas in Figure 2.11 have been explored), but the majority of authors assumed massless, inextensible tethers (quadrant 1) [15, 24, 25, 33, 36, 37, 77]. Others kept their tethers as massless, but allowed for the elasticity (quadrant 2) [26, 47].

Very few individuals would consider modeling tethers in quadrant 3, since it would seem that flexibility and elasticity go hand-in-hand. Fortunately, Decou didn't see it that way. As a result, his work isolated the static shape of a tether with finite mass density under the influence of the centrifugal forces caused by rotation without the added complexity of elasticity or any disturbing dynamic forces [16]. Decou considered two cases: 1) three equal masses and three equal tethers (Fig. 2.12a); 2) three more equal masses added to the first formation midway between the original masses (Fig. 2.12b).

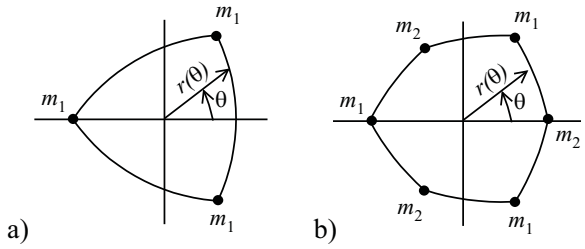


Figure 2.12: Decou's Static Tether Shape Cases [16]

Decou was able to identify two boundary conditions and a third constraint that must be satisfied for the static solution [16]. His solution to the statics problem became a foundation for studying the dynamic response of flexible tethers in the presence of gravity gradient, solar radiation pressure, atmospheric drag, and thermal expansion forces.

A number of studies allowed for the most detailed tether models, assuming the tethers had both mass and elasticity (quadrant 4 of Figure 2.11) [22, 23, 66, 67, 79]. Within this family of research, most chose to discretize the tethers into an arbitrary number of lumped masses or "beads" [5], while others tried elastic continuum techniques to model the tethers mass [79].

The tethers modeled in this present research are assumed at first to be massless and elastic (quadrant 2), with the intent to transition over to a discretized lumped mass approach (quadrant 4a) similar to Tragesser and Tuncay. In their configuration, there was a total of nine tethers: three ring tethers and six diagonal tethers. Each tether was modeled using two additional mass elements (see Figure 2.13), each element weighing about 1/100 of the system masses. They assumed a tether stiffness of 20N/m and a damping coefficient that was 1/1000 of the stiffness. As it turns out, the transition to the discretized lumped mass approach becomes unnecessary, as will be explained in Chapter V, therefore a massless/elastic tether model is used throughout this research. Tragesser and Tuncay's values for tether stiffness and damping coefficient are used as the baseline.

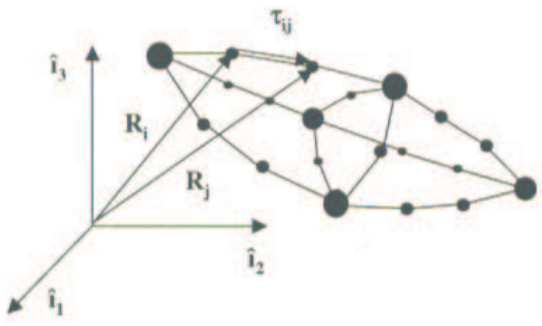


Figure 2.13: Tragesser's Tether Model [67]

2.4 Formation Control Using Tethers

Once the dynamics of a full tethered satellite system is successfully modeled and an equilibrium condition (or close to one) is found, it is desired to use some form of control to reject various disturbances on the system and keep the system "looking" where we want it to look.

Research Objective 4: *Apply control schemes to the tethered system to combat perturbations and maintain desired motion.*

The intent of this objective is not to broaden the field of control theory, but rather it is a necessary step for determining the relative utility of using tethers to perform formation stationkeeping. To this end, and without knowing what kind of control might be useful, a survey of various studies on tethered system control was conducted.

A number of authors have done research on control theory applied to various tethered systems. However, their specific applications typically differed from the mission of remote sensing [13, 22, 23, 34, 36, 41, 42] and/or the scope of control was more detailed than what this present research requires [24, 25, 48]. In the case of Mori et al. [41, 42], they established a coordinated feedback control method using tether reels, thrusters, and CMGs, however they assumed the torque created by gravity gradient was insignificant given high relative spin rates of their system. Likewise, Kim and Hall [24, 25] made a similar assumption about the impact of gravity gradient torques given that the SPECs mission was located at the Ł$_2$ Lagrangian point of the Sun-Earth system. Essentially, their adaptive output-feedback controller was used to control much finer detailed responses than what this current research requires.

As mentioned in a previous section, Kalantzis et al. [22] built upon the work of Misra et al. [34, 36] and Keshmiri et al. [23] by looking at attitude and vibrational control schemes on a "string-of-pearls" formation. Their analysis included thrusters and momentum-wheels to regulate the attitude of the individual links using a non-linear feedback linearization technique (FLT) as well as a robust linear quadratic Gaussian-

loop transfer recovery method to control vibrations using tether reels. By comparison, Keshmiri et al. were looking to control about much finer attitude librations than what were encountered in this present research.

In the case of Pradhan et al. [48], controllers were designed using tether length rate, tether tension, and offset (which is the time dependent variation of the tether attachment point at the platform end) to simultaneously regulate the tether dynamics as well as the platform dynamics. In this present research, attitude dynamics of the individual platforms is not addressed.

There were also a number of authors who focused their studies on the control laws necessary for deployment/retrieval of the tethered systems [17, 26, 28, 43, 44, 77]. Although deployment/retrieval is beyond the scope of this research (see Figure 2.1), many of the control algorithms used by these authors may prove beneficial in deriving a control scheme for the stationkeeping of a tethered system. Kumar and Yasaka, who investigated the cylindrical case of the three-body/three-tether triangular system and found the spin rate required for steady-spin motion (Section 2.1.3), also developed open-loop deployment/retrieval control laws for the tether reel rates [26]. These control laws were based on system orbit position and time allowed for system deployment/retrieval.

Williams [77] created an FLT optimal controller for a 3-body, spinning tethered formation with massless, inelastic tethers. He mainly demonstrated that tether length (hence tension) control can generate enough Coriolis forces without using thrusters to achieve the desired spin rate at the beginning and end of a deployment/retrieval. Alternatively, Nakaya et al. [43] used actual experimental hardware and demonstrated a 3-body tethered system deployment using a virtual structure approach control architecture [44].

As it turns out, and as explained in Chapter VI, only the most basic control schemes were applied in the this current work, therefore this present research does not build upon these previous studies in the area of tethered system control.

2.5 Formation Control Using Thrusters Only

As was illustrated on Figure 2.1, tethering satellites together is an alternative to using thrusters alone on free-flying spacecraft to perform the formation control (stationkeeping) task. The last, and most comprehensive, goal of this present research is to compare the relative utility of using tethers versus using thrusters alone.

Research Objective 5: *Assess the relative utility of tethered systems for formation control on continuous earth-facing aperture clusters.*

The previous studies related to tethered systems have been reviewed and discussed in the earlier sections of this Chapter. Once Objectives 1-4 have been accomplished, the performance of tethered systems for formation control will be established. It will be necessary to compare that performance with other methods of formationkeeping. In particular, a review of previous research in formation control using thrusters-only is called for.

A large number of authors have studied free-flying satellite formation dynamics [8, 11, 32, 56, 57, 61] and the examination of perturbation effects on thruster-only controllers [51, 54, 58, 62, 70, 76]. The majority of this work was done in the context of Clohessy and Wiltshire's [10] (CW) linearized solution as a reference orbit. M. de Queiroz et al. [51], for example, developed a Lyapunov-based, nonlinear, adaptive control law to maintain global asymptotic position tracking errors. The basis of their development was the CW reference dynamics.

On the other hand, Wiesel [76] took a fundamentally different approach by using a nearly circular periodic orbit as the reference solution and applying Floquet theory to include all zonal harmonics of the Earth's gravity field. Wiesel found that the accuracy of his solution was at least three orders of magnitude better than the CW solution, and his approach was generalized to any relative satellite motion.

Another departure from the linearized CW approach was Schaub et al. [55–57], who examined methods of determining initial conditions of satellite formations by

forcing the mean orbit elements of each satellite to be equal. They also presented a fuel-optimal, low-thrust, variable Isp propulsion scheme for orbit maintenance [56].

There is an entire subset of authors who focused their satellite cluster studies on the mission of earth observation (remote sensing), that is relative motion dynamics such that the cluster remains earth facing [11, 54, 58, 61, 62]. In 1999, both Sedwick et al. [58] and Sabol et al. [54] investigated earth facing satellite formation designs derived from the linearized CW dynamics solution and assessed the ΔV requirements to overcome various perturbations to the baseline free-flight. Sedwick et al. proposed a specific orbital configuration, characterized the perturbations, and found the total ΔV and thrust authority required to counteract them.

Sabol et al. similarly developed four formation designs and quantified the ΔV requirements to combat a comprehensive set of perturbations. The four formations they considered were in-plane, in-track, circular, and projected circular. Of these, the two of particular interest to this present research are the circular (in which the satellites maintain constant distances from each other and trace out a circular path in the orbit frame), and the projected circular (in which the satellite paths trace out a circular projection when seen from the Earth). These formations will be revisited in more detail in Chapter V. The perturbations considered by Sabol et al. were Earth's oblateness, atmospheric drag, and tesseral resonance.

In 2000, Sparks and Yeh [61] generalized the formations described by Sabol et al. They showed that the motion of these satellite formations can be described as the intersection of a plane and an elliptic cylinder of eccentricity $\sqrt{3}/2$ fixed in the orbit frame. The circular and projected circular formations mentioned above are both examples of this formation family. They also discussed the general control methods to maintain this class of satellite formations. Sparks [62] went on to develop a robust LQR feedback controller to maintain a 1 km projected circular formation in the presence of gravity perturbations, then assessed the amount of thruster propellent that would be required to do so.

For this research, these last few works (Sedwick et al., Sabol et al., and Yeh/Sparks) provide the best data for thruster-only control requirements to compare against the tethered system control requirements. Therefore, the pertinent details of those studies will be covered in more detail in Chapter VII.

2.6 Tethered Spaceflights To Date

To give the reader a sense of current state-of-the-art in actual tethered systems, this section provides an outline of the spaceflight experiments that have been flown to date.

TSS-1 (Tethered Satellite System - 1) and TSS-1R were flown in 1992 and 1996 using the Space Shuttle Orbiter as a parent spacecraft. TSS-1 demonstrated long distance deployment capabilities while TSS-1R validated the use of electrodynamic tethers in space plasma physics applications. Also in the early 1990's, the Small Expendable Deployer System (SEDS) had two successful missions. Both SEDS missions were flown as a secondary payload from Delta-II launches of GPS satellites. The first mission (SEDS-1) demonstrated the deorbiting capability of a tethered system. The second mission (SEDS-2) demonstrated a closed-loop control law for deploying a payload along the local vertical. Between the two SEDS flights, another tethered experiment was flown as a secondary payload from a Delta II – the Plasma Motor Generator (PMG) – which demonstrated that such a configuration could function as act as an orbit-boosting motor or an on-orbit electricity generator. In 1996, the Naval Research Laboratory, in cooperation with the National Reconnaissance Office (NRO), jettisoned the Tether Physics and Survivability Spacecraft (TiPS) experiment from a host spacecraft. The intent of this non-conducting tethered experiment was to study the long-term libration dynamics as well as tether survivability. Finally, the OEDIPUS (Observation of Electric-Field Distribution in the Ionospheric Plasma - a Unique Strategy) experiments were suborbital flights on two different missions. Both were launched and ejected from sounding rockets with the same objectives: to detect the natural electric field and to conduct novel bistatic propagation experiments. All

of this information was obtained from the same source [12], and confirmed through more recent sources. An overview of these previous missions is listed in Table 2.1.

Table 2.1: Previous Tethered Spaceflights

Experiment	Launched	Tether Length	Mission
OEDIPUS A	Jan 89	958 m	Suborbital Auroral Measurements
TSS-1	Jul 92	268 m	Long Distance Deployment
SEDS-1	Mar 93	20.0 km	De-orbit Capability
PMG	Jun 93	500 m	Conducting Tether
SEDS-2	Mar 94	20.0 km	Closed-Loop Deployment Control
OEDIPUS C	Nov 95	1.0 km	Suborbital Auroral Measurements
TSS-1R	Feb 96	19.7 km	Electrodynamic Tether
TiPS	Jun 96	4.0 km	Libration Dynamics and Survivability

Note that all of these experiments were limited to formations of the two-mass/one-tether variety. The concept of the present research involves larger formations.

2.7 Summary

This chapter presented an overview of previous work from the pertinent research areas and highlighted the research objectives of this present study as they arose from previous works. In the next chapter, the research objectives for this dissertation are discussed in sequential order, along with a roadmap for the research contained herein.

III. Roadmap for Present Research

With the background laid out from the previous chapter, it is appropriate to review the flow of study that was conducted for this present research. Recall the flow diagram originally shown in Figure 2.1. This chapter provides a brief methodology roadmap to that diagram to help the reader navigate along the research objectives, followed by an overview of the dissertation research that was accomplished.

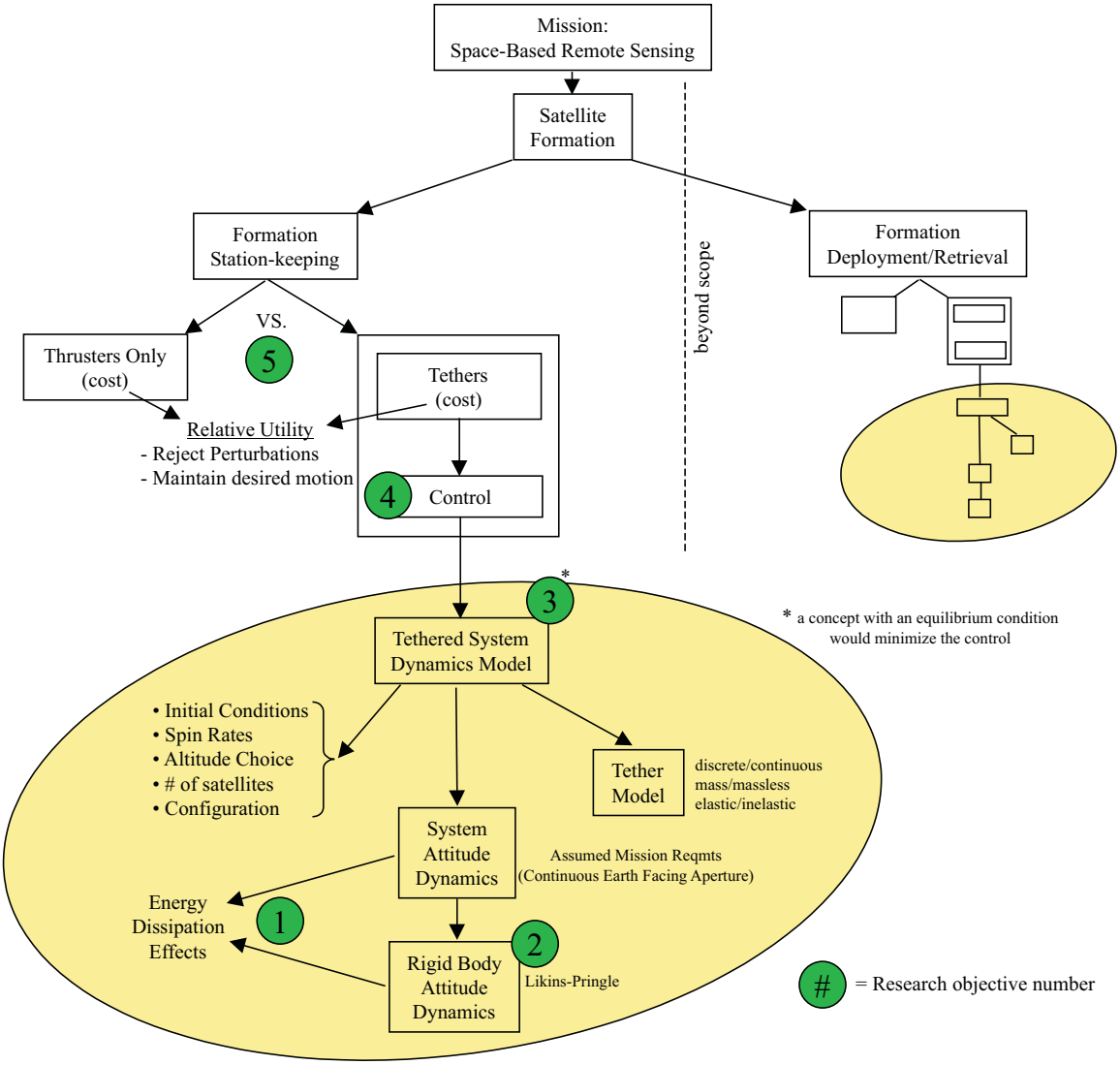


Figure 3.1: Research Area Flowchart

3.1 Research Methodology Roadmap

Generally speaking, to answer the big question of tethered system utility, we have to answer a series of smaller questions that lead up to it. How should we control the system? What do the natural tether dynamics look like? Is there an equilibrium condition (EC) for the tethered system? Is there an EC for a semi-rigid body that might help us generate one with the tethered system? How does energy dissipation effect the Likins-Pringle equilibria?

Essentially, by inverting the order of these questions, we have our sequential research objectives. The basic approach is to build-up from semi-rigid bodies to tethered systems, apply controls to those systems, then assess the cost of those controls to the cost of thruster-only control. Therefore, we start by working with rigid body dynamics to discern the effects of energy dissipation on Likins-Pringle equilibria conditions.

Objective 1: *Determine the effects of energy dissipation on semi-rigid bodies that are in/near Likins-Pringle dynamic equilibria.*

Expanding on the work from Objective 1, we attempt to find a new equilibrium condition by first working with semi-rigid body attitude dynamics, then applying it to the tethered system attitude dynamics.

Since the term "equilibrium condition" will be used often in the research, it is important to define what we mean by this. For the purpose of this work, a "perfect" equilibrium condition would be a dynamic state where the nadir projection of the aperture remains unchanged with respect to a frame that rotates with the orbit. For a spinning aperture, this would mean the spin axis would be completely fixed in a rotating orbit frame. A generally nadir-looking closed path would be considered acceptable.

If an equilibrium condition exists for a semi-rigid body, we can extend this to a possible way of finding an equilibrium for the tethered system.

Objective 2: *Define and/or determine the existence of an equilibrium condition for a semi-rigid body with a continuous earth-facing component in the presence of energy dissipation.*

The next step has the most impact to the final question of tethered system utility – finding an EC for the cluster formation. The tethered formation EC is investigated by exploring a number of realms, including tether model, initial conditions, formation configuration, and system attitude dynamics (aided, of course, by what is learned in Objective 2). The entirety of developing the best system model that is in (or close to) an equilibrium condition is shown as the yellow oval in Figure 3.1 and taken as a whole represents Objective 3.

Objective 3: *Define and/or determine the existence of an equilibrium condition for a flexible tethered satellite system with a continuous earth-facing component.*

With the system dynamics established as close to (or in) an equilibrium condition, the research then turns to applying basic control methods to the tethered system. Whether or not the EC is found, control can still be applied, although finding the EC obviates the minimization of the control costs.

Objective 4: *Apply control schemes to the tethered system to combat perturbations and maintain desired motion.*

Finally, costs for the applied control methods in Objective 4 are determined and compared to the costs of cluster formation control using thrusters only. An assessment can then be made on the relative utility of tethers for conducting formation control on remote sensing clusters.

Objective 5: *Assess the relative utility of using tethered systems for formation control on continuous earth-facing aperture clusters.*

Note that this research is limited to the study of stationkeeping (or formationkeeping). The relative costs/benefits of using tethers versus thrusters for deployment/retrieval of the formation is interesting and certainly very much related (hence the duplicate flowchart in the diagram), albeit beyond the scope of this work. To put

it bluntly, this research is less concerned with *how the system arrives* at a desired reference motion than it is about the system's *ability to maintain* a desired reference motion.

3.2 Dissertation Overview

This dissertation is organized by the categories of work that are accomplished in order to fulfill the research objectives defined above. A diagram of these incremental research categories is shown in Figure 3.2.

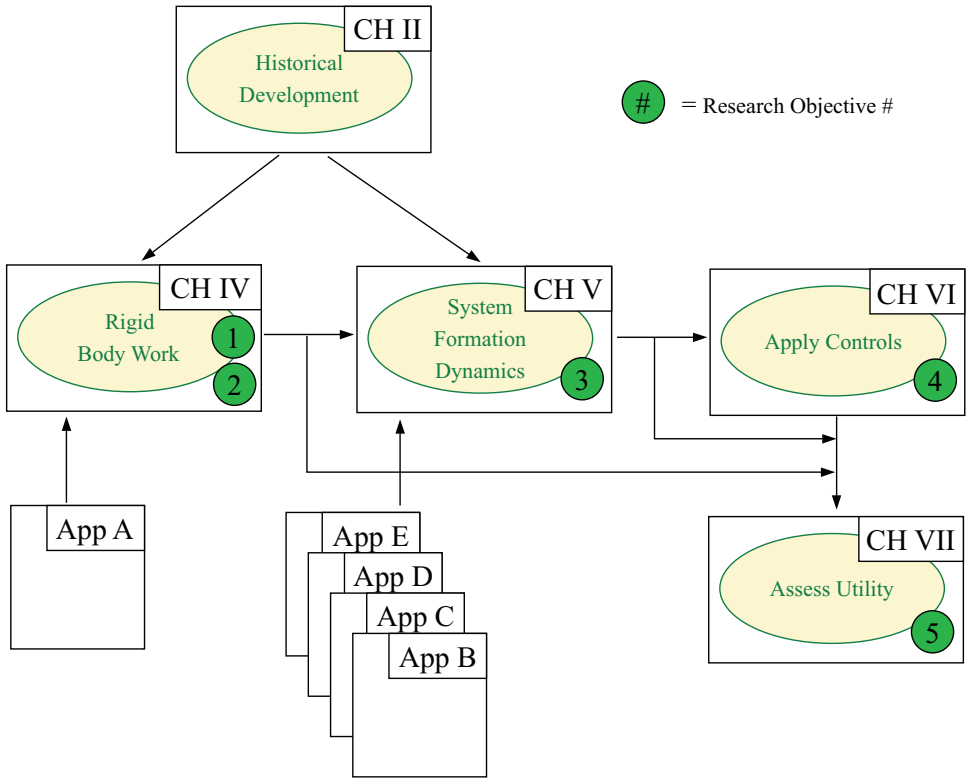


Figure 3.2: Dissertation Overview

Each block represents a chapter that details the work for that particular research area and the research objectives are identified with the appropriate chapter. Chapter IV covers all of the rigid and semi-rigid body dynamics development and analysis, and addresses objectives 1 and 2. Energy dissipation is found to have an adverse impact on Likins-Pringle equilibria, and a near-"limit cycle" is found for oblate objects. This

rigid body work builds the foundation for, and helps answer questions about, the multi-body tethered system.

Chapter V handles all of the tethered system dynamics and the hunt for an equilibrium condition. It is shown through exhaustive investigation that an equilibrium condition for fixed-length tethered formations does not exist, yet a new perspective is gained on a previously known free-flying equilibrium condition. This chapter addresses research objective 3.

Chapter VI discusses the results of applying various control schemes to the tethered system and represents objective 4. Whether applying variable-length tethers or adding thrusters to the system, these controls either do not maintain the tethered system desired motion, or the control costs are high.

Chapter VII is where all the information from the previous chapters is assembled into an argument on the utility of tethered systems for the purpose of space-based remote sensing. The primary comparison of the control costs for a tethered system vs. a thruster-only system show that the tethered system is simply too costly or cannot maintain the formation for *continuously* earth-facing aperture clusters.

3.3 Summary

This chapter presented an overview of the research that was conducted and the overall methodology, including a step-by-step roadmap of the sequential research objectives. The next chapter covers the specific work accomplished in the area of rigid and semi-rigid bodies: research objectives 1 and 2.

IV. Rigid and Semi-Rigid Body Dynamics

Of the five steps outlined in the previous chapter, the first two deal with semi-rigid body dynamics: effects of energy dissipation on Likins-Pringle equilibria and finding an equilibrium condition for an earth-facing semi-rigid body. The development and results of these analyses are presented here in this chapter.

In order to ensure high confidence in the accuracy of the results, a methodical build-up approach is used in developing the models. First, the basic equations-of-motion (EOM) are derived for a general axially-symmetric rigid-body model, then gravity gradient torques are calculated for a circular orbit. The initial conditions necessary for conical Likins-Pringle equilibria are then computed and verified with the model. Once satisfied the rigid-body model is working properly, energy dissipation is then added in a couple of different ways. With energy dissipation successfully included, the Likins-Pringle equilibria conditions are once again introduced and the effects of the energy dissipation are analyzed. At each step, after the equations are derived, modular MATLAB® code is generated to numerically and graphically demonstrate the dynamics.

4.1 Rigid Body Development

To begin, we assume we are dealing with an axially-symmetric rigid body of general proportions. That is, anything from a tuna can (oblate object) to a rod (prolate object) as shown in Figure 4.1.

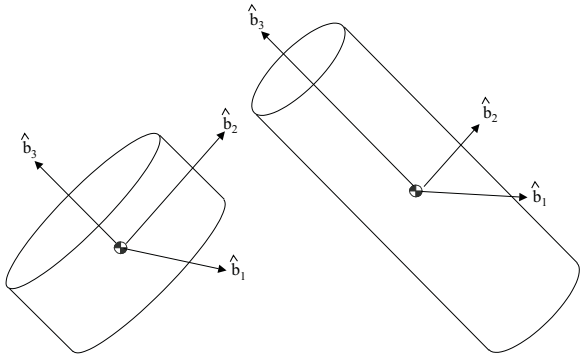


Figure 4.1: Axisymmetric Rigid Bodies of Interest

4.1.1 Reference Frames.

The next step in deriving the equations-of-motion for the basic rigid body model is to set up the relevant coordinate reference frames. As shown in Figure 4.2, three frames are defined. The inertial frame, called the $\hat{i}$-frame, is an earth-centered cartesian coordinate frame with axes $\hat{i}$, $\hat{j}$, $\hat{k}$. Using a point mass model for the earth, the orbit of the rigid body is assumed, without loss of generality, to be in the inertial $\hat{i}$-$\hat{j}$ plane. To appreciate the other two coordinate frames, the chosen attitude parameters must be defined. The 3-1-3 Euler angle set is introduced with ϕ, θ, and ψ as the classical Euler angles [75]. The $\hat{a}$-frame (which is simply an intermediate frame) is defined after the first attitude rotation from the inertial frame about the 3-axis by an angle ϕ. Hence, the $\hat{a_1}$ axis becomes a sort of "line-of-nodes". The last two rotations about the 1 and 3 axes by angles θ and ψ (respectively) result in the third reference frame, the body frame or $\hat{b}$-frame as shown in Figures 4.1 and 4.2. The $\hat{b_3}$ axis is assumed to be along the symmetry axis, with $\hat{b_1}$ and $\hat{b_2}$ in the transverse directions.

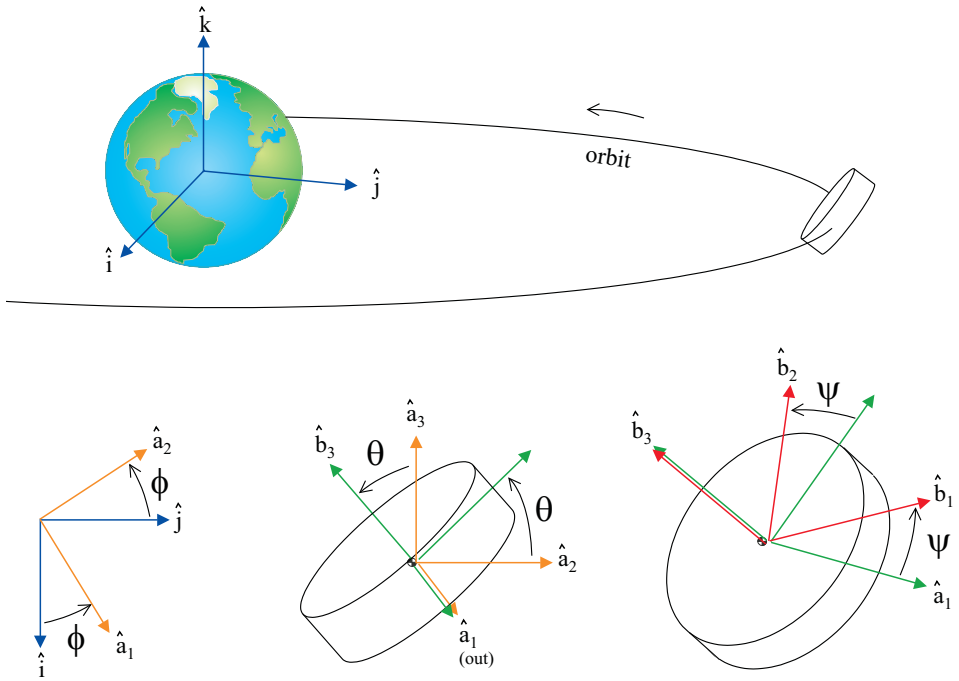


Figure 4.2: Coordinate Reference Frames and Rotations

The moment of inertia (MOI) matrix for the axisymmetric rigid body is defined as:

$$ {}^{\hat{b}}I_b^{\oplus} = \begin{bmatrix} A & 0 & 0 \\ 0 & A & 0 \\ 0 & 0 & C \end{bmatrix} \tag{4.1} $$

where A and C are the transverse and axial moments of inertia, respectively. The nomenclature on I means: the moment of inertia *of* the rigid body (b), *about* the center of mass ($\oplus$), *expressed in* the $\hat{b}$ frame. Since the MOI is assumed to always be about the center of mass, and the discussion (for now) will be limited to a single rigid body, the $\oplus$ and b notation will be dropped.

To determine the transformations between different reference frames, it is helpful to recall the elementary rotation matrices, R_i. These matrices are the direction cosine matrices of a rotation about the first, second, or third axis by an arbitrary angle α_i:

$$ R_1(\alpha_1) = \begin{bmatrix} 1 & 0 & 0 \\ 0 & \cos(\alpha_1) & \sin(\alpha_1) \\ 0 & -\sin(\alpha_1) & \cos(\alpha_1) \end{bmatrix} \tag{4.2} $$

$$ R_2(\alpha_2) = \begin{bmatrix} \cos(\alpha_2) & 0 & -\sin(\alpha_2) \\ 0 & 1 & 0 \\ \sin(\alpha_2) & 0 & \cos(\alpha_2) \end{bmatrix} \tag{4.3} $$

$$ R_3(\alpha_3) = \begin{bmatrix} \cos(\alpha_3) & \sin(\alpha_3) & 0 \\ -\sin(\alpha_3) & \cos(\alpha_3) & 0 \\ 0 & 0 & 1 \end{bmatrix} \tag{4.4} $$

Therefore, the complete rotation matrix, C^{bi}, from the $\hat{i}$-frame to the $\hat{b}$-frame (shown in Figure 4.2) is given by:

$$C^{bi} = R_3(\psi)R_1(\theta)R_3(\phi) \tag{4.5}$$

such that

$$\begin{Bmatrix} \hat{b}_1 \\ \hat{b}_2 \\ \hat{b}_3 \end{Bmatrix} = C^{bi} \begin{Bmatrix} \hat{i} \\ \hat{j} \\ \hat{k} \end{Bmatrix} \tag{4.6}$$

$$C^{bi} = \begin{bmatrix} \cos\psi\cos\phi - \cos\theta\sin\psi\sin\phi & \cos\psi\sin\phi + \cos\theta\sin\psi\cos\phi & \sin\psi\sin\theta \\ -\sin\psi\cos\phi - \cos\theta\cos\psi\sin\phi & -\sin\psi\sin\phi + \cos\theta\cos\psi\cos\phi & \cos\psi\sin\theta \\ \sin\theta\sin\phi & -\sin\theta\cos\phi & \cos\theta \end{bmatrix} \tag{4.7}$$

Likewise, to convert from the $\hat{b}$-frame to the $\hat{i}$-frame:

$$\begin{Bmatrix} \hat{i} \\ \hat{j} \\ \hat{k} \end{Bmatrix} = C^{ib} \begin{Bmatrix} \hat{b}_1 \\ \hat{b}_2 \\ \hat{b}_3 \end{Bmatrix} = R_3(-\phi)R_1(-\theta)R_3(-\psi) \begin{Bmatrix} \hat{b}_1 \\ \hat{b}_2 \\ \hat{b}_3 \end{Bmatrix} \tag{4.8}$$

where

$$C^{ib} = \begin{bmatrix} \cos\psi\cos\phi - \cos\theta\sin\psi\sin\phi & -\sin\psi\cos\phi - \cos\theta\cos\psi\sin\phi & \sin\psi\sin\theta \\ \cos\psi\sin\phi + \cos\theta\sin\psi\cos\phi & -\sin\psi\sin\phi + \cos\theta\cos\psi\cos\phi & -\cos\psi\sin\theta \\ \sin\theta\sin\psi & \sin\theta\cos\psi & \cos\theta \end{bmatrix} \tag{4.9}$$

The rotation from the $\hat{b}$-frame to the $\hat{a}$-frame is given by the rotation matrix C^{ab} and

$$\begin{Bmatrix} \hat{a}_1 \\ \hat{a}_2 \\ \hat{a}_3 \end{Bmatrix} = C^{ab} \begin{Bmatrix} \hat{b}_1 \\ \hat{b}_2 \\ \hat{b}_3 \end{Bmatrix} = R_1(-\theta)R_3(-\psi) \begin{Bmatrix} \hat{b}_1 \\ \hat{b}_2 \\ \hat{b}_3 \end{Bmatrix} \tag{4.10}$$

where

$$C^{ab} = \begin{bmatrix} \cos\psi & -\sin\psi & 0 \\ \cos\theta\sin\psi & \cos\theta\cos\psi & -\sin\theta \\ \sin\theta\sin\psi & \sin\theta\cos\psi & \cos\theta \end{bmatrix} \tag{4.11}$$

4.1.2 Euler's Equations-of-Motion.

With the reference frames defined, the equations-of-motion can now be derived from the fact that the applied external torque ($\vec{M}$) is equal to the time rate of change of the angular momentum ($\dot{\vec{H}}$)

$$\vec{M} = \dot{\vec{H}} \tag{4.12}$$

The right side of Equation 4.12 is the inertial frame time derivative of

$$\vec{H} = {}^{\hat{b}}I \; {}^{\hat{b}}\vec{\omega}^{bi} \tag{4.13}$$

where ${}^{\hat{b}}I$ is from Equation 4.1 and ${}^{\hat{b}}\vec{\omega}^{bi}$ is the angular velocity of the rigid body with respect to the inertial frame expressed in the body frame. For simplicity, the $\hat{b}$ superscripts will be dropped from here on out (unless needed due to different frames being used). As Likins [29] demonstrates, the vector derivatives of an arbitrary vector $\vec{Z}$ in any two reference frames is related by :

$${}^{\hat{i}}\frac{d}{dt}\vec{Z} = {}^{\hat{b}}\frac{d}{dt}\vec{Z} + \vec{\omega}^{bi} \times \vec{Z} \tag{4.14}$$

Applying Equation 4.14 to the angular momentum ($\vec{H}$), 4.12 becomes:

$$\vec{M} = {}^{\hat{i}}\frac{d}{dt}(I\vec{\omega}^{bi}) = {}^{\hat{b}}\frac{d}{dt}(I\vec{\omega}^{bi}) + \vec{\omega}^{bi} \times (I\vec{\omega}^{bi}) \tag{4.15}$$

Since I is defined in terms of the body frame, it is constant. Thus [75],

$$\vec{M} = I\dot{\vec{\omega}}^{bi} + \vec{\omega}^{bi} \times I\vec{\omega}^{bi} \tag{4.16}$$

where $\dot{\vec{\omega}}^{bi}$ is the body frame time derivative of $\vec{\omega}^{bi}$. By letting $\vec{\omega}^{bi}$ have the body frame components ω_1, ω_2, ω_3, then Equation 4.16 can be re-written as three Euler's Equations [19]:

$$M_1 = A\dot{\omega}_1 + (C - A)\omega_2\omega_3 \tag{4.17}$$

$$M_2 = A\dot{\omega}_2 + (A - C)\omega_1\omega_3 \tag{4.18}$$

$$M_3 = C\dot{\omega}_3 \tag{4.19}$$

Solving these equations for the $\dot{\omega}_i$, we get "three coupled, nonlinear, first-order differential equations (that) constitute one-half of the rotational equations-of-motion for a rigid body" [75]. These are our *Euler's Equations-of-Motion*:

$$\dot{\omega}_1 = \frac{M_1}{A} + \frac{(A - C)}{A}\omega_2\omega_3 \tag{4.20}$$

$$\dot{\omega}_2 = \frac{M_2}{A} + \frac{(C - A)}{A}\omega_1\omega_3 \tag{4.21}$$

$$\dot{\omega}_3 = \frac{M_3}{C} \tag{4.22}$$

or in matrix notation

$$\dot{\vec{\omega}} = I^{-1}\vec{M} - I^{-1}\vec{\omega}^x I\vec{\omega} \tag{4.23}$$

with

$$\vec{\omega}^x = \begin{bmatrix} 0 & -\omega_3 & \omega_2 \\ \omega_3 & 0 & -\omega_1 \\ -\omega_2 & \omega_1 & 0 \end{bmatrix}$$

In order for these equations-of-motion to be useful, we need to find $\vec{\omega}^{bi}$ (or $\vec{\omega}$) and $\vec{M}$. $\vec{\omega}^{bi}$ is the inertial angular velocity and can be expressed in multiple reference frames as

$$^{\hat{*}}\vec{\omega}^{bi} = \dot{\psi}\hat{b}_3 + \dot{\phi}\hat{a}_3 + \dot{\theta}\hat{a}_1 \tag{4.24}$$

However, from 4.11 we get

$$\hat{a}_3 = \sin\psi\sin\theta\hat{b}_1 + \cos\psi\sin\theta\hat{b}_2 + \cos\theta\hat{b}_3 \tag{4.25}$$

$$\hat{a}_1 = \cos\psi\hat{b}_1 - \sin\psi\hat{b}_2 \tag{4.26}$$

therefore, substituting Equations 4.25 and 4.26 into Equation 4.24 we get

$$^{\hat{b}}\vec{\omega}^{bi} = \omega_1\hat{b}_1 + \omega_2\hat{b}_2 + \omega_3\hat{b}_3 \tag{4.27}$$

where

$$\begin{aligned}
\omega_1 &= \dot{\phi}\sin\psi\sin\theta + \dot{\theta}\cos\psi \\
\omega_2 &= \dot{\phi}\cos\psi\sin\theta - \dot{\theta}\sin\psi \\
\omega_3 &= \dot{\phi}\cos\theta + \dot{\psi}
\end{aligned} \tag{4.28}$$

The external torques ($\vec{M}$) must also be defined. For this problem, it is assumed that the earth's gravity is the only external force acting on the rigid body, so the only torques that will be applied will be due to gravity gradient. This is a reasonable assumption since third body influences are much lower order perturbations than the basic dynamics being analyzed here.

To compute the gravity gradient torques, a fourth reference frame will be useful. The $\hat{e}$-frame is an earth-centered, orbit fixed frame. This frame rotates in the orbit plane such that the $\hat{e_r}$ axis (actually, the only axis of interest) is always pointed at the orbiting rigid body (see Figure 4.3). The angle ν measures the difference between the $\hat{j}$ axis and the $\hat{e_r}$ axis.

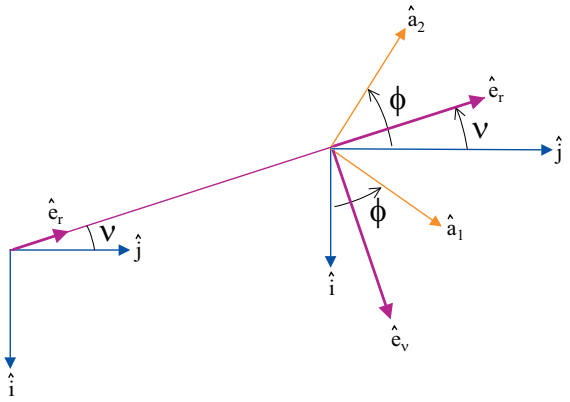


Figure 4.3: $\hat{e_r}$ axis relative to $\hat{i}$ and $\hat{a}$ frames

We can now define a vector $\vec{R}$ from the origin of the inertial frame to the rigid body as ${}^{e}\vec{R} = R\hat{e}_r$, where $\hat{e}_r = (-\sin\nu)\,\hat{i} + (\cos\nu)\,\hat{j}$ and R is the scalar distance from the center of the earth to the rigid body. Furthermore, R is assumed to be constant as we are only considering a circular orbit. In the $\hat{i}$-frame, $\vec{R}$ is rewritten as:

$$ {}^{\hat{i}}\vec{R} = (-R\sin\nu)\,\hat{i} + (R\cos\nu)\,\hat{j} \tag{4.29} $$

which is converted to $\hat{b}$-frame coordinates $(X,\, Y,\, Z)$ as

$$ {}^{\hat{b}}\vec{R} = C^{bi}\ {}^{i}\vec{R} = X\hat{b}_1 + Y\hat{b}_2 + Z\hat{b}_3 \tag{4.30} $$

where

$$ X = -R(\sin\nu\cos\psi\cos\phi - \sin\nu\cos\theta\sin\psi\sin\phi - \cos\nu\cos\psi\sin\phi - \cos\nu\cos\theta\sin\psi\cos\phi) $$
$$ Y = R(\sin\nu\sin\psi\cos\phi + \sin\nu\cos\theta\cos\psi\sin\phi - \cos\nu\sin\psi\sin\phi + \cos\nu\cos\theta\cos\psi\cos\phi) $$
$$ Z = -R(\sin\nu\sin\theta\sin\phi + \cos\nu\sin\theta\cos\phi) $$

Following the development in Wiesel [75], if we assume the rigid body is small compared to the earth and note that our body frame is aligned with the principle axes and has its origin at the center of mass, then the gravity gradient torque components expressed in the body frame are:

$$
\begin{aligned}
M_1 &= 3\mu_{\oplus} R^{-5} YZ(C-A) \\
M_2 &= 3\mu_{\oplus} R^{-5} XZ(A-C) \\
M_3 &= 3\mu_{\oplus} R^{-5} XY(A-A) = 0
\end{aligned}
\tag{4.31}
$$

where $\mu_{\oplus}$= $GM_{\oplus}$ is the gravitational constant for the Earth, G is the universal gravitational constant, $M_{\oplus}$ is the mass of the Earth, and X, Y, Z are the body frame components of the orbit position vector as shown above in 4.30. By going back to Equation 4.23 and inserting the results for $\vec{\omega}$ (Equation 4.28) and $\vec{M}$ (Equation 4.31), we get the complete set of *Euler's Equations-of-Motion*:

$$
\begin{Bmatrix} \dot{\omega}_1 \\ \dot{\omega}_2 \\ \dot{\omega}_3 \end{Bmatrix} = \begin{bmatrix} \frac{1}{A} & 0 & 0 \\ 0 & \frac{1}{A} & 0 \\ 0 & 0 & \frac{1}{C} \end{bmatrix} \begin{bmatrix} M_1 \\ M_2 \\ M_3 \end{bmatrix} - \begin{bmatrix} \frac{1}{A} & 0 & 0 \\ 0 & \frac{1}{A} & 0 \\ 0 & 0 & \frac{1}{C} \end{bmatrix} \begin{bmatrix} 0 & -\omega_3 & \omega_2 \\ \omega_3 & 0 & -\omega_1 \\ -\omega_2 & \omega_1 & 0 \end{bmatrix} \begin{bmatrix} A & 0 & 0 \\ 0 & A & 0 \\ 0 & 0 & C \end{bmatrix} \begin{bmatrix} \omega_1 \\ \omega_2 \\ \omega_3 \end{bmatrix}
\tag{4.32}
$$

where

$$
\begin{aligned}
M_1 &= 3\mu_{\oplus} R^{-5} YZ(C-A) \\
M_2 &= 3\mu_{\oplus} R^{-5} XZ(A-C) \\
M_3 &= 0
\end{aligned}
$$

$$
\begin{aligned}
\omega_1 &= \dot{\phi} \sin\psi \sin\theta + \dot{\theta} \cos\psi \\
\omega_2 &= \dot{\phi} \cos\psi \sin\theta - \dot{\theta} \sin\psi \\
\omega_3 &= \dot{\phi} \cos\theta + \dot{\psi}
\end{aligned}
$$

These equations make up only the first half of our total rotational equations-of-motion.

4.1.3 Orientation Equations-of-Motion.

The other half of the equations-of-motion come from the orientation angles and are derived from Equation 4.28, which can be re-written as:

$$\vec{\omega}^{bi} = \begin{bmatrix} \dot{\phi}\sin\psi\sin\theta + \dot{\theta}\cos\psi \\ \dot{\phi}\cos\psi\sin\theta - \dot{\theta}\sin\psi \\ \dot{\phi}\cos\theta + \dot{\psi} \end{bmatrix} = \begin{bmatrix} \sin\psi\sin\theta & \cos\psi & 0 \\ \cos\psi\sin\theta & -\sin\psi & 0 \\ \cos\theta & 0 & 1 \end{bmatrix} \begin{Bmatrix} \dot{\phi} \\ \dot{\theta} \\ \dot{\psi} \end{Bmatrix} \tag{4.33}$$

If we let

$$K = \begin{bmatrix} \sin\psi\sin\theta & \cos\psi & 0 \\ \cos\psi\sin\theta & -\sin\psi & 0 \\ \cos\theta & 0 & 1 \end{bmatrix}$$

and define $\vec{\varepsilon} = [\phi\ \theta\ \psi]^T$ as the vector of Euler angles, then

$$\vec{\omega}^{bi} = K\dot{\vec{\varepsilon}} \tag{4.34}$$

or

$$\dot{\vec{\varepsilon}} = K^{-1}\,\vec{\omega}^{bi} \tag{4.35}$$

Therefore, the *Orientation Equations-of-Motion* are:

$$\dot{\vec{\varepsilon}} = \begin{Bmatrix} \dot{\phi} \\ \dot{\theta} \\ \dot{\psi} \end{Bmatrix} = \frac{1}{\sin\theta} \begin{bmatrix} \sin\psi & \cos\psi & 0 \\ \cos\psi\sin\theta & -\sin\psi\sin\theta & 0 \\ -\sin\psi\cos\theta & -\cos\psi\cos\theta & \sin\theta \end{bmatrix} \begin{Bmatrix} \omega_1 \\ \omega_2 \\ \omega_3 \end{Bmatrix} \tag{4.36}$$

These three equations, along with the three equations from 4.32 constitute the six rotational equations-of-motion for the axisymmetric rigid body in a circular orbit. The state vector, X, for these equations-of-motion are the three Euler angles and the three components of the angular velocity vector.

$$\vec{X} = \begin{Bmatrix} \phi & \theta & \psi & \omega_1 & \omega_2 & \omega_3 \end{Bmatrix}^T \tag{4.37}$$

4.1.4 Likins-Pringle Equilibria.

As mentioned in Chapter II, Hughes [20] has described the relative equilibria of a spinning axisymmetric satellite in circular orbit such that its spin axis remains fixed with respect to an orbiting frame. As with Tragesser [66], we are primarily interested in the conical equilibria, so called for the shape the spin axis sweeps through as it precesses around the earth. The idea is to balance the free precession (caused by $\vec{H}$ and $\vec{\omega}$ not being aligned), the forced precession (caused by gravitational torques), and the orbit rate such that the rigid body precesses at the same rate as the orbit, thus ensuring the body keeps the same 'face' towards the earth at all times.

The general development for the Likins-Pringle equilibria can be found in Likins [30], Hughes [20], or Tuncay [69], and the detailed development for our particular dynamic model is shown in Appendix A, but the key relationship is shown below in Equation 4.40. As is shown in the next two sections, these relative equilibria are achieved simply by finding the correct initial conditions for the three Euler angles (ϕ, θ, and ψ) and the angular velocity ($\vec{\omega}^{bi}$).

4.1.5 Euler Angle Initial Conditions.

The Euler angles are somewhat arbitrary. As the "spin angle", ψ, is going to grow large over time, so its starting point is not crucial. θ, which is the angle of the spin axis from the orbit normal, can be almost any angle except multiples of $\pi/2$ where the 'cone' would get squashed into a plate or extended into a cylinder. In addition, $\theta = 0$ is also a singularity in the equations-of-motion (see Equation 4.36) and should be avoided (note that this condition also corresponds to the Thomson equilibrium). The initial value of ϕ, the rotation angle between the inertial frame and the orbit frame, is also arbitrary, but it will drive the value of ν as depicted in Figure 4.3.

4.1.6 Angular Velocity Initial Conditions for Likins-Pringle.

Recall from Equation 4.33 that $\vec{\omega}^{bi}$ is a function of the Euler angles and their velocities. With the Euler angles already determined above, the last step to establishing the relative equilibrium condition would be to find their velocities.

To get a constant cone angle sweep by the spin axis, θ should remain unchanged, hence

$$\dot{\theta} = 0 \tag{4.38}$$

Since the goal is to have the orbit frame rotate at the same rate as the orbit itself,

$$\dot{\phi} = \dot{\nu} \tag{4.39}$$

Finally, and most importantly, the spin rate is calculated as a function of orbit rate ($\dot{\nu}$), cone angle (θ), and the moments of inertia of the axisymmetric orbiting body (A, C):

$$\dot{\psi} = \dot{\nu}\cos\theta\,(4\,(A - C))/C \tag{4.40}$$

The development of this equation is shown in Appendix A. Equation 4.40 represents all of the conical Likins-Pringle equilibria as shown in Figure 4.4. Note that this plot is similar in nature to Tragesser's "equilibrium angles" plot [67], although he uses his own non-dimensional variables. Here we use a re-arrangement of Equation 4.40

$$\frac{\dot{\psi}}{\dot{\nu}} = 4\cos\theta\left(\frac{1}{C/A} - 1\right) \tag{4.41}$$

and the moments-of-inertia to construct the plot of equilibrium conditions.

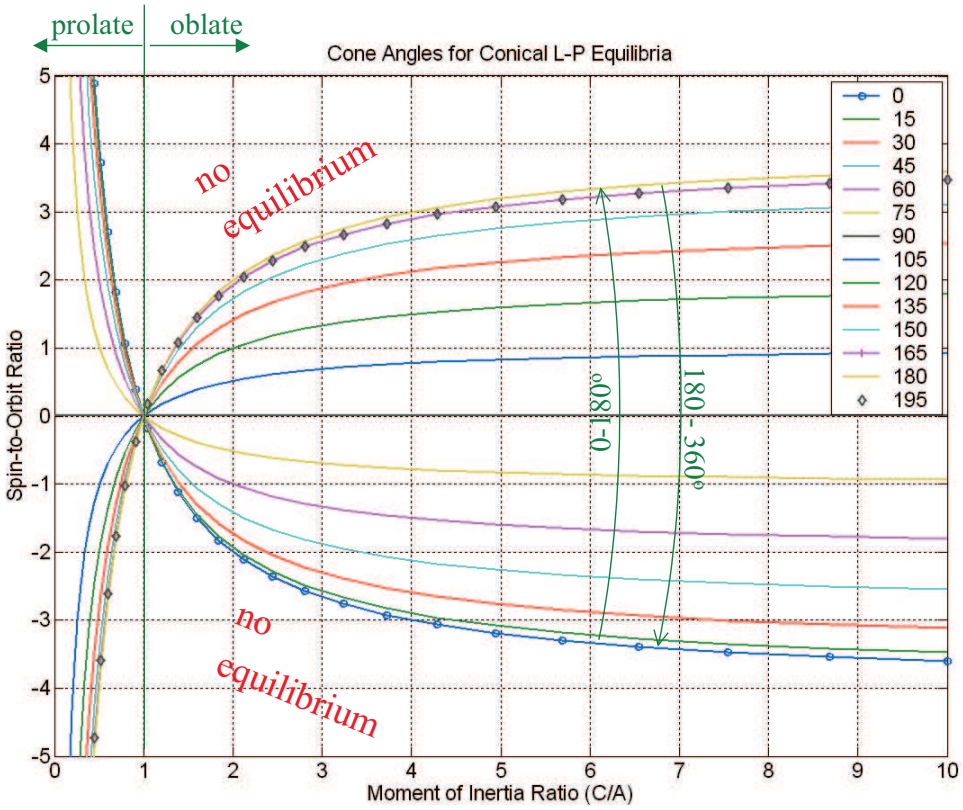


Figure 4.4: Conical Equilibrium Conditions: Spin-to-Orbit Rate Ratio vs Cone Angle

4.2 Rigid Body Simulations

With the equations-of-motion established and initial conditions for the relative equilibria identified, the next step is to define the various constants and run numerical simulations to verify the model. Note that the initial Euler angles are arbitrarily chosen to be $\phi_0 = 0$, $\theta_0 = \pi/4$, $\psi_0 = 0$. The values chosen for the various constants are shown in Table 4.1.

Table 4.1: Rigid Body Constant Values.

Constant	Value	Based On
$\vec{R}$	9378145 m	3000 km circular orbit altitude
ν_0	0	$\phi_0 = 0$
$\dot{\nu}$	0.0006952 rad/sec	orbit altitude
$\mu_\oplus$	3.986004415 x 10^8 m^3/sec^2	Vallado [71]
A, C	$10, 50$	oblate body
A, C	$50, 10$	prolate body

A MATLAB® simulation was created that uses the ODE45 integrator to propagate the equations-of-motion from the previous sections. The specific code is shown in Appendix F. The key results of these simulations take the form of several kinds of plots:

- $\vec{H}$ and $\vec{\omega}$ in the body frame.
- $\vec{H}$, $\vec{\omega}$, and the $\hat{b_3}$-axis in the inertial frame
- $\hat{b_3}$-axis in the rotating orbit frame
- Angles-over-time between $\vec{H}$, $\vec{\omega}$, and the $\hat{b_3}$-axis (constant for a rigid body)
- The six states of the rigid body over time
- 3-D movie of rigid body orientation in inertial space (not shown here)

Note: the spatial figures described above are solely used to provide a visualization of the relative behavior of the $\hat{b_3}$-axis, the angular velocity vector and angular momentum vector. To provide the best visualization, each vector is normalized from its individual physical units to unity. Furthermore, $\vec{H}$ and $\vec{\omega}$ magnitudes are set to one-half unity in order to more easily distinguish the different vectors on the plots. In addition, diamonds are added to the first 10 time steps of each spatial plot to denote the starting location of each vector.

4.2.1 Results for the Torque-Free Rigid Body.

To ensure the model is accurate, both prolate and oblate objects are first tested with the gravity gradient torques turned off. Figures 4.5-4.6 show typical results for a rigid body in a torque-free environment with initial $\dot{\phi} = 0.2$ and initial $\dot{\psi} = 0.5$. The response is very much as expected.

In this torque-free situation, the angular momentum ($\vec{H}$) remains fixed for all time as it should, but the object still precesses (see Figure 4.5). This is the "free" precession. These results are what was expected for a prolate object. Similarly expected results were found for oblate objects as well, but are not shown here for brevity's sake.

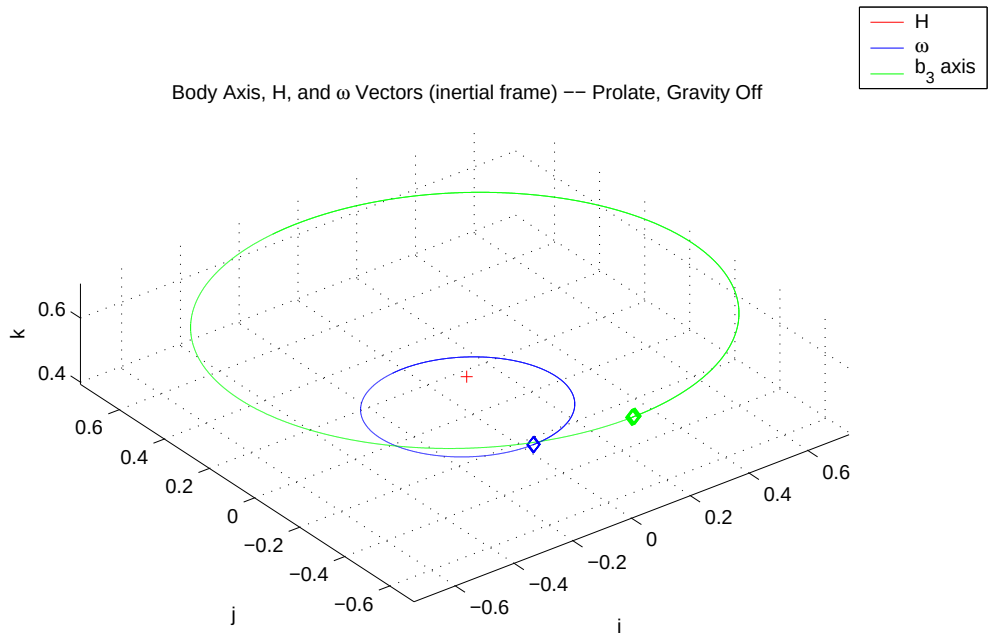


Figure 4.5: $\vec{H}$, $\vec{\omega}$, and the $\hat{b_3}$-axis in the inertial frame (Prolate Rigid Body, Gravity Off)

The cone angles of Figure 4.6 rightfully do not change over time. This is true in both the prolate and oblate cases (prolate shown). This can best be visualized by the rolling of a body fixed cone over a space cone as depicted by Hand and Finch [19]. As shown in Figure 4.7, the rolling of the body cone about the space cone will result in free precession of the $\hat{b_3}$-axis, but there is no cause for the cones themselves to change shape, thus the angles remain fixed.

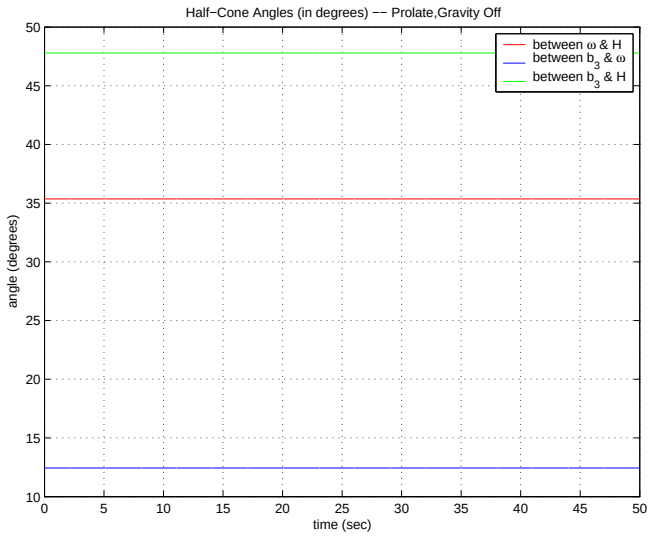


Figure 4.6: Angles-over-time (Prolate Rigid Body, Gravity Off)

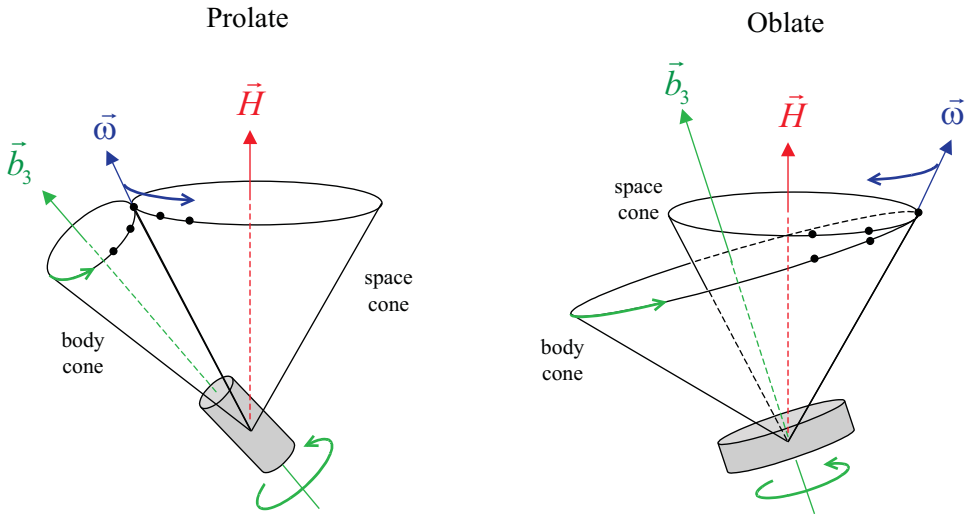


Figure 4.7: Dynamic Cones of Torque-Free Rigid Bodies

4.2.2 Results for the Likins-Pringle Rigid Body.

Satisfied that the model is working properly based on the torque-free results, the next step is to turn the gravity on and set the initial conditions such that the rigid body is in a stable Likins-Pringle conical equilibrium. These Likins-Pringle or "L-P" results are shown in Figures 4.8-4.14. The plots show the motion of the rigid body over 10 orbits and confirm that the spin axis does in fact rotate to keep 'facing' the earth.

In the body frame, we see steady rotation of the $\vec{H}$ and $\vec{\omega}$ vectors (Figure 4.8) and that they maintain constant angles with respect to the $\hat{b_3}$-axis (Figure 4.9). This is seen in both the oblate and prolate cases (prolate shown here), and as before, it is best explained as the *free precession*.

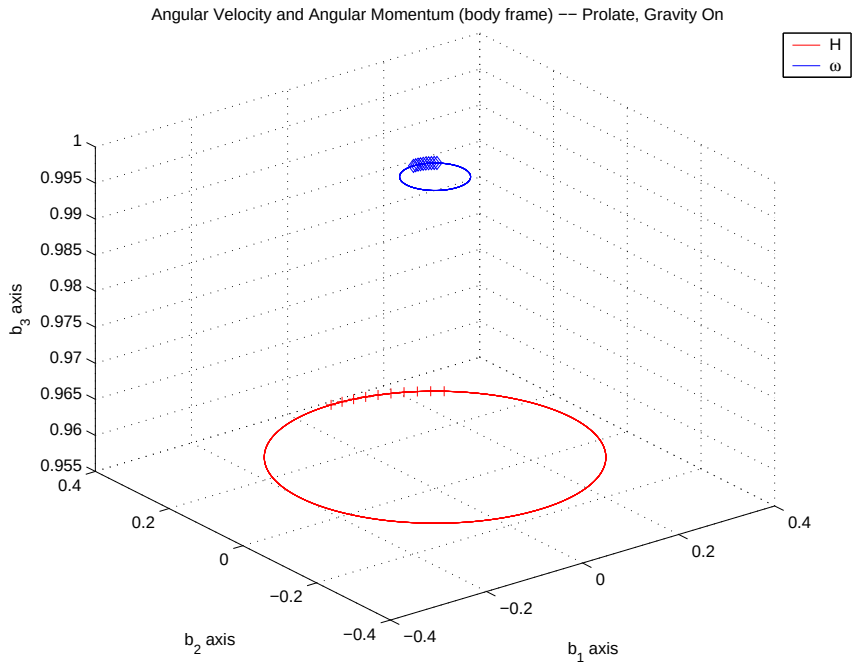


Figure 4.8: $\vec{H}$ and $\vec{\omega}$ in the body frame (Prolate Rigid Body, L-P)

With the addition of gravity gradient torques, however, we now have some *forced precession*. Hence in Figure 4.10 we see that $\vec{H}$ oscillates inertially rather than staying fixed. This is the expected result and was seen for both the oblate and prolate cases.

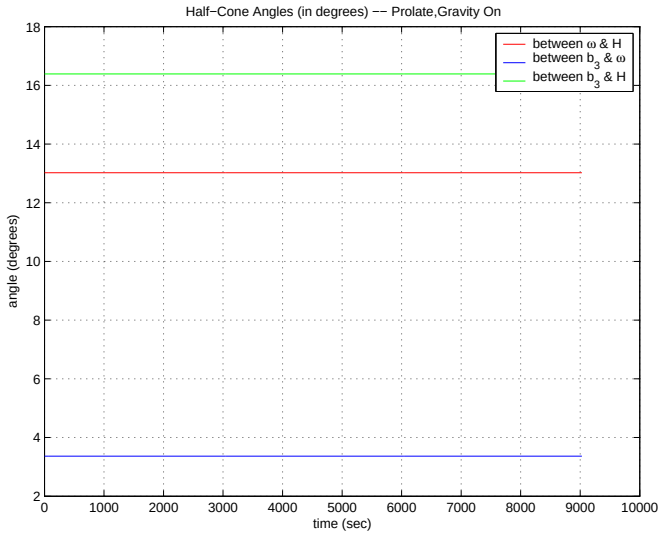


Figure 4.9: Angles-over-time (Prolate Rigid Body, L-P)

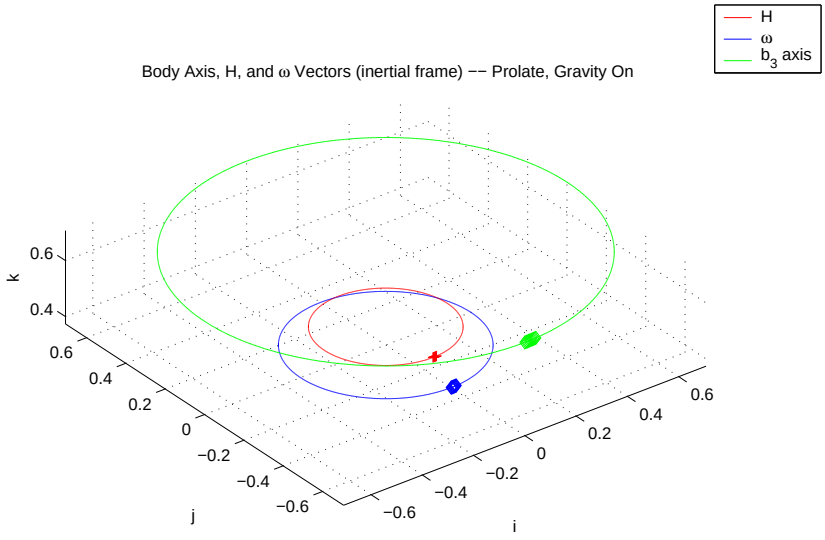


Figure 4.10: $\vec{H}$, $\vec{\omega}$, and the $\hat{b_3}$-axis in the inertial frame (Prolate Rigid Body, L-P)

The real question however is: Does the symmetry axis ($\hat{b_3}$-axis) remain fixed with respect to the rotating orbit reference frame? The answer is yes! Figures 4.10 and 4.11 show the $\hat{b_3}$-axis (green) in a stable periodic oscillation about the inertial

$\hat{k}$ axis for both prolate and oblate objects after 10 orbits. The code also produces a graphical animation in inertial space to give the viewer a better understanding of the dynamics. Unfortunately, this cannot be shown here. What can be shown however, is the motion of the $\hat{b_3}$-axis with respect to the orbit frame (Figure 4.12). Clearly, this axis is not moving with respect to the orbit frame and therefore presents the desired constant 'face' in the nadir direction.

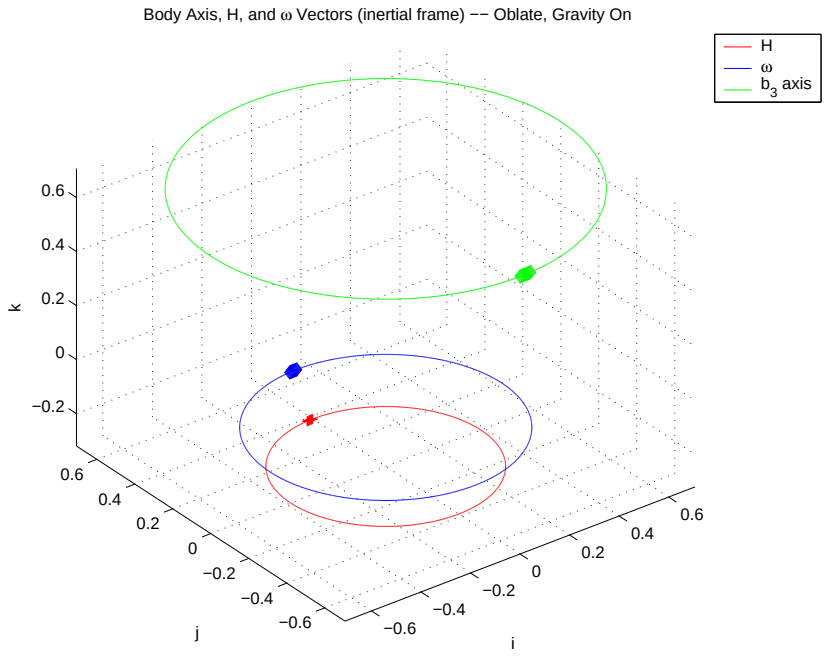


Figure 4.11: $\vec{H}$, $\vec{\omega}$, and the $\hat{b_3}$-axis in the inertial frame (Oblate Rigid Body, L-P)

Further evidence of the desired equilibria is seen in the state plots. As can be seen in Figures 4.13 and 4.14, θ doesn't deviate over ten orbits.

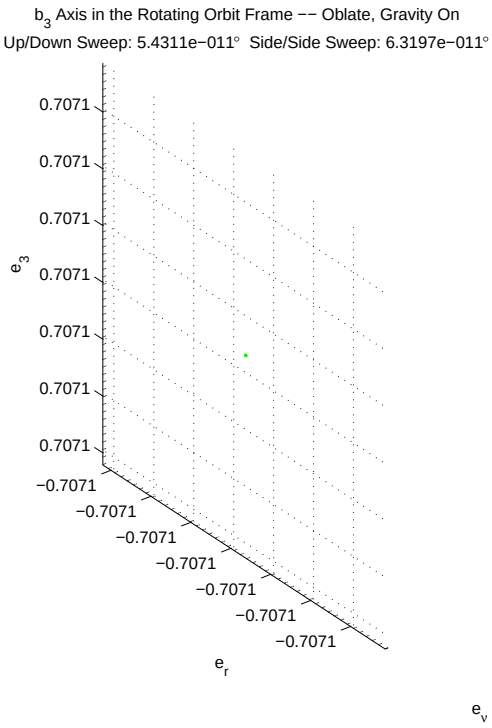


Figure 4.12: $\hat{b_3}$-axis in the orbit frame (Oblate Rigid Body, L-P)

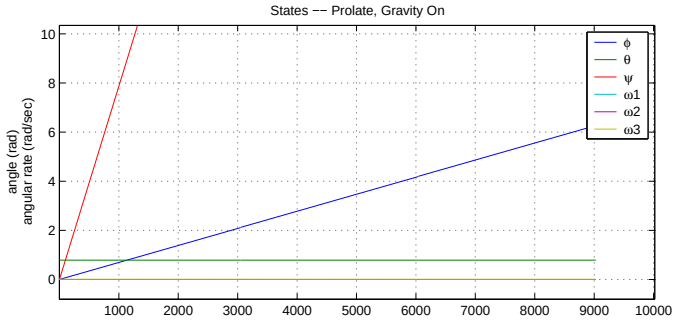


Figure 4.13: States (Prolate Rigid Body, L-P)

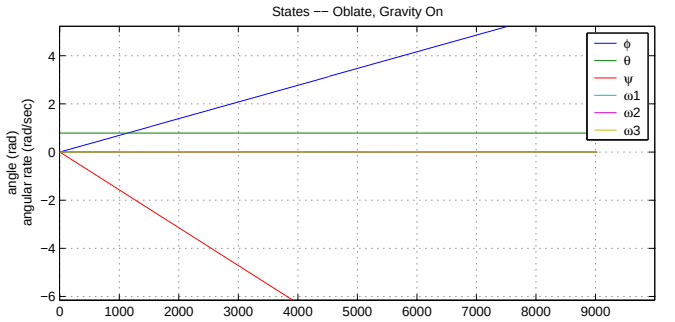


Figure 4.14: States (Oblate Rigid Body, L-P)

Thus far we have demonstrated a working model of an axisymmetric rigid body and have been able to create the conditions for Likins-Pringle conical equilibria for both oblate and prolate objects. The next step is to add energy dissipation to analyze the effects on these L-P equilibria.

4.3 Semi-Rigid Body Development

For the purposes of this work, a "semi-rigid body" is defined as a rigid body with energy dissipation added. In order to introduce energy dissipation into the model, three identical rotor disks are added to the system – one for each principle axis of the main body. Each rotor has its symmetry axis co-aligned with one of the main body axes and is free to spin, with damping, around that axis only (see Figure 4.15). The reader must suspend disbelief for this theoretical set of rotors as all three have their center of mass co-located with the main body's center of mass. In addition, it is assumed that the main body and all three rotors have uniform mass distributions. We have now graduated from a rigid body to a semi-rigid body given the movement of the rotors relative to the main body. While there are a number of ways one could add energy dissipation to create a semi-rigid body, this method was chosen since it is conceptually easy to visualize.

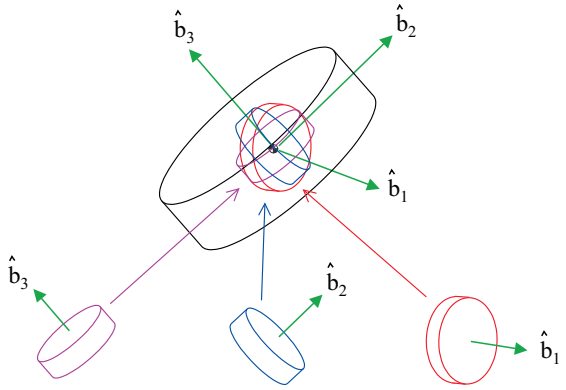


Figure 4.15: 3-Rotor Set Added to the System

4.3.1 Total System Angular Momentum.

We have from Equation 4.13 that the angular momentum for the body alone is:

$$\vec{H}_b = {}^{\hat{b}}I_b \; {}^{\hat{b}}\vec{\omega}^{bi} = \begin{bmatrix} A & 0 & 0 \\ 0 & A & 0 \\ 0 & 0 & C \end{bmatrix} \begin{bmatrix} \omega_1 \\ \omega_2 \\ \omega_3 \end{bmatrix} \tag{4.42}$$

We define the angular momenta of the three individual rotors as

$$\vec{H}_{r_1} = C^{br_1} \; {}^{\hat{r}_1}I_{r_1} \; C^{r_1 b} \; {}^{\hat{b}}\vec{\omega}^{r_1 i} = C^{br_1} \begin{bmatrix} D_1 & 0 & 0 \\ 0 & E_1 & 0 \\ 0 & 0 & F_1 \end{bmatrix} C^{r_1 b} \begin{bmatrix} \omega_1 + \sigma_1 \\ \omega_2 \\ \omega_3 \end{bmatrix} \tag{4.43}$$

$$\vec{H}_{r_2} = C^{br_2} \; {}^{\hat{r}_2}I_{r_2} \; C^{r_2 b} \; {}^{\hat{b}}\vec{\omega}^{r_2 i} = C^{br_2} \begin{bmatrix} D_2 & 0 & 0 \\ 0 & E_2 & 0 \\ 0 & 0 & F_2 \end{bmatrix} C^{r_2 b} \begin{bmatrix} \omega_1 \\ \omega_2 + \sigma_2 \\ \omega_3 \end{bmatrix} \tag{4.44}$$

$$\vec{H}_{r_3} = C^{br_3} \; {}^{\hat{r}_3}I_{r_3} \; C^{r_3 b} \; {}^{\hat{b}}\vec{\omega}^{r_3 i} = C^{br_3} \begin{bmatrix} D_3 & 0 & 0 \\ 0 & E_3 & 0 \\ 0 & 0 & F_3 \end{bmatrix} C^{r_3 b} \begin{bmatrix} \omega_1 \\ \omega_2 \\ \omega_3 + \sigma_3 \end{bmatrix} \tag{4.45}$$

where D_i, E_i, and F_i are the moments of inertia for the i^{th} rotor and σ_i is the relative spin velocity of the i^{th} rotor compared to the main body. Since the rotors are axisymmetric, we can say that $E_1 = F_1$, $D_2 = F_2$, and $D_3 = E_3$, hence C^{br_i} and $C^{r_i b}$ are identity matrices and

$${}^{\hat{r}_1}I_{r_1} = {}^{\hat{b}}I_{r_1} = \begin{bmatrix} D_1 & 0 & 0 \\ 0 & E_1 & 0 \\ 0 & 0 & E_1 \end{bmatrix}$$

$$^{\hat{r}_2}I_{r_2} = {}^{\hat{b}}I_{r_2} = \begin{bmatrix} D_2 & 0 & 0 \\ 0 & E_2 & 0 \\ 0 & 0 & D_2 \end{bmatrix}$$

$$^{\hat{r}_3}I_{r_3} = {}^{\hat{b}}I_{r_3} = \begin{bmatrix} D_3 & 0 & 0 \\ 0 & D_3 & 0 \\ 0 & 0 & F_3 \end{bmatrix}$$

for all time. Furthermore, since the rotors are identical the their major and minor moments of inertia will also match. Therefore, we define two new terms for these inertias: $J = E_1 = D_2 = D_3$ (minor moment); and $D = D_1 = E_2 = F_3$ (major moment). All of this reduces Equations 4.43-4.45 to

$$\vec{H}_{r_1} = \begin{bmatrix} D & 0 & 0 \\ 0 & J & 0 \\ 0 & 0 & J \end{bmatrix} \begin{bmatrix} \omega_1 + \sigma_1 \\ \omega_2 \\ \omega_3 \end{bmatrix} \tag{4.46}$$

$$\vec{H}_{r_2} = \begin{bmatrix} J & 0 & 0 \\ 0 & D & 0 \\ 0 & 0 & J \end{bmatrix} \begin{bmatrix} \omega_1 \\ \omega_2 + \sigma_2 \\ \omega_3 \end{bmatrix} \tag{4.47}$$

$$\vec{H}_{r_3} = \begin{bmatrix} J & 0 & 0 \\ 0 & J & 0 \\ 0 & 0 & D \end{bmatrix} \begin{bmatrix} \omega_1 \\ \omega_2 \\ \omega_3 + \sigma_3 \end{bmatrix} \tag{4.48}$$

The sum of the three equations above, along with Equation 4.42, become the total system angular momentum, $\vec{H}_{sys}$:

$$\vec{H}_{sys} = \vec{H}_b + \vec{H}_{r_1} + \vec{H}_{r_2} + \vec{H}_{r_3} \tag{4.49}$$

or

$$\vec{H}_{sys} = \begin{bmatrix} A & 0 & 0 \\ 0 & A & 0 \\ 0 & 0 & C \end{bmatrix} \begin{bmatrix} \omega_1 \\ \omega_2 \\ \omega_3 \end{bmatrix} + 2J \begin{bmatrix} \omega_1 \\ \omega_2 \\ \omega_3 \end{bmatrix} + D \begin{bmatrix} \omega_1 + \sigma_1 \\ \omega_2 + \sigma_2 \\ \omega_3 + \sigma_3 \end{bmatrix} \tag{4.50}$$

which reduces to

$$\vec{H}_{sys} = \begin{bmatrix} (A + D + 2J)\omega_1 + D\sigma_1 \\ (A + D + 2J)\omega_2 + D\sigma_2 \\ (C + D + 2J)\omega_3 + D\sigma_3 \end{bmatrix} \tag{4.51}$$

4.3.2 3-Rotor Equations-of-Motion.

The equations-of-motion for the new system can now be developed. Clearly, the *Orientation Equations-of-Motion* (Equation 4.36) are identical to those developed before the rotors were added, therefore only the *Euler's Equations-of-Motion* need to be derived. Recalling Equation 4.14 from the earlier section, we take the inertial derivative of $\vec{H_{sys}}$,

$${}^{i}\frac{d}{dt}\vec{H}_{sys} = {}^{b}\frac{d}{dt}(\vec{H}_{sys}) + \vec{\omega}^{bi} \times (\vec{H}_{sys}) \tag{4.52}$$

which yields

$$\dot{\vec{H}}_{sys} = \begin{bmatrix} (A + D + 2J)\dot{\omega}_1 + D\dot{\sigma}_1 \\ (A + D + 2J)\dot{\omega}_2 + D\dot{\sigma}_2 \\ (C + D + 2J)\dot{\omega}_3 + D\dot{\sigma}_3 \end{bmatrix} + \begin{bmatrix} 0 & -\omega_3 & \omega_2 \\ \omega_3 & 0 & -\omega_1 \\ -\omega_2 & \omega_1 & 0 \end{bmatrix} \begin{bmatrix} (A + D + 2J)\omega_1 + D\sigma_1 \\ (A + D + 2J)\omega_2 + D\sigma_2 \\ (C + D + 2J)\omega_3 + D\sigma_3 \end{bmatrix}$$

After the multiplying everything and canceling terms, we are left with the kernel of our Equations-of-Motion:

$$\dot{\vec{H}}_{sys} = \bar{M} = \begin{bmatrix} (A + D + 2J)\dot{\omega}_1 + D\dot{\sigma}_1 \\ (A + D + 2J)\dot{\omega}_2 + D\dot{\sigma}_2 \\ (C + D + 2J)\dot{\omega}_3 + D\dot{\sigma}_3 \end{bmatrix} + \begin{bmatrix} (C - A)\omega_2\omega_3 - D\omega_3\sigma_2 + D\omega_2\sigma_3 \\ (A - C)\omega_1\omega_3 + D\omega_3\sigma_1 - D\omega_1\sigma_3 \\ -D\omega_2\sigma_1 + D\omega_1\sigma_2 \end{bmatrix} \tag{4.53}$$

Of course, with the addition of the three rotors we have introduced three new states, namely their relative spin rates, σ_i. Subsequently, we need the following three additional governing equations for the rotors:

$$D(\dot{\sigma}_1 + \dot{\omega}_1) = \mu_d \sigma_1 \tag{4.54}$$

$$D(\dot{\sigma}_2 + \dot{\omega}_2) = \mu_d \sigma_2 \tag{4.55}$$

$$D(\dot{\sigma}_3 + \dot{\omega}_3) = \mu_d \sigma_3 \tag{4.56}$$

These can be rewritten in terms of the $\dot{\sigma}_i$ and become three of our new equations-of-motion:

$$\dot{\sigma}_1 = -\dot{\omega}_1 - \frac{\mu_d}{D}\sigma_1 \tag{4.57}$$

$$\dot{\sigma}_2 = -\dot{\omega}_2 - \frac{\mu_d}{D}\sigma_2 \tag{4.58}$$

$$\dot{\sigma}_3 = -\dot{\omega}_3 - \frac{\mu_d}{D}\sigma_3 \tag{4.59}$$

where μ_d is the viscous damping coefficient. Inserting Equations 4.57-4.59 into Equation 4.53 and solving for the ω_i, we get the last of our 3-Rotor Equations-of-Motion. The complete set of nine equations-of-motion now are:

$$\dot{\omega}_1 = \frac{M_1}{A+2J} + \frac{(A-C)\omega_2\omega_3 + D\omega_3\sigma_2 - D\omega_2\sigma_3 + \mu_d\sigma_1}{A+2J} \tag{4.60}$$

$$\dot{\omega}_2 = \frac{M_2}{A+2J} + \frac{(C-A)\omega_1\omega_3 - D\omega_3\sigma_1 + D\omega_1\sigma_3 + \mu_d\sigma_2}{A+2J} \tag{4.61}$$

$$\dot{\omega}_3 = \frac{M_3}{C+2J} + \frac{D\omega_2\sigma_1 - D\omega_1\sigma_2 + \mu_d\sigma_3}{C+2J} \tag{4.62}$$

$$\dot{\sigma}_1 = -\left(\frac{M_1}{A+2J} + \frac{(A-C)\omega_2\omega_3 + D\omega_3\sigma_2 - D\omega_2\sigma_3 + \mu_d\sigma_1}{A+2J}\right) - \frac{\mu_d}{D}\sigma_1 \tag{4.63}$$

$$\dot{\sigma}_2 = -\left(\frac{M_2}{A+2J} + \frac{(C-A)\omega_1\omega_3 - D\omega_3\sigma_1 + D\omega_1\sigma_3 + \mu_d\sigma_2}{A+2J}\right) - \frac{\mu_d}{D}\sigma_2 \tag{4.64}$$

$$\dot{\sigma}_3 = -\left(\frac{M_3}{C+2J} + \frac{D\omega_2\sigma_1 - D\omega_1\sigma_2 + \mu_d\sigma_3}{C+2J}\right) - \frac{\mu_d}{D}\sigma_3 \tag{4.65}$$

$$\begin{Bmatrix} \dot{\phi} \\ \dot{\theta} \\ \dot{\psi} \end{Bmatrix} = \frac{1}{\sin\theta} \begin{bmatrix} \sin\psi & \cos\psi & 0 \\ \cos\psi\sin\theta & -\sin\psi\sin\theta & 0 \\ -\sin\psi\cos\theta & -\cos\psi\cos\theta & \sin\theta \end{bmatrix} \begin{Bmatrix} \omega_1 \\ \omega_2 \\ \omega_3 \end{Bmatrix} \tag{4.66}$$

The state vector for these equations-of-motion are the three components of the bodies angular velocity vector, the relative spin velocities of the three rotors, and the three Euler angles.

$$\vec{X} = \begin{Bmatrix} \phi & \theta & \psi & \sigma_1 & \sigma_2 & \sigma_3 & \omega_1 & \omega_2 & \omega_3 \end{Bmatrix}^T \tag{4.67}$$

4.3.3 Kinetic Energy.

One of the evaluation parameters to look at during energy dissipation analysis is obviously the energy itself to ensure it is in fact decreasing. The total kinetic energy (KE) of the system is the sum of the body's KE and the KE of the three individual rotors. As stated previously, the relation for finding rotational kinetic energy is [75]

$$KE = \frac{1}{2}\vec{\omega} \cdot I\vec{\omega} \tag{4.68}$$

After a little bit of math from Equations 4.43-4.45 and 4.42, the final equation for total system kinetic energy is

$$KE = \frac{1}{2}\left[A\omega_1^2 + A\omega_2^2 + C\omega_3^2\right] + \left[J\omega_1^2 + J\omega_2^2 + J\omega_3^2\right]$$

$$+\frac{1}{2}D\left[(\omega_1+\sigma_1)^2 + (\omega_2+\sigma_2)^2 + (\omega_3+\sigma_3)^2\right] \tag{4.69}$$

4.4 Semi-Rigid Body Simulations

The original MATLAB® code used for the rigid body earlier in this chapter is modified to include the new equations-of-motion with the rotors added. The same Euler angle initial conditions are used as before ($\phi_0 = 0$, $\theta_0 = \pi/4$, $\psi_0 = 0$) and

the rotors' initial relative velocities are all set to zero. Using the fuel slug example from Wie [74] as a guideline, the damping coefficient (μ_d) is set to 0.5 – roughly two orders of magnitude less that the main rotor's transverse MOI. The axial MOI for each rotor is set to 1 (arbitrarily chosen, but $D << A$ or C), while the transverse MOI is set to 0.0001 (also arbitrary, but $J << A$, C or D). The same kinds of plots used to evaluate the rigid body dynamics are again used to examine the semi-rigid body response. As before, the specific code is shown in Appendix F.

4.4.1 Torque-Free Energy Dissipation Effects.

As before, to ensure the new energy dissipative model is accurate, both prolate and oblate objects are first tested with the gravity gradient torques turned off. Once again, the initial Euler angle velocities for the torque-free condition are set to $\dot{\phi} = 0.2$, $\dot{\theta} = 0$, and $\dot{\psi} = 0.5$.

Figures 4.16-4.21 show the results of energy dissipation on the prolate body. As would be expected for a torque-free condition, the angular momentum vector ($\vec{H}$) stays fixed in inertial space (as denoted by a red '+' in the center of Figure 4.17) but walks around in the body frame until a minimum energy state is reached (Figure 4.16).

Once the minimum energy state is reached, $\vec{H}$ then becomes fixed at an arbitrary location in the $\hat{b_1} - \hat{b_2}$ plane (shown as a magenta diamond in Fig. 4.16). This behavior corresponds perfectly to the discussion Wiesel [75] gives of polhodes that are modified by energy dissipation. In his book, Wiesel describes polhodes as a family of curves traced out by $\vec{\omega}$ that is created by the intersection of the kinetic-energy and angular-momentum ellipsoids (Fig. 4.18). For an axisymmetric body in a constant energy state, the polhode (shaped much like a football) would roll on the invariable plane along one of the polhode paths. If the same body were to lose energy, the $\vec{\omega}$ vector would trace out a spiraling path that cuts through the constant energy polhode curves until finally converging on a state of pure spin about the major inertia axis as shown in Figure 4.19.

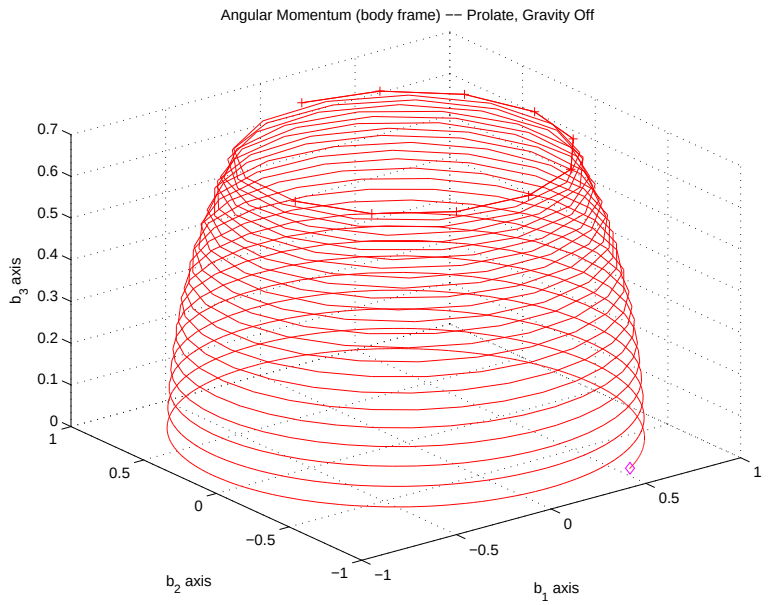


Figure 4.16: $\vec{H}$ in the body frame (Prolate Semi-Rigid Body, Gravity Off)

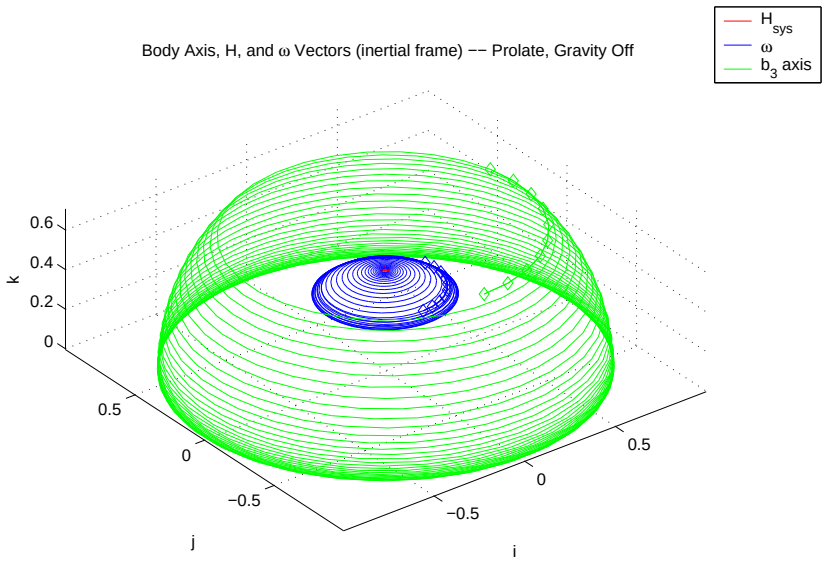


Figure 4.17: $\vec{H}$, $\vec{\omega}$, and the $\hat{b_3}$-axis in the inertial frame (Prolate Semi-Rigid Body, Gravity Off)

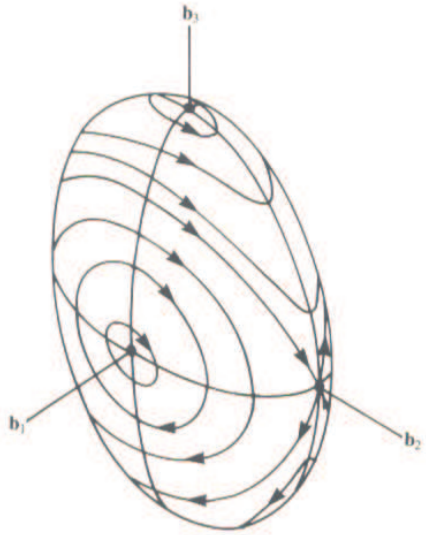


Figure 4.18: Polhodes of Different Constant Energy Levels [75]

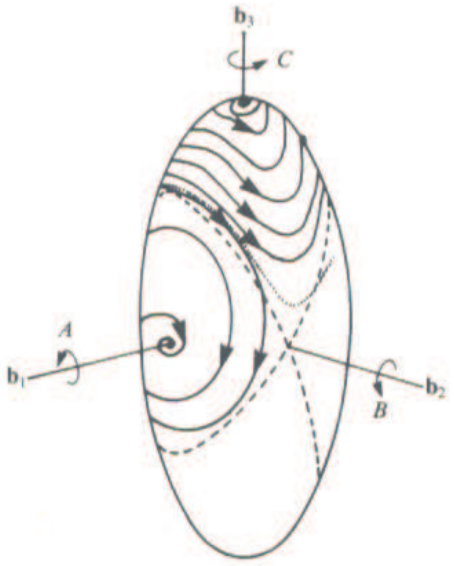


Figure 4.19: Polhodes with Energy Dissipation [75]

This is exactly what we see happening with our model. Figure 4.17 shows $\vec{\omega}$ spiraling down to a state of pure spin (with $\vec{\omega}$ and $\vec{H}$ aligned about the major axis as the $\hat{b_3}$ axis settles into a pure sweep about the $\vec{\omega}$, $\vec{H}$ vectors, which are now fixed in an arbitrary direction in the $\hat{b_1} - \hat{b_2}$ plane).

Unlike the rigid body, the angles plotted in Figure 4.20 show that they do not remain constant in the presence of energy dissipation. It can be shown that these cone angles are in fact changing in a manner that is expected in the presence of energy dissipation, but this will not be detailed here.

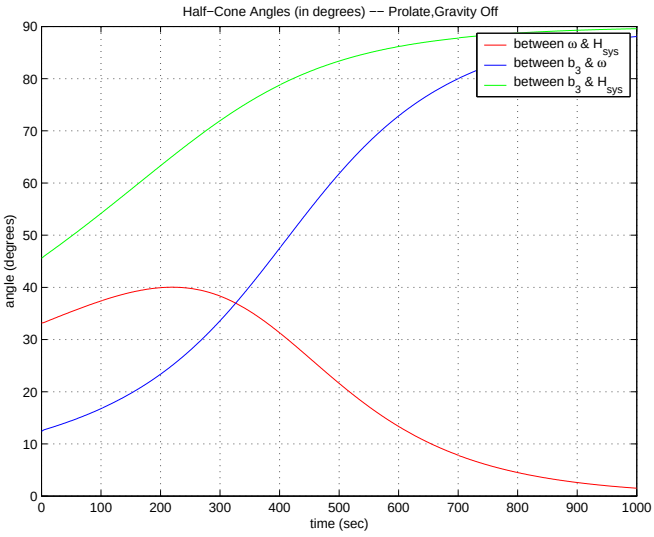


Figure 4.20: Angles-over-time (Prolate Semi-Rigid Body, Gravity Off)

The plots of the states and kinetic energy also support that the model works according to theory. As seen in Figure 4.21, the states settle into pure spin about transverse axis. Although off the chart, ψ rolls off to a constant value while θ is shown to oscillate about a flat spin plane (approximately 90 degrees). Also, $\vec{\omega}$ stabilizes in the $\hat{b_1} - \hat{b_2}$ body plane as the σ_i's drop to zero (that is, as the rotors 'catch up' to the body, the relative velocities go away). Finally, the kinetic energy is shown to drop off until it approaches some minimum value.

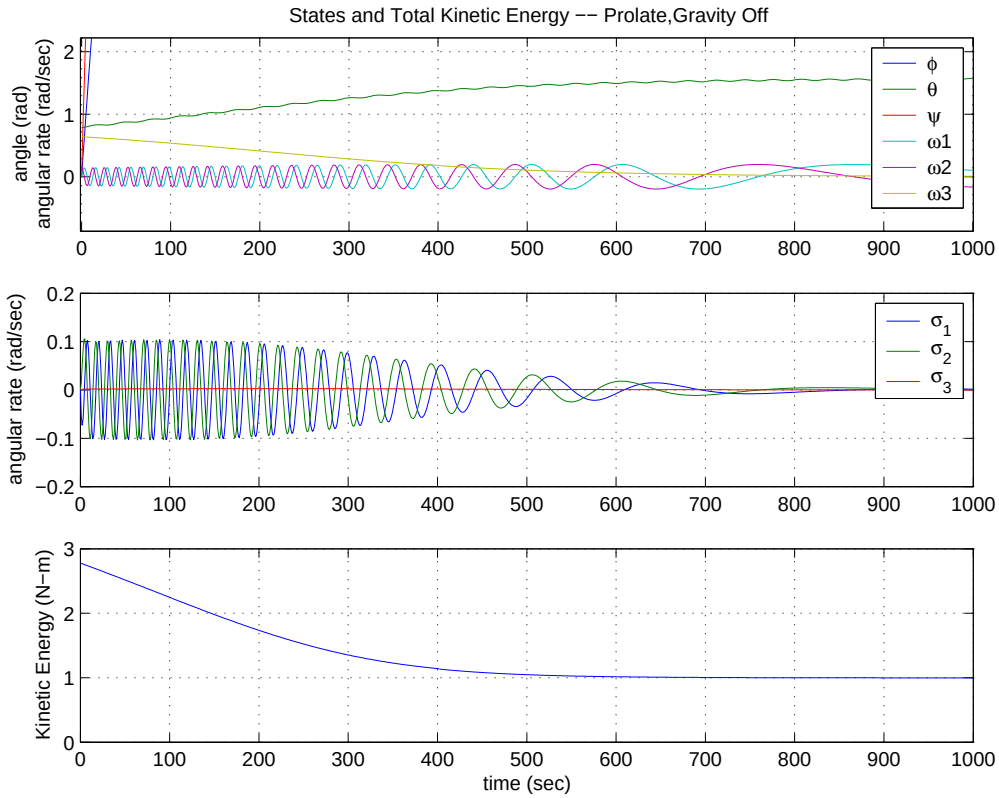


Figure 4.21: States and Kinetic Energy (Prolate Semi-Rigid Body, Gravity Off)

Figures 4.22-4.25 show the results of energy dissipation on the oblate body. As with the prolate case, the oblate results proves equally reasonable. In Figure 4.22, $\vec{H}$ and $\vec{\omega}$ both spiral down together to a state of pure spin about the $\hat{b_3}$ axis.

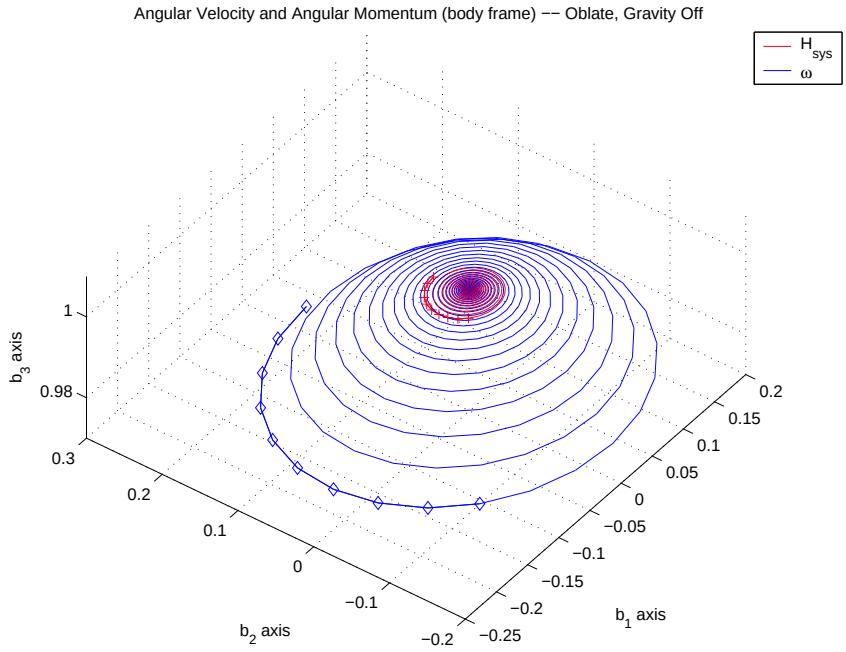


Figure 4.22: $\vec{H}$ and $\vec{\omega}$ in the body frame (Oblate Semi-Rigid Body, Gravity Off)

In the inertial frame, angular momentum stays fixed again as $\vec{\omega}$ and $\hat{b_3}$ spiral in towards $\vec{H}$ (see Figure 4.23). The angles in Figure 4.24 show this happening from another perspective. As can be seen, the cone angles rapidly collapse to zero since a spinning oblate object is already near it's major axis (i.e. minimum energy state).

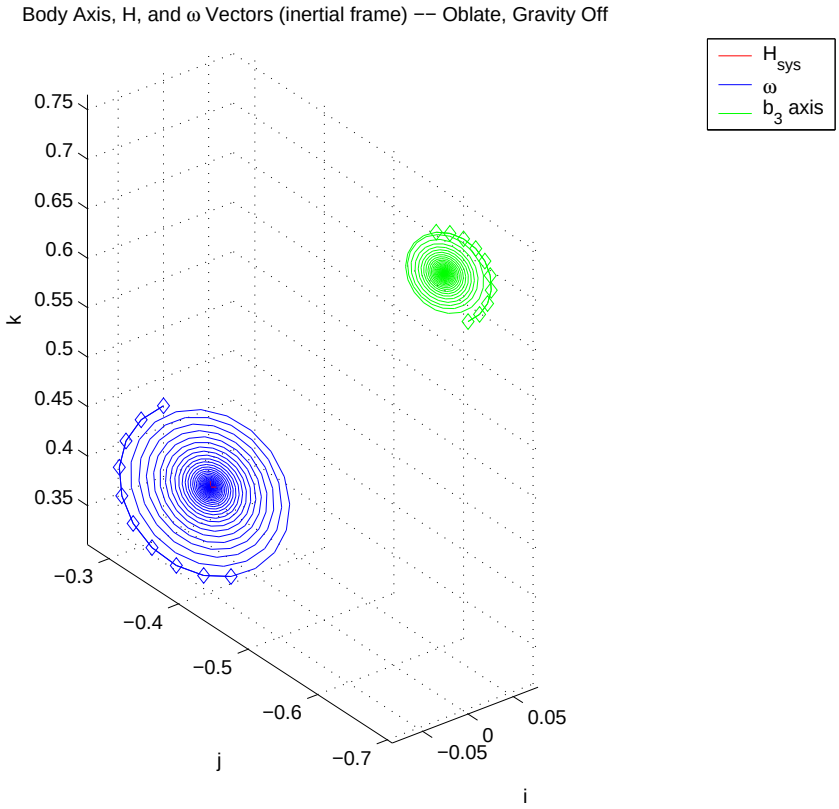


Figure 4.23: $\vec{\omega}$ and the $\hat{b_3}$-axis in the inertial frame (Oblate Semi-Rigid Body, Gravity Off)

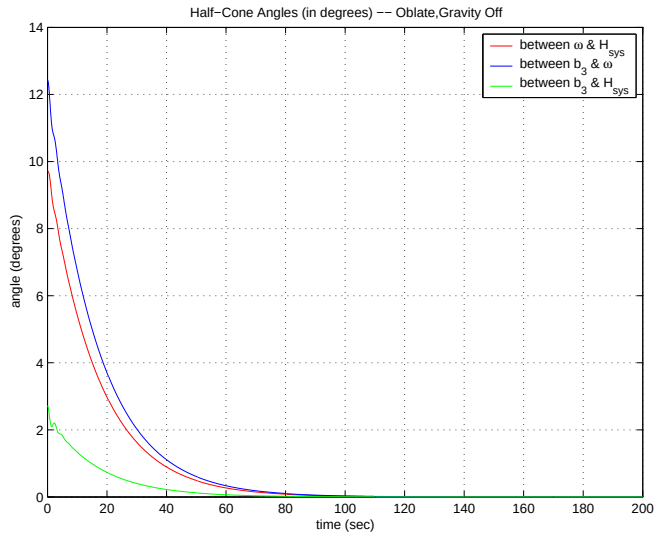


Figure 4.24: Angles-over-time (Oblate Semi-Rigid Body, Gravity Off)

In Figure 4.25, the states and kinetic energy quickly settle down into pure spin about major (symmetry) axis. ω_1, ω_2 and all σ_i's drop to zero as ω_3 picks up all of their magnitude and stabilizes at a constant value itself.

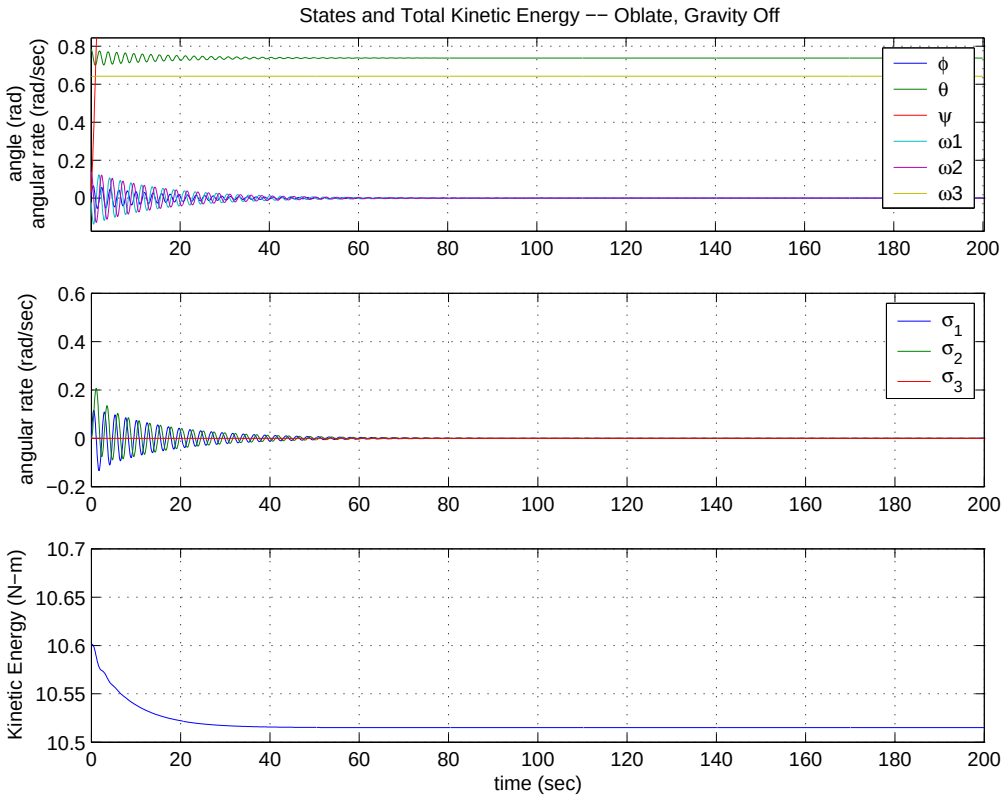


Figure 4.25: States and Kinetic Energy (Oblate Semi-Rigid Body, Gravity Off)

All of these results indicate that the semi-rigid body model realistically simulates the effects of energy dissipation on the attitude dynamics of the main body.

4.4.2 Energy Dissipation Effects on Likins-Pringle.

Confident that the semi-rigid body model works properly for the general torque-free case, the initial conditions for a Likins-Pringle conical equilibria are used and gravity torques are turned on. The results of these simulations are shown here and answer the first question of this research: *What effect does energy dissipation have on the Likins-Pringle equilibria?*

The effect is best shown by looking at the behavior of the $\hat{b_3}$ axis in the inertial frame and the orbit frame. Recall that for Likins-Pringle, we expect the $\hat{b_3}$ axis to be in a stable periodic oscillation about the $\hat{k}$ axis of the inertial frame and fixed in the orbit frame (refer back to Figures 4.10, 4.11, and 4.12).

We first look at the case of the prolate object. Figure 4.26 shows the prolate object with energy dissipation after only one orbit. Clearly the $\hat{b_3}$ axis is not in a stable oscillation as it fails to return to its original position after one revolution. Indeed, as the simulation is run out to ten orbits (Figure 4.27), the departure is even greater.

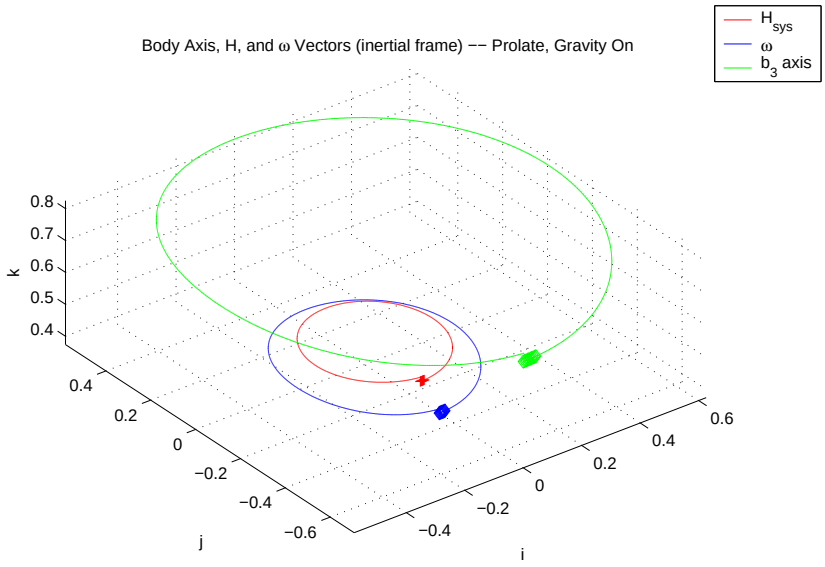


Figure 4.26: $\vec{H}$, $\vec{\omega}$, and the $\hat{b_3}$-axis in the inertial frame (Prolate Semi-Rigid Body, L-P, 1-Orbit)

The most telling sign that energy dissipation adversely effects the equilibria is the position of the $\hat{b_3}$ axis in the orbit frame (Figure 4.28). Rather than staying in a fixed position in this rotating frame (which would be required for a perfect equilibrium), the $\hat{b_3}$ axis sweeps through a dramatic pattern that is approximately 12 degrees high and 9 degrees across. Obviously this would be an undesirable behavior

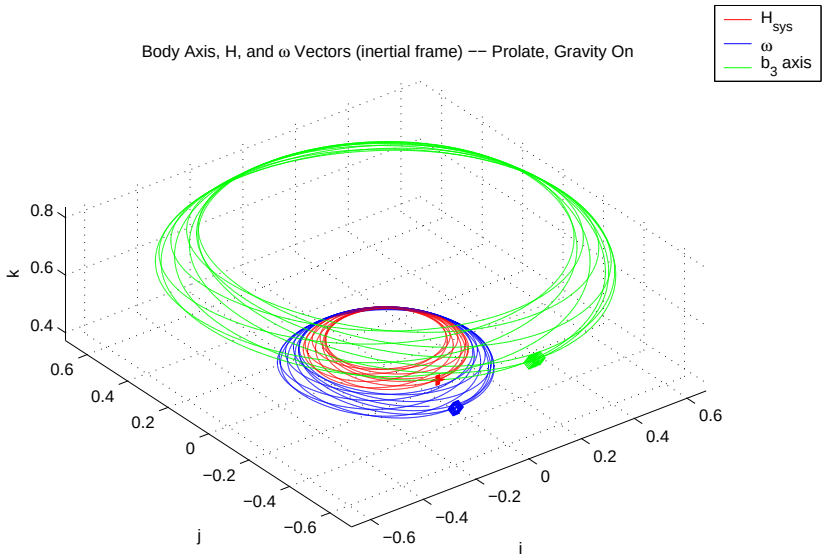


Figure 4.27: $\vec{H}$, $\vec{\omega}$, and the $\hat{b_3}$-axis in the inertial frame (Prolate Semi-Rigid Body, L-P, 10-Orbits)

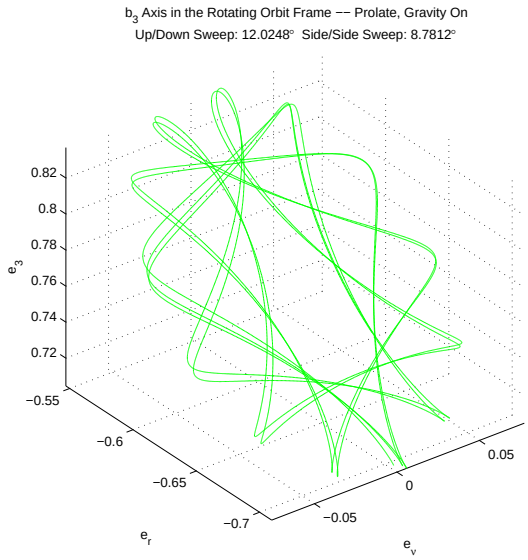


Figure 4.28: $\hat{b_3}$-axis in the Rotating Orbit Frame (Prolate Semi-Rigid Body, L-P, 10-Orbit)

for the remote sensing mission.

The oblate L-P case, by comparison, is much better albeit still adversely affected by the energy dissipation. After one orbit, the desired motion seems to be achieved, as shown in Figure 4.29. The $\hat{b_3}$ axis appears to return to its original position after one revolution, but it turns out to only delay the inevitable. Figure 4.30 shows that eventually, the $\hat{b_3}$ axis departs the nominal oscillation.

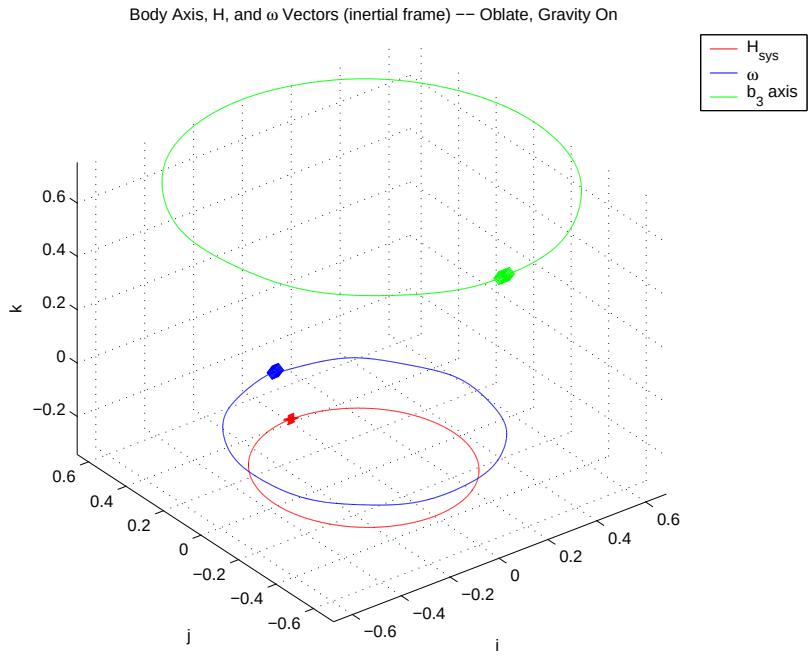


Figure 4.29: $\vec{H}$, $\vec{\omega}$, and the $\hat{b_3}$-axis in the inertial frame (Oblate Semi-Rigid Body, L-P, 1-Orbit)

Looking at the orbit frame behavior, the oblate case deviation is more suppressed but the $\hat{b_3}$ axis still cannot hold a fixed position in the rotating reference frame (Figure 4.31). The up and down nodding is limited to about 4 degrees and the side to side motion is less than 3 degrees – far less than the prolate case, but still undesirable when the goal is to remain fixed.

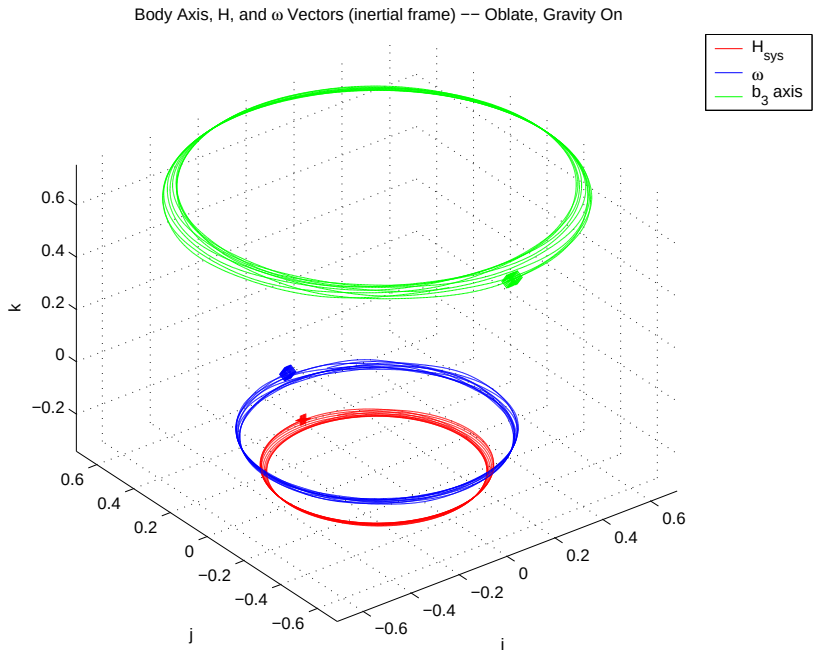


Figure 4.30: $\vec{H}$, $\vec{\omega}$, and the $\hat{b_3}$-axis in the inertial frame (Oblate Semi-Rigid Body, L-P, 10-Orbits)

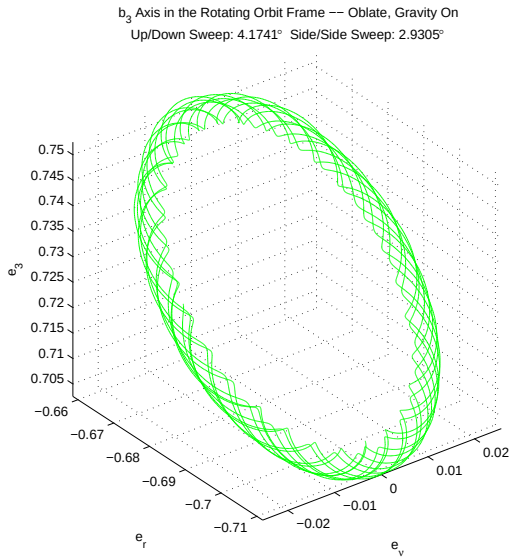


Figure 4.31: $\hat{b_3}$-axis in the Rotating Orbit Frame (Oblate Semi-Rigid Body, L-P, 10-Orbit)

Clearly, energy dissipation has a de-stabilizing effect on the conical L-P equilibria regardless of the shape of the object. That is, in the presence of energy dissipation, the $\hat{b_3}$ axis of a semi-rigid body in a L-P equilibrium does not remain fixed in the orbit frame (although it is worth noting that the behavior is still generally earth-facing). This result could likely explain some of the instabilities that Tragesser [67] encountered, particularly with his prolate tethered formations. The energy dissipation effect may be a major reason his configurations eventually diverged from the nominal motion.

The de-stabilization is much more pronounced in the prolate case (Figures 4.27 and 4.28) due to the impact of the Major Axis Rule which causes a prolate object to drift towards a flat spin about an arbitrary transverse moment of inertia. Looking forward to the case of a prolate *tethered* system, a flat spin of this kind would mean essentially no spin rate for the ring satellites, hence no tether tension in the ring tethers. On the other hand, the oblate case has a much less erratic, although still de-stabilizing, response to energy dissipation. Armed with that knowledge, we put aside the prolate tethered formation concepts and focus the remainder of this research on oblate configurations only.

Overall, the effect of energy dissipation on the conical L-P equilibria is unsuitable for the mission if not compensated for.

4.4.3 Equilibrium Condition for Semi-Rigid Bodies.

With the first objective complete, the next question to answer is: Can we find an equilibrium condition for an earth facing semi-rigid body? Surprisingly, an answer to this for the oblate case is much closer than we think.

While the effects of energy dissipation on L-P are initially (1 to 10 orbits) de-stabilizing to the fixed equilibrium condition, we find that over a long period of time (150 orbits), the higher order oscillations caused by energy dissipation have settled out and we are left with a near-"limit cycle": simple circularized behavior that remains earth-facing, and nearly repeats itself in the orbit frame. The average cone angle

grows very slowly once this near limit cycle is reached. An example of this is shown in Figure 4.32, which is the same semi-rigid body scenario shown in Figure 4.31, but after many more orbits. Notice the higher frequency behavior vanishes leaving a simple, near-periodic motion in the orbit frame. This "calming" effect is only observed in the oblate case.

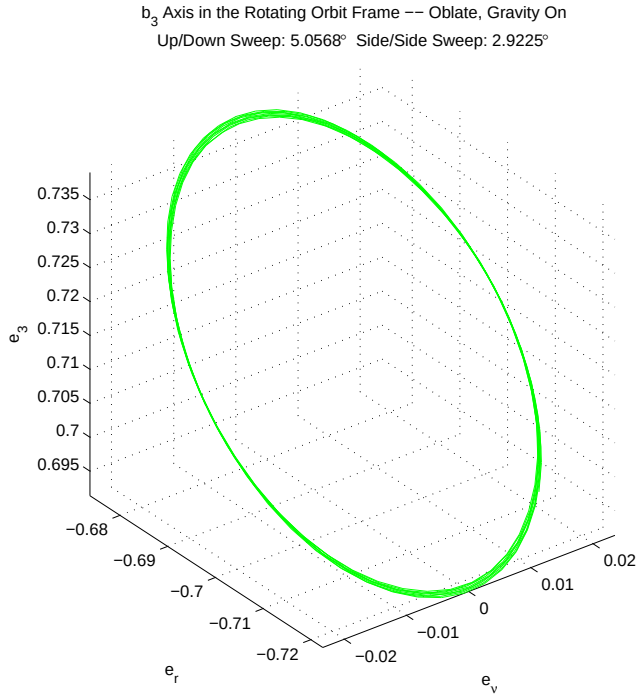


Figure 4.32: $\hat{b_3}$-axis in the Rotating Orbit Frame (Oblate Semi-Rigid Body, L-P, Orbits 140-150)

To visualize why this would happen only for the oblate case, the following concept is offered: imagine a polhode on an invariable plane, except now we have an "invariable" plane that is varying (in a periodic fashion) due to the gravity torques. The oblate object's polhode rolls around on the "variable" plane in the vicinity of its major inertia axis and despite being constantly nudged by the continual motion of our varying plane, it still wants to stay in the vicinity of the major axis. Conversely, the prolate object's polhode starts rolling near its minor inertia axis initially, but naturally wants to gravitate toward its major axis.

A cursory review of a limited number of scenario's shows that this long-term slow cone angle growth (on the order of thousandths of degrees per orbit) is insensitive to reasonable changes in damping parameters, initial cone angle, and orbit altitude.

One of the more obvious reasons for desiring the oblate body's long-term, simple, circular response over the prolate body's complex, unbounded, motion is the mission engineer's eventual need to manage sensor gimbals to counter the effects of the non-nadir pointing. The more erratic the motion, the higher the cost to maintain pointing. If we relax our constraint about a perfect equilibrium and accept (as an equilibrium condition) behavior that is somewhat fixed in the orbit frame with oscillations that are small, periodic, and simple (i.e. without the higher order patterns), then we can consider the long term oblate L-P response as shown in Figure 4.32 to be an acceptable near-equilibrium condition for an oblate semi-rigid body.

Since a near-equilibrium condition is found for the semi-rigid oblate case, no other analytic approaches are investigated to find a perfect equilibrium. The oblate L-P equilibria are used in the next step to base initial conditions for the multiple body system.

4.5 Summary

This chapter detailed the work that was accomplished in the area of rigid (no energy dissipation) and semi-rigid (with energy dissipation) body dynamics. Specifically, it discussed the development and numerical simulation of rigid and semi-rigid body models to determine the effects of energy dissipation on Likins-Pringle equilibria and to find an equilibrium condition for an earth-facing semi-rigid body.

Energy dissipation was found to have an adverse, de-stabilizing effect on Likins-Pringle equilibria in general. However, over the long term, an oblate semi-rigid body that starts in a Likins-Pringle equilibria settles into a simple, near-periodic motion that is acceptable to use as a basis for system dynamics. With this new understanding of the effects of energy dissipation on Likins-Pringle in hand, we have a unique contri-

bution to science. It is reasonable to now use the oblate rigid body L-P configurations to create initial conditions for the multi-body system model.

Modeling and simulation of the multi-body system dynamics is the subject of the next chapter.

V. Multi-body Formation Dynamics

With the rigid body work completed in the previous chapter, we now turn to multiple body formations. In this chapter, we develop models of the system dynamics and use oblate rigid body Likins-Pringle configurations as initial conditions for these multi-body systems. Next, evaluate the multi-body simulations and modify the models to deal with challenges as they arise. A main goal of this chapter is to find an answer to research objective 3: *Define and/or determine the existence of an equilibrium condition for a flexible tethered satellite system with a continuous earth-facing component.*

As with the rigid body work, a build-up approach is followed for the development of the system models, beginning with a simple two-body system. For each system, reference frames, coordinates and states are defined, equations-of-motion are derived, and modular MATLAB® code is written to numerically and graphically demonstrate the dynamics.

5.1 Two-Body Model Development

The general algorithm that is used for the two-body model is shown in Figure 5.1. We assume a massless, extensible tether connecting two single point masses (m_i) such that $m_i << M_\oplus$. A breakdown of this diagram, including an explanation of the constants, states and generalized coordinates is presented in the following subsections.

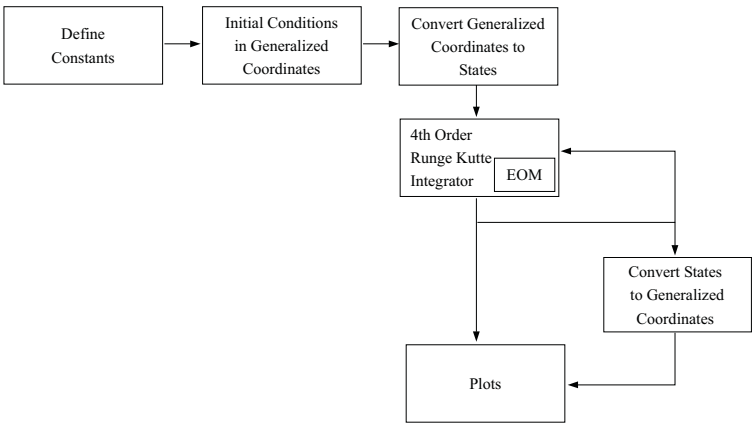


Figure 5.1: Block Diagram for System Model

5.1.1 Reference Frames and Generalized Coordinates. The relevant coordinate reference frames for the two-body system are shown in Figure 5.2.

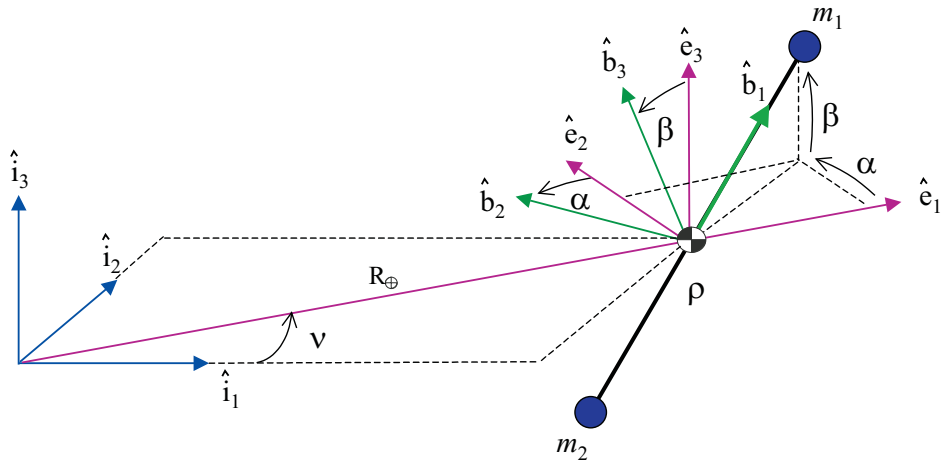


Figure 5.2: Two-Body Reference Frames

The inertial $\hat{i}$-frame is the same earth-centered cartesian coordinate frame discussed in Chapter IV. Once again, the orbit of the two-body system's center of mass (CoM) is assumed to be in the inertial $\hat{i}_1$-$\hat{i}_2$ plane. For our system work, we redefine our orbit frame ($\hat{e}$-frame) a little differently than we did in the rigid body chapter. The $\hat{e}$-frame is now centered on the center of mass of our system, and rotates in the orbit plane about its $\hat{e_3}$ axis such that the $\hat{e_1}$ axis is always pointing opposite nadir. The angle ν measures the difference between the $\hat{i}_1$ axis and the $\hat{e_1}$ axis. A third frame (the $\hat{b}$-frame) is defined by two rotations from the $\hat{e}$-frame,

$$C^{be} = R_2(-\beta)R_3(\alpha) \tag{5.1}$$

such that the $\hat{b_1}$ axis is always pointed at m_1 and $\hat{b_2}$ is always in the orbit plane. The $\hat{b_2}$ and $\hat{b_3}$ axes are both normal to the tether line connecting the two masses. The angles α and β can be thought of as angular polar coordinates (right ascension/declination) of m_1 relative to the $\hat{e}$-frame. Note that this $\hat{b}$-frame is not the same as the body frame used for rigid bodies.

The transformation from the inertial frame to the $\hat{b}$-frame is given by:

$$C^{bi} = R_2(-\beta)R_3(\alpha + \nu) \tag{5.2}$$

For two satellites in three-dimensional space, we would normally want six generalized coordinates. However, since we are restricting CoM to be in the $\hat{i}_1$-$\hat{i}_2$ plane, we have one constraint, therefore only five coordinates are necessary. We define our generalized coordinates as α, β, ν, $\vec{R}_\oplus$, and ρ, where ρ is the the distance between the two masses, and ${}^{\hat{i}}\vec{R}_\oplus$ is the inertial position of the system CoM. These are chosen because they are easy to visualize when defining initial conditions.

5.1.2 Initializing States from Generalized Coordinates. The states of this two-body model are the inertial positions and velocities of the two masses in the inertial frame:

$$\vec{X} = \left\{ \begin{array}{cccc} \vec{R}_1 & \vec{R}_2 & \vec{V}_1 & \vec{V}_2 \end{array} \right\}^T \tag{5.3}$$

While the generalized coordinates (α, β, ν, $\vec{R}_\oplus$, ρ) are easier to visualize, the inertial positions and velocities are easier to propagate with straight-forward equations of motion. Therefore, we must convert the initial generalized coordinates, along with their velocities, to the initial states.

To begin, relative position vectors with respect to the CoM, r_i, are defined in the body frame as:

$${}^{\hat{b}}\vec{r}_1 = \left[\begin{array}{ccc} l_1 & 0 & 0 \end{array} \right]^T = \left[\begin{array}{ccc} \frac{\rho m_2}{m_1+m_2} & 0 & 0 \end{array} \right]^T \tag{5.4}$$

$${}^{\hat{b}}\vec{r}_2 = \left[\begin{array}{ccc} -l_2 & 0 & 0 \end{array} \right]^T = \left[\begin{array}{ccc} \frac{-\rho m_1}{m_1+m_2} & 0 & 0 \end{array} \right]^T \tag{5.5}$$

where l_i are the tether lengths for each mass from the system CoM. Since ${}^{\hat{i}}\vec{R}_\oplus$ is the inertial position vector of the system CoM, then the inertial position vectors of the

two bodies, ${}^{\hat{i}}\vec{R}_i$, are

$$ {}^{\hat{i}}\vec{R}_i = {}^{\hat{i}}\vec{R}_\oplus + C^{i\hat{b}\hat{b}}\vec{r}_i \tag{5.6} $$

Similarly, to get the inertial velocities of the two bodies, ${}^{\hat{i}}\vec{V}_i$, we use

$$ {}^{\hat{i}}\vec{V}_i = {}^{\hat{i}}\vec{V}_\oplus + {}^{\hat{i}}\vec{v}_i \tag{5.7} $$

where ${}^{\hat{i}}\vec{v}_i$ is how $\vec{r}_i$ changes with respect to the inertial frame. Recalling the relationship of Equation 4.14, we get

$$ {}^{\hat{i}}\vec{v}_i = {}^{\hat{i}}\frac{d}{dt}{}^{\hat{b}}\vec{r}_i = {}^{\hat{b}}\frac{d}{dt}{}^{\hat{b}}\vec{r}_i + {}^{\hat{b}}\vec{\omega}^{bi} \times {}^{\hat{b}}\vec{r}_i \tag{5.8} $$

Since we are assuming our initial conditions will be at a nominal steady-state tether length, we can assume that r_i does not change with respect to the $\hat{b}$-frame, therefore ${}^{\hat{b}}\frac{d}{dt}{}^{\hat{b}}\vec{r}_i = 0$.

As with the rigid body, $\vec{\omega}^{bi}$ is the inertial angular velocity of the system and can be expressed in multiple reference frames as

$$ \vec{\omega}^{bi} = \dot{\nu}\hat{i}_3 + \dot{\alpha}\hat{e}_3 + \dot{\beta}\hat{b}_2 \tag{5.9} $$

and in the $\hat{b}$-frame as

$$ {}^{\hat{b}}\vec{\omega}^{bi} = C^{bi}\begin{bmatrix} 0 \\ 0 \\ \dot{\nu} \end{bmatrix} + C^{be}\begin{bmatrix} 0 \\ 0 \\ \dot{\alpha} \end{bmatrix} + \begin{bmatrix} 0 \\ \dot{\beta} \\ 0 \end{bmatrix} \tag{5.10} $$

where $\dot{\nu}$ is the angular orbit rate of the system around the Earth. We know from Bate et al. [3] that we can determine specific angular momentum, h, of our two-body system in a two ways:

$$h = \left| {}^{\hat{i}}\vec{R}_{\oplus} \times {}^{\hat{i}}\vec{V}_{\oplus} \right| = \dot{\nu} \left| {}^{\hat{i}}\vec{R}_{\oplus} \right|^2 \tag{5.11}$$

By re-arranging, it is shown that $\dot{\nu}$ is calculated from our initial reference orbit; that is, the inertial position and velocity of our system CoM:

$$\dot{\nu} = \frac{\left| {}^{\hat{i}}\vec{R}_{\oplus} \times {}^{\hat{i}}\vec{V}_{\oplus} \right|}{\left| {}^{\hat{i}}\vec{R}_{\oplus} \right|^2} \tag{5.12}$$

The approach for selecting initial values for $\dot{\alpha}$ and $\dot{\beta}$ is dependent on the specific initial configuration being modeled. As it turns out, it is easier for our Likins-Pringle scenario to re-package $\dot{\alpha}$ and $\dot{\beta}$ into a new value, $\dot{\psi}$, which is the spin rate of the system about its own center of mass. This is discussed more in Section 5.1.5.

5.1.3 Equations-of-Motion. With the initial positions and velocities calculated in the inertial frame, the states can be run through a fourth order Runge-Kutte numerical integrator (RK4) using the equations-of-motion shown in this section. Recalling the state vector, $\vec{X}$, from Equation 5.3, we need expressions for $\dot{\vec{X}}$. The first two equations-of-motion, derivatives of the positions, are obviously:

$$\dot{\vec{R}}_i = \vec{V}_i \tag{5.13}$$

The derivatives of the velocities are broken out into two categories to assist "toggling" them on and off in the model: accelerations due to gravity; and accelerations from the tether. The gravity acceleration can be taken from any astrodynamics text [71, 73]:

$$\dot{\vec{V}}_{i_{gravity}} = \ddot{\vec{R}}_{i_{gravity}} = \frac{-\mu_{\oplus}}{\left| \vec{R}_i \right|^3} \vec{R}_i \tag{5.14}$$

For elastic tethers, they are treated as partial springs, like a bungee cord. That is, they are springs that can only hold tension, not compression. To model this we use equations for a damped spring (Equations 5.15 and 5.16), but only engage those accelerations (forces) when the current distance between the two masses (ρ) is greater than the unstretched tether length (ρ_o). The accelerations on each mass from a spring-damper are:

$$\dot{\vec{V}}_{i_{spring}} = \ddot{\vec{R}}_{i_{spring}} = \begin{cases} \frac{\delta_i K_s(\rho-\rho_o)}{m_i}\left(\frac{\vec{r}_{12}}{\rho}\right) & \text{if} \quad (\rho-\rho_o) \geq 0 \\ 0 & \text{if} \quad (\rho-\rho_o) < 0 \end{cases} \tag{5.15}$$

$$\dot{\vec{V}}_{i_{damper}} = \ddot{\vec{R}}_{i_{damper}} = \begin{cases} \frac{\delta_i \mu_d \dot{\rho}}{m_1}\left(\frac{\vec{r}_{12}}{\rho}\right) & \text{if} \quad (\rho-\rho_o) \geq 0 \quad \text{and} \quad \dot{\rho} > 0 \\ 0 & \text{else} \end{cases} \tag{5.16}$$

where

$$\delta_i = \begin{cases} 1 & \text{if} \quad i = 1 \\ -1 & \text{if} \quad i = 2 \end{cases} \tag{5.17}$$

and K_s is the tether stiffness (or coefficient of elasticity), μ_d is the tether damping coefficient, and $\vec{r}_{12}$ is the vector from m_1 to m_2 given by

$$\vec{r}_{12} = {}^{\hat{i}}\vec{R}_2 - {}^{\hat{i}}\vec{R}_1 \tag{5.18}$$

The time rate of change of tether length, $\dot{\rho}$, is determined by calculating the projection of $\vec{V}_{12}$ in the $\vec{r}_{12}$ direction:

$$\dot{\rho} = \frac{\vec{r}_{12} \cdot \vec{V}_{12}}{|\vec{r}_{12}|} \tag{5.19}$$

where

$$\vec{V}_{12} = {}^{\hat{i}}\vec{V}_2 - {}^{\hat{i}}\vec{V}_1 \tag{5.20}$$

While not as elegant as using energy methods, these equations-of-motion allow us to easily select/de-select the various accelerations (forces) during the simulations.

5.1.4 Converting States to Generalized Coordinates. As the states are propagated forward in time, it is useful to look at the behavior of the generalized coordinates (α, β, and ρ). To convert from the states to α, we use

$$\alpha = \tan^{-1}\left(\frac{\vec{R}_1 \cdot \hat{i}_2 - \vec{R}_\oplus \cdot \hat{i}_2}{\vec{R}_1 \cdot \hat{i}_1 - \vec{R}_\oplus \cdot \hat{i}_1}\right) - \tan^{-1}\left(\frac{\vec{R}_\oplus \cdot \hat{i}_2}{\vec{R}_\oplus \cdot \hat{i}_1}\right) \tag{5.21}$$

To get β, use $\vec{r}_{12}$ from Equation 5.18,

$$\beta = \sin^{-1}\left(\frac{\vec{r}_{12} \cdot \hat{i}_3}{\rho}\right) \tag{5.22}$$

while ρ is simply the magnitude of $\vec{r}_{12}$.

5.1.5 Initial Conditions for Likins-Pringle. Recall that it is desirable to use an oblate rigid body Likins-Pringle configuration to generate the initial conditions for this multi-body system. To simplify this process, we can make certain choices on the set-up without loss of generality. Assume our spinning two body system is mimicking a disk that is initially located some distance out along the $\hat{i_1}$ axis with a rigid body cone angle of θ (see Figure 5.3).

In this case, the initial generalized coordinates for the system would be:

$$\begin{aligned} {}^{\hat{i}}\vec{R}_\oplus &= X_\oplus \hat{i}_1 \\ {}^{\hat{i}}\vec{V}_\oplus &= \sqrt{\frac{\mu_\oplus}{|{}^{\hat{i}}\vec{R}_\oplus|}}\hat{i}_2 \\ \rho &= \text{arbitrary} \\ \alpha &= 0 \\ \beta &= \theta \end{aligned} \tag{5.23}$$

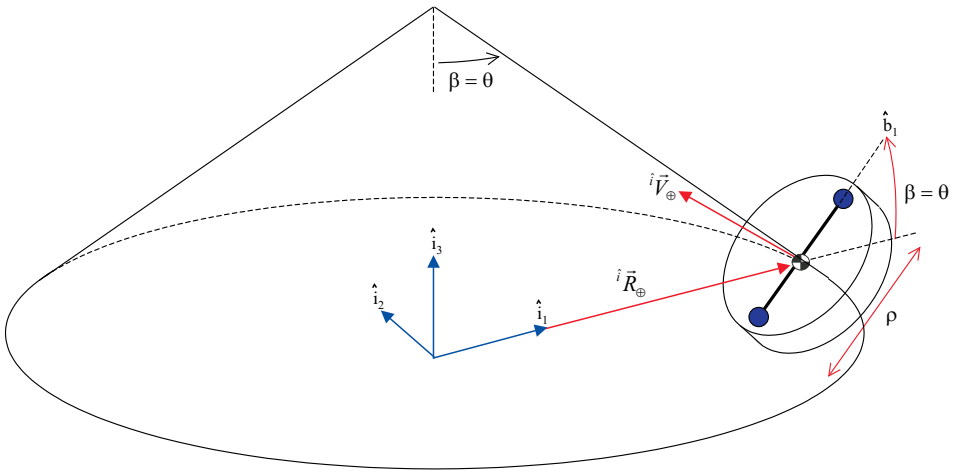


Figure 5.3: Two-Body Likins-Pringle Set-up

which can be used to generate the initial state positions from Equation 5.6. Getting the initial state velocities requires a little more thought. Since we are mimicking an oblate rigid body that spins at a rate $\dot{\psi}$, it seems more intuitive to use that variable in calculating $\vec{\omega}^{bi}$ in Equation 5.9 rather than deriving $\dot{\alpha}$ and $\dot{\beta}$. Therefore, the initial inertial angular velocity of the system and can be expressed in multiple reference frames as

$$\vec{\omega}^{bi} = \dot{\psi}\hat{b}_3 + \dot{\nu}\hat{i}_3 \,(\hat{e}_3) \tag{5.24}$$

and in the $\hat{b}$-frame as

$$^{\hat{b}}\vec{\omega}^{bi} = \begin{bmatrix} 0 \\ 0 \\ \dot{\psi} \end{bmatrix} + C^{be} \begin{bmatrix} 0 \\ 0 \\ \dot{\nu} \end{bmatrix} \tag{5.25}$$

Recall from Equation 4.40 in the last chapter that the spin rate for a rigid body in a conical Likins-Pringle equilibria is (repeated here):

$$\dot{\psi} = \dot{\nu}\cos\theta\,(4\,(A - C))/C \tag{5.26}$$

However, in the case of a system of bodies connected by elastic tethers, a given spin rate generates a new value for a steady state tether length ρ_{ss} as the tether stretches, which in-turn changes the moments-of-inertia of the system (C and A), which in-turn generates yet a new spin rate, and so on (Figure 5.4). To generate a true initial value for $\dot{\psi}_{ss}$, this calculation loop is iteratively computed until the difference between successive values of ρ_{ss} is below some error value.

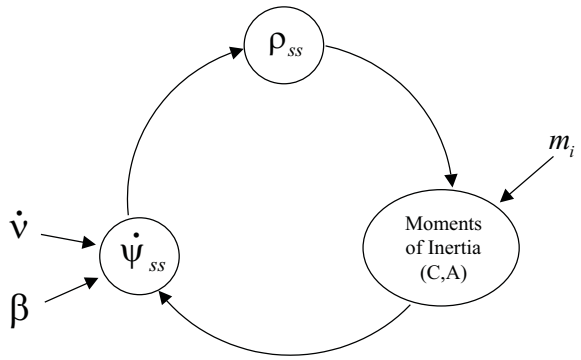


Figure 5.4: Likins-Pringle $\dot{\psi}$ Iteration Loop

The calculation to determine ρ_{ss} from $\dot{\psi}_{ss}$ is derived by balancing the centrifugal force with the force of the tether:

$$ml\dot{\psi}_{ss}^2 = K_s(\rho_{ss} - \rho_o) \tag{5.27}$$

By re-arranging and noting that $l = \rho/2$, we get

$$\rho_{ss} = \frac{K_s\rho_o}{K_s - \frac{m}{2}\dot{\psi}_{ss}^2} \tag{5.28}$$

All that remains is a method to calculate the moments-of-inertia from ρ_{ss}. Getting the axial moment-of-inertia (C_{sys}) is fairly straightforward:

$$C = \sum_i m_i \left(r_{ss}\right)^2 = \sum_i m_i \left(\frac{\rho_{ss}}{2}\right)^2 \tag{5.29}$$

Unfortunately, the transverse moment-of-inertia (A_{sys}) of a multi-body system is not a constant value in the two-body case. In fact, if n is the number of bodies in the multi-body flat ring system the transverse MOI is:

$$A_{sys}^{\oplus} = \begin{cases} m\left(r_{ss}\right)^2\left(\frac{n}{2}\right) & n > 2 \\ 2m\left(r_{ss}\right)^2\cos^2\sigma & n = 2 \end{cases} \tag{5.30}$$

where σ is an arbitrary aspect angle from which the transverse MOI is being calculated (see Figure 5.5. In other words, for n=2, the transverse moment-of-inertia oscillates as the system spins relative to the gravity forces, therefore the Likins-Pringle equilibria will not hold. The derivation of Equation 5.30 is shown in Appendix B.

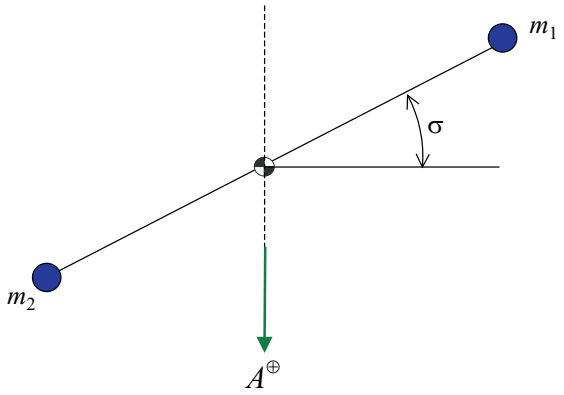


Figure 5.5: Two-body Transverse MOI

Since the transverse moment-of-inertia is completely independent of σ for all $n > 2$ (as seen in Equation 5.30), we continue the build-up approach by moving on to a three-body model using many of the same principles used to develop the two-body model. It also should be noted that a 2-D array ($n > 2$) is the desired configuration for this study.

5.2 Three-Body Model Development

The construction of the three-body model follows closely with the development of the two-body case in the last section. In fact, the general algorithm used is exactly the same as the one shown in Figure 5.1. The primary difference, of course, is that now we have three single point masses (m_i) distributed evenly in a ring formation and connected by massless, extensible tethers (ρ_{ij}) (see Figure 5.6).

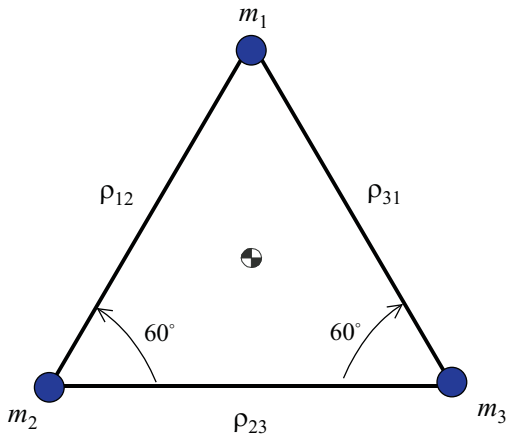


Figure 5.6: Three-Body Ring Formation (assuming Equal Masses)

5.2.1 Reference Frames. The frames from the two-body model are used once again. The $\hat{i}$-frame is still earth-centered inertial and the $\hat{e}$-frame (orbit frame) is still CoM-centered while rotating by an angle ν about its $\hat{e_3}$ axis such that the $\hat{e_1}$ axis is always pointing opposite nadir (Figure 5.7).

The $\hat{b}$-frame is still defined by the two rotations (α and β) from the orbit frame such that the $\hat{b_1}$ axis is pointed at mass 1, but now the $\hat{b}$-frame is only going to be used for determining the initial configuration for the simulations. Instead, a fourth frame is introduced for observing desired behavior during the simulations: the stroboscopic frame or $\hat{s}$-frame (see Figure 5.8). The stroboscopic frame is called so by Hughes [20] because, although not fixed in the $\hat{b}$-frame, it coincides with the $\hat{b}$-frame after completing each rotation with respect to the orbit frame.

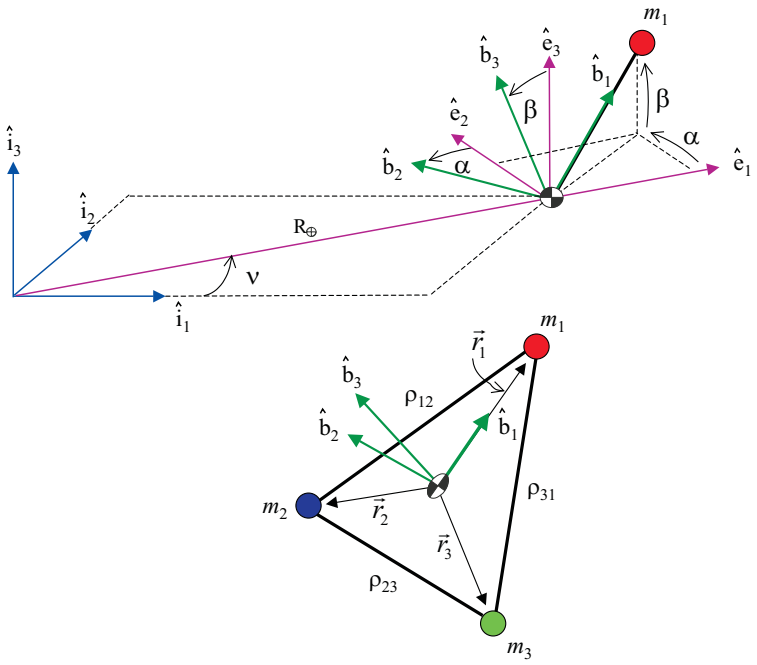


Figure 5.7: Three-Body Reference Frames (Set-up)

The best way to visualize the $\hat{s}$-frame is start with the orbit frame and simply do a rotation about the $\hat{e_2}$ axis by the angle $-\beta$. Essentially, the stroboscopic frame rotates with the orbit, keeping its $\hat{s_3}$ axis fixed to the same inertial point in space and sweeping out a cone around the Earth (the same cone mentioned for conical Likins-Pringle equilibria). Looking ahead, if a ring formation were to confine its motion to the $\hat{s_1}$-$\hat{s_2}$ plane, we define that motion as "strobo-planar".

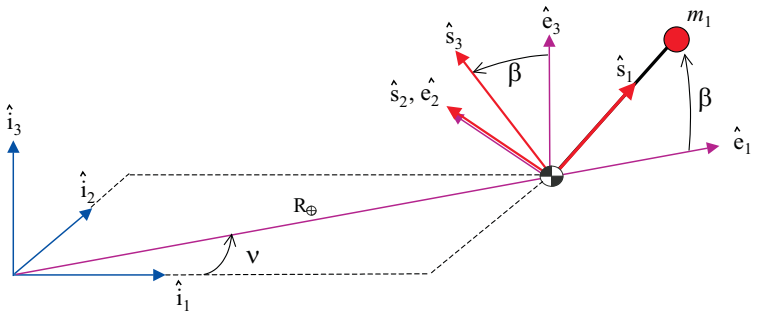


Figure 5.8: Stroboscopic Frame (for Observation)

5.2.2 Initializing States from Generalized Coordinates. Since another body has been added, the state vector must obviously grow by an additional inertial position and velocity (note that the order has also been changed from the two-body case):

$$\vec{X} = \left\{ \begin{array}{cccccc} \vec{R}_1 & \vec{V}_1 & \vec{R}_2 & \vec{V}_2 & \vec{R}_3 & \vec{V}_3 \end{array} \right\}^T \tag{5.31}$$

With three satellites, nine generalized coordinates would normally be necessary, however we have a couple of constraints and other considerations. The first constraint comes from our restricting the CoM to the $\hat{i}_1$-$\hat{i}_2$ plane. Next, since we are only using these generalized coordinates to establish initial conditions, we restrict the three satellites to the $\hat{s}_1$-$\hat{s}_2$ plane. Finally, we assume that all three tethers start at the same length. Therefore, we have a total of four constraints, which means the five generalized coordinates from before can once again suffice (α, β, ν, $\vec{R}_\oplus$, ρ), although now ρ accounts for all three distances between the objects.

As with the two-body case, we want to initialize this state vector by converting from the familiar set of easily assignable generalized coordinates and their respective velocities to the vectors in Equation 5.31. All of the conversions for three-body scenarios are identical to those shown in Section 5.1.2 for the two-body case. For the assumption that the three objects have equal mass, the only difference is that now the relative position vectors with respect to the CoM are

$$^{\hat{b}}\vec{r}_1 = \left[\begin{array}{ccc} \frac{\sqrt{3}}{3}\rho & 0 & 0 \end{array} \right]^T \tag{5.32}$$

$$^{\hat{b}}\vec{r}_2 = \left[\begin{array}{ccc} \frac{-\sqrt{3}}{6}\rho & \frac{\rho}{2} & 0 \end{array} \right]^T \tag{5.33}$$

$$^{\hat{b}}\vec{r}_3 = \left[\begin{array}{ccc} \frac{-\sqrt{3}}{6}\rho & \frac{-\rho}{2} & 0 \end{array} \right]^T \tag{5.34}$$

All other general conversion equations from Section 5.1.2 remain unchanged for the three-body case:

$$^{\hat{i}}\vec{R}_i = {}^{\hat{i}}\vec{R}_\oplus + C^{ib\hat{b}}\vec{r}_i \tag{5.35}$$

$$^{\hat{i}}\vec{V}_i = {}^{\hat{i}}\vec{V}_\oplus + {}^{\hat{i}}\vec{v}_i \tag{5.36}$$

$$^{\hat{i}}\vec{v}_i = {}^{\hat{i}}\frac{d}{dt}{}^{\hat{b}}\vec{r}_i = {}^{\hat{b}}\frac{d}{dt}{}^{\hat{b}}\vec{r}_i + {}^{\hat{b}}\vec{\omega}^{bi} \times {}^{\hat{b}}\vec{r}_i \tag{5.37}$$

$${}^{\hat{b}}\vec{\omega}^{bi} = C^{bi}\begin{bmatrix} 0 \\ 0 \\ \dot{\nu} \end{bmatrix} + C^{be}\begin{bmatrix} 0 \\ 0 \\ \dot{\alpha} \end{bmatrix} + \begin{bmatrix} 0 \\ \dot{\beta} \\ 0 \end{bmatrix} \tag{5.38}$$

$$\dot{\nu} = \frac{\left|{}^{\hat{i}}\vec{R}_\oplus \times {}^{\hat{i}}\vec{V}_\oplus\right|}{\left|{}^{\hat{i}}\vec{R}_\oplus\right|^2} \tag{5.39}$$

5.2.3 Initial Conditions for Likins-Pringle. To create the specific scenario of having the three-body ring formation in the initial set-up that mimics the oblate Likins-Pringle equilibria (Figure 5.9), the same general process is used from the two-body case (Section 5.1.5). To visualize the approach, imagine a tuna can (or disk) in a conical Likins-Pringle equilibria at some arbitrary cone angle. Now paint three even spaced "dots" on the tuna can such that one of the dots is at the apex of the can and in the $\hat{e}_1$-$\hat{e}_3$ plane.

The initial generalized coordinates for the system are still:

$$\begin{gathered} {}^{\hat{i}}\vec{R}_\oplus = X_\oplus \hat{i}_1 \\ {}^{\hat{i}}\vec{V}_\oplus = \sqrt{\frac{\mu_\oplus}{\left|{}^{\hat{i}}\vec{R}_\oplus\right|}}\hat{i}_2 \\ \rho = \text{arbitrary} \\ \alpha = 0 \\ \beta = \theta \end{gathered} \tag{5.40}$$

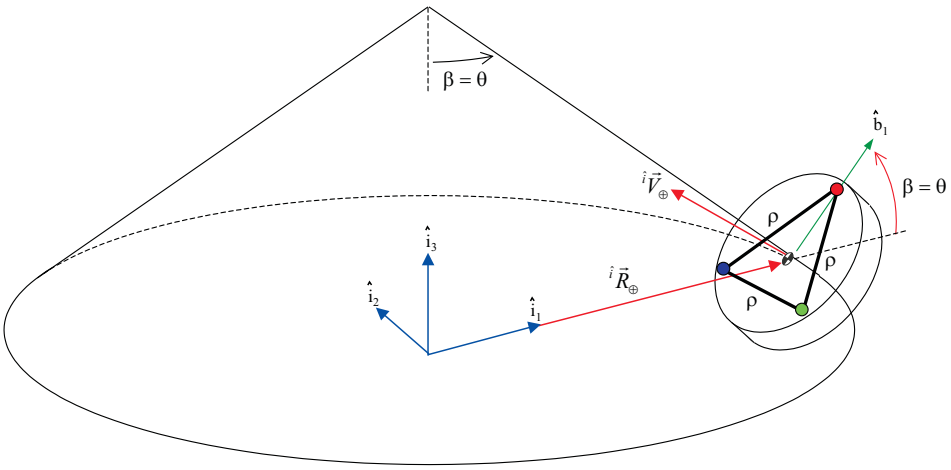


Figure 5.9: Three-Body Likins-Pringle Set-up

while the initial inertial angular velocity of the system is still:

$$^{\hat{b}}\vec{\omega}^{bi} = \begin{bmatrix} 0 \\ 0 \\ \dot{\psi} \end{bmatrix} + C^{be} \begin{bmatrix} 0 \\ 0 \\ \dot{\nu} \end{bmatrix} \tag{5.41}$$

The only change in the three-body Likins-Pringle set-up compared to the two-body version is in the calculations of the initialization iteration loop shown back in Figure 5.4. Specifically, the new equation for determining the steady-state tether length (ρ_{ss}) for a given spin rate ($\dot{\psi}_{ss}$) is now

$$\rho_{ss} = \frac{K_s \rho_o}{K_s - \frac{m}{3}\left(\dot{\psi}_{ss} + \left(\dot{\nu}\hat{e}_3 \cdot \hat{b}_3\right)\right)^2} \tag{5.42}$$

Furthermore, to calculate appropriate values for the moments-of-inertia from Equations 5.29 and 5.30, noting that $n = 3$ and r_{ss}=$\frac{\sqrt{3}\rho_{ss}}{3}$,

$$C_{sys} = 3m\left(r_{ss}\right)^2 \tag{5.43}$$

$$A_{sys} = m\left(r_{ss}\right)^2\left(\frac{3}{2}\right) \tag{5.44}$$

In other words, the ratio of C_{sys}:A_{sys} is 2:1. We now have an initialized state vector that is ready for numerical integration once the equations-of-motion are determined.

5.2.4 Equations-of-Motion. The states are run through an RK4 numerical integrator using $\dot{\vec{X}} = f(\vec{X}, t)$ where

$$\dot{\vec{R}}_i = \vec{V}_i \tag{5.45}$$

$$\dot{\vec{V}}_i = \ddot{\vec{R}}_i \tag{5.46}$$

A number of vectors are defined as shown in Figure 5.10 where $\vec{R}_i$ are vectors from the inertial frame origin to mass i, $\vec{r}_i$ are vectors from the system center of mass to mass i, and $\vec{r}_{ij}$ are vectors from mass i to mass j.

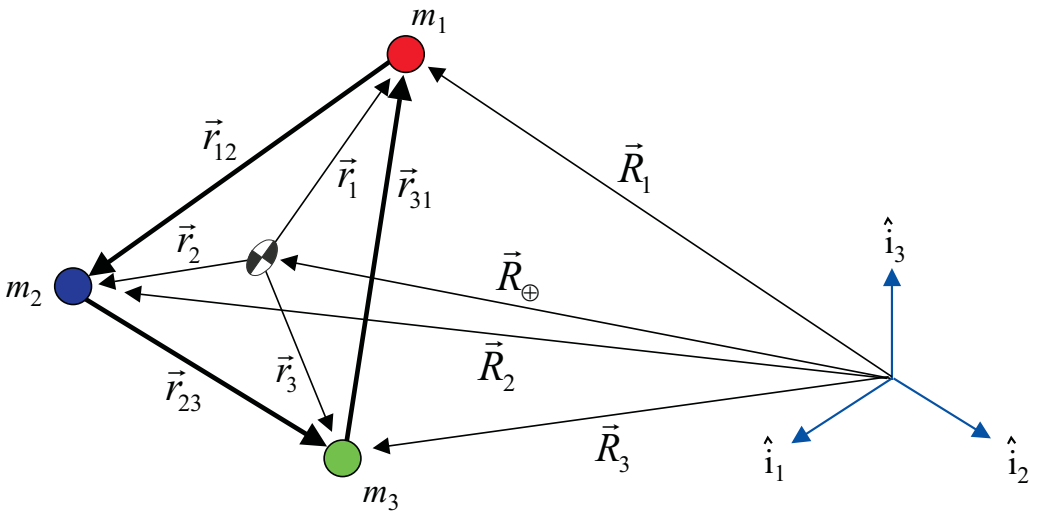


Figure 5.10: Three-Body Model Vectors

As before, the equations for $\ddot{\vec{R}}_i$ on each mass are separated into "accelerations due to gravity" and "accelerations due to the tethers". The accelerations due to gravity are unchanged from the two-body case:

$$\ddot{\vec{R}}_{i_{gravity}} = \frac{-\mu_{\oplus}}{\left|\vec{R}_i\right|^3}\vec{R}_i \tag{5.47}$$

Likewise, the accelerations due to the tethers are again treated as viscously damped springs that can only hold tension when stretched beyond ρ_o:

$$\ddot{\vec{R}}_{i_{spring}} = \begin{cases} \frac{\delta_{nm}K_s(\rho_{ij}-\rho_o)}{m_i}\left(\frac{\vec{r}_{ij}}{\rho_{ij}}\right) & \text{if} \quad (\rho_{ij}-\rho_o) \geq 0 \\ 0 & \text{if} \quad (\rho_{ij}-\rho_o) < 0 \end{cases} \tag{5.48}$$

$$\ddot{\vec{R}}_{i_{damper}} = \begin{cases} \frac{\delta_{nm}\mu_d\dot{\rho}_{ij}}{m_i}\left(\frac{\vec{r}_{ij}}{\rho_{ij}}\right) & \text{if} \quad (\rho_{ij}-\rho_o) \geq 0 \quad \text{and} \quad \dot{\rho}_{ij} > 0 \\ 0 & \text{else} \end{cases} \tag{5.49}$$

where

$$\vec{r}_{ij} = {}^{\hat{i}}\vec{R}_j - {}^{\hat{i}}\vec{R}_i \tag{5.50}$$

$$\rho_{ij} = |\vec{r}_{ij}| \tag{5.51}$$

$$\dot{\rho}_{ij} = \frac{\vec{r}_{ij}\cdot\vec{V}_{ij}}{\rho_{ij}} \tag{5.52}$$

$\vec{V}_{ij}$ is the velocity of mass j with respect to mass i:

$$\vec{V}_{ij} = {}^{\hat{i}}\vec{V}_j - {}^{\hat{i}}\vec{V}_i \tag{5.53}$$

The term δ_{nm} is simply used to change the direction (sign) of the force acting on the i^{th} body:

$$\delta_{nm} = \begin{cases} 1 & \text{if} \quad n = i \\ -1 & \text{if} \quad m = i \\ 0 & \text{else} \end{cases} \tag{5.54}$$

noting that n and m are compared to the subscripts on the relative position vectors $\vec{r}_{ij}$ and that $n \neq m$. For example, if we are applying Equation 5.49 to body i=1, then δ_{nm} will be positive for the forces acting along $\vec{r}_{12}$ and negative for the forces acting along $\vec{r}_{31}$.

Therefore, the complete set of equations-of-motion for the three-body ring formation looks like:

$$\dot{\vec{R}}_1 = \vec{V}_1 \tag{5.55}$$

$$\dot{\vec{R}}_2 = \vec{V}_2 \tag{5.56}$$

$$\dot{\vec{R}}_3 = \vec{V}_3 \tag{5.57}$$

$$\dot{\vec{V}}_1 = \frac{-\mu_\oplus}{\left|\vec{R}_1\right|^3}\vec{R}_1 + \frac{K_s(\rho_{12}-\rho_o)}{m_1}\left(\frac{\vec{r}_{12}}{\rho_{12}}\right) - \frac{K_s(\rho_{31}-\rho_o)}{m_1}\left(\frac{\vec{r}_{31}}{\rho_{31}}\right) + \frac{\mu_d\dot{\rho}_{12}}{m_1}\left(\frac{\vec{r}_{12}}{\rho_{12}}\right) - \frac{\mu_d\dot{\rho}_{31}}{m_1}\left(\frac{\vec{r}_{31}}{\rho_{31}}\right) \tag{5.58}$$

$$\dot{\vec{V}}_2 = \frac{-\mu_\oplus}{\left|\vec{R}_2\right|^3}\vec{R}_2 + \frac{K_s(\rho_{23}-\rho_o)}{m_2}\left(\frac{\vec{r}_{23}}{\rho_{23}}\right) - \frac{K_s(\rho_{12}-\rho_o)}{m_2}\left(\frac{\vec{r}_{12}}{\rho_{12}}\right) + \frac{\mu_d\dot{\rho}_{23}}{m_2}\left(\frac{\vec{r}_{23}}{\rho_{23}}\right) - \frac{\mu_d\dot{\rho}_{12}}{m_2}\left(\frac{\vec{r}_{12}}{\rho_{12}}\right) \tag{5.59}$$

$$\dot{\vec{V}}_3 = \frac{-\mu_\oplus}{\left|\vec{R}_3\right|^3}\vec{R}_3 + \frac{K_s(\rho_{31}-\rho_o)}{m_3}\left(\frac{\vec{r}_{31}}{\rho_{31}}\right) - \frac{K_s(\rho_{23}-\rho_o)}{m_3}\left(\frac{\vec{r}_{23}}{\rho_{23}}\right) + \frac{\mu_d\dot{\rho}_{31}}{m_3}\left(\frac{\vec{r}_{31}}{\rho_{31}}\right) - \frac{\mu_d\dot{\rho}_{23}}{m_3}\left(\frac{\vec{r}_{23}}{\rho_{23}}\right) \tag{5.60}$$

where we select/de-select various components as required for analysis.

5.2.5 Converting States to Variables of Interest (VOI). At each step in the integration, we want to save dynamic information in a form that is easy to visualize and/or important to the evaluation. To accomplish this, the states are converted into particular "Variables of Interest" (VOI).

The first VOI are the inertial position and velocity of the center of mass of the system. These are calculated using Equations 5.61 and 5.62.

$$^{\hat{i}}\vec{R}_{\oplus} = \vec{R}_1\frac{m_1}{\sum_i m_i} + \vec{R}_2\frac{m_2}{\sum_i m_i} + \vec{R}_3\frac{m_3}{\sum_i m_i} \tag{5.61}$$

$$^{\hat{i}}\vec{V}_{\oplus} = \vec{V}_1\frac{m_1}{\sum_i m_i} + \vec{V}_2\frac{m_2}{\sum_i m_i} + \vec{V}_3\frac{m_3}{\sum_i m_i} \tag{5.62}$$

The updated $^{\hat{i}}\vec{R}_{\oplus}$ and $^{\hat{i}}\vec{V}_{\oplus}$ are then used to determine the next VOI: $^{\hat{i}}\vec{r}_i$, the relative positions of the individual bodies, expressed in the inertial frame; and $^{\hat{i}\hat{i}}\vec{v}_i$, how $\vec{r}_i$ changes with respect to the inertial frame, expressed in the inertial frame.

$$^{\hat{i}}\vec{r}_i = {}^{\hat{i}}\vec{R}_i - {}^{\hat{i}}\vec{R}_{\oplus} \tag{5.63}$$

$$^{\hat{i}\hat{i}}\vec{v}_i = {}^{\hat{i}\hat{i}}\vec{V}_i - {}^{\hat{i}\hat{i}}\vec{V}_{\oplus} \tag{5.64}$$

By crossing the individual relative positions with their velocities and summing the products, we form what we'll call the "local angular momentum" ($\vec{h}$) of the system in the inertial frame:

$$^{\hat{i}}\vec{h} = \sum_i {}^{\hat{i}}\vec{r}_i \times m_i {}^{\hat{i}\hat{i}}\vec{v}_i \tag{5.65}$$

or, if all m_i are equal,

$$^{\hat{i}}\vec{h} = m\sum_i {}^{\hat{i}}\vec{r}_i \times {}^{\hat{i}\hat{i}}\vec{v}_i \tag{5.66}$$

This local angular momentum acts as a sort of "spin axis" for the system, conceptually similar to the rigid body's spin axis. For "strobo-planar" motion, this local angular momentum vector lies entirely along the $\hat{s}_3$ axis. The final set of VOI's are the tether lengths (ρ_{ij}'s) and the tether length rates ($\dot{\rho}_{ij}$'s) calculated using Equations 5.50-5.52.

These VOI's, especially the relative positions and local angular momentum, are the main tool for analyzing the dynamic behavior of the system. Recall that the equilibrium condition desired is a dynamic state where the nadir projection of the aperture remains unchanged with respect to a frame that rotates with the orbit (that is, the spin axis remains fixed or in a closed path in a rotating orbit frame). Therefore, to aid in our analysis, we take these key VOI's that are calculated in the inertial ($\hat{i}$) frame and rotate them into the two frames that would interest us: the rotating orbit frame ($\hat{e}$-frame) and/or the stroboscopic frame ($\hat{s}$-frame). To rotate into the orbit frame,

$$\begin{aligned} {}^{\hat{e}}\vec{r}_i &= C^{ei\hat{i}}\vec{r}_i \\ {}^{\hat{e}}\vec{h}_i &= C^{ei\hat{i}}\vec{h}_i \\ C^{ei} &= R_3(\nu) \\ \nu &= \tan^{-1}\left(\tfrac{Y_\oplus}{X_\oplus}\right) \end{aligned} \tag{5.67}$$

Similarly, to rotate into the stroboscopic frame,

$$\begin{aligned} {}^{\hat{s}}\vec{r}_i &= C^{si\hat{i}}\vec{r}_i \\ {}^{\hat{s}}\vec{h}_i &= C^{si\hat{i}}\vec{h}_i \\ C^{si} &= R_2(-\beta_o)\,R_3(\nu) \end{aligned} \tag{5.68}$$

where β_o is the initial cone angle (denoted as θ in the rigid body work) as was shown in Figure 5.8.

5.3 Initial Three-Body Simulations

With equations-of-motion and a way to determine initial conditions in hand, a modular MATLAB® model is built for numerical simulation using the same algorithm as before (Figure 5.1). The specific code is shown in Appendix F.

The Earth's gravitational constant is assumed to be 398600.4415 $^{km^3}/_{s^2}$ per Vallado [71]. The three satellites are assumed to be identical, therefore the masses are all given arbitrary (but realistic) values of 200 kg. The tether stiffness, K_s, is estimated from the previous work of Pizarro-Chong and Misra [47]:

$$\mathrm{K_s} = \frac{E_Y A_{tether}}{\rho_o} \tag{5.69}$$

where E_Y is the Young's modulus of the tether and A_{tether} is the cross sectional area. They assumed that E_Y is similar to that of Kevlar 29 and the cross-sectional area of the tether is 1 mm^2. For a 10 km tether, $\mathrm{K_s} \approx 20$ N/m. The damping coefficient is assumed to be approximately 1/1000 of the stiffness, also based on Pizarro-Chong and Misra, therefore $\mu_d = 0.05$. The baseline value for unstretched tether length (ρ_o) for these simulations is 10 km. A listing of these key constants is listed in Table 5.1.

Table 5.1: Baseline 3-body Constant Values

Constant	Value	Based On
$\mu_\oplus$	3.986004415 x 10^8 m^3/sec^2	Vallado [71]
m_i	200 kg	typical small satellite size
K_s	20.0 N-m	Pizarro-Chong and Misra [47]
μ_d	0.05 kg/s	Pizarro-Chong and Misra [47]
ρ_o	10.0 km	Large Aperture

For analysis, the results of the MATLAB® simulations are presented consistently, as follows:

- 2-D plot of tether length (ρ_{ij}) over time. Note: this is simply the distance between bodies i and j, even though it is called "tether length".

- 2-D plot of body distance from system CoM (r_i) over time.
- 3-D plot of body positions relative to the system CoM over time – shown in terms of (ito) the frame of choice (inertial, orbit, stroboscopic).
- 3-D movie of body positions relative to the system CoM over time (not shown here)

The 3-D output figures also show the tethers connecting the bodies and whether they are in tension (black) or slack (grey) at any given time. In addition, the local angular momentum may be shown as a magenta vector. The 2-D plots also show a "max difference" value, which is the largest separation for that particular variable after the mid-point of the simulation. The max difference is only listed for the first item in the legend.

A number of general scenarios are run to verify that the model works properly, but for brevity's sake only one example is shown here. In this simple example, the satellite ring lies completely in the orbit plane ($\beta_o = 0$ deg) with α_o arbitrarily chosen to be 75 deg. The formation is located at 1.1 DU's along the $\hat{i}_1$ axis and is initially spinning at a modest rate in the orbit plane ($\dot{\alpha} = 5$ deg/s, $\dot{\beta} = 0$ deg/s). To show how the tethers restore themselves and settle out at ρ_{ss}, the initial tether length $\rho(0)$ is set to 10.5 km for a ρ_o of only 10 km. The results of this example verification run are shown in Figures 5.11 and 5.12.

As can be seen in Figure 5.12, the tethers do in fact restore themselves from their stretched position to a value of ρ_{ss} that is consistent with with Equation 5.42. The system stabilizes with the tethers in tension and in the orbit plane. The local angular momentum or "spin axis" holds constant (shown by the magenta vector in Figure 5.11) and normal to the orbit plane.

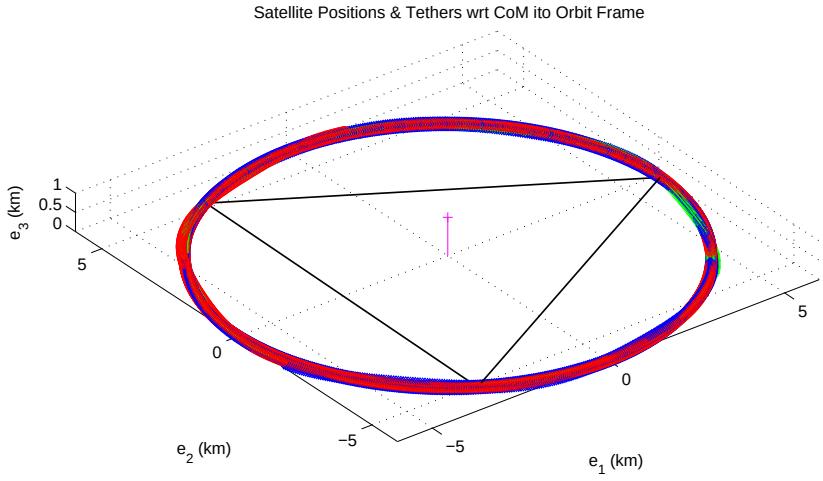


Figure 5.11: Body Positions Relative to System CoM (Orbit Frame, 3 Body, Verification Example, 400 secs)

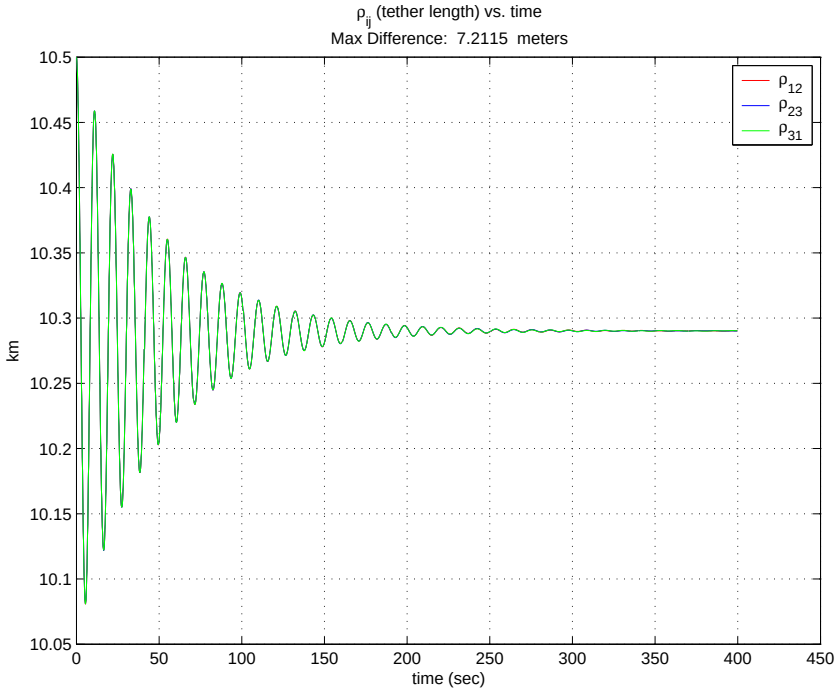


Figure 5.12: Tether Length over Time (3 Body, Verification Example)

Confident that the model works properly, we begin the investigation of Likins-Pringle equilibria for the three body system using a build-up approach. The initial conditions used for Likins-Pringle equilibria are shown in Table 5.2. Recall that Appendix A shows the development of the rigid body conical L-P equilibria. It also discusses the stability criteria for those equilibria. Specifically, for our moment-of-inertia ratio of 2:1 that was determined in Section 5.2.3, the stability range of Likins-Pringle cone angles is calculated to be $-46.4°$ to $+46.4°$. For simulations, we choose a cone angle of $\beta = 40°$ because, within that range, we would like a large projection of the aperture facing the Earth without getting too close to the stability boundary. This is the *baseline scenario* used throughout this research.

Table 5.2: Baseline Initial Condition Variables for L-P.

Variable	Value	Based On
ρ_o	10 km	Arbitrary
$\rho(0)$	ρ_o	No initial excitation
α_o	$0°$	Body 1 at top of the "tuna can"
β_o	$40°$	Stable L-P cone angle for a rigid body
${}^{\hat{i}}\vec{R}_{\oplus}$	1.1 DU $\hat{i}_1$	Visualization
${}^{\hat{i}}\vec{V}_{\oplus}$	$\sqrt{\frac{\mu_{\oplus}}{1.1DU}}\hat{i}_2$	${}^{\hat{i}}\vec{R}_{\oplus}$

A separate MATLAB® module (Get-3B-LP-ICs.m), shown in Appendix F uses these initial conditions and generates the initial state vector per the calculations shown in Section 5.1.5. The initial state, as defined by the Table 5.2, looks like Figure 5.13 with respect to the orbit frame. In this view, the Earth is off to the left at all times.

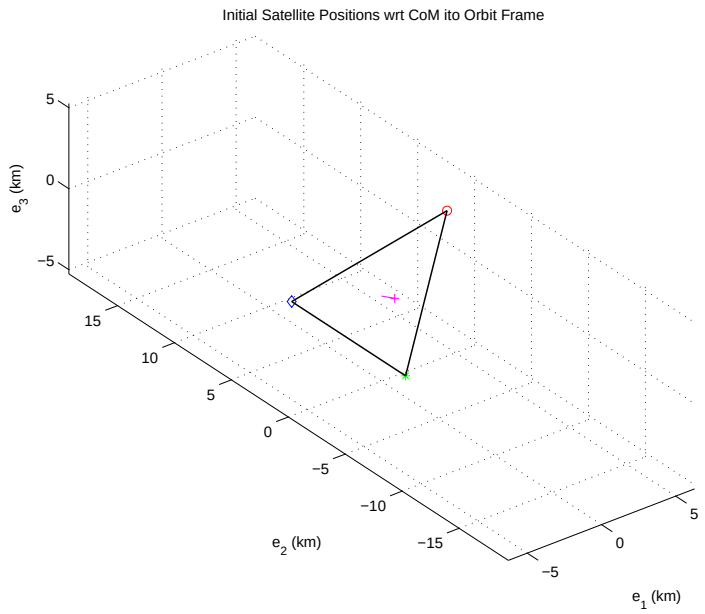


Figure 5.13: Initial Body Positions Relative to System CoM (Orbit Frame, 3 Body, β=40°)

5.3.1 L-P Free Flight. The first step is to look at the natural, unperturbed behavior of the individual bodies without any connecting tethers. That is, given the initial conditions generated by the rigid body Likins-Pringle equilibria, what is the resulting satellites motion? The answer is an *equilibrium condition* – that is, each satellite's motion is strobo-planar and periodic. While this is not a tethered solution, the discovery of an EC is definitely worth exploration before moving on.

Looking at the orbit frame view of the baseline scenario over 10,000 seconds (about 1.7 orbits), each body follows a planar, repeating ellipsoid (Figure 5.14). In fact, by looking at the same motion in the stroboscopic plane (Figure 5.15), we see that these ellipsoids are completely in the $\hat{s_1}$-$\hat{s_2}$ plane (strobo-planar). The plot of "tether lengths" over time is shown in Figure 5.16. Note that "tether lengths" for the free-flying scenarios are actually just the distances between a pair of satellites.

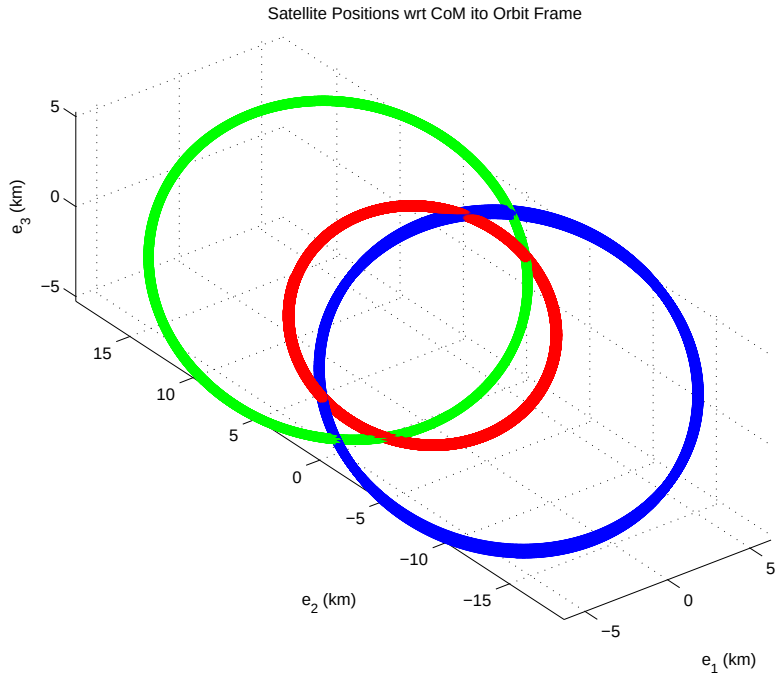


Figure 5.14: Body Positions Relative to System CoM (Orbit Frame, 3 Body, Free Flight, β=40°, 10K secs)

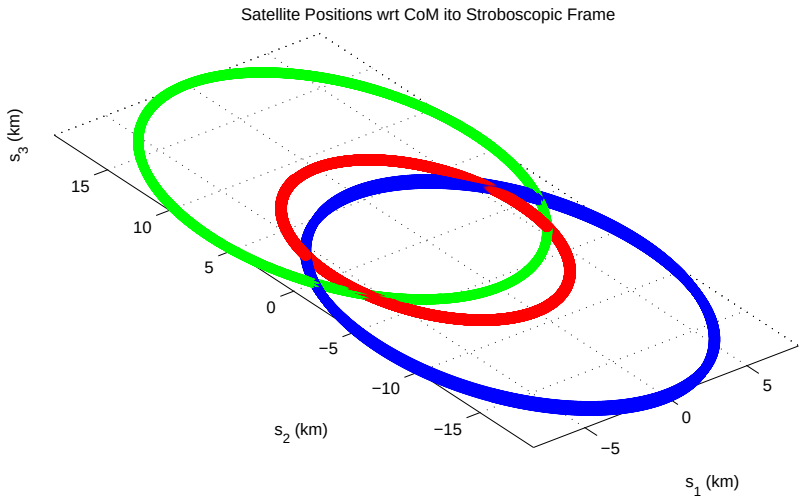


Figure 5.15: Body Positions Relative to System CoM (Stroboscopic Frame, 3 Body, Free Flight, β=40°, 10K secs)

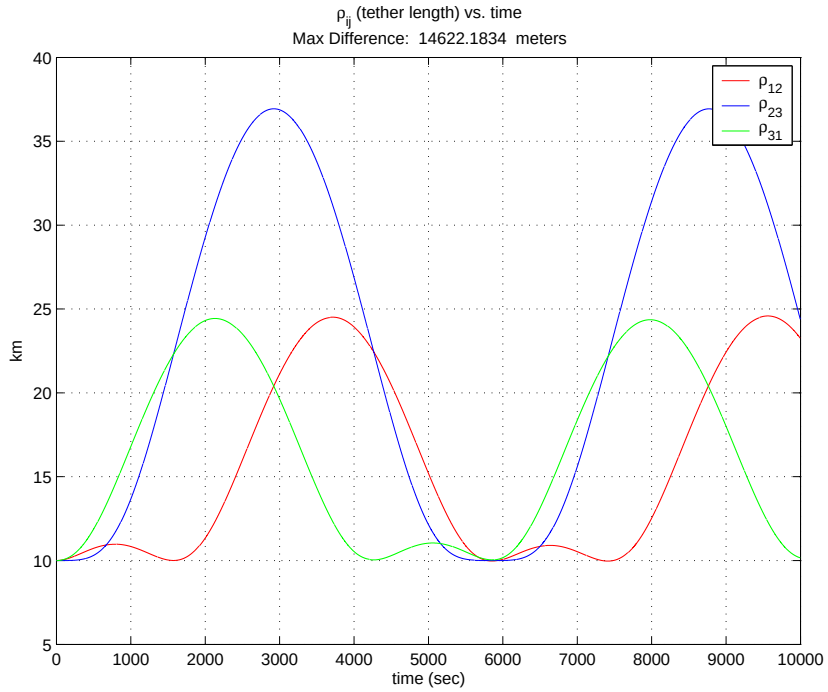


Figure 5.16: Tether Length over Time (3 Body, Free Flight, β=40°)

Over longer periods of time, a slight in-track drift is discernable. Body 1 (red – starts on the "top" of the formation) drifts forward approximately 48 m per orbit with respect to the system CoM, while bodies 2 and 3 (blue and green – starting on the bottom of the formation) drift backward 25 m per orbit. If desired, period matching can be employed to eliminate the remainder of the drift (shown in Appendix C), but it isn't necessary. Even with the slight drift, this strobo-planar, periodic behavior is precisely the kind of equilibrium condition we desire for this mission, since any restoring force that might be supplied by the tethers will also be limited to strobo-planar.

Each ellipse hovers about essentially the same circular reference orbit – the only difference between the three reference orbits is a shift of true anomaly. For example, if we take Figure 5.14 and overlay it on an inertial picture (Figure 5.17), we see that all three reference orbits are identical. If body 1's (red) orbit position is the baseline, then body 2's (blue) orbit position is simply shifted back (7km in this case), while

body 3's (green) relative orbit position is shifted forward about the same amount. If desired, one could pick any of the three ellipses and distribute multiple bodies on that single path, but a few extra computations would be required (this will be addressed again in Section 6.2.1).

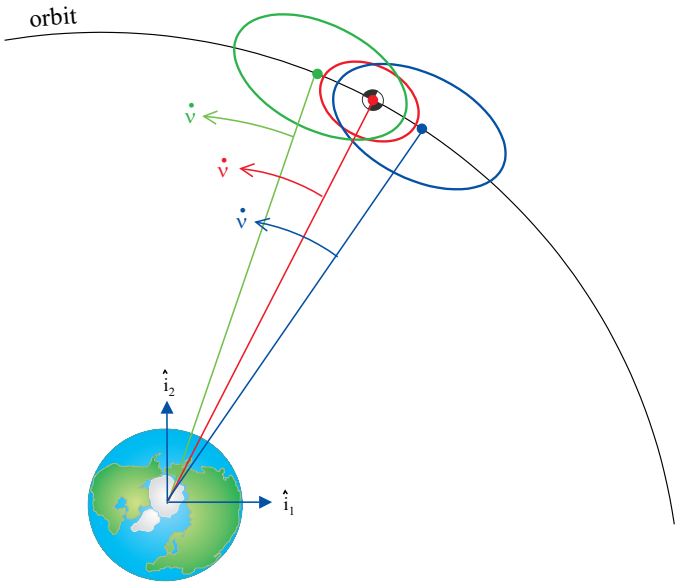


Figure 5.17: L-P Free Flight Ellipses – True Anomaly Shift

Even more interesting is that these equilibria occur regardless of the cone angle that is selected for the Likins-Pringle cone as demonstrated in Figures 5.18 and 5.19. Figure 5.18 shows the same Likins-Pringle free flight set-up with a 25° cone angle, while Figure 5.19 has a 70° cone angle. Notice the difference is simply the shape of the ellipse. Even so, the common thread among all these equilibria is that regardless of cone angle, the projection of the ellipses on the "in-track/radial" plane is always a 2:1 ellipse. Furthermore, these equilibria hold for any altitude that is attempted.

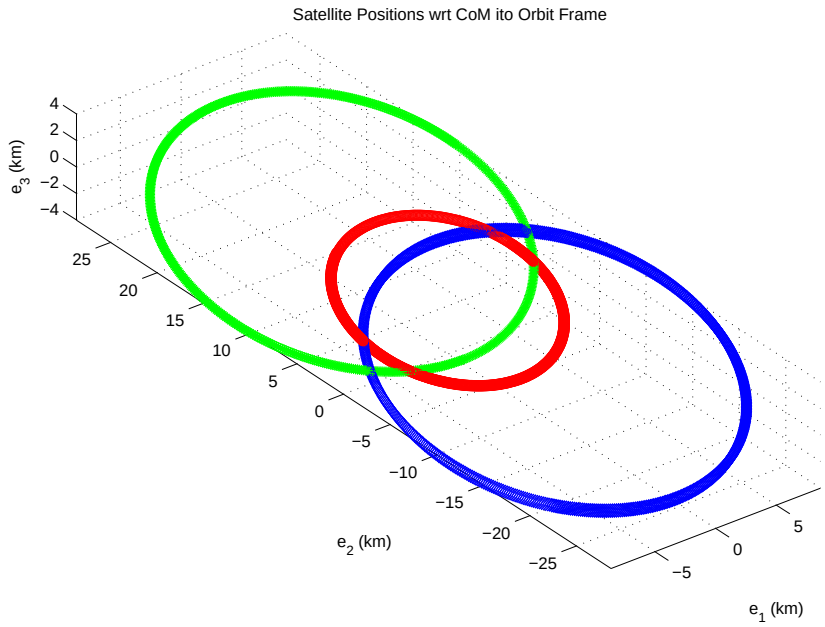


Figure 5.18: Body Positions Relative to System CoM (Orbit Frame, 3 Body, Free Flight, β=25°, 10K secs)

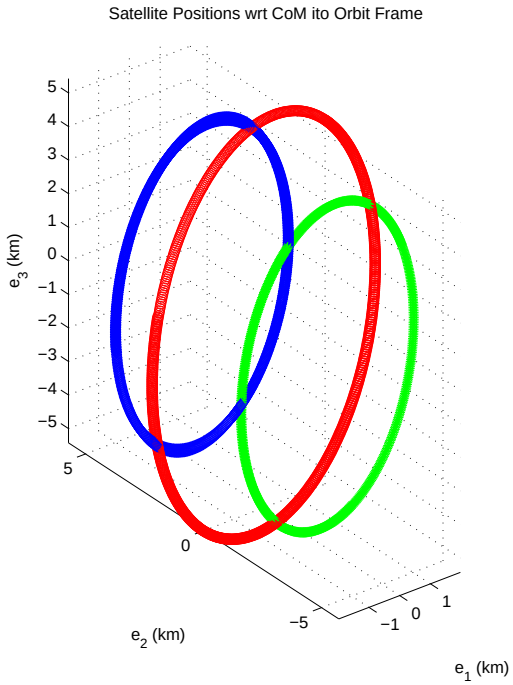


Figure 5.19: Body Positions Relative to System CoM (Orbit Frame, 3 Body, Free Flight, β=70°, 10K secs)

To confirm that we are looking at true relative equilibria, we analyze the orbit periods. From the numerical simulations, we know the orbit periods of body 2 and 3 match perfectly, and the orbit periods of bodies 2/3 match body 1 to within 9/1000 of a second. Therefore, we corroborate our numerical findings with an analytical comparison of the orbit periods of body 1 and body 2 from the general Likins-Pringle configuration. The detailed analytical examination of the two periods is shown in Appendix D, but the bottom line is that the difference in the energies ΔE of the orbits of body 1 vs body 2 takes the form:

$$\Delta E = -1/4 \frac{\mu_\oplus}{X_\oplus^3} \rho_o^2 \left(\cos^2 \beta + 1/2 \right) + O\left(\frac{\rho}{X_\oplus} \right)^3 \tag{5.70}$$

which is a fairly small number (10^{-5}) for low earth orbit ($X_\oplus = 1.1DU$) and apertures as large as $\rho_o = 10km$, regardless of the cone angle (β). Of course, as the altitude increases or the aperture decreases, the difference in energy gets even smaller. Therefore, when the total energy of the orbit is, in this case, 10^{+2}, a ΔE of 10^{-5} yields a difference in period of:

$$\Delta P = 2\pi\mu_\oplus \left((-2E)^{-3/2} - (-2(E + \Delta E))^{-3/2} \right) \approx 10^{-3}\text{secs} \tag{5.71}$$

This order of magnitude for ΔP is not only exactly what we see in the numerics, but it also highlights the insignificance of the difference of the orbit periods, and therefore the assurance that *we do in fact generate an equilibrium condition when we use Likins-Pringle configurations.*

Recall from earlier that the common thread among all the equilibria derived from L-P initial conditions is that the projection of the ellipses on the "in-track/radial" plane is always a 2:1 ellipse. This is interestingly similar to the results shown by Sabol et al. [54] and Yeh and Sparks [61] who claimed that all satellite formation solutions to Hill's equations are determined by the intersection of a plane and an elliptic cylinder of eccentricity $\sqrt{3}/2$. Two specific examples detailed in Sabol were the "Circular" and

"Projected Circular" formations, both of which can be produced using L-P equilibria for the initial conditions. To get the "Circular" formation, a L-P cone angle of β=60° is used (see Figure 5.20). This case is unique in that: 1) all three bodies map out a circle in the orbit frame; and 2) it is the only L-P case where all three bodies use the same reference orbit without a discernible shift in true anomaly (reference Figure 5.17). That is, it is the only case where all three bodies map out nearly the same circular path without any further computations. The "Projected Circular" formation is achieved via L-P simply by picking the cone angle β=63.435°. This value is the complement of the angle used by Sabol et al., because their inclination is measured from the opposite direction that our cone angle is measured.

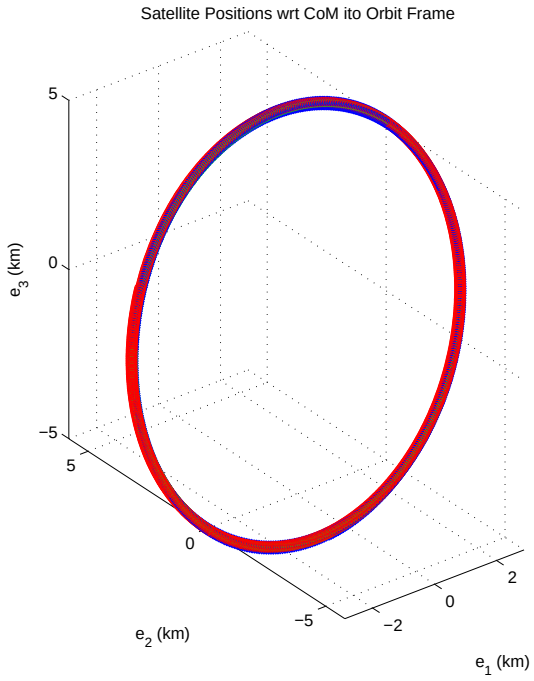


Figure 5.20: Body Positions Relative to System CoM (Orbit Frame, 3 Body, Free Flight, β=60°, 10K secs)

Since our equilibrium conditions (determined from L-P) and Sabol's equilibrium conditions (derived from linearized C-W equations) look so similar, it is appropriate to compare the key calculations in both methods to determine if we have arrived at the same equilibrium solutions from different perspectives.

In the Sabol paper, they derive the formation from Hill's linearized equations of relative motion and end up with a relation that must be satisfied to effectively "match the periods" [54]:

$$\dot{y}_0 = -2nx_0 \tag{5.72}$$

where n is our $\dot{\nu}$, x_0 is the displacement of a body along the $\hat{e}_1$ axis, and $\dot{y}_0$ is the velocity of a body along the $\hat{e}_2$ axis. Looking at Figure 5.21, and considering the initial conditions for body 1 in our Likins-Pringle configuration, we can see then relations between Sabol's parameters and ours, namely $x_0 = r\cos\beta$ and $\dot{\psi} = \dot{y}_0/r$. Therefore,

$$\dot{y}_0 = -2\dot{\nu}r\cos\beta \tag{5.73}$$

$$\dot{\psi} = -2\cos\beta\dot{\nu} \tag{5.74}$$

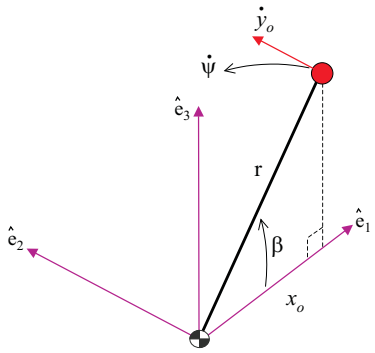


Figure 5.21: Relationship of C-W vs L-P parameters

Back in Equation 5.26, we defined the key relation for conical Likins-Pringle equilibria:

$$\dot{\psi} = \dot{\nu}\cos\theta\,(4\,(A - C))/C \tag{5.75}$$

which, for the oblate disk where the MOI are $A = C/2$, we get

$$\dot{\psi} = \dot{\nu} \cos\theta \left(4\left(C/2 - C\right)\right) C^{-1} \tag{5.76}$$

regardless of the value for C (axial moment-of-inertia). This reduces to

$$\dot{\psi} = \dot{\nu} \cos\theta \, (-2) \tag{5.77}$$

which clearly matches Equation 5.74, therefore we can confidently say that the math behind both approaches accomplishes the same goal. Furthermore, given all the evidence, it appears that the Likins-Pringle geometric approach to assigning initial conditions for a system creates the same equilibrium conditions that the C-W linearization solutions approximate.

5.3.2 Strategy for Adding Springs and Tethers. Knowing that the Likins-Pringle technique creates equilibria for free flying formations, we now continue the methodical build-up by adding springs and tethers to the same set-up. To do this, we recognize that there is an array of methods for modeling the connections between the bodies. The key methods considered are (in order of applicability):

1. ***Massless Springs.*** Allows for both tension and compression, but the springs are not flexible. This is the most like a rigid body. Referring back to Figure 2.11, this is a precursor to those categories in the spirit of a "build-up approach".
2. ***Massless Tethers.*** Allows only for tension, and the tethers are elastic, but not flexible. This is the basis for the model that is discussed earlier in section 5.2. It also represents quadrant 2 of Figure 2.11.
3. ***Flexible Tethers (w/ unbowed ICs).*** Allowing tension only, these tethers are both elastic and flexible (quadrant 4 of Figure 2.11), but their initial conditions (ICs) are straight lines between the bodies. Once the simulation

is running, the tethers bow out due to the spin rate and potentially oscillate radially.

4. ***Flexible Tethers (w/ bowed ICs).*** Elastic, flexible tethers with initial conditions such that they begin the simulation already bowed out in accordance with the steady state spin rate (also quadrant 4 of Figure 2.11).

In his 2000 paper [66], Tragesser demonstrated that Method 1 produced stable formations while Method 3 did not. Method's 2 and 4 were not tried. The instabilities in Tragesser's Method 3 may have been caused by oscillations due to the tethers starting in a straight configuration, then bowing out. Method 4 could possibly be the solution if the tethers are initially bowed out such that they are already in an equilibrium. Alternatively, Tragesser's Method 3 instabilities could have been caused by the tethers simply because they were elastic, regardless of the initial conditions or flexibility. That is, perhaps it was the elasticity (not the flexibility) that caused the instability. In that light, rather than jump right into Method 4, it is useful to first corroborate Tragesser's massless springs (Method 1), then look at massless tethers (Method 2). If the massless tethers work, we can then move to Method 4. If, on the other hand, massless tethers don't work, then it is a moot point to study Method 4 as we know it would not work either.

5.3.3 Method 1: L-P Massless Springs. Of the four methods described above for connecting the formation, massless springs offer the closest behavior to that of a rigid body. To model massless springs, we use the same model developed earlier (Section 5.2) but remove the conditional restrictions in Equations 5.48 and 5.49 – essentially letting the spring provide forces even if the tether length is less than ρ_o. The results of massless springs connecting our original baseline scenario (β=40°) are shown in Figures 5.22 - 5.24.

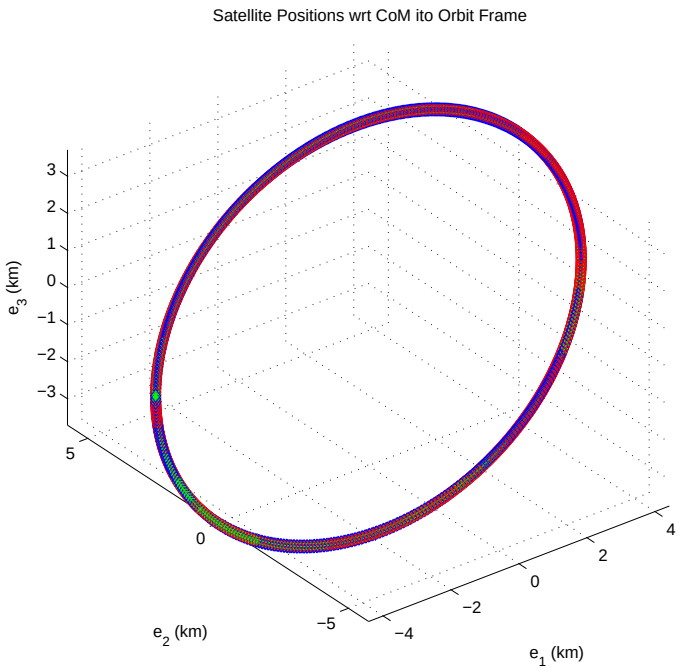


Figure 5.22: Body Positions Relative to System CoM (Orbit Frame, 3 Body, Full Springs, β=40°, 10K secs)

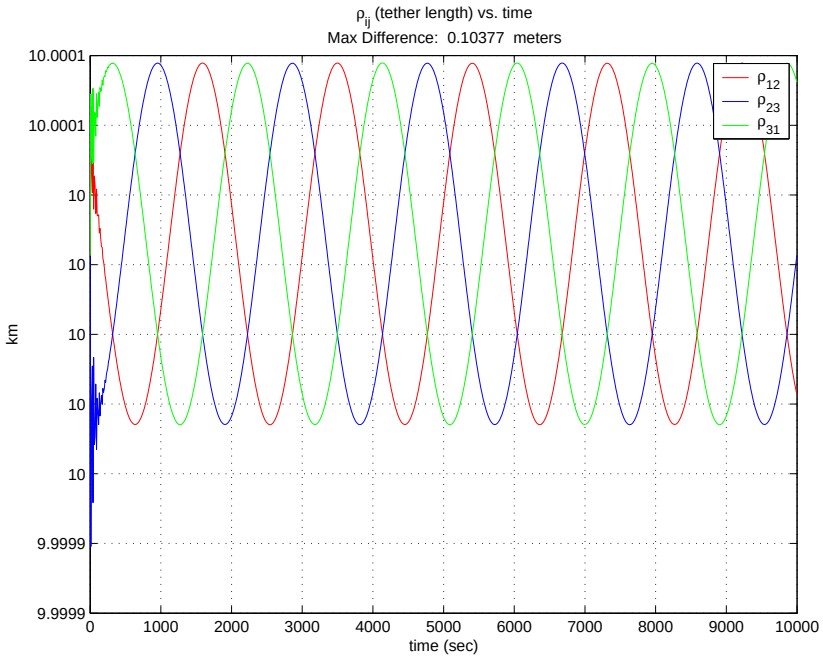


Figure 5.23: "Spring" Length over Time (3 Body, Full Springs, β=40°)

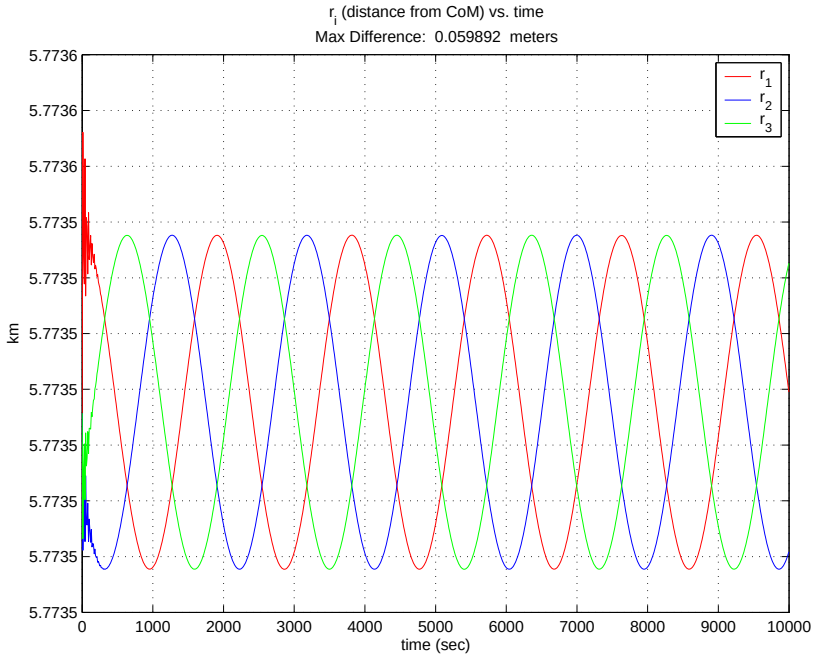


Figure 5.24: Distance from System CoM over Time (3 Body, Full Springs, β=40°)

Clearly, this is the desired equilibrium. The force of the springs keeps the "tether length" (really the spring length in this case) to within 10cm of ρ_{ss} (Figure 5.23). The presence of the springs converts the paths of the three bodies from three individual ellipses (recall Figure 5.14) to a single circularized path as shown in Figure 5.22. The result is that the formation emulates the conical Likins-Pringle equilibria as though it were very close to being a rigid body. That is, the formation circularizes to within 6 cm (Figure 5.24) and is strobo-planar (Figure 5.23). Closer examination of the oscillations in spring length and radial distance show that these correspond to the changing aspect of gravity gradient forces as the system rotates. When a tether/spring is closest to vertical, gravity gradient has its largest effect. Alternatively, when the tether/spring is horizontal, gravity gradient has no effect. Since these three bodies are evenly spaced, the oscillations will occur 120 degrees out of phase with each other as shown in Figures 5.23 and 5.24. The overall effect is that the aperture "breathes" radially by about 6cm.

As mentioned earlier (Section 5.3), and calculated in Appendix A, not all rigid body conical L-P equilibria are stable. For our MOI ratio, only cone angles $0° - 46.4°$ would produce stable results for a rigid body. Similarly, the "system with massless springs" will only produce equilibrium behavior when β is set in that stable range. Conveniently, our baseline case (β=40°) fits nicely in that stable range.

On the other hand, when we pick a higher cone angle that corresponds to a L-P equilibria outside the rigid body stable range, the system does not remain stroboplanar. For example, consider the L-P case of β=60° – the same case that produces the equivalent of Sabal et al.'s circular formation in free flight. For this higher cone angle, when we attach our massless springs, we get the response shown in Figures 5.25 and 5.26.

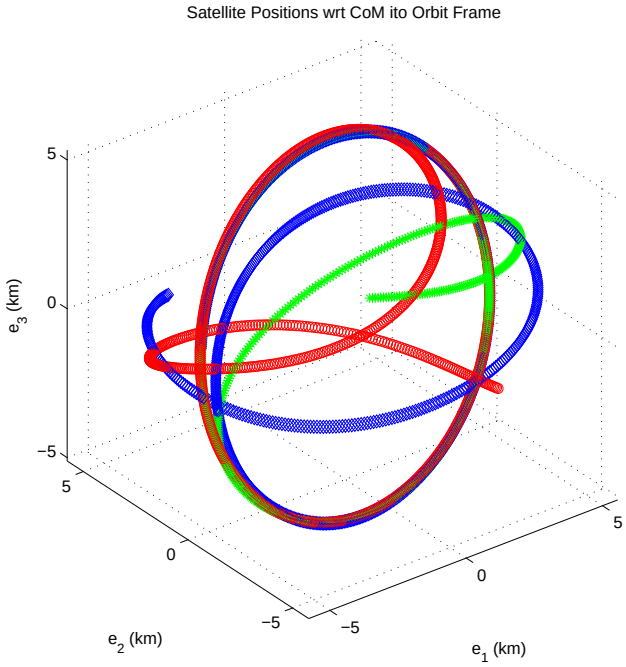


Figure 5.25: Body Positions Relative to System CoM (Orbit Frame, 3 Body, Full Springs, β=60°, 10K secs)

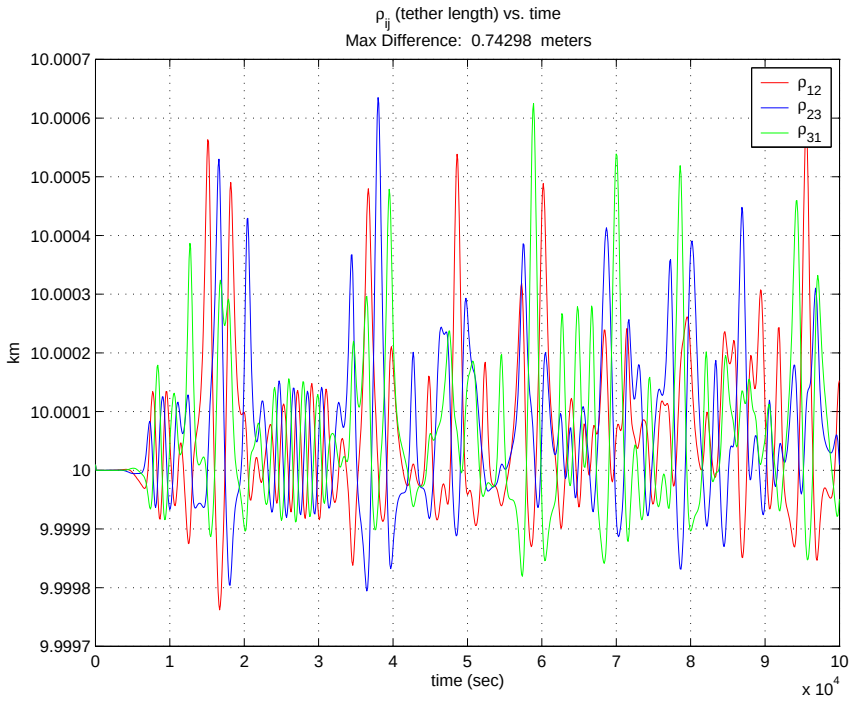


Figure 5.26: "Spring" Length over Time (3 Body, Full Springs, β=60°)

As can be seen, the springs keep the bodies separated at the requisite distance to within 1 meter (Figure 5.26) even for a long time, but the formation orientation quickly diverges (Figure 5.25). The system is no longer strobo-planar. Even if period matching is used to correct the slight in-track drift mentioned earlier in the free flight cases, the system orientation eventually diverges since we are emulating a rigid body that would be unstable for this Likins-Pringle equilibrium condition. The result is only cone angles that are based on stable rigid body L-P equilibria, such as our baseline case (β=40°) will produce stable configurations for the massless spring case.

5.3.4 Method 2: L-P Massless, Elastic Tethers. The next step is to replace the springs with massless, elastic tethers. To do this we use the model developed in section 5.2) without any changes – that is, we honor the conditional restrictions on the spring/damper such that they only engage when the distance between two bodies is greater than the unstretched tether length. The results for our baseline case (β=40°) are shown in Figures 5.27 and 5.28.

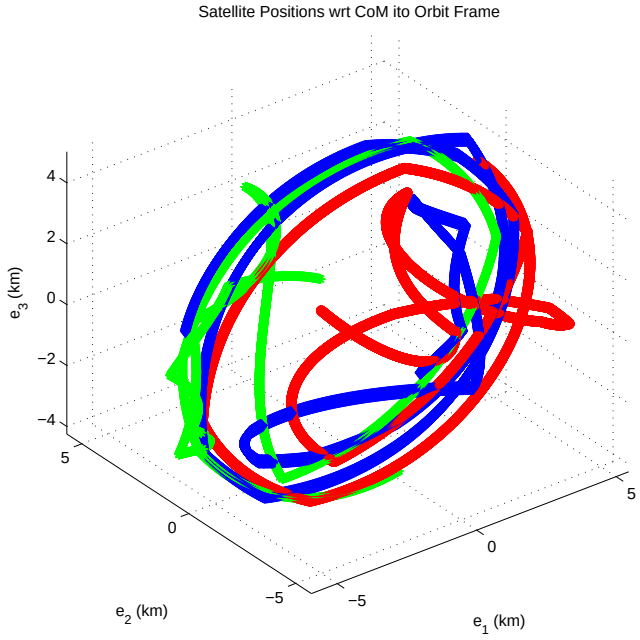


Figure 5.27: Body Positions Relative to System CoM (Orbit Frame, 3 Body, Massless Tethers, β=40°, 10K secs – Baseline)

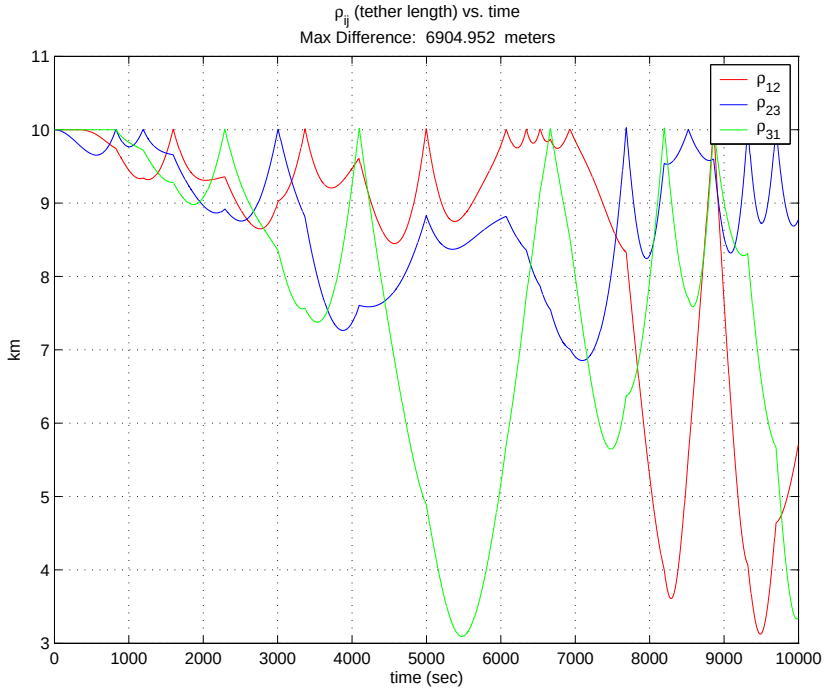


Figure 5.28: Tether Length over Time (3 Body, Massless Tethers, β=40° – Baseline)

With tethers, the formation suffers in two ways: orientation and integrity. First, the *orientation* of the formation is undesirable since it does not remain strobo-planar (Figure 5.27). Second, the formation *integrity* breaks down in that the individual tethers slacken and lose the necessary tension to "rigidize" the system. Looking at Figure 5.28, we notice the first tether to slacken (almost immediately after simulation start) is ρ_{23} (blue), followed by ρ_{12} (red). An explanation for this follows.

The layman's way of explaining the reason for this slacking is: the gravity gradient forces are trying to collapse the formation at a higher rate than the spin rate of the formation can counter. To see this, consider the β=0° case and imagine the initial configuration of these bodies/tethers and the forces acting on them as shown in Figure 5.29, where ρ_{23} starts the simulation totally horizontal and the other two tethers are more vertically oriented.

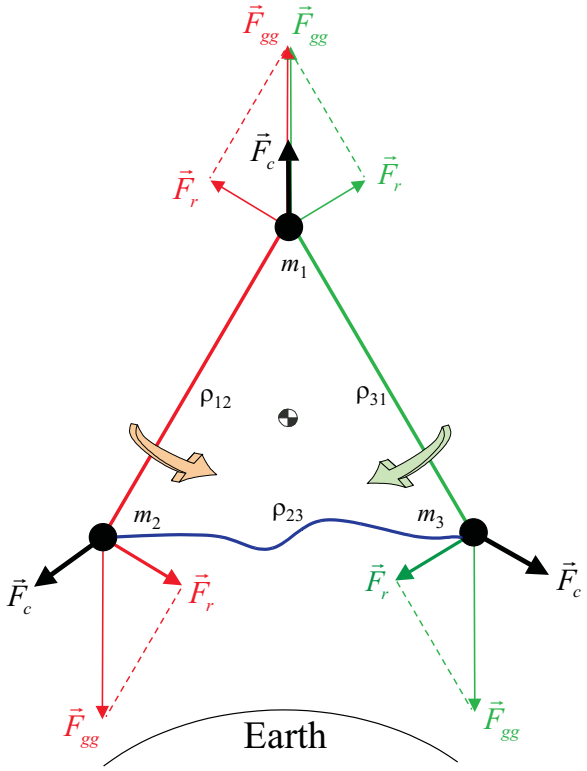


Figure 5.29: Why Tethers Initially Go Slack

F_c is the centrifugal force acting radially on the bodies and is tied to the spin rate. The gravity gradient restoring forces F_r are paired up for each tether, such that

at this snapshot in time, the green tether (ρ_{31}) is being restored in a clockwise fashion while the red tether (ρ_{12}) is being restored in a counter-clockwise fashion. The result is a collapsing of the blue tether (ρ_{23}) unless F_c is big enough to counter F_r.

Note that this visualization for explaining tether slacking is equally valid for other cone angles, but it is just easier to 'see' at β=0°. In addition, by looking at β=0° we can determine a "back-of-the-envelope" calculation of minimum spin rate to compare with the "Kumar Range" values as presented in Chapter II. From our simple calculation (shown in detail in Appendix E), we estimate that the spin rate ratio (SR) must be:

$$\frac{\dot{\psi}}{\dot{\nu}} < -2.61 \quad \text{or} \quad 0.61 > \frac{\dot{\psi}}{\dot{\nu}} \tag{5.78}$$

which compares quite nicely with the detailed Kumar Range values of -2.58 and 0.58 [26]. The spin rate ratio (SR) associated with the baseline (β=40°) case is:

$$SR = \frac{\dot{\psi}}{\dot{\nu}} = -1.532 \tag{5.79}$$

which is not in the range calculated above. For now, we assume that the Kumar Range represents a lower bound for all possible cone angles, therefore based on spin rate alone, we would not expect the centrifugal force to counter the gravity gradient restoring force, and hence we would expect slacking in our horizontal tethers.

Now, go back and look at the tether distances for the baseline tether case in Figure 5.28. Tether ρ_{23} does go slack almost immediately as the analysis above would indicate. Also, with a clockwise rotation, ρ_{12} is rightfully the next tether to go horizontal and hence become slack from the lack of centrifugal force/spin rate.

In addition to tether slacking, there is another complication with the integrity of the tethered formation. As the tethers rotate into a more vertical orientation, the gravity gradient forces help stretch the tether distances and undo the slack. Unfortunately, once the tether distances reach the unstretched tether length (ρ_o), the

tethers tend to "snap" back quickly into a slackened state. This behavior is undesirable enough for a single tether, but the snapping of any one tether has the additional unwelcome effect of causing the other two tethers to snap (or decrease their rate of recovery) as well. This undesirable "snapping interaction" can be seen in Figure 5.28. Notice that any time a tether reaches 10 km, all three tethers snap simultaneously, which only promulgates the problem of slacking-snapping even further. Therefore, our problem of the formation integrity breaking down continues to get worse as the tether distances drop to almost 3 km within two orbit periods.

The problems of tether "slacking" and the subsequent "snapping interaction" are present regardless of the cone angle chosen. Essentially, the Likins-Pringle initial conditions do not generate enough spin rate to keep the tethers taut.

5.3.5 Summary. The results of the initial simulations are summarized in Figure 5.30. The Likins-Pringle initial conditions in *free flight* generate strobo-planar, nearly-periodic, elliptical paths for each body relative to the center of mass for the system – these equilibrium conditions occur regardless of the cone angle.

The addition of full *massless springs* circularizes the free flight ellipses and generates a system-level equilibrium condition, but only for the Likins-Pringle initial conditions that are associated with stable rigid body equilibria (cone angles less than 46.4°). For the initial conditions associated with unstable rigid body equilibria, the system attached with springs can keep its formation integrity, but cannot hold the desired orientation. *Massless tethers* do not hold the system in an equilibrium condition, regardless of cone angle. Tether slacking and the snapping interaction between tethers (called "snapping" from here on out) causes the formation to lose both its integrity and its orientation. The basic cause for the tether slack and subsequent snapping is insufficient spin rate. We can increase the spin rate to maintain formation integrity, but the orientation suffers as the spin axis no longer stays fixed in the orbit frame.

	Oblate L-P Conditions used as System's Initial Conditions	
	Cone angles (< 46.4 deg) that produce **stable** rigid body equilibria	Cone angles (> 46.4 deg) that produce **unstable** rigid body equilibria
Full Spring	**Equilibrium**	Oreintation diverges (even w/ period matching)
Tether Only	Tether slacking/snapping causes failure in formation integrity and orientation	Tether slacking/snapping causes failure in formation integrity and orientation
Free Flight	**Strobo-planar, periodic ellipses for individual s/c**	**Strobo-planar, periodic ellipses -- Circ E.C. @ 60 deg cone**

Figure 5.30: Summary of Initial Three-body Results

As mentioned earlier, since massless tethers (Method 2) fail to hold the desired formation, it is unnecessary to investigate the flexible tether technique (Methods 3 and 4), since we know it would also fail to provide an equilibrium condition. Instead, a number of strategies to solve the slacking/snapping problem (other than increasing spin rate) for massless tethers were attempted – these strategies are presented in the next five sections.

5.4 Strategy: Non-Linear Spring in Tether Model

One of the first strategies to solve the snapping interaction problem is to make adjustments to the tether model. Any tether model that would produce a favorable result could then suggest how to physically build the required tether. Specifically in this case, instead of modeling the tether as a tension-only linear spring, we consider a non-linear spring model. The idea here is that by using non-linear spring forces in the tethers, perhaps we take the "sharpness" out of the response when the tethers hit the unstretched length limit and therefore decrease the severity of the snapping interaction that causes further slacking.

To use non-linear spring forces in the tether, the equations-of-motion module in the code is modified so that the tether forces now obey:

$$\ddot{\vec{R}}_{i_{spring}} = \begin{cases} \frac{\delta_{nm} K_s (\rho_{ij} - \rho_o)^2}{m_i} \left(\frac{\vec{r}_{ij}}{\rho} \right) & \text{if} \quad (\rho_{ij} - \rho_o) \geq 0 \\ 0 & \text{if} \quad (\rho_{ij} - \rho_o) < 0 \end{cases} \tag{5.80}$$

where

$$\delta_{nm} = \begin{cases} 1 & \text{if} \quad n = i \\ -1 & \text{if} \quad m = i \\ 0 & \text{else} \end{cases} \tag{5.81}$$

noting that n and m are compared to the subscripts on the relative position vectors $\vec{r}_{ij}$ and that $n \neq m$.

The results of the baseline case with non-linear tethers is shown in Figures 5.31 and 5.32. By comparing this response to the original linear tether baseline (Figure 5.28), we see that the impact was insignificant. The slacking/snapping still occurs with the non-linear tethers and the formation still diverges.

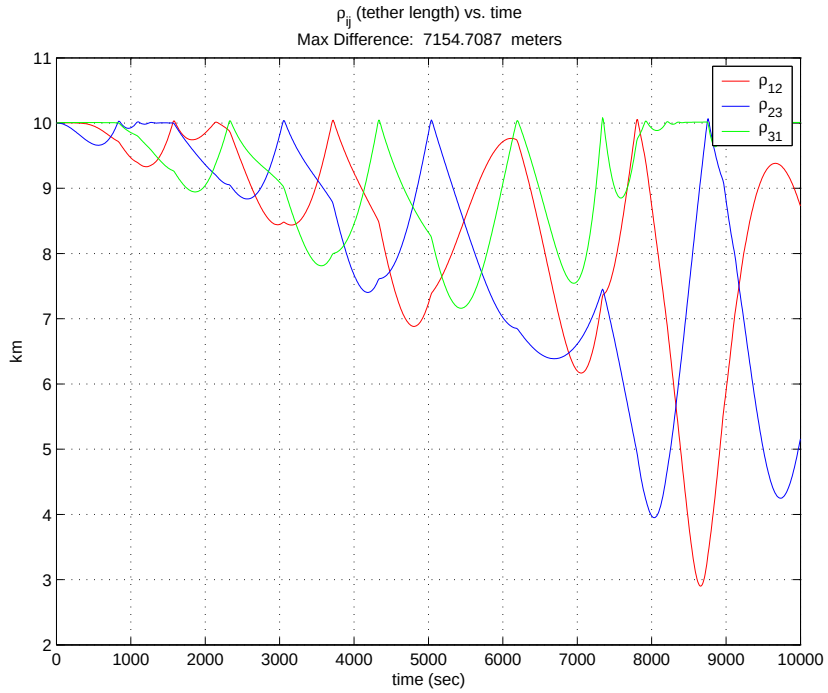


Figure 5.31: Tether Length over Time (3 Body, Non-Linear Tethers, β=40°)

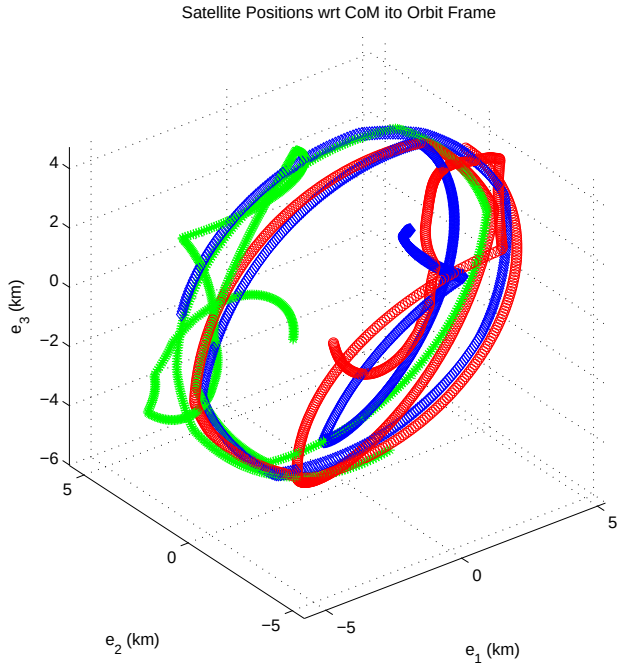


Figure 5.32: Body Positions Relative to System CoM (Orbit Frame, 3 Body, Non-Linear Tethers, β=40°, 10K secs)

5.5 *Strategy: Modify Tether and Formation Parameters*

The next strategy to solve the snapping interaction problem is to evaluate the impact of changing various parameters such as K_s, μ_d, $X_\oplus$, and ρ_o.

5.5.1 Tether Stiffness. Similar to the rationale for the non-linear spring, changing the tether stiffness (K_s) may take the sharpness out of the response when the tethers hit the unstretched length limit and therefore decrease the severity of the snapping interaction that causes further slacking. Keeping all other parameters identical to the baseline case, the tether stiffness is changed from 20 kg/s^2 to a range of other values (0.002 - 2000). The simulation results for these new values of K_s are best shown in the tether length plots (Figures 5.33-5.36) and are compared to the baseline tether length plot (Figure 5.28).

Decreasing the tether stiffness from 20 to 2 kg/s^2 does decrease the severity of the slacking in the tethers (Figure 5.33), but the snapping interaction is still present. Likewise, for K_s=0.2 we still see the snapping interaction between tethers but the resulting slacking is even more attenuated (Figure 5.34).

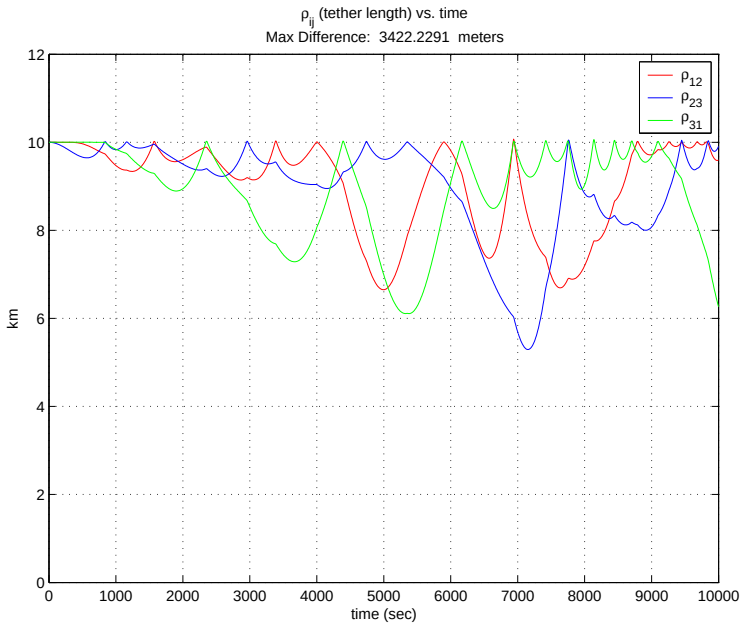


Figure 5.33: Tether Length over Time (3 Body, Tethers, β=40°, K_s=2.0)

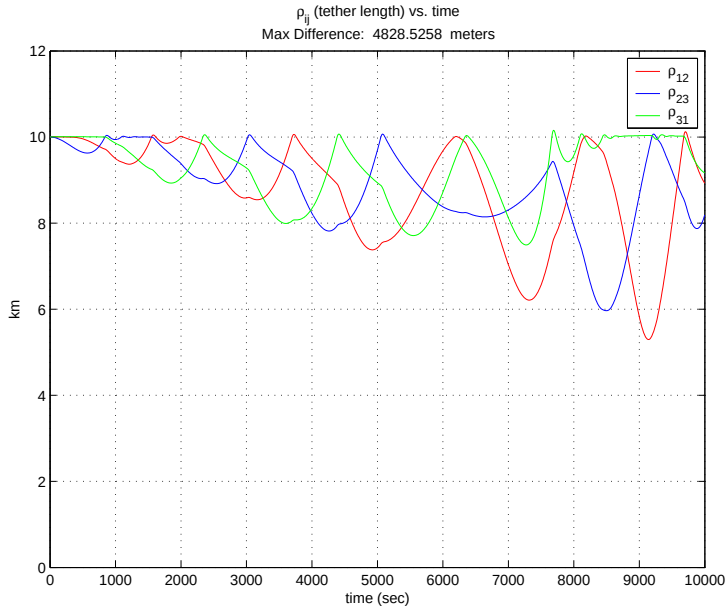


Figure 5.34: Tether Length over Time (3 Body, Tethers, β=40°, K_s=0.2)

If tether stiffness is decreased too far, such as Figure 5.35 (K_s=0.002 kg/s^2), the snapping interaction problem is mitigated but the tether lengths diverge since the tethers provide very little constraint.

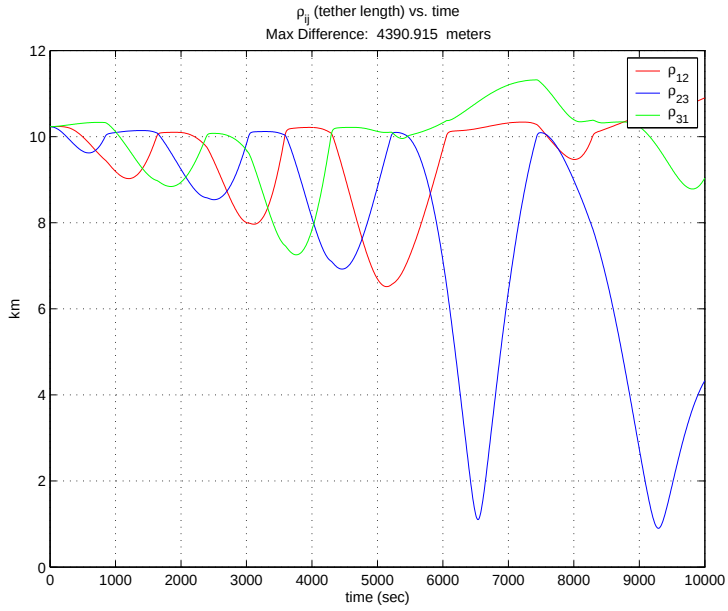


Figure 5.35: Tether Length over Time (3 Body, Tethers, β=40°, K_s=0.002)

Increasing the tether stiffness didn't appear to help at all. For K_s=200 (Figure 5.36), we get the same slacking and snapping problem as the baseline and the system tether lengths definitely diverge at about the same rate as the baseline case. The results for K_s=2000 are not shown here, but as one might expect, the system goes unstable very quickly for such a high tether stiffness, spiking out of control within one-half of an orbit.

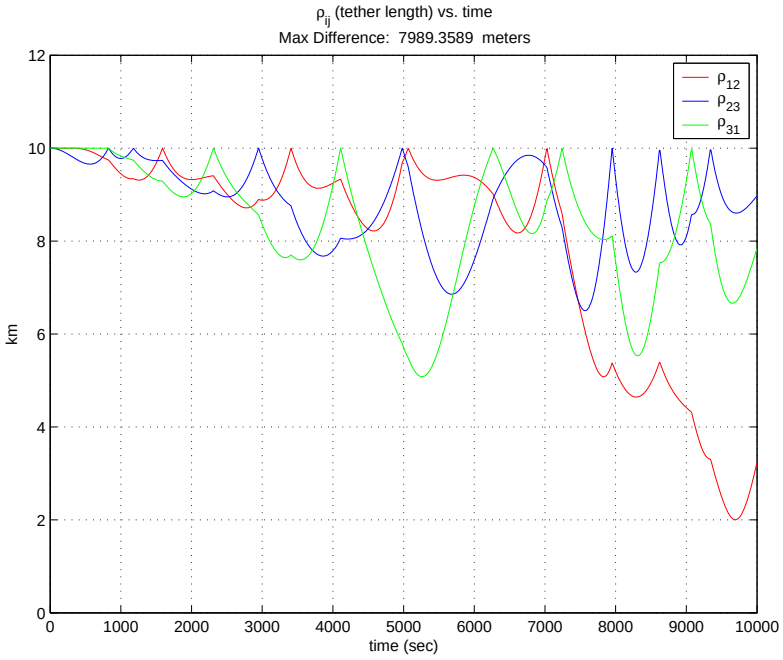


Figure 5.36: Tether Length over Time (3 Body, Tethers, β=40°, K_s=200)

5.5.2 Damping Coefficient. As with most mechanical systems, higher damping can be used to attenuate undesirable oscillations. Therefore, the damping coefficient of the tethers is dialed up from the baseline value of μ_d=0.05 kg/s to evaluate the impact on the undesirable snapping interaction. Two examples are shown below in Figures 5.37 (μ_d=0.5) and 5.38 (μ_d=0.9). Comparing these results to the baseline case (Figure 5.28), we can see that the higher damping does attenuate the severity of slacking that is produced from each snap. That is, the "dips" in tether length are more shallow here than in the baseline case. Even so, the snapping interaction between the tethers is still present and eventually the tether lengths diverge.

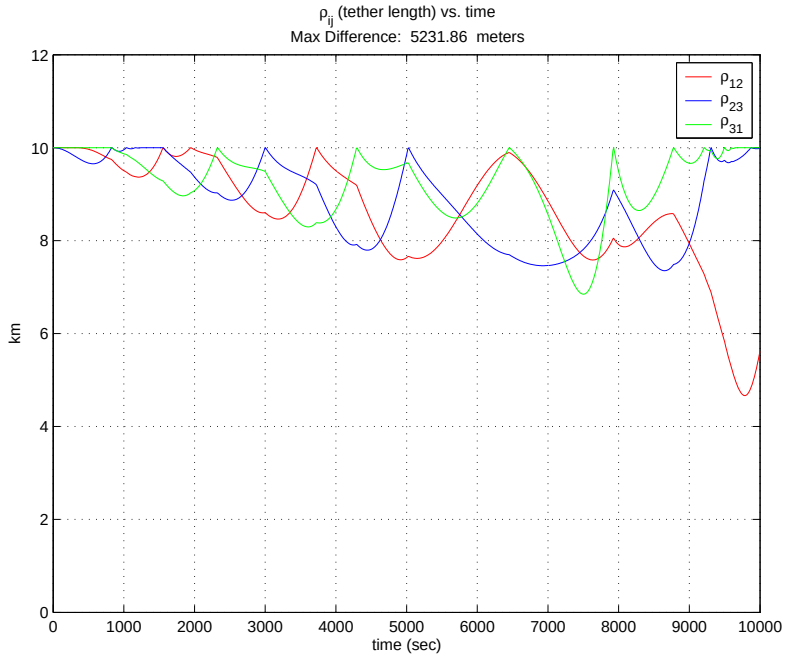


Figure 5.37: Tether Length over Time (3 Body, Tethers, β=40°, μ_d=0.5)

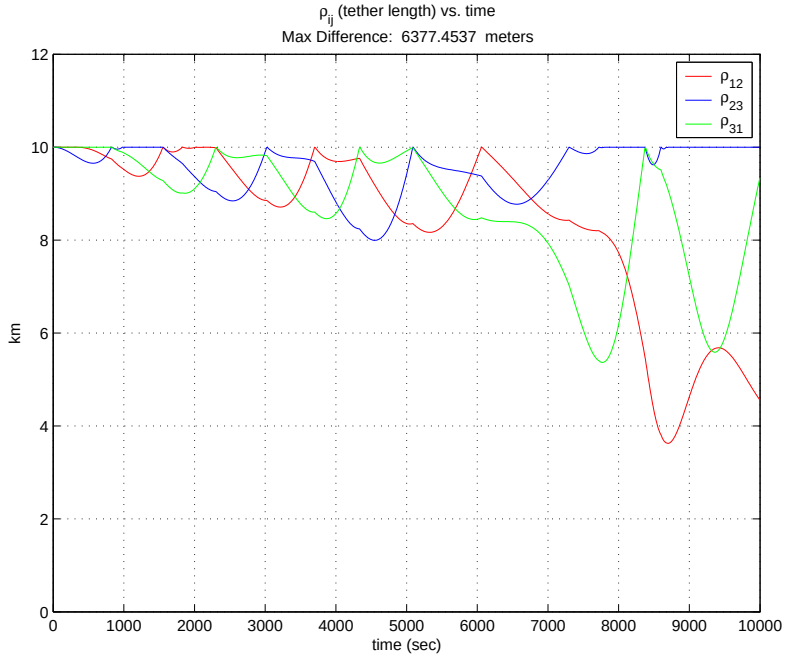


Figure 5.38: Tether Length over Time (3 Body, Tethers, β=40°, μ_d=0.9)

5.5.3 System Altitude. The original choice for system altitude (1.1 DU) is absolutely arbitrary and is based on typical low earth satellites. Since Likins-Pringle equilibria change proportionally with altitude, it is reasonable to assume that the system orientation dynamics will be unaffected by altitude choice. However, it is still worth looking at other altitudes to discern if there are any appreciable effects to the slacking/snapping of the tethers, or if nothing else, to demonstrate that there is no difference. To compare against the baseline of 1.1 DU, we use an altitude on the other end of the "typical" range for satellites: geosynchronous (6.6 DU). The results are shown in Figures 5.39 and 5.40.

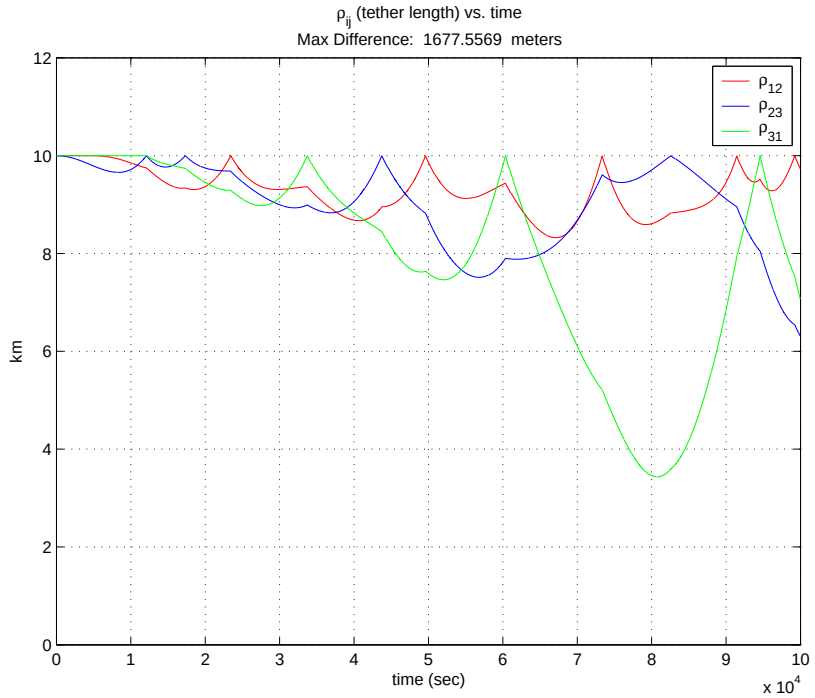


Figure 5.39: Tether Length over Time (3 Body, Tethers, β=40°, $X_{\oplus}$=6.6 DU)

Notice that we still have the original problems of slacking and snapping interaction in Figure 5.39, although the tether slacking is slightly attenuated compared to the baseline case (Figure 5.28). As with every other tether scenario, this slacking/snapping not only breaks down formation integrity, but also causes formation orientation problems (Figure 5.40). Since this higher system orbits, and hence spins, at a much

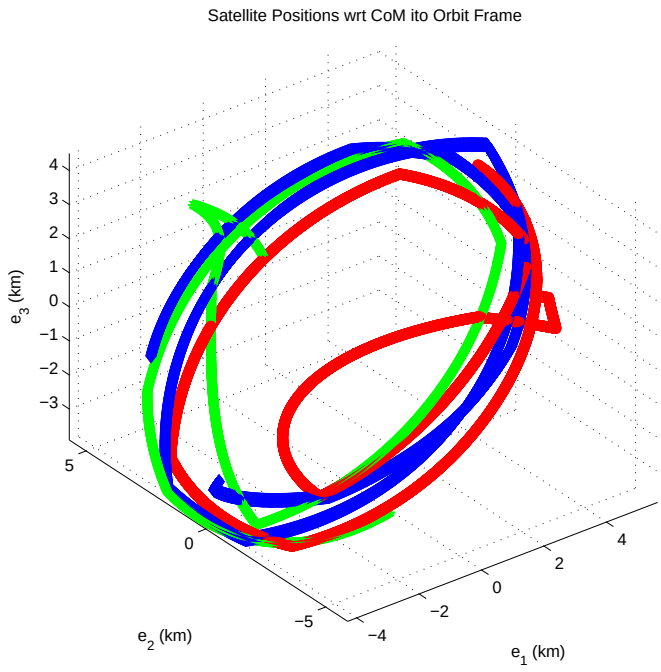


Figure 5.40: Body Positions Relative to System CoM (Orbit Frame, 3 Body, Tethers, β=40°, $X_{\oplus}$=6.6 DU, 100K secs)

slower rate than the low altitude scenario, the simulations for these geosynchronous altitudes are run for 100,000 seconds in order to show equivalent dynamic responses.

5.5.4 Tether Length. As with altitude, Likins-Pringle equilibria for an oblate disk change proportionally with the size of the disk. Therefore, one would not expect the orientation dynamics to be different based on tether length. However, using the same logic as the altitude section above, the tethers were shortened to 1 km (from the baseline of 10 km) to see if there are any improvements to formation integrity. The results for 1 km tethers are shown in Figure 5.41.

As expected, changing the tether length didn't change the response much. The slacking and snapping interaction are still present with approximately the same magnitude of slack that we see in the baseline case. In fact, by looking at the first 4000 seconds alone, it appears that the 1 km case may be slightly worse than the 10 km case.

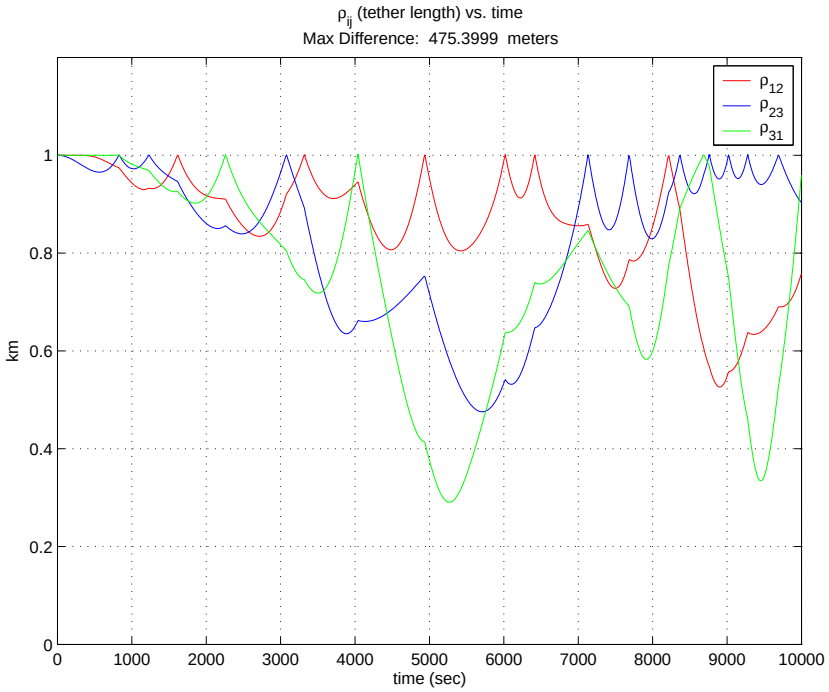


Figure 5.41: Tether Length over Time (3 Body, Tethers, β=40°, ρ_o=$\rho(0)$=1 km)

5.5.5 Combining the Best. So far, changing any one of the parameters mentioned above had varying impact (ranging from insignificant to noticeable) on mitigating the slacking and snapping interaction. Now, we create an "optimized case" where the best settings of each individual parameter are used simultaneously (Table 5.3).

Table 5.3: "Optimized" Formation Parameters.

Parameter	Value
K_s	0.2 kg/s^2
μ_d	0.5 kg/s
$X_\oplus$	6.6 DU
ρ_o	10 km

The results for these "optimized" parameters are shown in Figures 5.42 through 5.46.

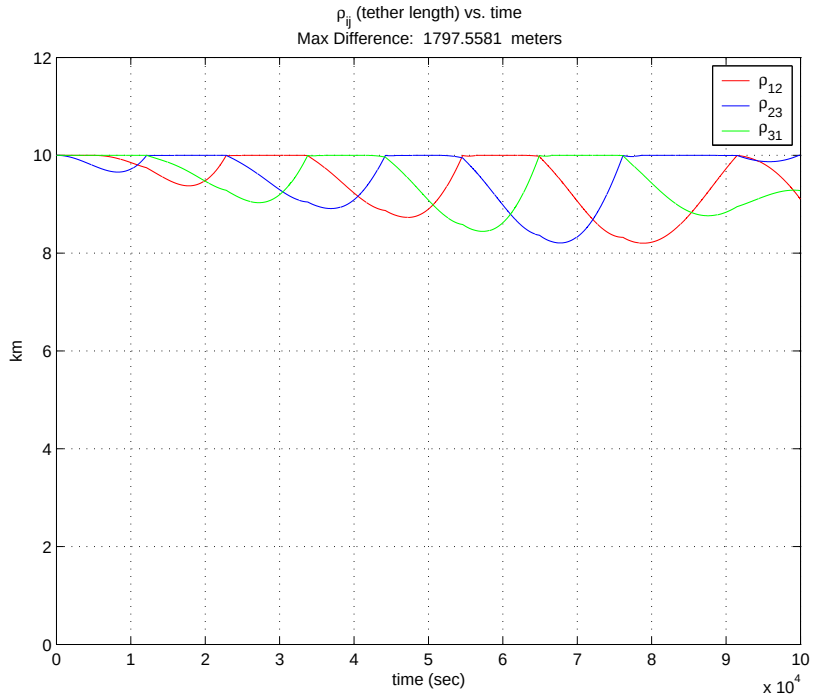


Figure 5.42: Tether Length over Time (3 Body, Tethers, β=40°, Optimized Parameters)

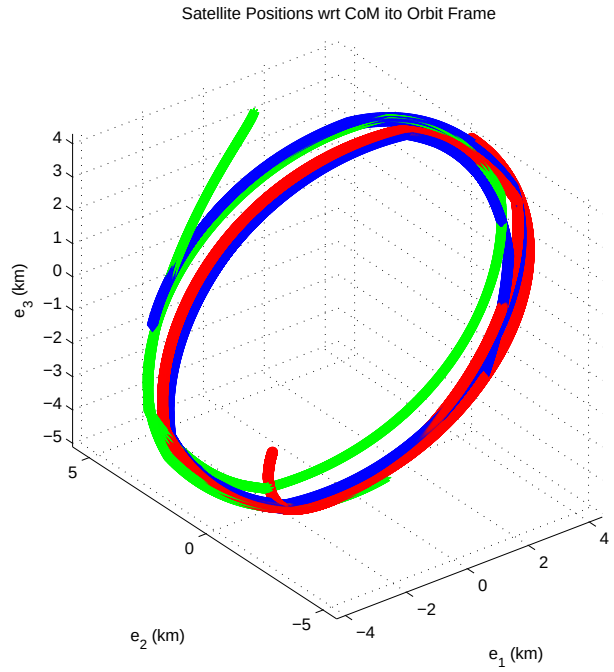


Figure 5.43: Body Positions Relative to System CoM (Orbit Frame, 3 Body, Tethers, β=40°, Optimized Parameters, 100K secs)

Clearly, by combining the best of these parameters, we see that the initial slacking remains unchanged, but the sharpness of the snapping interaction is significantly reduced and therefore the magnitude of subsequent tether slacking is greatly attenuated. Each tether manages to return to the unstretched length and stay there for approximately 3 hours. While not quite perfect, even the orientation of the formation remains strobo-planar for the first orbit (Figure 5.43).

Even so, there is still some snapping interaction between the tethers and eventually the formation begins to collapse into a purely vertical gravity gradient shape (as shown in Figures 5.44-5.46). Figure 5.44 shows a snapshot of the formation at t=460,000 seconds (about 5.4 orbits), where bodies 1 and 3 (red and green) are lower altitude and librating about nadir and body 2 (blue) is the higher altitude object. Figure 5.45 shows all body positions for 1 million seconds, so the librating gravity gradient motion is seen as a blue "blob" on the right (away from the earth), and a red/green "blob" closer to the earth.

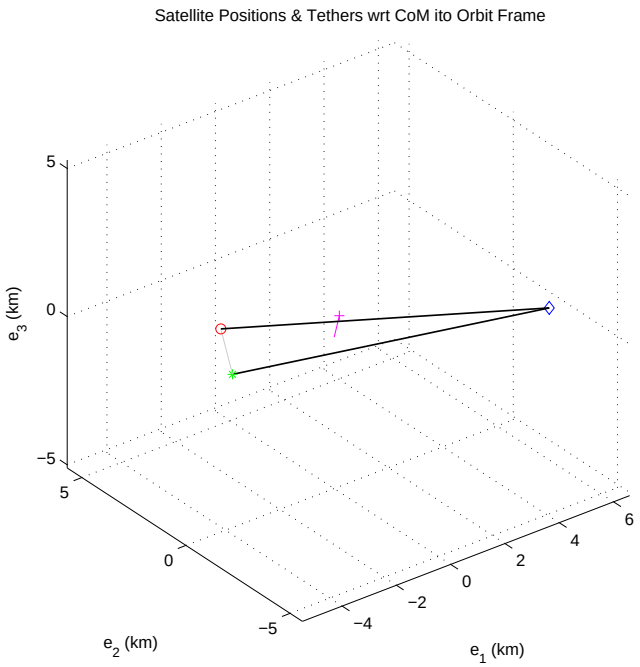


Figure 5.44: Body Positions Relative to System CoM (Orbit Frame, 3 Body, Tethers, β=40°, Optimized Parameters, t=460K s)

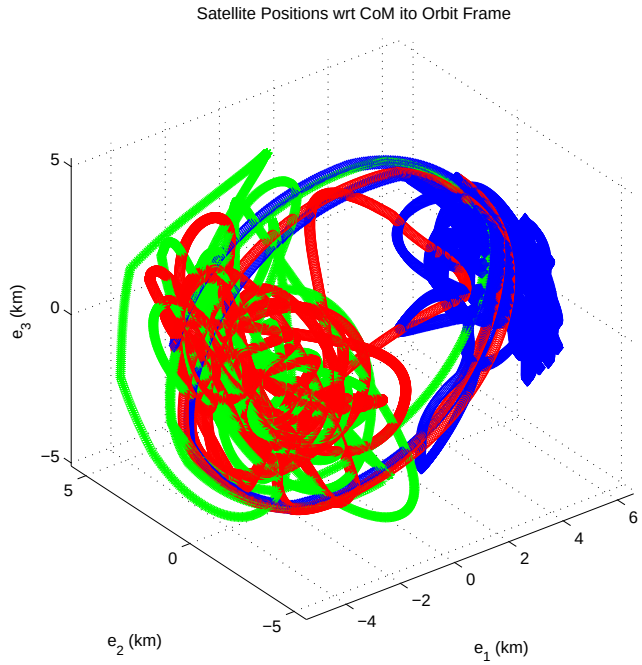


Figure 5.45: Body Positions Relative to System CoM (Orbit Frame, 3 Body, Tethers, β=40°, Optimized Parameters, 1M secs)

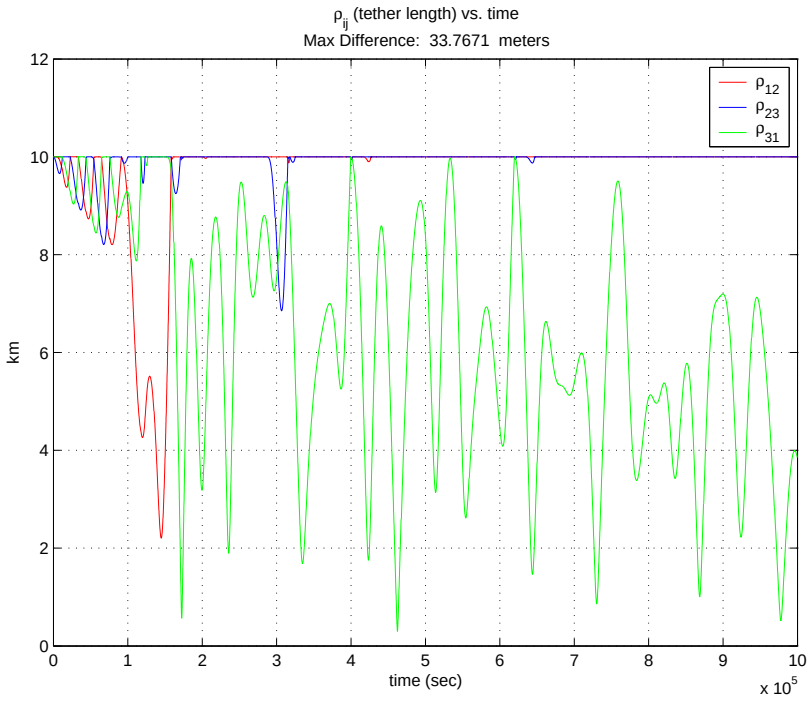


Figure 5.46: Tether Length over Time (3 Body, Tethers, β=40°, Optimized Parameters)

5.6 Strategy: Four-Body Hub-and-Spoke

The next idea for mitigating the snapping interaction between tethers is to look at radial configurations as opposed to the baseline ring configuration. With a radial configuration, the ring tethers are removed and the bodies are connected in a hub-and-spoke (H-A-S) fashion where the tethers represent the spokes emanating from a massive master hub in the center of the formation as shown in Figure 5.47.

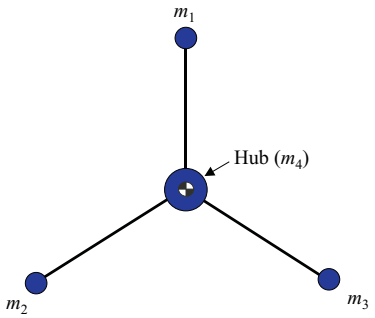


Figure 5.47: 4-Body Hub-and-Spoke Formation

5.6.1 Rationale for Radial Configurations. In a ring scenario, the ring tethers create direct interaction between the peripheral bodies. The concept behind a H-A-S formation is that a relatively large hub with much more mass than the peripheral bodies would act as a damper and attenuate the inter-tether snapping that is seen in the ring formations. Furthermore, Pizarro and Misra determined that the hub-and-spoke configuration could be made stable when four bodies are used [47]. They found that greater than four bodies required ring tethers to be added to the H-A-S system for stability.

5.6.2 Model Development. The model development for the 4-body H-A-S is very similar to that of the original 3-body model. The main difference is that six new states are added: inertial position ($\vec{R}_4$) and velocity ($\vec{V}_4$) vectors for the hub. Therefore, the new state vector is

$$\vec{X} = \left\{ \begin{array}{cccccccc} \vec{R}_1 & \vec{V}_1 & \vec{R}_2 & \vec{V}_2 & \vec{R}_3 & \vec{V}_3 & \vec{R}_4 & \vec{V}_4 \end{array} \right\}^T \tag{5.82}$$

All equations from Sections 5.2.2-5.2.5 are still applicable with the following exceptions or additions:

- The hub is assumed to start at the system's center of mass, therefore the initial state for $\vec{R}_4$ and $\vec{V}_4$ are $\vec{R}_\oplus$ and $\vec{V}_\oplus$, respectively.
- Re-converting the states at each step into $\vec{R}_\oplus$ and $\vec{V}_\oplus$ are the same equations as before, but they will require additional terms for the hub.

$$^{\hat{i}}\vec{R}_\oplus = \sum_i \vec{R}_i \frac{m_i}{\sum_i m_i} \tag{5.83}$$

$$^{\hat{i}}\vec{V}_\oplus = \sum_i \vec{V}_i \frac{m_i}{\sum_i m_i} \tag{5.84}$$

- The relative position vectors with respect to the CoM ($\vec{r}_i$) are defined the same, but we no longer care about the distances between the peripheral bodies (ρ_{ij}). Instead, we pick up three new vectors from the hub to the outer bodies ($\vec{r}_{4i}$) that correspond to the radial tethers (Figure 5.48). These are calculated by:

$$\vec{r}_{4i} = \vec{R}_i - \vec{R}_4 \tag{5.85}$$

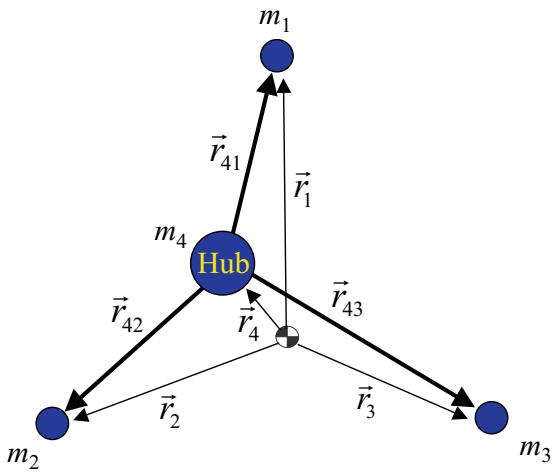


Figure 5.48: 4-Body Hub-and-Spoke Vectors of Interest

- Equations 5.48-5.52 are once again used but now we substitute $|\vec{r}_{4i}|$ for all ρ_{ij} and now the unstretched tether lengths are $|\vec{r}_o|$.
- The new acceleration equations of motion for the 4-body H-A-S system are:

$$\dot{\vec{V}}_i = \frac{-\mu_\oplus}{\left|\vec{R}_i\right|^3}\vec{R}_i - \frac{K_s(|\vec{r}_{4i}|-|\vec{r}_o|)}{m_i}\left(\frac{\vec{r}_{4i}}{|\vec{r}_{4i}|}\right) - \frac{\mu_d\left(\frac{\vec{r}_{4i}\cdot(\vec{V}_i-\vec{V}_4)}{|\vec{r}_{4i}|}\right)}{m_i}\left(\frac{\vec{r}_{4i}}{|\vec{r}_{4i}|}\right) \quad \text{for} \quad i=1,2,3 \tag{5.86}$$

$$\dot{\vec{V}}_4 = \frac{-\mu_\oplus}{\left|\vec{R}_4\right|^3}\vec{R}_4 + \sum_{i=1}^{3}\frac{K_s(|\vec{r}_{4i}|-|\vec{r}_o|)}{m_4}\left(\frac{\vec{r}_{4i}}{|\vec{r}_{4i}|}\right) + \sum_{i=1}^{3}\frac{\mu_d\left(\frac{\vec{r}_{4i}\cdot(\vec{V}_i-\vec{V}_4)}{|\vec{r}_{4i}|}\right)}{m_4}\left(\frac{\vec{r}_{4i}}{|\vec{r}_{4i}|}\right) \tag{5.87}$$

With the new model built, the original 3-body MATLAB® code is modified to accommodate the above equations. The choice of values for the masses is fairly arbitrary. For these runs, m_1=m_2=m_3=25 kg and m_4=300 kg. The plots are slightly different for these hub-and-spoke simulations. While the individual body positions with respect to the CoM in the desired reference frame are plotted as before, the tether length is now shown as the body distance from the hub. Notice that the body position plots also have the "local angular momentum" vector (shown in magenta) and the position of the hub (shown in black).

5.6.3 4-Body H-A-S Results. To verify the new model/code works properly, we begin with a Thomson equilibrium condition discussed in Chapter II where the system spins at a modest rate in the plane of the orbit (β=0°, SR=8.123). Notice the Spin Rate Ratio (SR) is well outside the "Kumar Range". This verification run is shown in Figures 5.49-5.51. As expected, the formation holds its circular integrity in the orbit frame and the hub (shown in black) does not move very much as shown in Figure 5.49.

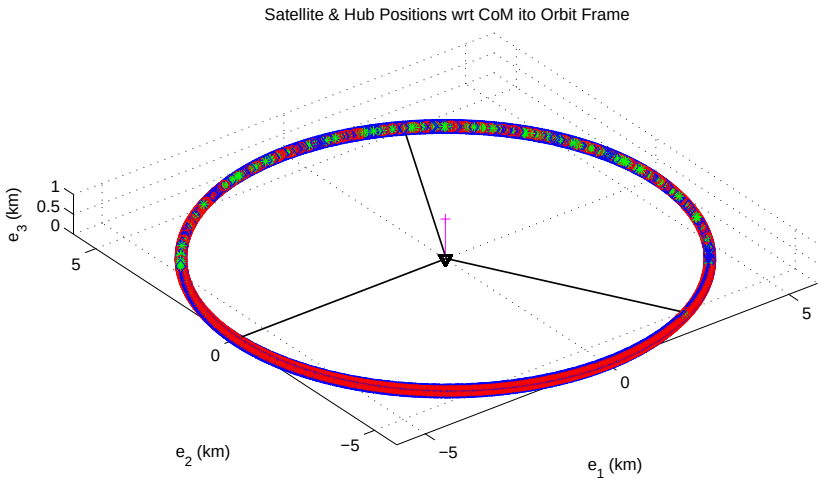


Figure 5.49: Body Positions Relative to System CoM (Orbit Frame, 4-Body H-A-S, Tethers, β=0°, SR=8.123, 100K secs)

Close examination of the body distances from the hub show that they settle down into a small oscillation with an amplitude of less than 10 centimeters. Figure 5.50 shows the first 1000 seconds, while Figure 5.51 shows the entire run (100,000 seconds). As was discussed with the massless spring earlier, this small oscillation is due to the changing aspect of gravity gradient forces as the system rotates.

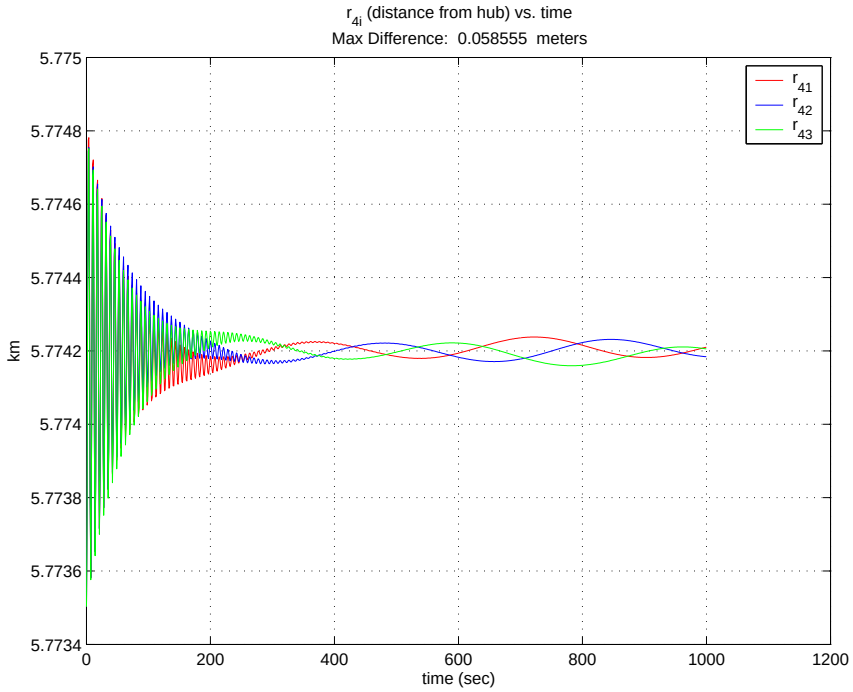


Figure 5.50: Tether Length over Time (4-Body H-A-S, Tethers, β=0°, SR=8.123)

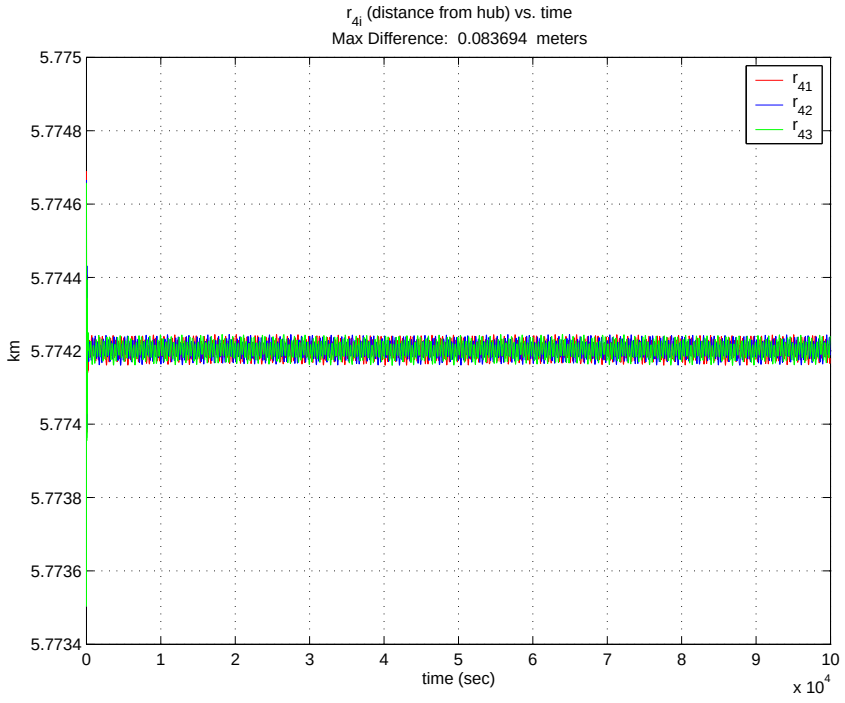


Figure 5.51: Tether Length over Time (4-Body H-A-S, Tethers, β=0°, SR=8.123)

As we slow the spin rate of the system by an order of magnitude, the spin ratio becomes 0.812, but is still outside the "Kumar Range" (-2.58 to 0.58). Even so, the results (shown in Figures 5.52 and 5.53) are mixed. On one hand, the tethers no longer have the snapping interaction problem. They completely stabilize at about 10 km in length, and even when an individual tether slacks/recovers/snaps again, it does not cause slacking in the other tethers (Figure 5.52). Despite this positive effect, the problem can be seen in Figure 5.53 – the formation completely breaks down. Each individual body swings around the hub fairly independently and the hub itself moves a great deal. The original equilateral triangle ring collapses into a librating, vertically-oriented, gravity gradient pendulum.

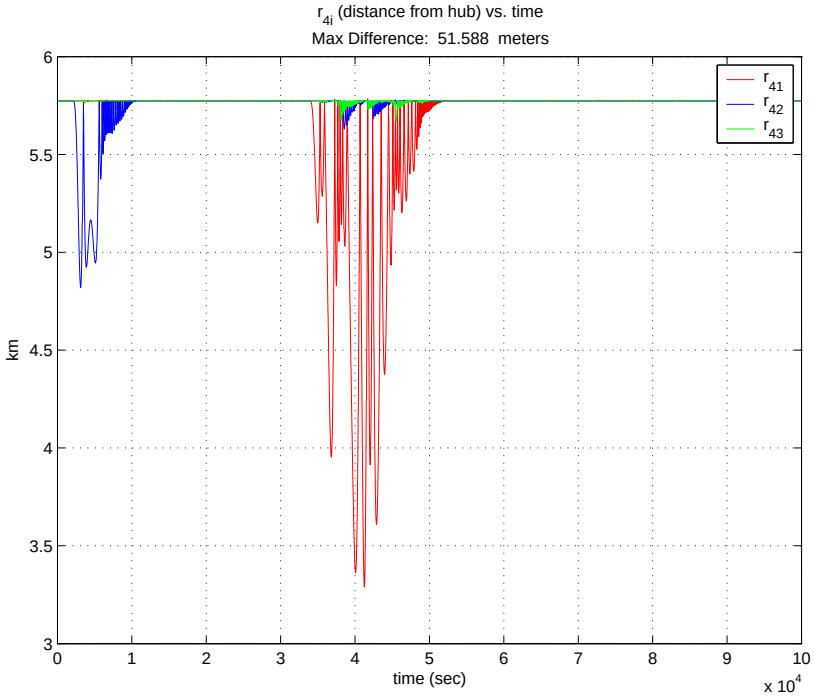


Figure 5.52: Tether Length over Time (4-Body H-A-S, Tethers, β=0°, SR=0.812)

We now apply conical Likins-Pringle conditions to the 4-Body H-A-S configuration: β=40° and SR=-1.532. As discussed before, this SR falls inside the "Kumar Range". Once again, the tethers stabilize in length, and the snapping interaction between tethers is minimal (Figure 5.54). The problem is still that the formation

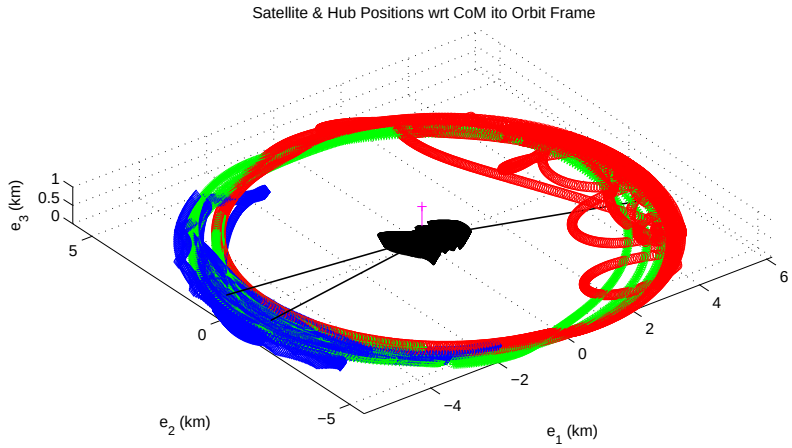


Figure 5.53: Body Positions Relative to System CoM (Orbit Frame, 4-Body H-A-S, Tethers, β=0°, SR=0.812, 100K secs)

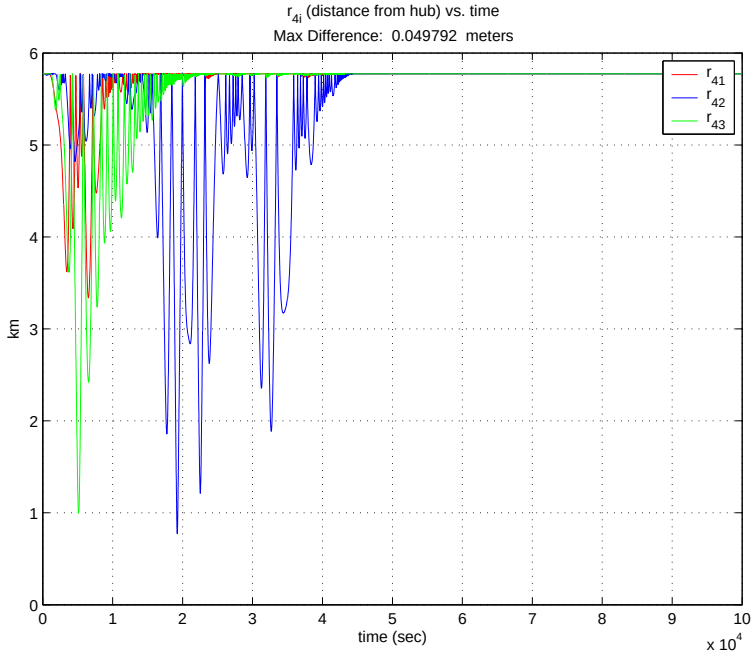


Figure 5.54: Tether Length over Time (4-Body H-A-S, Tethers, β=40°, SR=-1.532, L-P)

breaks down (Figure 5.55). Individual bodies continue to swing independently and the hub motion is still dramatic. As before, the original equilateral triangle ring collapses into a set of librating, vertically-oriented, gravity gradient pendulums.

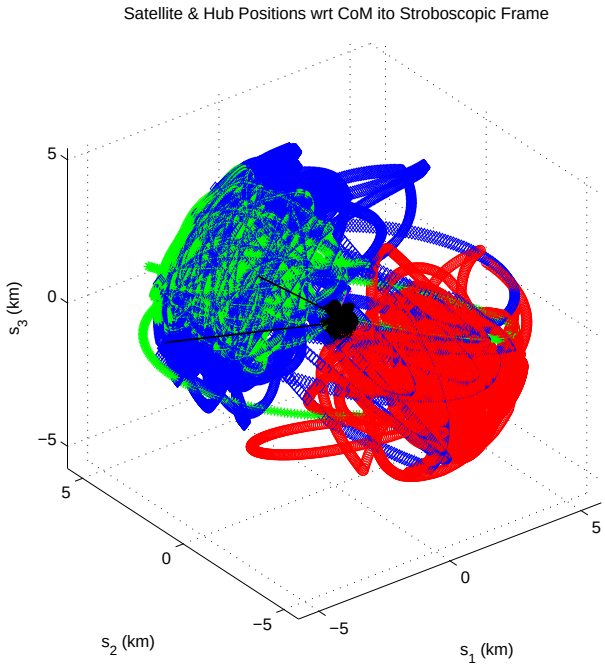


Figure 5.55: Body Positions Relative to System CoM (Strobo Frame, 4-Body H-A-S, Tethers, β=40°, SR=-1.532, L-P, 100K secs)

Essentially, the benefit of the H-A-S system is freedom for each body to rotate about the hub fairly independent of the other bodies. Unfortunately, while this solves the snapping interaction problem, it creates a totally different one.

Other 4-body H-A-S scenarios are attempted but not shown here (higher altitude, full springs, higher hub mass, period matching, "Circular Formation" IC's, etc.). All of these have the same basic results: fixes snapping, but can't maintain the formation. In fact, most of the H-A-S attempts successfully stabilize tether length very well, but only as the system collapses into a gravity gradient pendulum arrangement.

5.7 Strategy: Six-Body Ring

The next idea for mitigating the snapping interaction between tethers is to add more bodies to the original 3-body ring formation. The rationale, model modifications, and results of a six-body ring formation are discussed below.

5.7.1 Rationale for Additional Ring Satellites. It is hypothesized that the cause of snapping interaction between tethers (where the slacking, recovery, and subsequent snap of one tether has a snapping effect on the other tethers) is due to the geometry of the 3-body configuration itself. Consider the diagram in Figure 5.56, where three bodies are connected by distances a, b, and c. Without loss of generality, let's say all three tethers are slack. Furthermore, for the sake of argument, let's also say bodies 1 and 2 remain fixed while body 3 drifts slightly to take up the slack. Now consider the relationship of the distance rates. Distance c will not change initially as body 3 moves, but notice that as distance a gets longer so does distance b. Once the tether between bodies 2 and 3 becomes taut, distance a "snaps" inward which also causes distance b to snap inward. This correlation is always going to be true as long as the angle between two tethers (subtended at one of the bodies) is less than 90°.

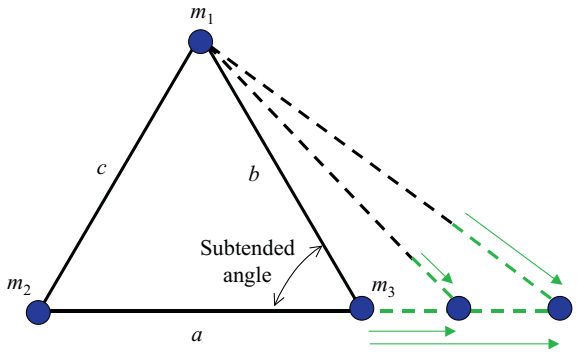


Figure 5.56: Tether Interaction – Subtended Angles $< 90°$

Conversely, if the subtended angle between a and b is greater than 90° (as shown in Figure 5.57), then the correlation reverses. Now a growth in a causes a shortening of b, and a "snap" shortening of a would cause growth in b. We refer to this explanation as the "subtended angle argument".

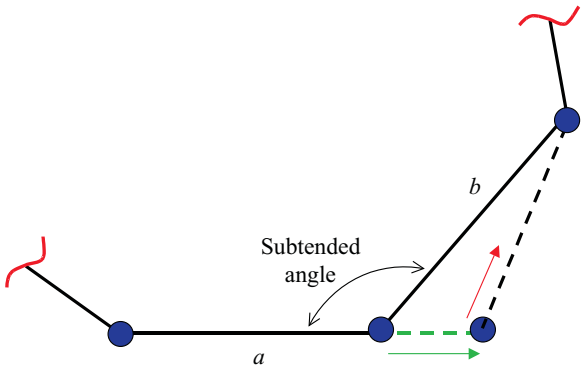


Figure 5.57: Tether Interaction – Subtended Angles > 90°

By definition, the subtended angle of a 3-body ring is 60°, so we expect the snapping of one tether to have an adverse interaction effect on the other two tethers. To fix this, we consider the addition of enough extra ring satellites such that the subtended angle is above 90°. The smallest number of ring satellites to create a subtended angle greater than 90° is n=5. For simplicity, we add another body for a total of six as shown in Figure 5.58. Therefore, the subtended angle between any two ring tethers is 120°.

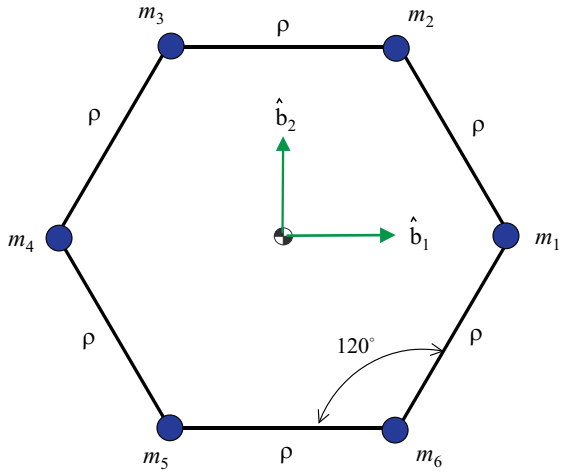


Figure 5.58: Six Body Ring Formation

5.7.2 Model Development. The development for the 6-body model is relatively trivial since it follows perfectly with the development of the original 3-body model. The only difference is the addition of 18 new states (inertial position and velocity vectors of the three new bodies), as well as the new initial relative position vectors with respect to the center-of-mass:

$$
\begin{aligned}
{}^{\hat{b}}\vec{r}_1 &= \begin{bmatrix} \rho & 0 & 0 \end{bmatrix}^T \\
{}^{\hat{b}}\vec{r}_2 &= \begin{bmatrix} \frac{\rho}{2} & \frac{\sqrt{3}}{2}\rho & 0 \end{bmatrix}^T \\
{}^{\hat{b}}\vec{r}_3 &= \begin{bmatrix} \frac{-\rho}{2} & \frac{\sqrt{3}}{2}\rho & 0 \end{bmatrix}^T \\
{}^{\hat{b}}\vec{r}_4 &= \begin{bmatrix} -\rho & 0 & 0 \end{bmatrix}^T \\
{}^{\hat{b}}\vec{r}_5 &= \begin{bmatrix} \frac{-\rho}{2} & \frac{-\sqrt{3}}{2}\rho & 0 \end{bmatrix}^T \\
{}^{\hat{b}}\vec{r}_6 &= \begin{bmatrix} \frac{\rho}{2} & \frac{-\sqrt{3}}{2}\rho & 0 \end{bmatrix}^T
\end{aligned}
\tag{5.88}
$$

5.7.3 6-Body Ring Results. Once again the Thomson "starter" case is used where tether coefficients and lengths are the same as the original baseline, but a 0° cone angle and modest spin rate (SR=8.123) are used to validate the model. Figures 5.59 and 5.60 show the behavior of this initial system. Clearly, the system is at least in a marginally stable equilibrium that maintains a generally circular configuration as it spins, but the formation does "flex" in and out over the course of the simulation. This flexing is indicated by the low order oscillation in Figure 5.59 and the thickness of the band in Figure 5.60.

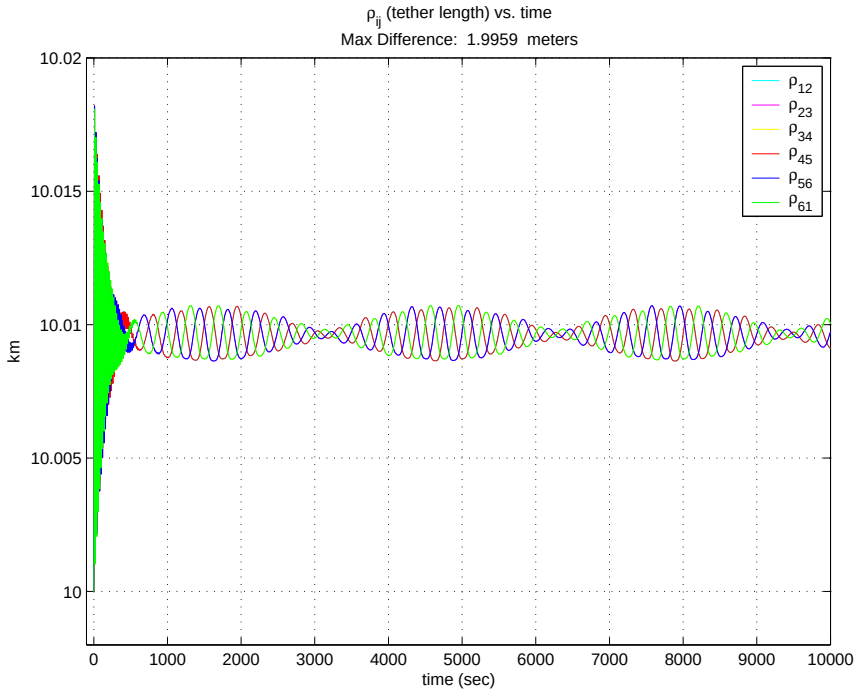


Figure 5.59: Tether Length over Time (6-Body Ring, Tethers, β=0°, SR=8.123)

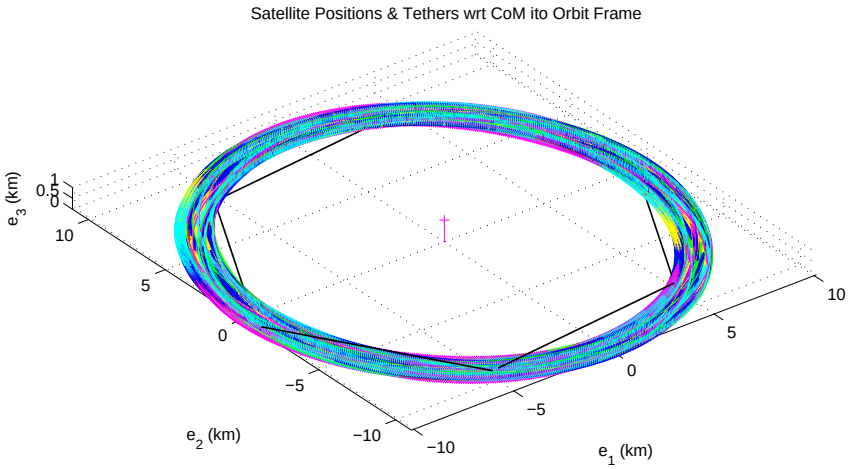


Figure 5.60: Body Positions Relative to System CoM (Orbit Frame, 6-Body, Tethers, β=0°, SR=8.123, 10K secs)

When we slow the spin rate such that the spin ratio is an order of magnitude lower (SR=0.812), the flexing motion of the formation becomes much more dramatic. The full 10,000 second simulation is shown in Figure 5.61, while snapshots of the first 125 seconds are shown in Figure 5.62. It appears that the formation begins to deform or partially collapse from a hexagon to a box almost immediately after the start of the simulation. This deformation is caused, once again, by gravity gradient forces that are stronger than the centrifugal forces created by the spin rate.

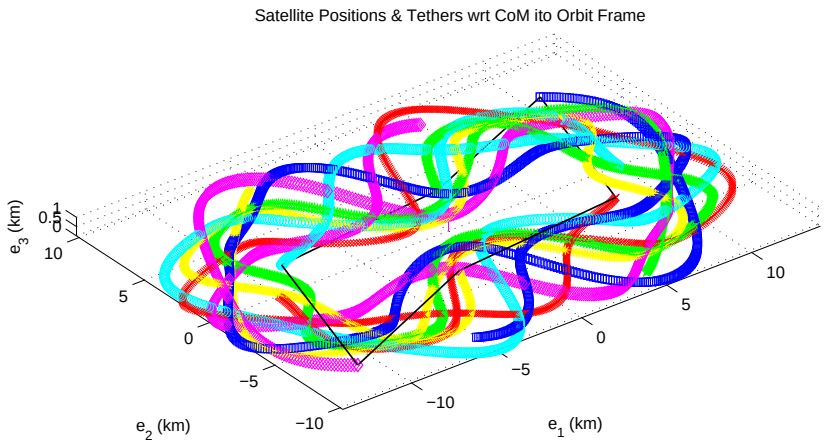


Figure 5.61: Body Positions Relative to System CoM (Orbit Frame, 6-Body, Tethers, β=0°, SR=0.812, 10K secs)

To understand the nature of this "hex-to-box" deformation, consider the diagram of the 6-body ring only 20 seconds after simulation start (Figure 5.62.b). We redraw this instantaneous snapshot looking down the $\hat{e}_3$-axis as shown by the multi-colored tethers in Figure 5.63. Also displayed in Figure 5.63 are the individual pairs of gravity gradient restoring forces from each tether (paired by color) on each body. For sake of simple explanation, the restoring forces are added up graphically in vector

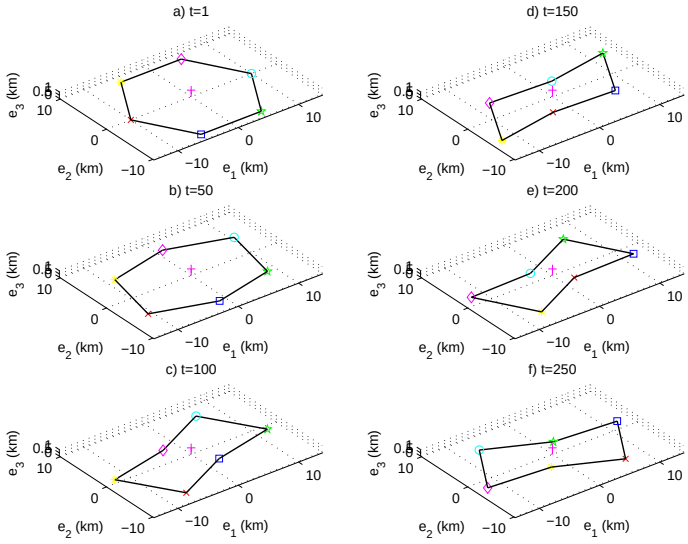


Figure 5.62: Body Positions Relative to System CoM (Orbit Frame, 6-Body, Tethers, β=0°, SR=0.812, Snapshots)

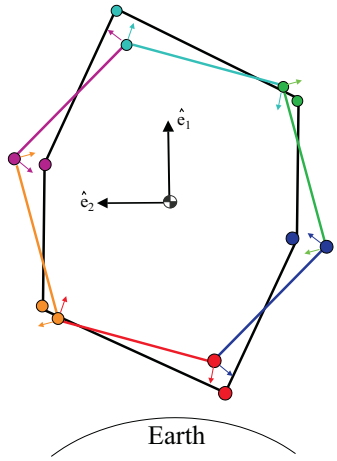


Figure 5.63: Initial Motion of 6-Body Formation

fashion and resultant "new body positions" are shown with black tethers. These new body positions correspond quite nicely with the snapshot taken 20 seconds later in Figure 5.62.c.

One can now imagine that as the spin rate is increased (such as the previous Thompson case) the centrifugal force will counter the gravity gradient effects and

keep the formation from collapsing into an "undulating box", although some flexing is still present (as shown back in Figures 5.59 and 5.60).

As with other strategies, we now apply conical Likins-Pringle conditions to the 6-Body ring configuration: β=40° and SR=-1.532. The result is clearly undesirable as can be seen in Figures 5.64-5.66. Figure 5.64 is an orbit frame plot of the body position over the entire 10,000 second simulation, while Figure 5.65 shows snapshots over the first 250 seconds. Obviously, things begin to break down immediately due to inadequate spin rate and the result is a complete loss of formation integrity and orientation. Ironically enough, while there is plenty of tether slacking and snapping, there is no snapping interaction *between* the tethers as was predicted for this strategy. Of course, given the complete breakdown of the formation, this is of little consolation.

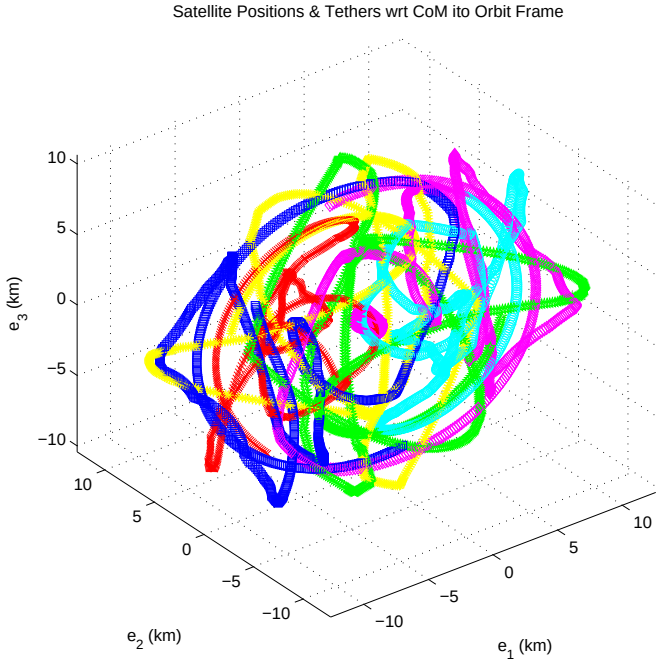


Figure 5.64: Body Positions Relative to System CoM (Orbit Frame, 6-Body Ring, Tethers, β=40°, SR=-1.532, L-P, 10K secs)

Several modifications to this strategy are attempted (such as higher altitude, shorter tethers, and inclusion of period matching), but all result in the same response: the snapping interaction problem is solved but the formation breaks down.

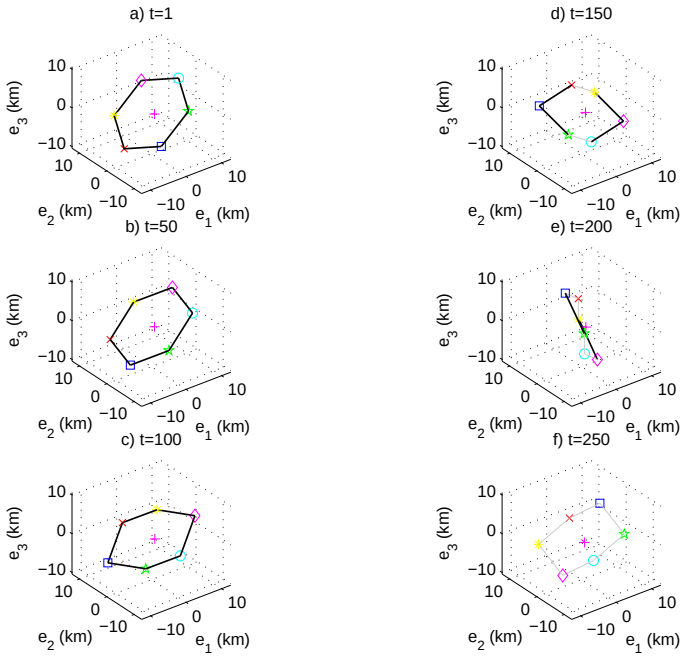


Figure 5.65: Body Positions Relative to System CoM (Orbit Frame, 6-Body Ring, Tethers, β=40°, SR=-1.532, L-P, Snapshots)

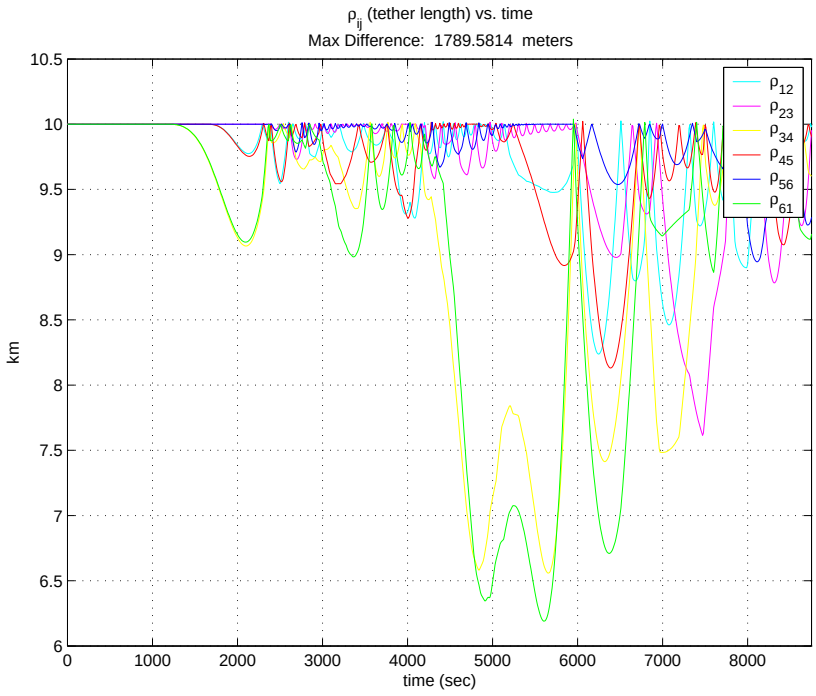


Figure 5.66: Tether Length over Time (6-Body Ring, Tethers, β=40°, SR=-1.532, L-P)

5.8 Strategy: Seven-Body Closed-Hub-and-Spoke

The next strategy for trying to counter the snapping interaction problem of the tethered system is to combine two of the previous strategies: add more satellites to the ring and use spoke tethers in addition to the ring tethers.

5.8.1 Rationale for a C-H-A-S. As mentioned in an earlier section, Pizarro and Misra determined that the Hub-and-Spoke configuration were stable when four or less bodies are used, but more than four bodies required ring tethers as well [47]. They called this combination of H-A-S and ring tethers a Closed-Hub-and-Spoke (C-H-A-S) configuration. Given Pizarro and Misra's findings, a combination of the last two strategies is attempted. Three additional ring satellites (for a total of six) are used to address the "subtended angle argument" while a central hub body and spoke tethers are added to potentially attenuate inter-tether snapping (Figure 5.67). Essentially, the benefits of a hub-and-spoke system can be enjoyed, without the complication of each satellite swinging freely about the hub (as seen in the pure hub-and-spoke case without ring tethers).

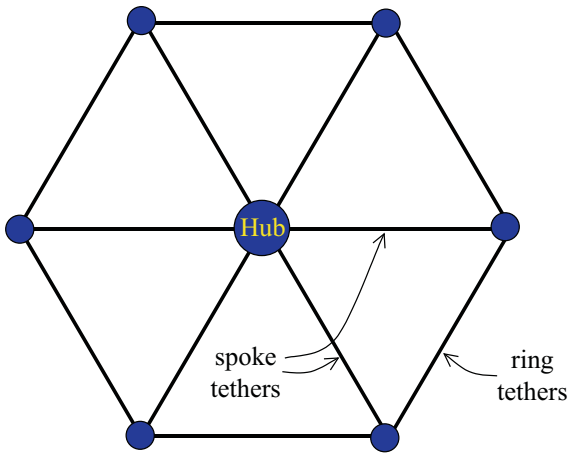


Figure 5.67: 7-Body Closed-Hub-and-Spoke System

5.8.2 Model Development. As with the 6-body model, the development of the 7-body model is somewhat trivial, because it simply involves combining the principles from the 4-body H-A-S case (for the spoke tethers' EOM and the addition of a

hub) and the 6-body ring case (for the additional bodies and ring tethers' EOM). Specific modifications to the original 3-body MATLAB® model are found in the previous two sections.

5.8.3 7-Body C-H-A-S Results. For these simulations, the hub is given a mass of 300 kg while the other six ring bodies are 25 kg masses. As with all the other strategies, the Thomson "starter" case of β=0° and SR=8.123 is used to verify this new model. It is no surprise that this relatively high spin rate system remains stable for the entire simulation (see Figures 5.68 and 5.69)

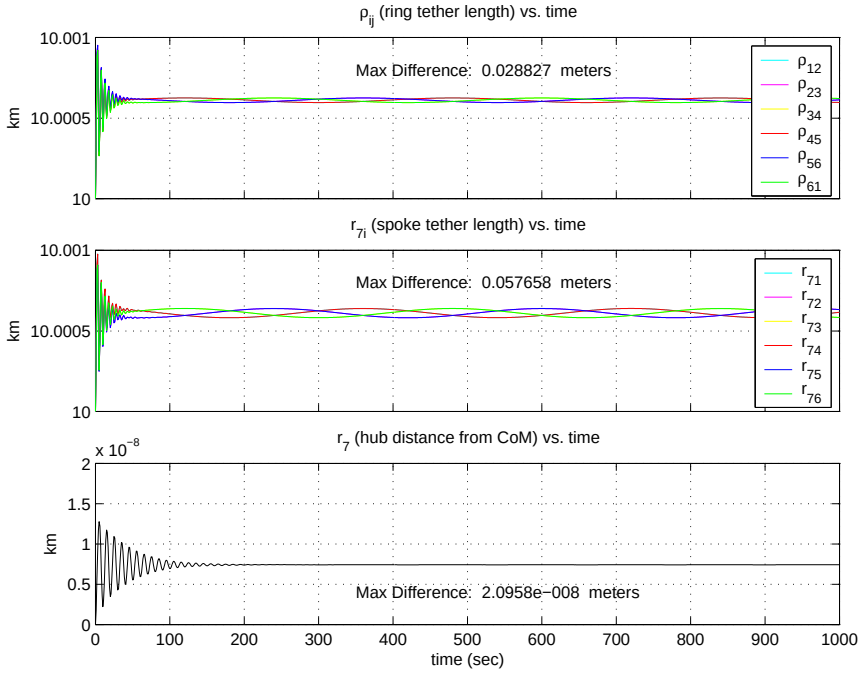


Figure 5.68: Tether Lengths and Hub Movement over Time (7-Body C-H-A-S, Tethers, β=0°, SR=8.123)

The ring tethers and spoke tethers both quickly settle into the now familiar, low-amplitude, 120°-phased, "breathing" oscillations in tether length created by the changing aspect of the gravity gradient forces on the spinning formation. This breathing is on the order of a few centimeters – 6 orders of magnitude lower than the aperture size. Hub motion with respect to the center of mass is also insignificant.

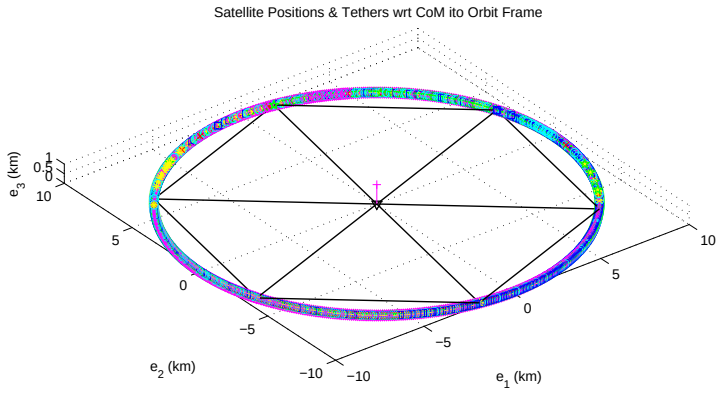


Figure 5.69: Body Positions Relative to System CoM (Orbit Frame, 7-Body C-H-A-S, Tethers, β=0°, SR=8.123, 10K secs)

As before, we next slow the spin rate by an order of magnitude such that SR=0.812. Even with this slower spin rate, the formation remains stable as shown in Figures 5.70 and 5.71.

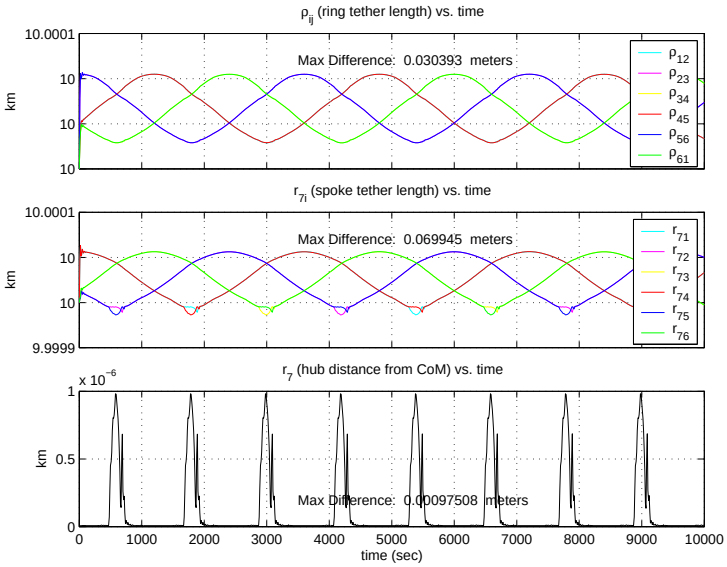


Figure 5.70: Tether Lengths and Hub Movement over Time (7-Body C-H-A-S, Tethers, β=0°, SR=0.812)

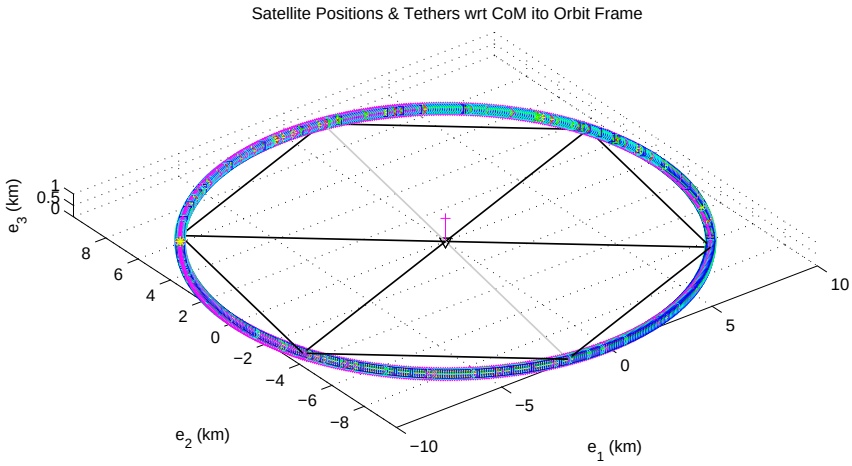


Figure 5.71: Body Positions Relative to System CoM (Orbit Frame, 7-Body C-H-A-S, Tethers, β=0°, SR=0.812, 10K secs)

Notice in Figure 5.71 that the final tether positions are shown at the end of the 10,000 second simulation and that all but two tethers are in tension (black). The two tethers that are slack (shown as grey) are in the vicinity of being perpendicular to nadir and as such experience little gravity gradient forces, hence why they go slack. Observation of the real-time simulation shows that each pair of radial tethers goes slack (depicted as grey in the figure) as they approach the horizontal, then returns to tension (depicted as black in the figure) as they become more vertical. Figure 5.70 shows the low-amplitude "breathing" oscillations as before with very brief excursions that correspond to the radial tether pairs entering the horizontal conditional and becoming slack. Refer back to Figure 5.63 to understand the geometry of this phenomenon.

Despite the small excursions, a spin rate ratio of 0.812 on a 7-body C-H-A-S system is clearly stable, which is a vast improvement over the 4-body H-A-S and the 6-body ring results for the same spin rate ratio. In fact, the 7-body C-H-A-S system

is able to maintain a stable Thomson configuration (β=0°) even for cases where the SR is just outside the "Kumar Range". This gives hope for the Likins-Pringle cases, which have SR's well inside the "Kumar Range".

With that optimism in hand, the Likins-Pringle conditions (β=40° and SR=-1.532) are now applied to the 7-body C-H-A-S configuration. Unfortunately, what results is a complete breakdown, as is clearly seen in Figure 5.72. Perhaps the best way to see the how the dynamic behavior develops over 100,000 seconds is to look at several snapshots of the bodies positions as shown in Figure 5.73. From the initial L-P conditions (Figure 5.73-a), the 7-body C-H-A-S system begins to break down. Within 10 minutes (about 1/10th of an orbit) the system loses tether tension in all but the most vertical tethers (Figure 5.73-b). By the time the system has completed one orbit, the formation has completely collapsed (Figure 5.73-c). Within 6 orbits, the formation eventually starts to take on a new general shape similar to a "shuttlecock" with the massive hub librating about the nadir direction and the individual bodies swinging above in a random manner (Figure 5.73-d). This behavior occurs whether period matching is used on the initial conditions or not.

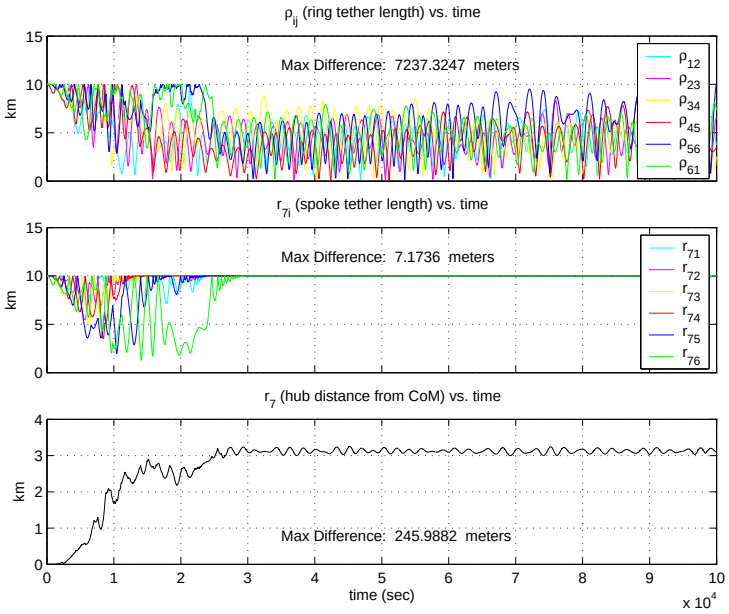


Figure 5.72: Tether Lengths and Hub Movement over Time (7-Body C-H-A-S, Tethers, β=40°, SR=-1.532, L-P)

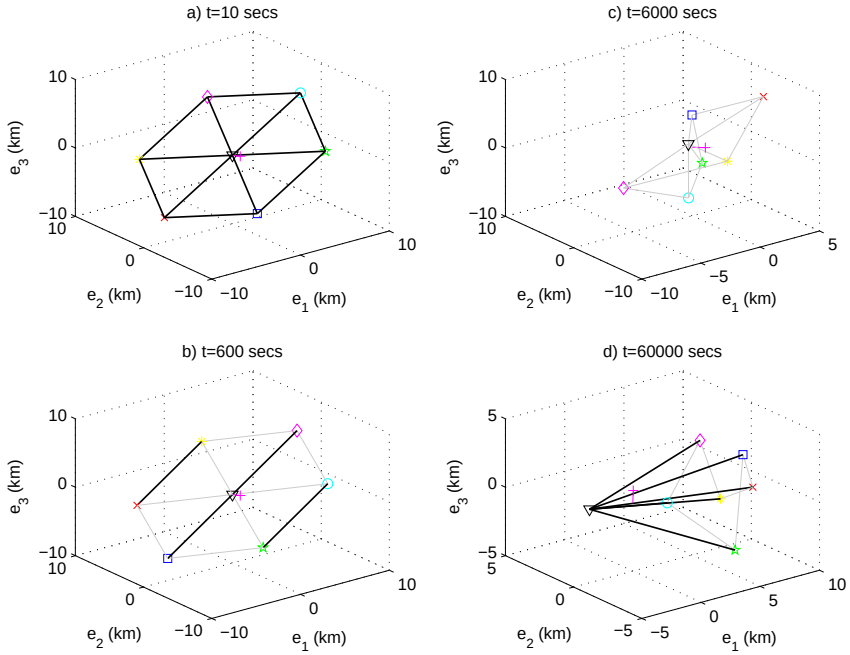


Figure 5.73: Body Positions Relative to System CoM (Orbit Frame, 7-Body C-H-A-S, Tethers, β=40°, SR=-1.532, L-P, Snapshots)

The 7-body C-H-A-S configuration is further investigated by replacing the tethers with full springs per Section 5.3.3. When this is done, the system behaves as desired (Figure 5.74).

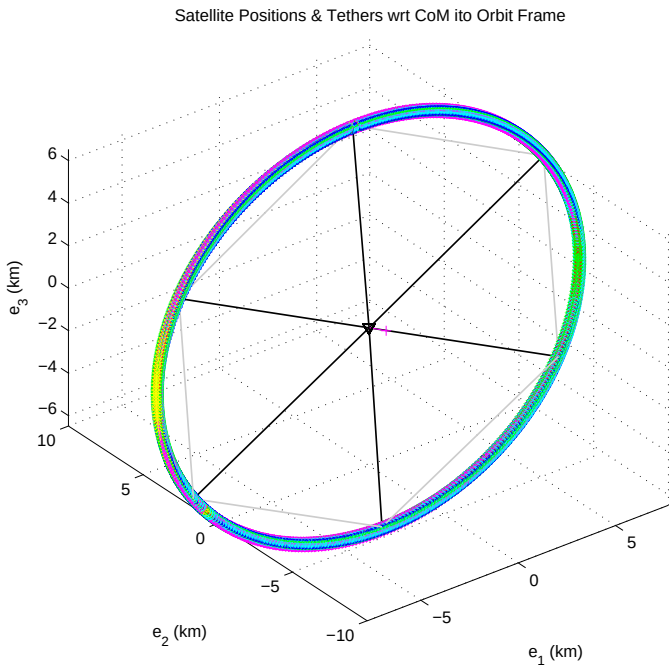


Figure 5.74: Body Positions Relative to System CoM (Orbit Frame, 7-Body C-H-A-S, Full Springs, β=40°, SR=-1.532, L-P, 100K secs)

However, any combination of tethers in this configuration (whether on the spokes or rings) results in the formation breaking down. Even using the "optimal" parameters case (K_s=0.2 kg/s^2, μ_d=0.5 kg/s, $X_\oplus$=6.6 DU), the system formation integrity collapses when tethers are used instead of full springs. The obvious bottom line for the 7-body C-H-A-S is that this configuration is an improvement over both the 4-body H-A-S and the 6-body ring configurations, but it is still unable to maintain the original desired formation.

5.9 Strategy: Select Prograde Likins-Pringle Conditions

Recall from Equation 5.77 that the SR relationship for Likins-Pringle is

$$SR = \frac{\dot{\psi}}{\dot{\nu}} = -2\cos\beta \tag{5.89}$$

which means that for $0° < \beta < 90°$, the SR is negative and for $90° < \beta < 180°$ the SR is positive. When the SR is negative, we'll refer to this as a "retrograde" Likins-Pringle condition. When the SR is positive we'll call it "prograde". Up until now, this research was focused on the retrograde L-P conditions (our baseline cone angle is 40°).

Our final strategy for avoiding the adverse effects of slacking/snapping involves a closer examination of the SR's and the potential use of prograde Likins-Pringle conditions.

5.9.1 Torque Required to Precess. To begin, consider the 3-D graph of torque required to precess a spinning disk (so that the aperture is always facing the earth) as a function of cone angle and SR (Figure 5.75). This 3-D plot is created using the equation for required torque:

$$\left|\vec{M}_{req}\right| = \dot{\nu}\left\{-\sin\theta\left(C\dot{\psi} + C\cos\theta\dot{\nu}\right) + A\cos\theta\sin\theta\dot{\nu}\right\} \tag{5.90}$$

where the $C = 20,000\ kg\ km^2$, $A = 10,000\ kg\ km^2$, and the circular orbit altitude is 1.1 DU. The detailed development of this equation is shown in Section 6.3.1.

It is easiest to visualize this plot by breaking down the individual independent components. For cone angle, imagine a disk over the range of 0°-90°. When the disk is spinning in the orbit plane (β=0°), there is no precession required therefore there is no torque required. As β increases for a retrograde SR, the precession cone that is swept out grows accordingly. Likewise, the torque required for this precession grows until reaching a maximum at β=90°. Above 90°, the precession/torque required

decreases again until, at 180° we are back to a disk spinning in the orbit plane and no precession/torque is required.

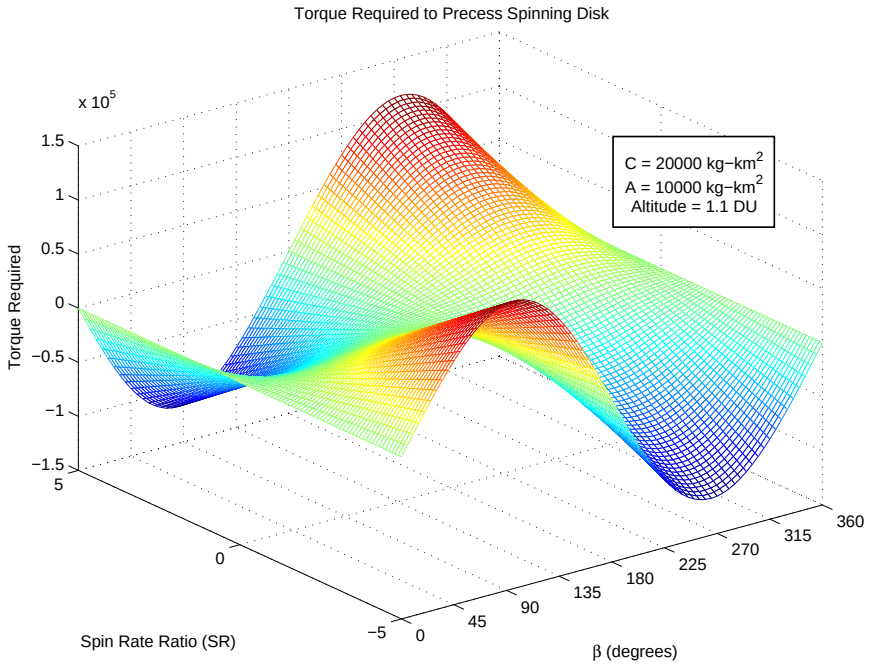


Figure 5.75: Torque Required to Precess Spinning Disk

The effect of SR on required torque is straightforward: as the absolute value of the SR increases, so too does the torque required to precess the spinning disk. So everything discussed about cone angle is scaled with SR. For prograde SR's we have an inverted mirror image of the retrograde side – since the spin is in the opposite direction, the torque required is also in the opposite sense. Beyond cone angles of 180°, everything is also inverted since the disk is essentially upside down.

5.9.2 Torque Generated by Gravity Gradient. Next, consider the torque generated on a disk from gravity gradient forces as a function of cone angle. Figure 5.76 shows a disk under the effects of gravity gradient (F_{gg}) and the resulting restoring forces (F_r) over a progression of cone angles.

Notice that when the cone angle is very low (approximately 0°), F_{gg} is at its maximum, but the component of F_{gg} that constitutes F_r approaches zero. As the cone angle increases to 45°, the total F_{gg} decreases somewhat, but the F_r component of F_{gg} increases to its maximum. When β approaches 90°, the gravity gradient forces disappear, hence both F_{gg} and F_r approach zero.

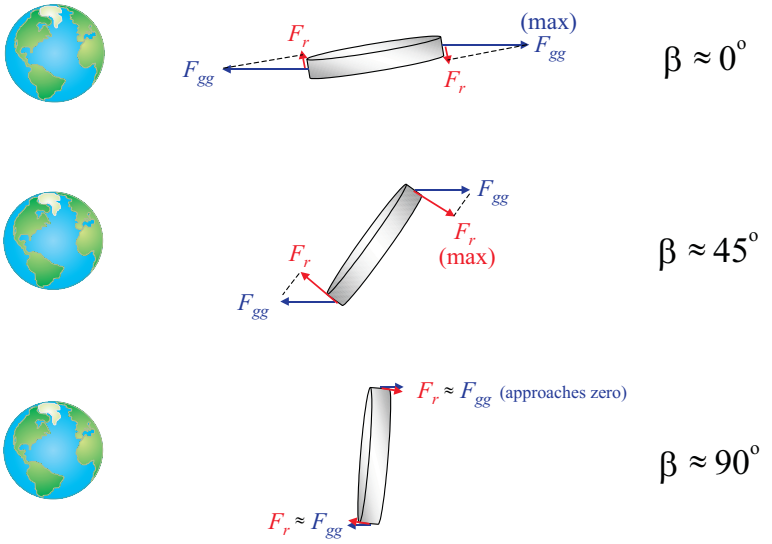


Figure 5.76: Gravity Gradient Forces Acting on Disks

Mathematically, we can use the equations for gravity gradient torque (Equation 4.31) to find that the amplitude of the torque provided by gravity gradient forces acting on such a disk reduces to

$$\left|\vec{M}_{gg}\right| = \frac{3\mu_{\oplus}}{R^3}(C - A)\cos\beta\sin\beta \tag{5.91}$$

Using our moments-of-inertia and orbit altitude from the last section, we can plot the gravity gradient torque versus cone angle (Figure 5.77). This torque is completely independent of the instantaneous spin rate of the disk.

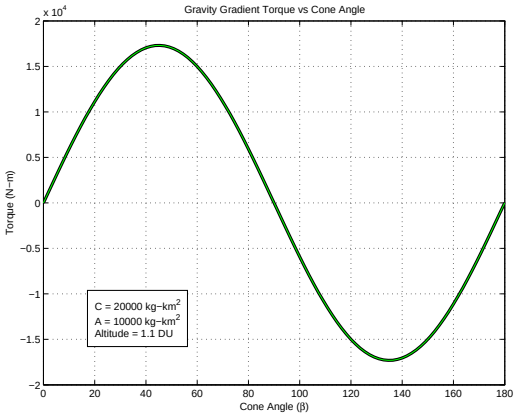


Figure 5.77: Gravity Gradient Torque vs Cone Angle

5.9.3 Graphical Explanation of Likins-Pringle. Going back to the 3-D graph of required torque, we superimpose the torque generated by gravity gradient forces as shown in Figure 5.78.

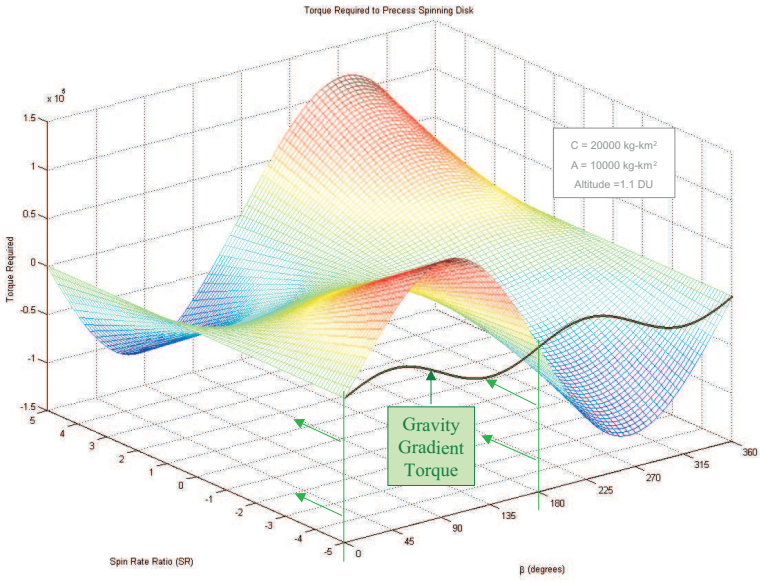


Figure 5.78: Torque Required and Gravity Gradient Torques Generated

Since the gravity gradient torques are independent of spin rate, imagine taking the gravity gradient torque line and sweeping that constant function along all values of SR in Figure 5.78. The points of contact that result draw a contour along the original 3-D plot that indicate where the conical Likins-Pringle equilibrium conditions occur – that is, where 100 percent of the torque required is produced by gravity gradient.

If we project that 3-D contour into the 2-D plane of SR vs. cone angle, we get the Spin Rate Plot shown in Figure 5.79. For this discussion, only cone angles 0°-180° are shown. Notice that the Likins-Pringle equilibria are color-coded based on their rigid body stability criteria as shown in Appendix A. Specifically, the cone angles below 46.4° or above 133.6° are stable (shown as blue in Figure 5.79) while all other β correspond to unstable equilibria (shown as red). The mesh colors on the Spin Rate

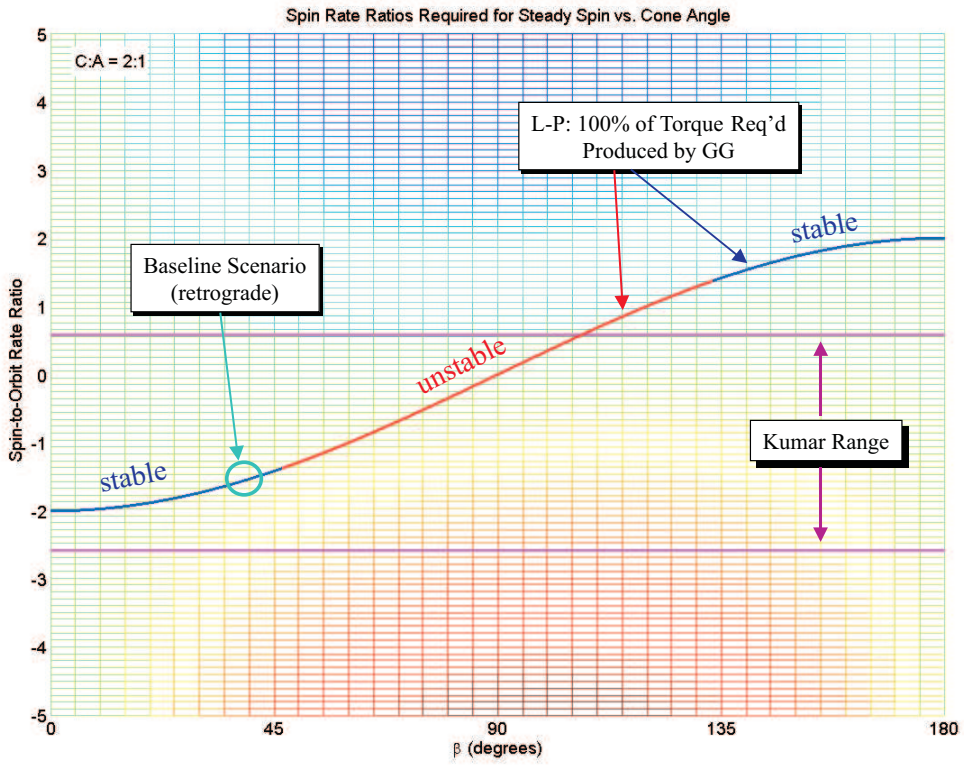


Figure 5.79: Spin Rate Plot with Kumar Range

Plot indicate the torque required to precess a spinning disk at the orbital rate. The red "peak" and blue "valley" simply indicate a difference in polarization of the required torque. Also note that the further one gets from the L-P curve the greater the vertical (out-of-page) differential between what gravity supplies and additional torque required.

It is important to recognize that Figures 5.78 and 5.79 are specific to the C:A ratio of 2:1 and are insensitive to orbit altitude. If the orbit altitude is changed, only the vertical component of the 3-D graph will be affected. That is, the appearance of the 3-D plot will remain the same, the the scale of the torques will have an inverse relationship with altitude. For example, increasing orbit altitude results in the same proportional differential between required torque and gravity gradient torque, however the absolute magnitude of that difference will decrease. Not only does the vertical scale of the 3-D plot change with altitude, but any altitude changes would generate a commensurate change in spin rate to maintain the same $\frac{\dot{\psi}}{\dot{\nu}}$ and remain on the same Likins-Pringle curve.

Now recall the Kumar Range that says system steady-spin motion only occurs for SR's less than -2.58 or greater than 0.58. As stated in section 5.3.4, we initially assume that this Kumar Range for β=0° would apply for all β. This is shown on the Spin Rate Plot (Figure 5.79) as the magenta lines. Inside this magenta window, we would expect instability – outside the magenta band we expect steady-spin motion.

5.9.4 Prograde Likins-Pringle Conditions. If the last sentence is true, then it is no surprise that our baseline scenario (marked on Figure 5.79) does not produce stable tethered system dynamics, since it is inside the Kumar Range band. Conversely, the prograde Likins-Pringle equilibria on the right side of the Spin Rate Plot are clearly outside of the Kumar Range.

By selecting one of these prograde, stable, Likins-Pringle, equilibrium conditions as shown in Figure 5.79, we might expect better results than the baseline case. To

this end, the original model is simulated using a cone angle of β=140°. The results are shown in Figures 5.80 and 5.81.

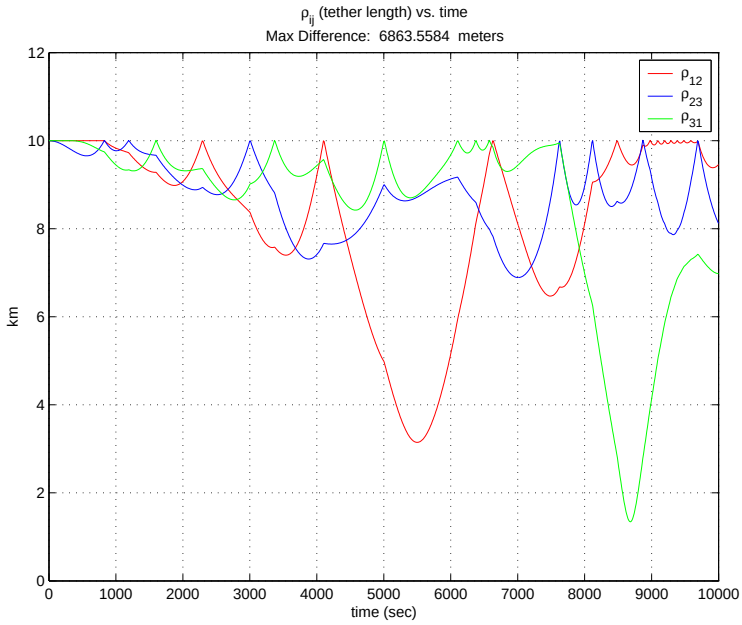


Figure 5.80: Tether Length over Time (3 Body, Tethers, β=140° – Prolate L-P)

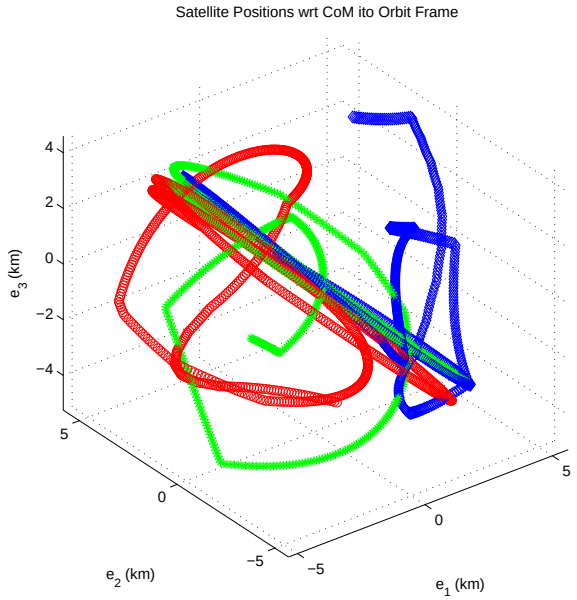


Figure 5.81: Body Positions Relative to System CoM (Orbit Frame, 3 Body, Tethers, β=140°, 10K secs – Prolate L-P)

Obviously, there is no improvement. In fact, close examination shows that the response for β=140° is almost identical to the baseline response (Figures 5.28 and 5.27). Tether slacking and the snapping interaction between tethers is equally present in both cases. The only difference is the that the initial "pitch" of the formation is mirrored with respect to the orbit plane. Additional prograde cases are run using full springs in place of tethers as well as higher cone angles closer to 180°. All of these scenarios produce the same (mirrored) results as the initial retrograde simulations in Section 5.3.

This means two things: 1) the strategy of changing the Likins-Pringle criteria to the prograde side does not work; and 2) the "Kumar Range" is not constant for all cone angles.

5.9.5 How the "Kumar Range" Changes. Since we now know that the "Kumar Range" is not constant over all cone angles, it would be nice to know exactly how it changes with β.

First, we make some observations. Recall from Section 2.1.3 that the "Kumar Range" is defined as the range of spin-to-orbit rate ratios between -2.58 and 0.58. Note that the central value of that range (SR=-1.0) corresponds a situation where the spin of the system exactly counters the apparent spin due to the rotation of the orbit frame, keeping the system inertially fixed. Mathematically, this comes from the fact that for the cylindrical case (β=0°), the orbit rate contributes 100 percent of its rotational energy to the inertial "spin rate" of the system (see Appendix E for an example of this). The "Kumar Range" then is symmetric about SR=-1.0 by +/- 1.58. So, for instance, when the SR is at -0.8, the system is spinning in the negative direction with respect to the orbit frame, but inertially the system is rotating in a positive direction.

On the other hand, as the cone angle increases, less than 100 percent of the orbit rate gets included in the spin rate, so that the symmetry value starts to migrate from -1 towards 0. When the cone angle reaches 90°, the symmetry of the SR range

would be about 0. As we continue to increase the angle cone past 90°, the symmetry value switches polarity and eventually settles at +1 for θ=180°.

With this general observation in hand, we next look at analytically deriving the "Kumar Range" for $\beta \neq 0°$. Unfortunately, when Kumar and Yasaka [26] derived the original "Kumar Range" for β=0°, they were able to make a number of simplifying assumptions that cannot be made when $\beta \neq 0°$. Without those simplifying assumptions, the governing equations-of-motion expand into an unruly set of six coupled, non-linear, second degree, second order differential equations. Just one of these equations has over 130 terms, each with multiple transcendental functions of varying powers up to fourth order. As a result, the analytic approach to determining the "Kumar Range" over $\beta \neq 0°$ turns out to be somewhat intractable.

Alternatively, since we have a working model in hand, we can determine the new, changing, "Kumar Range" or "SR Range" simply by running our original 3-body model for various cone angles and changing the spin rate ratio (SR) until steady-spin motion is observed. In doing so, we take "slices" of the Spin Rate plot to see where the limits of the new "Kumar Range"/"SR Range" really are. Note that steady-spin motion means that the tethers do not have slacking/snapping interaction problems and keep the formation integrity intact – it does not speak to orientation issues, however.

After running nearly 200 additional simulations, enough data is collected to identify the new limits of the "SR Range" (previously called the "Kumar Range") for various slices of β. This new SR Range is shown with magenta in an updated Spin Rate Plot in Figure 5.82. The original "Kumar Range" is shown in cyan.

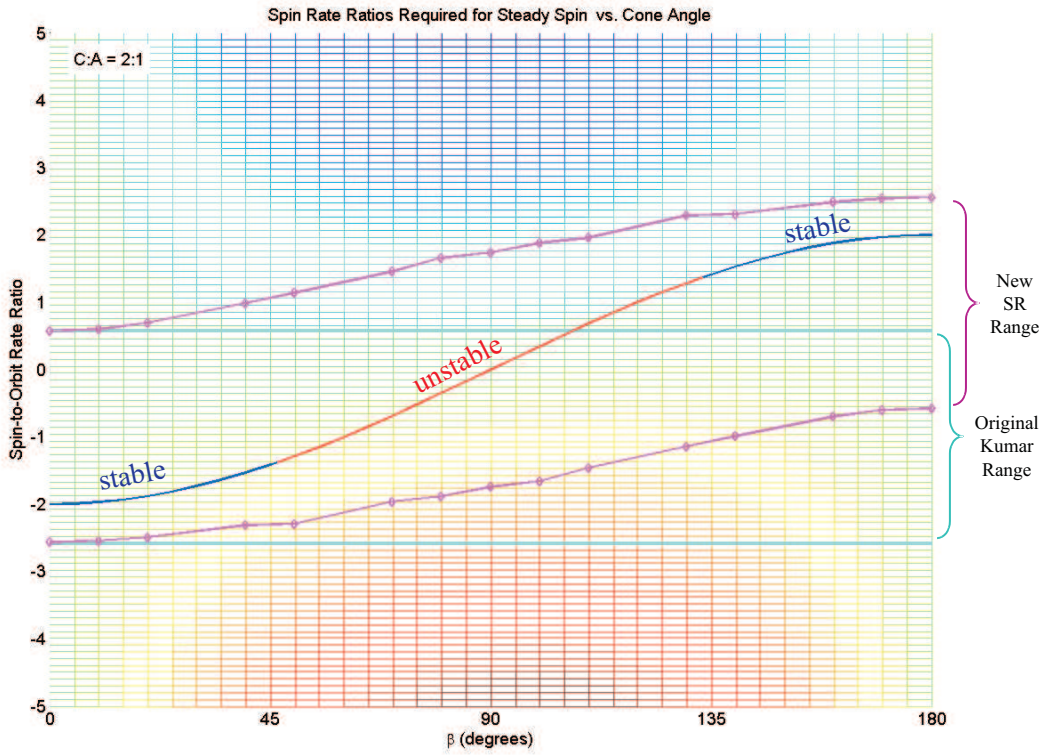


Figure 5.82: Spin Rate Plot with Updated SR Range

Clearly, the numerical results corroborate the original "Kumar Range" for β=0°, but they also show that the SR Range is not constant over all β. Also as predicted, the symmetry of the SR Range migrates from -1 through 0 to +1. Unfortunately, the width of the band remains somewhat constant as this migration occurs, therefore the new SR Range of unstable spin rates totally encapsulates the Likins-Pringle conditions for all values of β. Since the system must reside on the Likins-Pringle curve to produce the desired motion, this new SR Range means that *no equilibrium condition can be found such that the precession of the formation matches exactly with the orbit rate.* That is, the natural dynamics cannot produce the desired equilibrium condition.

Looking back to research objective 3 – "Define and/or determine the existence of an equilibrium condition for a flexible tethered satellite system with a continuous earth-facing component." – we have determined that the EC does *not* exist.

5.10 Summary

In this chapter, we developed models of system dynamics and used oblate rigid body Likins-Pringle configurations as initial conditions for these multi-body systems. The main focus was the three-body tethered ring system with variations as appropriate to investigate different solution concepts for finding an equilibrium condition. A summary of the results are shown in Figure 5.83. Green blocks indicate where equilibrium conditions were found, while amber blocks indicate where the system could not maintain an equilibrium.

	Oblate L-P Conditions used as System's Initial Conditions		Strategies to Solve Slacking/Snapping					
	Cone angles (< 46.4 deg) that produce **stable** rigid body equilibria	Cone angles (> 46.4 deg) that produce **unstable** rigid body equilibria	**Radial Configs** (large hub to minimize interaction) **4B HAS**	**7B CHAS**	**6B Ring** (subtended angles)	**Tether Model**	**Formation Param's**	**L-P E.C. outside of Kumar range**
Spring	**Equilibrium**	Oreintation Diverges (even w/ period matching)	Each body swings independently at slower spin rates					
er Only	Tether slacking/snapping causes failure in formation integrity and orientation	Tether slacking/snapping causes failure in formation integrity and orientation	Stopped snapping, but lost formation	Shuttle-cock	Stopped snapping, but collapses into librating string	Non-linear or low Ks: slight impr -- high mu: marginal impr	high altitude: slight imp -- short tether: slightly worse	No change -- Tether "snapping"
Flight	Strobo-planar, periodic ellipses for individual s/c	Strobo-planar, periodic ellipses -- **Circ E.C. @ 60 deg cone**	All same as original Free Flight					

Figure 5.83: Summary of Simulation Results

The Likins-Pringle initial conditions in free flight do generate strobo-planar equilibrium conditions for each body regardless of the cone angle. The addition of full springs circularizes the free flight ellipses and generates a system-level equilibrium condition, but only for the Likins-Pringle initial conditions that are associated with stable rigid body equilibria ($\beta < 46.4°$ or $> 133.6°$). For the initial conditions associated with unstable rigid body equilibria, the system attached with springs can keep its formation integrity, but cannot hold the desired orientation.

Massless tethers do not hold the system in an equilibrium condition, regardless of cone angle. Tether slacking and the snapping interaction between tethers cause the

formation to lose both its integrity and its orientation. The basic cause for the tether slack and subsequent snapping is insufficient spin rate. If the spin rate is increased to maintain formation integrity, the orientation would suffer as the spin axis no longer stayed fixed in the orbit frame. A number of strategies were attempted to solve the slacking/snapping problem without increasing the spin rate, but as the middle row of Figure 5.83 shows, none were successful.

A new Spin Rate Plot was generated that shows the regions of the only possible conditions where a tethered formation could be considered (shown as green in Figure 5.84).

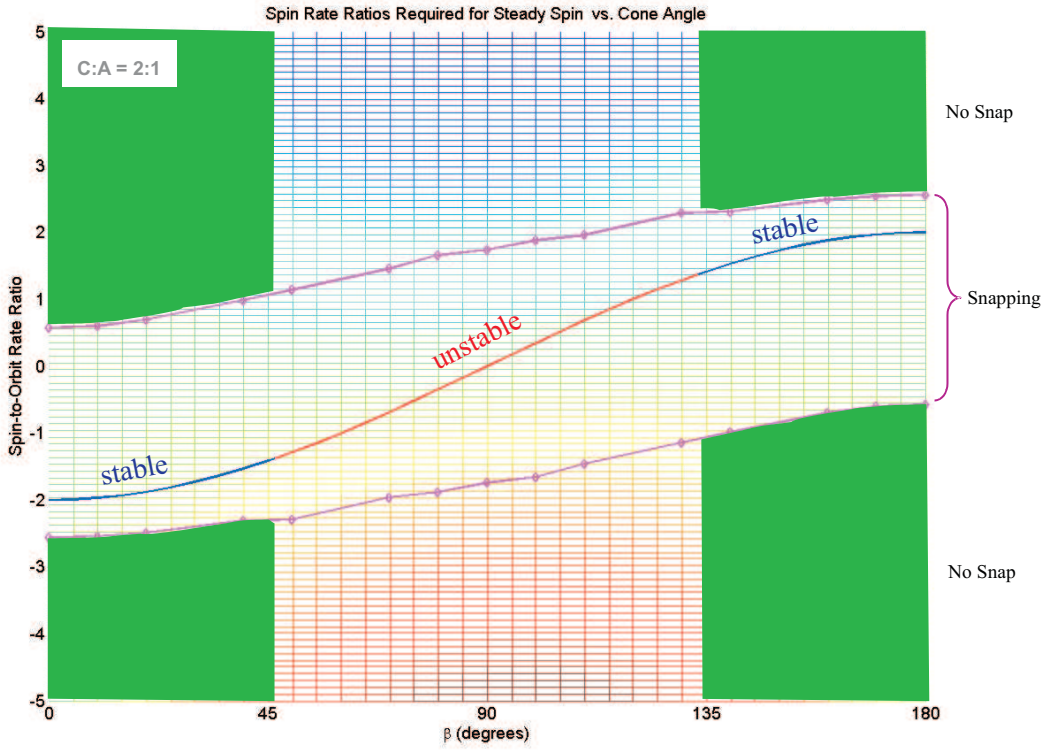


Figure 5.84: Spin Rate Plot with Possible Operating Regions

The cone angle must be less than 46.4° or greater than 133.6° (i.e. on the blue L-P curve along the x-axis) to avoid rigid body instability issues. Also, the Spin-to-Orbit Rate (SR) must be outside the magenta band to avoid the slacking/snapping issues. This leaves the four corners of the graph in Figure 5.84. Basically, the closest one

can get to the desired equilibrium condition for the tethered system is the minimum distance from one of these regions to the L-P curve, but since these regions never touch the L-P curve, the desired equilibrium conditions cannot be met for a tethered system. Note that this Spin Rate Plot is specifically for a MOI ratio of 2:1. Changing the MOI ratio may have some impact on the exact width of the magenta band as well as subtle amplitude changes in the L-P curve, but since 2:1 is the most extreme oblate case for a 2-D array, it is considered the most conservative. Changing other parameters, such as altitude and unstretched tether length, will yield the same Spin Rate Plot as above.

Therefore, the bottom line for tethered systems is that *an equilibrium condition for fixed length tethers does not exist.* Without a true equilibrium condition, the only remaining option for creating a continuously earth-facing aperture is to force the condition using various methods of control... which is the subject of the next chapter.

VI. Applying Controls to the Tethered System

In the previous chapter, the dynamics of the tethered system were thoroughly explored and it was determined that no equilibrium condition exists to keep a fixed-length tethered system in a continuously earth-facing orientation. In this chapter, attention is now turned to applying some basic control methods to try and force the system into the desired motion (overcoming the inherent passive instability), even in the face of perturbations. This chapter, in it's entirety, represents research objective 4: *Apply control schemes to the tethered system to combat perturbations and maintain desired motion.*

There are four basic control methods that are applied in this research:

- **Thrust to Mimic Spring Compression**
- **Programmed Tether Length Reels**
- **Thrust to Precess High Spin Rate**
- **Constant Tension Reels**

In each case, despite the non-existence of the desired equilibrium, dynamic conditions are chosen to be as close as possible to the desired equilibrium condition (or at an alternate equilibrium condition depending on the control method). Controls and perturbations are selectively added to the original 3-body models from previous chapters and the MATLAB® code is modified accordingly. The rest of this chapter discusses the details of the motivation of each method, and the approach of how each control scheme is implemented and the simulation results.

6.1 Control Method 1: Using Thrust to Mimic Spring Compression

Recall from Section 5.3.3 that massless springs between the satellites offer the closest behavior to that of a rigid body, and therefore produce the desired equilibrium condition as long as the cone angle is in the stable rigid body range (below 46.4° or above 133.6°). The baseline case using full, massless springs was shown back in

Figures 5.22-5.24. Recall also that the springs took the Likins-Pringle Free Flight equilibrium presented in Section 5.3.1, and circularized the multi-body ellipses into a single, circular equilibrium condition. Since tethers essentially make up one-half of a spring (tension only), the concept for this control method is to use thrusters to supply the other half of the spring (compression).

Using this control method, we allow the system dynamics to reside neatly on the Likins-Pringle curve that was shown on the Spin Rate Plot back in Chapter V (Figure 5.84). This means that the equilibrium condition used as a starting point for this control method is the multi-body Likins-Pringle Free Flight equilibrium. The β=40° case is chosen without loss of generality.

6.1.1 Model Modifications. Depending on the relative distances between the two bodies of interest (i.e. connected via a tether), one of three things happens:

1. When the distance is greater than ρ_o, the tether is in tension and is treated like a regular spring-damper.
2. When the distance is less than ρ_o by some threshold distance (Q_d), thrusters are fired to mimic compression forces.
3. When the distance is between ρ_o and Q_d, the two bodies are free flying in a limited "dead-band".

The original 3-body model equations-of-motion from Section 5.2 are used when the tether length is greater than ρ_o. However, when the tether length is less than ρ_o, those original acceleration equations (5.48 and 5.49) are modified. The new "spring" acceleration EOM used to modify the original MATLAB® code are:

$$\ddot{\vec{R}}_{i_{spring}} = \begin{cases} \frac{\delta_{nm} K_s (\rho_{ij} - \rho_o)}{m_i} \left(\frac{\vec{r}_{ij}}{\rho_{ij}} \right) & \text{if} \quad (\rho_{ij} - \rho_o) \geq 0 \\ 0 & \text{else} \end{cases} \tag{6.1}$$

$$\ddot{\vec{R}}_{i_{damper}} = \begin{cases} \frac{\delta_{nm}\mu_d\dot{\rho}_{ij}}{m_i}\left(\frac{\vec{r}_{ij}}{\rho_{ij}}\right) & \text{if} \quad (\rho_{ij}-\rho_o) \geq 0 \quad \text{and} \quad \dot{\rho}_{ij} > 0 \\ 0 & \text{else} \end{cases} \tag{6.2}$$

$$\ddot{\vec{R}}_{i_{thruster}} = \begin{cases} \frac{\delta_{mn}F_t}{m_i}\left(\frac{\vec{r}_{ij}}{\rho_{ij}}\right) & \text{if} \quad \rho_{ij} < (\rho_o - Q_d) \\ 0 & \text{else} \end{cases} \tag{6.3}$$

$$\delta_{nm} = \begin{cases} 1 & \text{if} \quad n = i \\ -1 & \text{if} \quad m = i \\ 0 & \text{else} \end{cases} \tag{6.4}$$

where F_t is the thruster force and Q_d is the threshold distance below the unstretched tether length that delays the firing of the thrusters. In the actual MATLAB® code, F_t is modeled as some proportion of the tether's spring constant, $F_t = K_s Q_t$ where Q_t and K_s are constants. For this research, it is initially assumed that the thrust is directed in a straight line toward the corresponding body to most closely represent a massless spring. Flexible springs would generate more complex (and more fuel costly) results, and consequently are not investigated.

Updating the MATLAB® model with the new EOM also includes keeping track of the amount of thrust required over a simulation period. It is assumed that the thrusters always fire in pairs to create the "spring" effect. At the end of each simulation, the total number of thruster firings is multiplied by the thruster force and the stepsize to get total ΔV. This calculation is due to the on/off nature of the thruster firings. Although not accomplished in this current study, variable (or throttleable) thrust levels could be used to allow the thrusters to behave more spring-like.

6.1.2 Baseline Case Results. Using the now-familiar Likins-Pringle scenario of β=40°, an initial thruster-tether spring case is built using baseline values for thruster force (F_t=2.0 $kg \cdot m/s^2$) and firing delay (Q_d=0.1m). All other parameters are identical to the original 3-body baseline scenario. Perturbations are not yet added.

The results of this baseline simulation are presented in Figures 6.1 and 6.2. As with the original massless springs, these thruster-tether springs once again produce the desired stable equilibrium. The "breathing" oscillations in tether length and radial distance have some small oscillations and have about twice the amplitude (14cm) compared to the pure spring results from Figures 5.23 and 5.24, but they are clearly still bounded. Over the course of the 10,000 second simulation, 6,835 thruster pair firings were required for a total ΔV of 136.7 m/s.

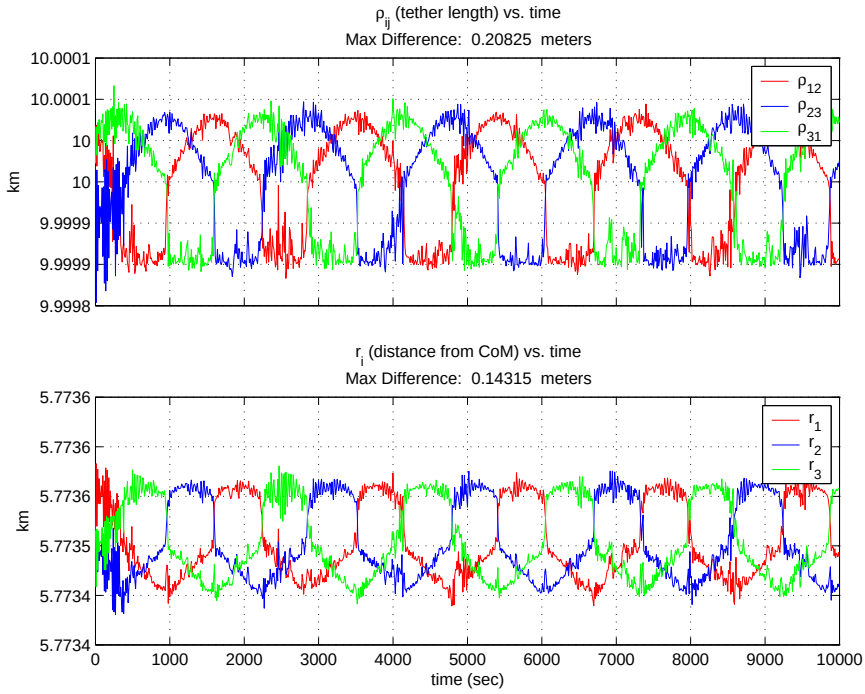


Figure 6.1: Tether Lengths and Distance from System CoM over Time (Thrusters as Half-Springs, F_t=2.0, Q_d=0.1 – Baseline)

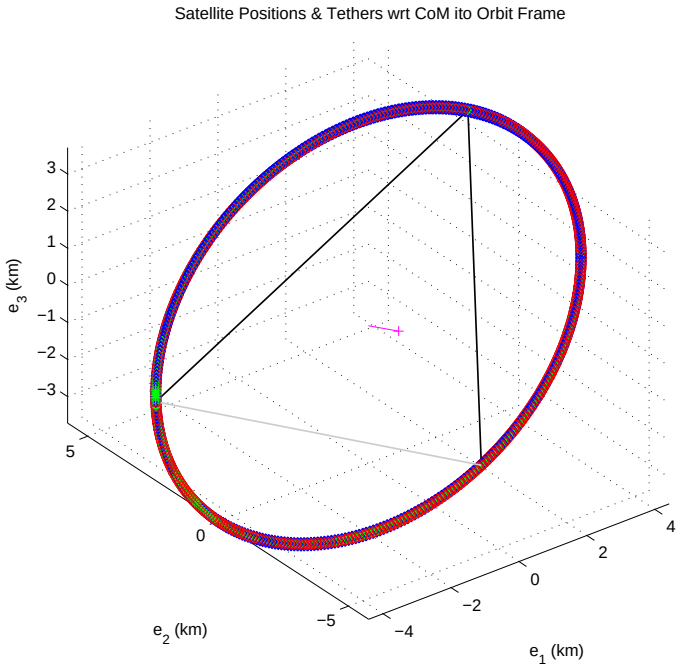


Figure 6.2: Body Positions Relative to System CoM (Orbit Frame, Thrusters as Half-Springs, F_t=2.0, Q_d=0.1, 10K secs – Baseline)

6.1.3 Sensitivity to Thrust Levels and Delay Times. An effort is made to evaluate the sensitivity of changing the thrust levels (F_t) and firing delay times (Q_d). All told, 12 cases are conducted, but figures from only the 4 most illustrative examples are shown in this section. They are listed below in Table 6.1, along with the baseline case.

Table 6.1: Case List for Thrust Levels and Delay Times.

	F_t	Q_d
Baseline	2.0	0.1
Case 1	20.0	1.0
Case 2	200.0	10
Case 3	0.2	0.1
Case 4	2.0	0.5

If both are increased F_t and Q_d, longer delays are allowed after the tether goes slack before firing thrusters, but the thrusters have higher output. In this situation, the system stays stable but the "breathing" oscillations in ρ and r_i are much more noisy and of higher amplitude. Examples of this are shown in Figures 6.3 (Case 1) and 6.4 (Case 2). In addition, while the number of required burns goes down in these cases, the total ΔV required goes up dramatically (221 m/s and 4454 m/s, respectively).

On the other hand, if delay times are decreased too much, the thrusters fire too soon/often (creating more ΔV than necessary) and if thrust levels are decreased too much (as in Case 3), the insufficient thrust levels are unable to prevent slacking (Figure 6.5), which eventually causes instability (Figure 6.6).

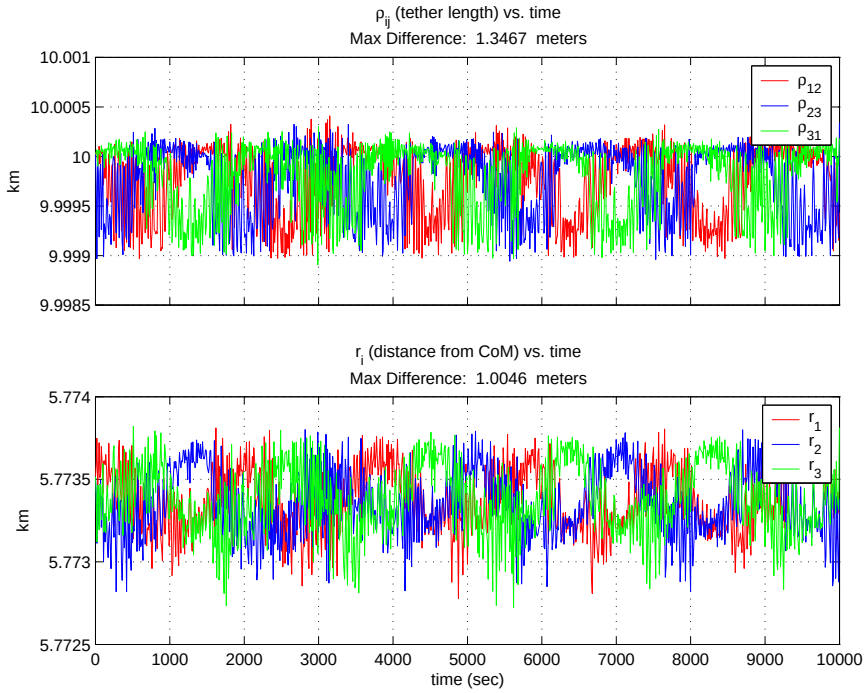


Figure 6.3: Tether Lengths and Distance from System CoM over Time (Thrusters as Half-Springs, F_t=20.0, Q_d=1.0 – Case 1)

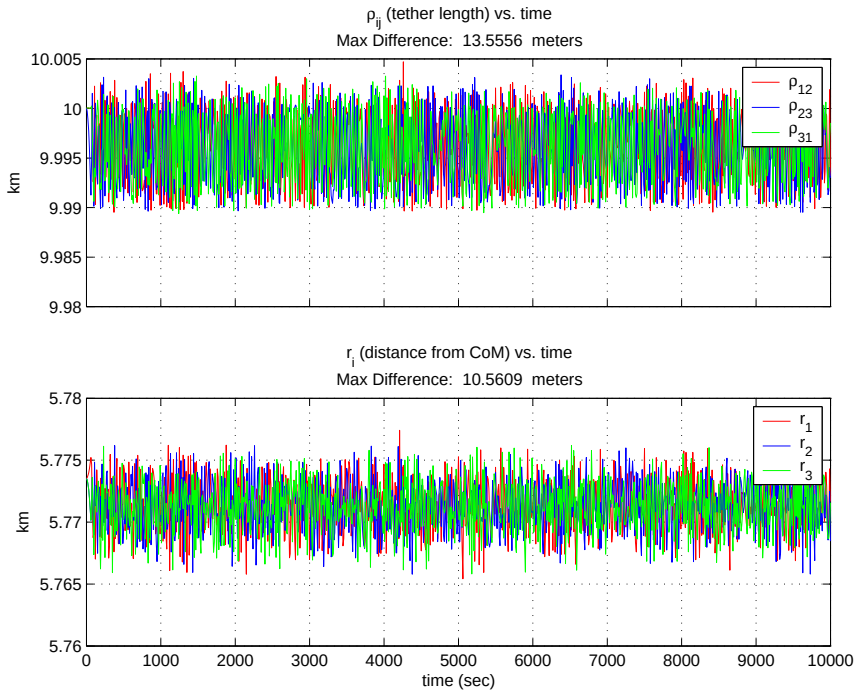


Figure 6.4: Tether Lengths and Distance from System CoM over Time (Thrusters as Half-Springs, F_t=200.0, Q_d=10.0 – Case 2)

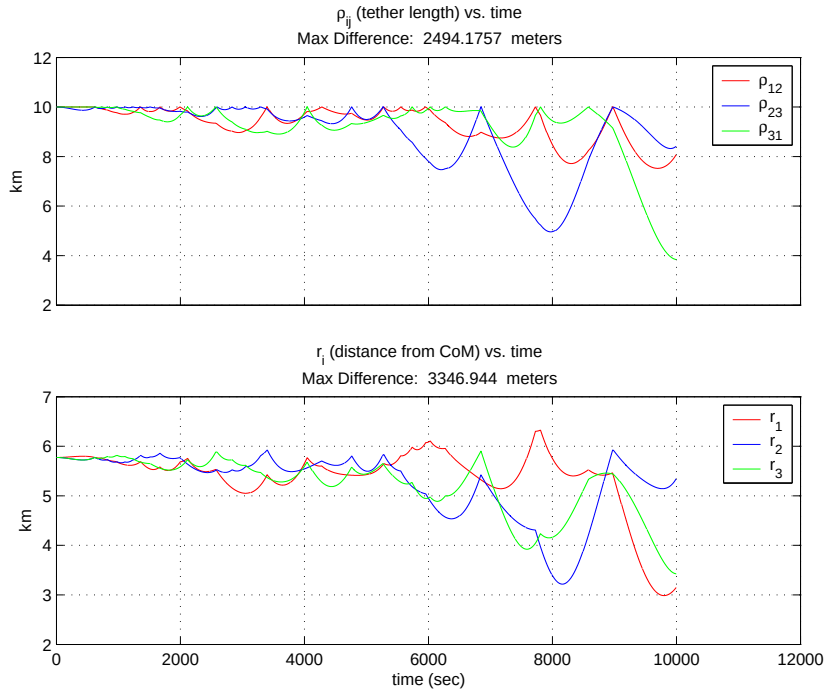


Figure 6.5: Tether Lengths and Distance from System CoM over Time (Thrusters as Half-Springs, F_t=0.2, Q_d=0.1 – Case 3)

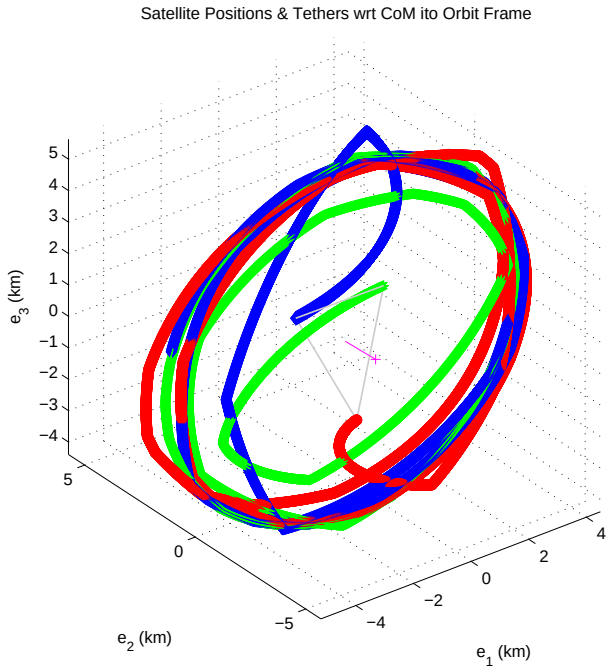


Figure 6.6: Body Positions Relative to System CoM (Orbit Frame, Thrusters as Half-Springs, F_t=0.2, Q_d=0.1, 10K secs – Case 3)

One of the best combinations is found using the original baseline value for F_t with a slight delay in the timing (Q_d=0.5 m) and a decreased step size of 0.1 second. With these values (Case 4), the system once again maintains the desired stable equilibrium (seen in Figure 6.7), but there is a slight improvement in total ΔV required: 134.8 m/s.

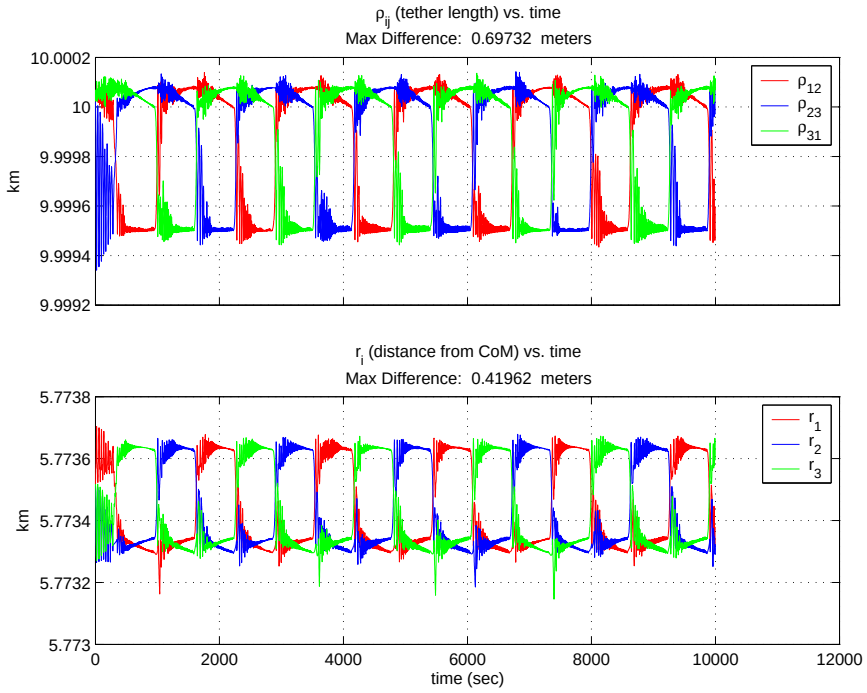


Figure 6.7: Tether Lengths and Distance from System CoM over Time (Thrusters as Half-Springs, F_t=2.0, Q_d=0.5 – Case 4)

6.1.4 Adding Perturbations. The most dominant perturbation for exo-atmospheric satellites is generated by the second zonal harmonic of the geopotential (also called the J_2 disturbing function). The accelerations on each body due to this aspherical potential can be developed per Vallado [71] as:

$$\ddot{\vec{R}}_{i_{J_2}} = \begin{bmatrix} \frac{-3J_2\mu_\oplus R_\oplus^2\left(\vec{R}_i\cdot\hat{i}_1\right)}{2\left|\vec{R}_i\right|^5}\left(1-\frac{\left(\vec{R}_i\cdot\hat{i}_3\right)}{\left|\vec{R}_i\right|^2}\right) \\ \frac{-3J_2\mu_\oplus R_\oplus^2\left(\vec{R}_i\cdot\hat{i}_2\right)}{2\left|\vec{R}_i\right|^5}\left(1-\frac{\left(\vec{R}_i\cdot\hat{i}_3\right)}{\left|\vec{R}_i\right|^2}\right) \\ \frac{-3J_2\mu_\oplus R_\oplus^2\left(\vec{R}_i\cdot\hat{i}_3\right)}{2\left|\vec{R}_i\right|^5}\left(1-\frac{\left(\vec{R}_i\cdot\hat{i}_3\right)}{\left|\vec{R}_i\right|^2}\right) \end{bmatrix} \quad \text{for} \quad i = 1...3 \tag{6.5}$$

We approximate perturbing effects on the thruster-tether spring system by adding these accelerations into the model's EOM and re-run the baseline simulation. The results show that even under the effects of these perturbations, thrusters and tethers combining to form a full spring can hold the desired equilibrium very well (Figures 6.8 and 6.9). The "breathing" oscillations are still held to less than 14 cm and the total ΔV required is about the same: 135.4 m/s.

This tells us that tethers do in fact help in successfully combating the effects of perturbations by taking advantage of their inherent passive tension. Furthermore, if thrusters were required to mimic both sides of a spring, the tethers would effectively save one-half of the fuel costs. What remains to be seen is the thruster cost for a half spring as compared to other thruster-only formationkeeping methods. This will be covered in the next chapter.

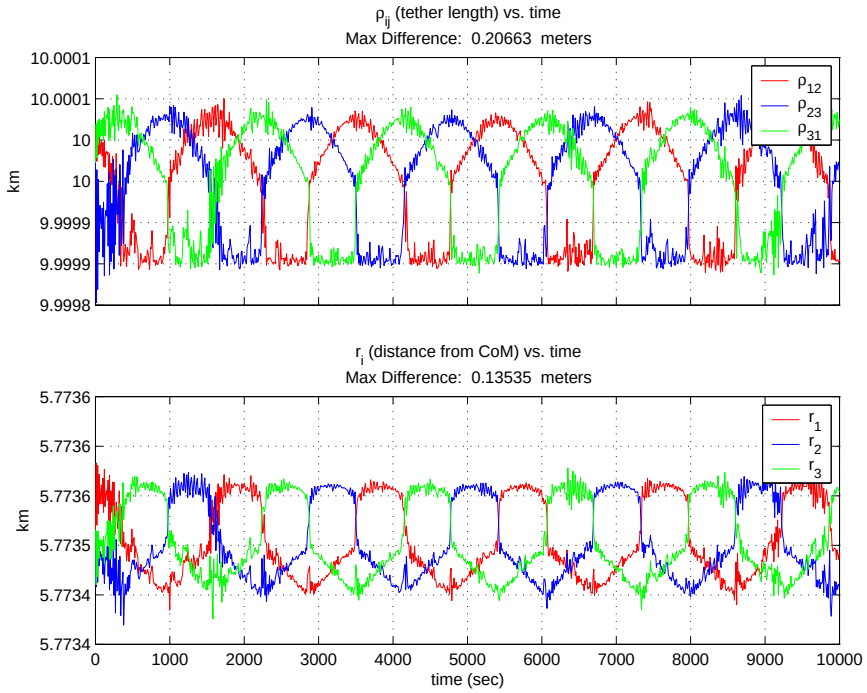


Figure 6.8: Tether Lengths and Distance from System CoM over Time (Thrusters as Half-Springs, F_t=2.0, Q_d=0.1, w/ Perturbations)

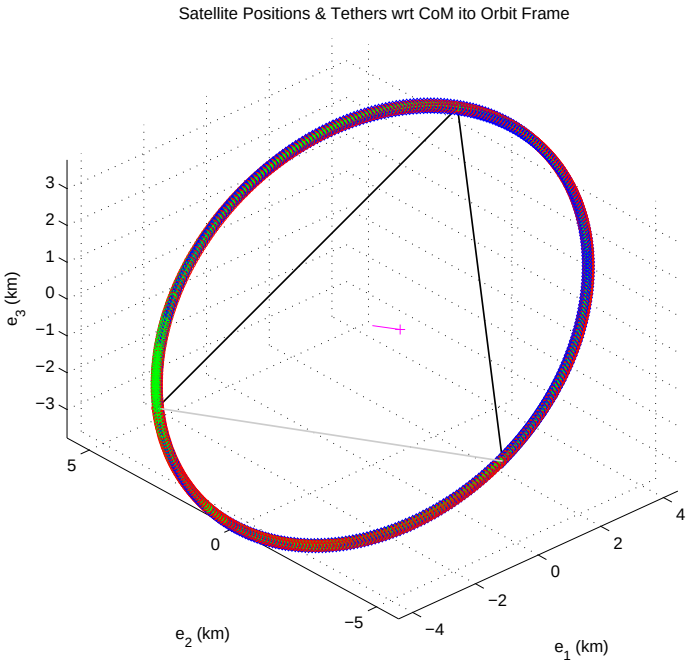


Figure 6.9: Body Positions Relative to System CoM (Orbit Frame, Thrusters as Half-Springs, F_t=2.0, Q_d=0.1, w/ Perturbations, 10K secs)

6.1.5 "Optimized" Formation Parameters Case. A final scenario for the thruster-tether spring incorporates the baseline thruster force and timing delay, J_2 perturbations, and the "optimized" formation parameters used in Section 5.5.5 to get a conservative estimate of how good this control method could get. As a reminder, the "optimized" formation parameters are shown in comparison to the baseline formation parameters in Table 6.2. The "optimized" values are simply a combination of the best performing values when evaluated separately in the uncontrolled case.

Table 6.2: "Optimized" and Baseline Formation Parameters.

Parameter	'Optimized' Value	Baseline Value
K_s	0.2 kg/s^2	20.0 kg/s
μ_d	0.5 kg/s	0.05 kg/s
$X_\oplus$	6.6 DU	1.1 DU
ρ_o	10 km	10 km

Since this scenario's altitude is at 6.6 DU's, the simulation is run for 100,000 seconds to get a comparative appreciation for the dynamics. Notice in Figure 6.10 that once again the equilibrium holds stable. In addition, the "breathing" oscillations in Figure 6.11 are much less noisy and the total ΔV required is only 6.14 m/s over 100,000 seconds.

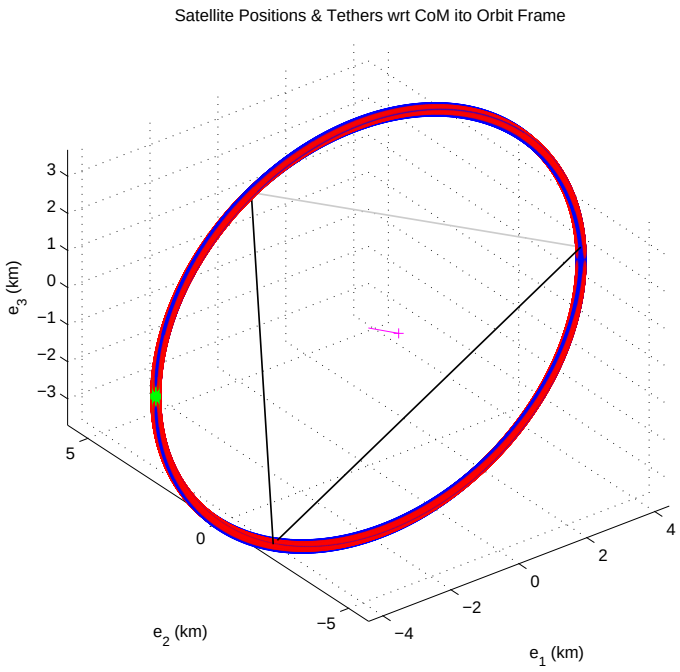


Figure 6.10: Body Positions Relative to System CoM (Orbit Frame, Thrusters as Half-Springs, F_t=2.0, Q_d=0.1, Optimized Parameters, w/ Perturbations, 100K secs)

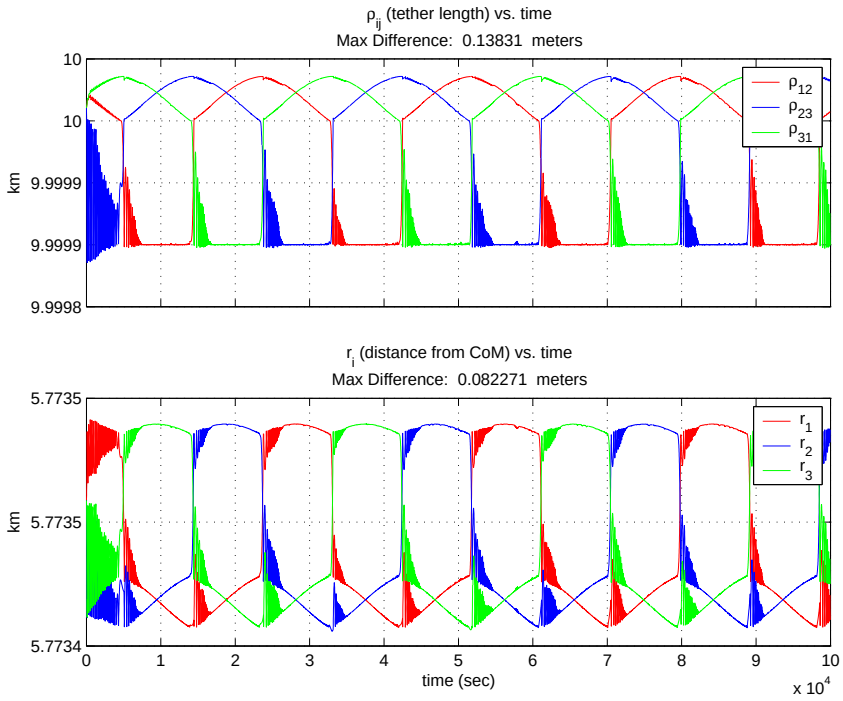


Figure 6.11: Tether Lengths and Distance from System CoM over Time (Thrusters as Half-Springs, F_t=2.0, Q_d=0.1, Optimized Parameters, w/ Perturbations)

6.2 Control Method 2: Programmed Reels

Instead of limiting the tethers to a single, fixed, unstretched length, the next concept involves variable-length tethers where tether reels are programmed to follow a repeating pattern based on the natural motion of the individual satellites (which can be pre-computed as will be shown).

6.2.1 Baseline "Single Satellite Ellipse" Equilibrium Condition. Recall from Section 5.3.1 that the natural, free-flying motion of each individual satellite that starts in Likins-Pringle conditions is a strobo-planar, repeating ellipsoid (shown again in Figure 6.12).

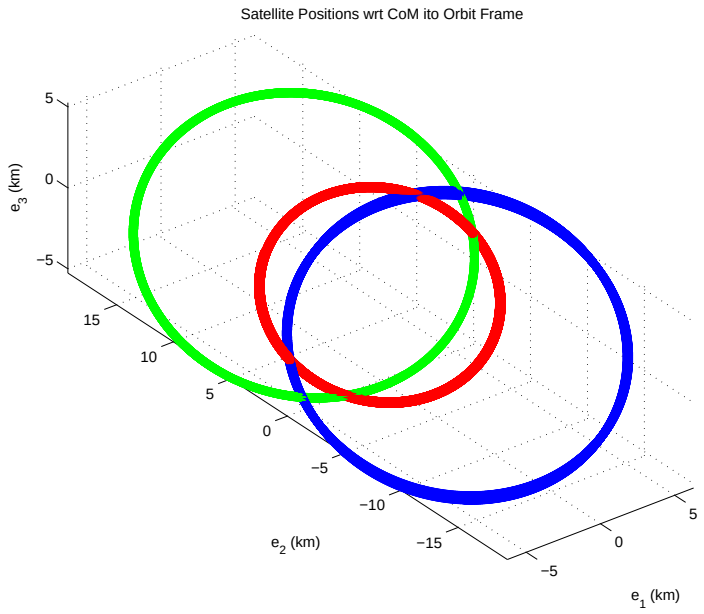


Figure 6.12: Body Positions Relative to System CoM (Orbit Frame, Free Flight, β=40°, 10K secs)

We can select one of those ellipses (say the red one from satellite 1), and assign all satellites to be on that single ellipse by matching the initial conditions of satellites 2 and 3 to the relative state of satellite 1 at arbitrary points in time. Figures 6.13 and 6.14 show an application of this, where all three satellites are following the same strobo-planar ellipse based on satellite 1's Likins-Pringle configuration with a 40°

cone angle. Remember, that this "Single Satellite Ellipse" still represents a viable equilibrium condition for all three objects, and is therefore the equilibrium condition about which this control method will be applied.

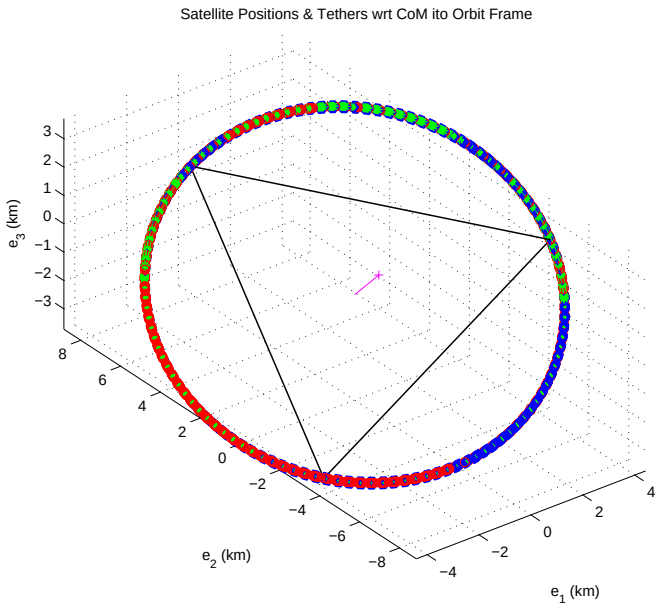


Figure 6.13: Body Positions Relative to System CoM (Orbit Frame, Free Flight – "Single Satellite Ellipse", β=40°, 100K secs)

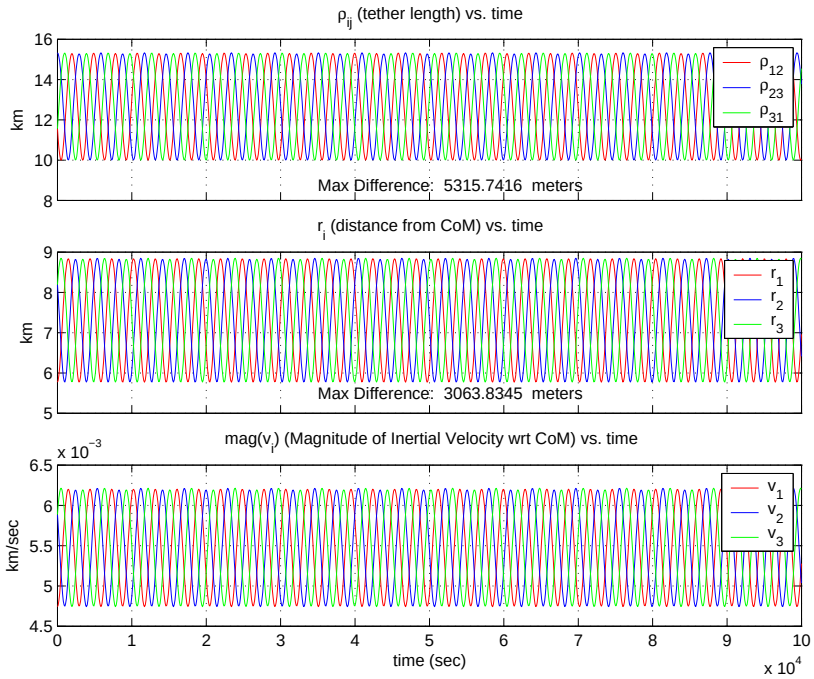


Figure 6.14: Tether Lengths, Radial Distance, and Velocity over Time (Free Flight – "Single Satellite Ellipse", β=40°)

6.2.2 Programming the Reels. Now looking at Figure 6.14, we see that the relative velocity of each satellite oscillates as it traverses the elliptical path. Obviously, since the velocities oscillate, so too will the tether lengths (ρ_{ij}) and radial distances from the CoM (r_i). Recognize that these repeating oscillations are no longer the "breathing" oscillations from before, but rather are due to the large elliptical path that is traversed. These repeating oscillations in ρ_{ij} are the patterns that are used to program open-loop control on the tether reels for all time.

In our original dynamic model, the decision of whether a spring/tether engaged was based on comparing the current length (ρ) to a single, fixed unstretched length (ρ_o). Under this new control method, current length is compared to a $\rho_o(t)$ that varies with the pattern shown in Figure 6.14. So, in actuality, since no tether "reel" shows up in our model, we program the $\rho_o(t)$ that is allowed. Therefore, in unperturbed free-flight, the system should propagate through time without ever required restoring forces from the tether/spring.

6.2.3 Baseline Case Results. To initially demonstrate this method, the baseline case of β=40° is used as shown above. Clearly, unless we have perturbing forces acting on the system, the springs/tethers should never engage since they are completely tracing the "Single Satellite Ellipse" equilibrium condition. It should be no surprise then, that whether springs or tethers are used, the response is identical to Figures 6.13 and 6.14.

As we add perturbations, however, the response is not quite so predictable. Shown in Figures 6.15 and 6.16 are the results of full springs with programmed ρ_o's adhering to the "Single Satellite Ellipse" equilibrium condition. That is, as J_2 perturbs the system, the springs are attempting to restore themselves back to the natural (albeit variable) programmed lengths. As can be seen in Figure 6.15, the springs are successful in maintaining the oscillatory patterns for ρ_{ij}. Unfortunately, the entire formation "flips" about the nadir direction after approximately one orbit, despite holding the equilibrium fairly well up to that point (Figure 6.16).

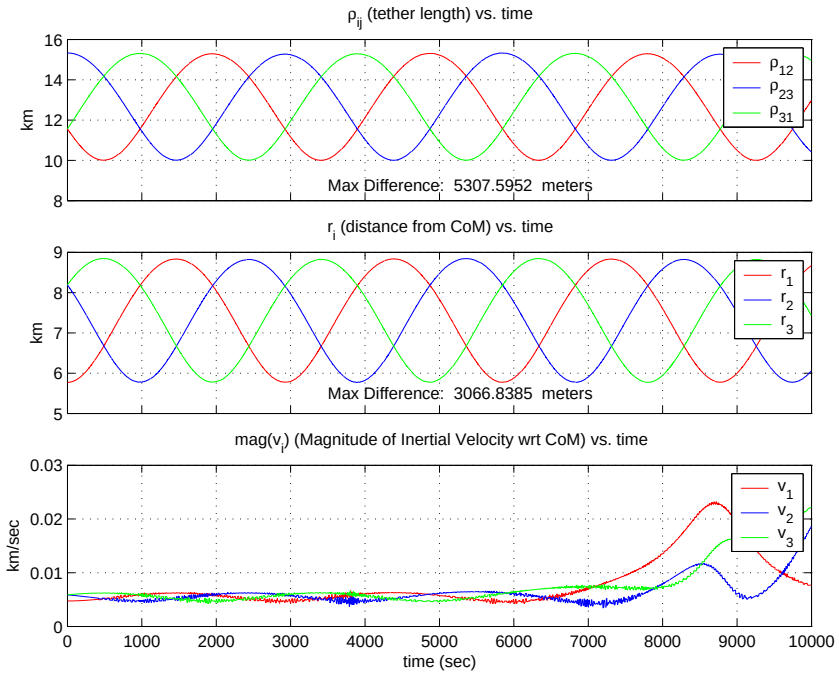


Figure 6.15: Tether Lengths, Radial Distance, and Velocity over Time (Full Springs, Programmed Reels – "Single Satellite Ellipse", β=40°, w/ Perturbations)

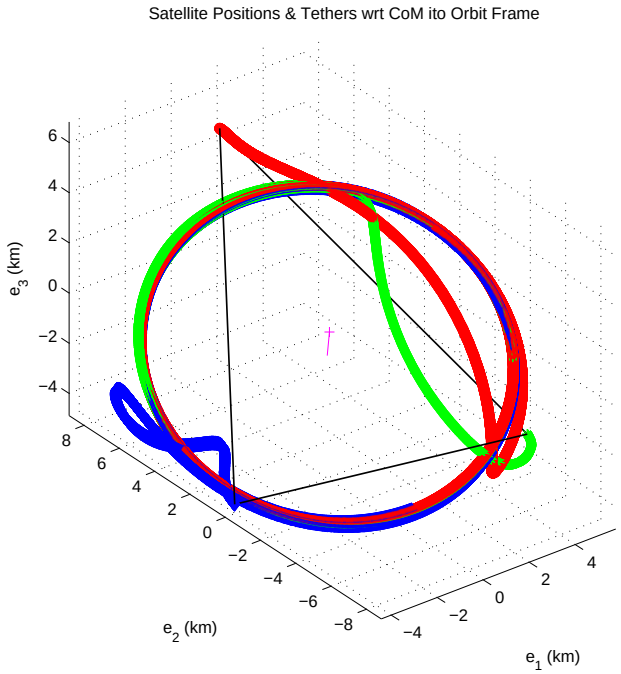


Figure 6.16: Body Positions Relative to System CoM (Orbit Frame, Full Springs, Programmed Reels – "Single Satellite Ellipse", β=40°, w/ Perturbations, 10K secs)

Obviously, this is a problem: formation integrity remains intact, but formation orientation completely breaks down. The likely reason for this behavior is that: even for full springs, as the programmed reels are allowed to change over time, so too do the MOI's; since the Likins-Pringle equilibria are fixed for given MOI values, then the orientation will change in the orbit frame as the MOI's are perturbed (hence the flip) – despite the fact that the springs are keeping the formation integrity intact. Since tethers are essentially half-springs and springs don't work, it is clear that this control method will also have the same (or worse) problems with tethers.

6.2.4 Circular Formation Case. There is a particular subclass of this control method worth considering that is associated with the Circular Formation. Recall from section 5.3.1 that the Circular Formation is the Likins-Pringle configuration where the cone angle is 60° and all three satellites map out a single circular path (shown again here in Figure 6.17)

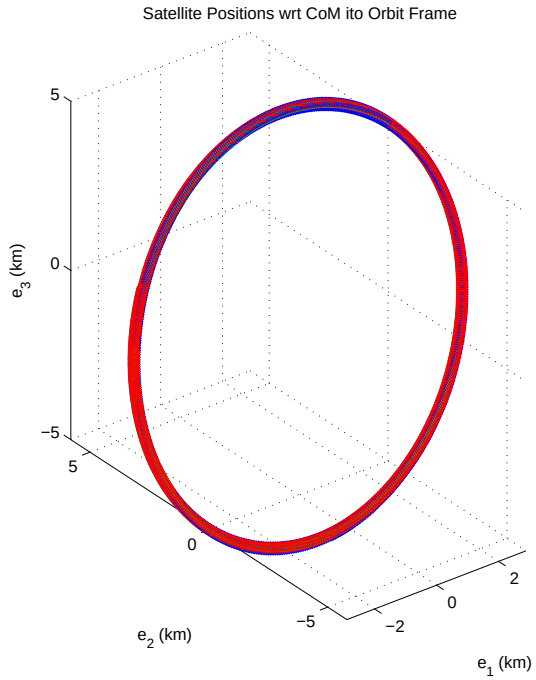


Figure 6.17: Body Positions Relative to System CoM (Orbit Frame, Free Flight, β=60° – Circular Formation, 10K secs)

When period matching (from Appendix C) is applied to this 60° case, a single circular path still emerges, and the tether lengths (ρ_{ij}) once again enter a repeating oscillation, but this time it is not sinusoidal. Instead the repeating oscillation takes on a unique shape as shown in Figure 6.18. These unique repeating patterns form the new program for our open-loop $\rho_o(t)$ controls on each tether/spring.

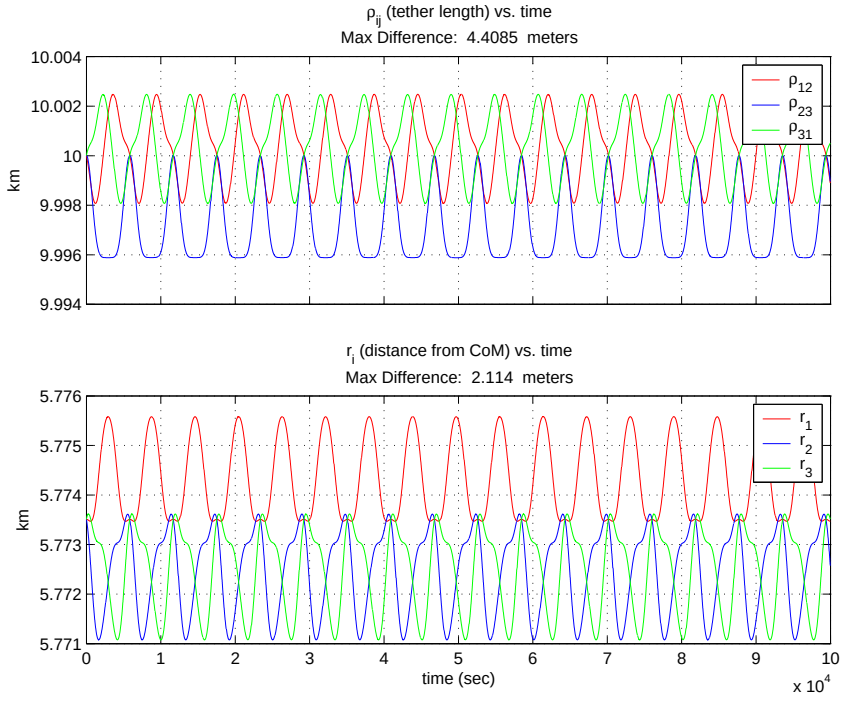


Figure 6.18: Tether Lengths and Radial Distance over Time (Free Flight, β=60° – Circular Formation)

As before, without perturbations, the response with programmed reels for the Circular Formation case (Figures 6.17 and 6.18) looks exactly like the 60° Free Flight results since there is nothing causing deviations from the Free Flight motion.

Next, with perturbations added (even with full springs), we get trouble similar to the previous 40° case: the springs restore themselves back to the natural repeating pattern (Figure 6.19), thus maintaining formation integrity, but orientation is lost as the formation begins to tumble after one orbit (Figure 6.20). Once again, since springs fail to maintain the desired equilibrium, tethers will not fare any better, therefore the investigation for this control method with tethers need not go any further.

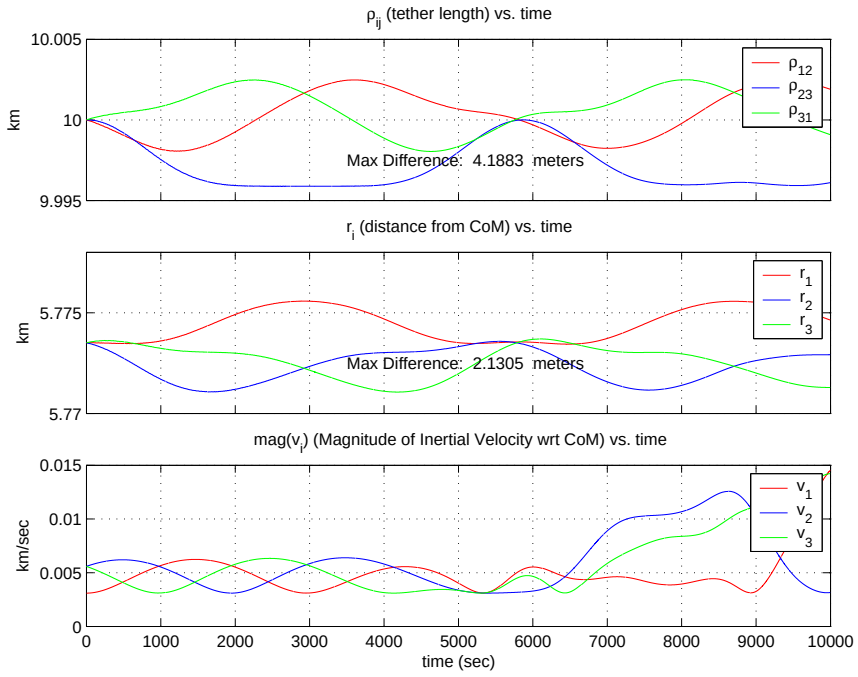


Figure 6.19: Tether Lengths, Radial Distance, and Velocity over Time (Full Springs, Programmed Reels – "Circular Formation", β=60°, w/ Perturbations)

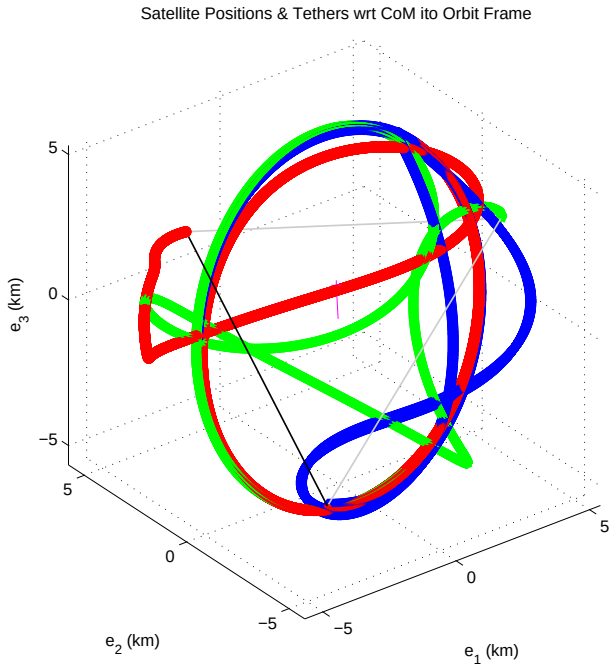


Figure 6.20: Body Positions Relative to System CoM (Orbit Frame, Full Springs, Programmed Reels – "Circular Formation", β=60°, w/ Perturbations, 10K secs)

6.3 Control Method 3: Thrust to Precess High Spin Rate

One can recall that the basic dynamic challenge for the desired equilibrium condition is a sort of "Catch-22" between spin rate and precession: the correct precession requires slow spin rates, which causes slacking/snapping; while high spin rates mean insufficient precession. Chapter V covered many strategies of leaving spin rates low and trying to deal with the tether slacking/snapping issues. Now we turn it around by spinning up the system and dealing with the lack of precession.

The approach of this next control scheme is to spin the system at a high enough rate such that formation integrity is no longer an issue, and now use thrusters to supply the additional torque required to keep the system in the desired orientation. Graphically speaking, with regard to the Spin Rate Plot from Chapter V, we are selecting a dynamic condition in one of the corner operating regions (Figure 6.21).

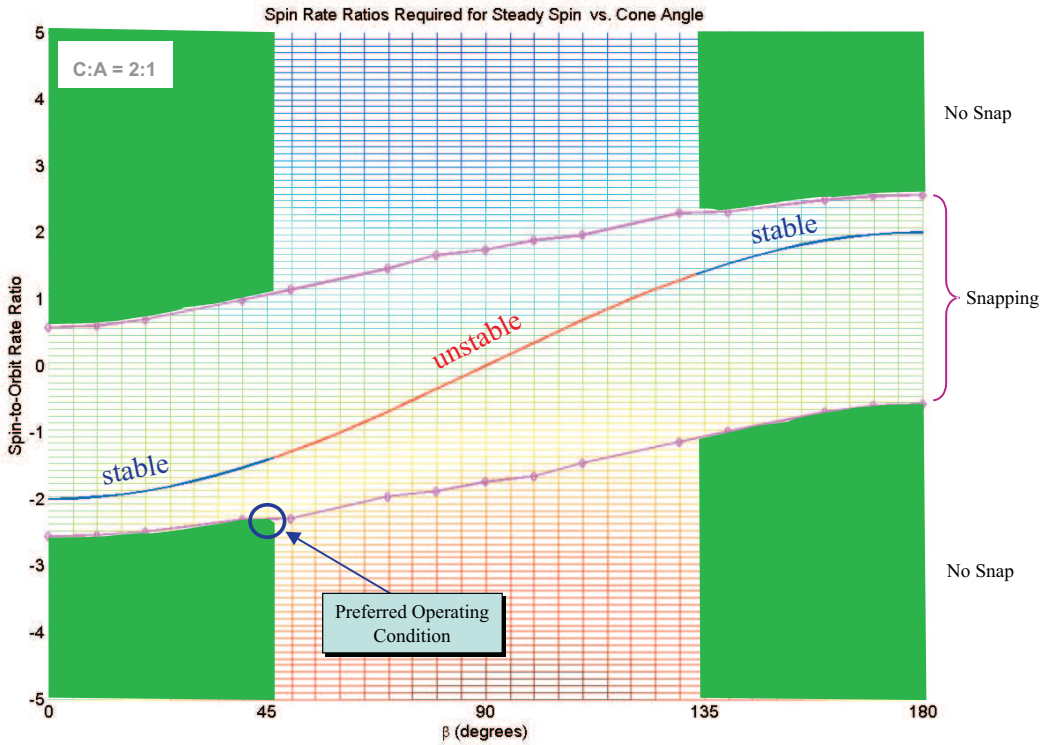


Figure 6.21: Spin Rate Plot with Possible Operating Regions

This means the system is not starting on an equilibrium condition, but conditions are chosen to get as close as possible to the stable L-P curve while maximizing cone angle and without entering the SR Range.

Given the complications of applying torques to a flexible system of multiple bodies, this concept is first applied to an equivalent rigid body to conservatively estimate the magnitude of the ΔV required.

6.3.1 Required Torques for a Rigid Body . To envision the torque required to precess a rigid body in the desired manner, consider the oblate disk in Figure 6.22. Notice that we momentarily return to our rigid body orbit frame ($\hat{e}_\nu$, $\hat{e}_r$, $\hat{e}_3$) as described in Chapter IV where $\hat{e}_r$ is always pointed opposite nadir and $\hat{e}_3$ is normal to the orbit plane. H_r and H_3 are the orbit frame components of the angular momentum, $\vec{H}$, due to the spin ($\dot{\psi}$). Generally, we are looking for the required torque defined in the orbit frame so that we can then rotate it into the body frame for ease of use in the rigid body MATLAB® code.

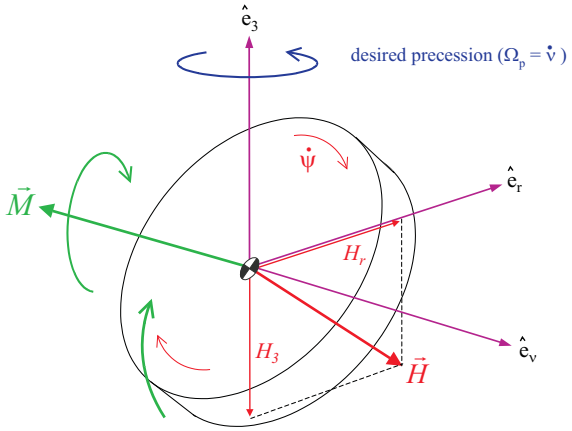


Figure 6.22: Desired Precession and Required Torque for an Oblate Rigid Body

The relation of precession (Ω_p) to the applied torque and angular momentum is given by [73]:

$$\vec{M} = \vec{\Omega}_p \times \vec{H} \tag{6.6}$$

The desired motion for this mission application is pure precession about the $\hat{e}_3$-axis at a rate equal to the orbit rate (shown in blue in Figure 6.22):

$$\vec{\Omega}_p = \dot{\nu}\hat{e}_3 \tag{6.7}$$

Therefore, from Equations 6.6 and 6.7 we get the required torque:

$$\vec{M}_{req} = \begin{vmatrix} \hat{e}_\nu & \hat{e}_r & \hat{e}_3 \\ 0 & 0 & \dot{\nu} \\ 0 & H_r & H_3 \end{vmatrix} = -\dot{\nu}H_r\hat{e}_\nu \tag{6.8}$$

The applied required torque ($\vec{M}_{req}$) must be entirely about the -$\hat{e}_\nu$-axis to get the desired precession. This agrees with the "common sense test" since we already know that gravity gradient forces create a torque entirely about the $\hat{e}_\nu$-axis and are responsible for the pure $\hat{e}_3$ precession in Likins-Pringle equilibria. The next step is to further define the required torque in $\hat{e}$-frame coordinates. That is, we need H_r to plug into Equation 6.8. Recall from the rigid body work that

$${}^b\vec{H} = {}^bI^b\vec{\omega}^{bi} = \begin{bmatrix} A & 0 & 0 \\ 0 & A & 0 \\ 0 & 0 & C \end{bmatrix} {}^b\vec{\omega}^{bi} \tag{6.9}$$

Also, from Equation 4.33, we get

$${}^b\vec{H} = \begin{bmatrix} A & 0 & 0 \\ 0 & A & 0 \\ 0 & 0 & C \end{bmatrix} \begin{bmatrix} \sin\psi\sin\theta & \cos\psi & 0 \\ \cos\psi\sin\theta & -\sin\psi & 0 \\ \cos\theta & 0 & 1 \end{bmatrix} \begin{Bmatrix} \dot{\phi} \\ \dot{\theta} \\ \dot{\psi} \end{Bmatrix} \tag{6.10}$$

and our desired motion is that $\dot{\phi} = \dot{\nu}$ and $\dot{\theta} = 0$. Therefore,

$$
{}^{b}\vec{H} = \begin{bmatrix} A\sin\theta\sin\psi\dot{\nu} \\ A\sin\theta\cos\psi\dot{\nu} \\ C\dot{\psi} + C\cos\theta\dot{\nu} \end{bmatrix} \tag{6.11}
$$

By rotating from the $\hat{b}$-frame to the $\hat{e}$-frame, we get the angular momentum and subsequently the required torque (from Equation 6.8), expressed in the $\hat{e}$-frame:

$$
{}^{e}\vec{H} = C^{ebb}\vec{H} = \begin{bmatrix} \cos\psi & -\sin\psi & 0 \\ \cos\theta\sin\psi & \cos\psi\cos\theta & -\sin\theta \\ \sin\psi\sin\theta & \cos\psi\sin\theta & \cos\theta \end{bmatrix} \begin{bmatrix} A\sin\theta\sin\psi\dot{\nu} \\ A\sin\theta\cos\psi\dot{\nu} \\ C\dot{\psi} + C\cos\theta\dot{\nu} \end{bmatrix} = \begin{bmatrix} H_\nu \\ H_r \\ H_3 \end{bmatrix} \tag{6.12}
$$

$$
{}^{e}\vec{M}_{req} = \begin{bmatrix} -\dot{\nu}H_r \\ 0 \\ 0 \end{bmatrix} = \begin{bmatrix} -\dot{\nu}\left\{-\sin\theta\left(C\dot{\psi} + C\cos\theta\dot{\nu}\right) + A\cos\theta\sin\theta\dot{\nu}\right\} \\ 0 \\ 0 \end{bmatrix} \tag{6.13}
$$

6.3.2 Rigid Body Model Modifications. The original rigid body model requires the torques to be expressed in the body frame, therefore

$$
{}^{b}\vec{M}_{req} = C^{bee}\vec{M}_{req} = \begin{bmatrix} -\cos\psi\dot{\nu}\left\{-\sin\theta\left(C\dot{\psi} + C\cos\theta\dot{\nu}\right) + A\cos\theta\sin\theta\dot{\nu}\right\} \\ \sin\psi\dot{\nu}\left\{-\sin\theta\left(C\dot{\psi} + C\cos\theta\dot{\nu}\right) + A\cos\theta\sin\theta\dot{\nu}\right\} \\ 0 \end{bmatrix} \tag{6.14}
$$

where C^{be} is the inverse of C^{eb} above. If Equation 6.14 is now used to replace the original gravity gradient torque Equation 4.32 in the rigid body model's EOM, we now have a rigid body model that generates the external torque required to precess the

disk at exactly the orbit rate. This calculation of required torque is independent of the calculation of the torque created by gravity gradient. Sometimes these two values will be equal (i.e. Likins-Pringle equilibria), while most times there is a difference (i.e. the rest of the Spin Rate Plot that is not on the L-P curve).

To validate that the "required torque" is calculated properly, a number of simulations are run to determine if the desired equilibrium is achieved regardless of spin rate, cone angle, and mass properties. An example of these validation runs is shown in Figures 6.23 and 6.24 for a disk spinning at four times faster than the orbit rate (SR=-4.0), a cone angle of 45°, and the moments of inertia from arbitrarily chosen to be A =25 and C =50. Clearly, the desired equilibrium motion is achieved: the disk's spin axis precesses inertially (Figure 6.23), but does so such that it never moves in the orbit frame (Figure 6.24). This response is seen in all cases and validates that Equation 6.14 is accurate.

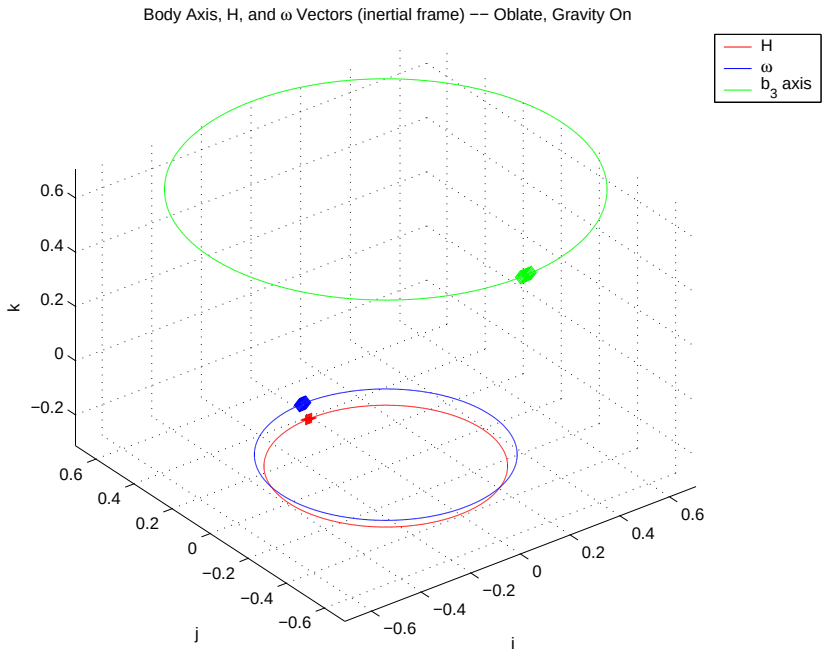


Figure 6.23: $\vec{H}$, $\vec{\omega}$, and the $\hat{b_3}$-axis in the inertial frame (Oblate Rigid Body, Calculated Torques Required for Precession)

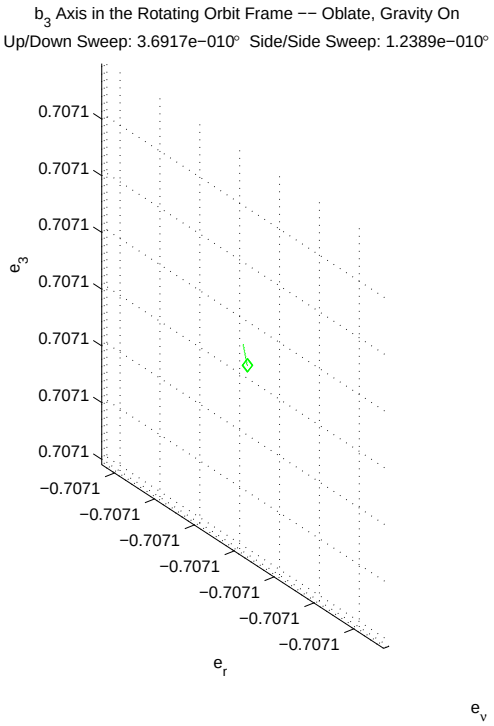


Figure 6.24: $\hat{b_3}$-axis in the Rotating Orbit Frame (Oblate Rigid Body, Calculated Torques, 3-Orbit)

6.3.3 Determining ΔV Required. As mentioned above, unless the dynamic conditions put us directly on the Likins-Pringle curve, there will be a difference between the torque required to "perfectly" precess and the torque provided by gravity gradient forces. This difference in torques, represented by a vertical differential on the notional 3-D plot in Figure 5.78, is what must be provided by the thrusters in this control scheme: $\vec{M}_{thrusters} = \vec{M}_{req}$ - $\vec{M}_{gg}$.

To get the ΔV associated with a given torque, we assume the thruster force is applied continuously at the periphery of the disk of radius r_{disk} and mass m_{disk}

$$\vec{F}_{thrusters} = \frac{\vec{M}_{thrusters}}{r_{disk}} = m_{disk}\Delta a = m_{disk}\frac{\Delta V}{\Delta t} \tag{6.15}$$

where Δt is the step size of the model simulation. Re-arranging, we calculate the ΔV from a given torque over a single time step as:

$$\Delta V = \frac{\vec{M}_{thrusters}\Delta t}{r_{disk}m_{disk}} \tag{6.16}$$

For example, if we simulate a 600 kg disk with a 5.7 km radius orbiting at a circular altitude of 1.1 DU, a spin rate ratio of -2.6, and a cone angle of 40°, we can generate the torques (and equivalent ΔV's) required for perfect precession and the torques (and equivalent ΔV's) generated by gravity gradient as shown in Table 6.3. The ΔV that would be required from thrusters is the difference and is shown in the last column of the table.

Table 6.3: Example Torques and ΔV's (SR=-2.6, θ=40°, r_{disk}=5.7km, m_{disk}=600kg, Δt=10s, Alt=1.1 DU).

	Total Required	Provided by Gravity Gradient	Required by Thruster
Torque (kg-m^2/s^2)	32895.41	17049.79	
ΔV (m/s)	0.095	0.0049	
ΔV over 10K secs (m/s)	949.53	492.14	457.38

By comparison, if we look at the same disk inclined all the way up to a cone angle of 90°, we get the ΔV values shown in Table 6.4. Note that the total torque required is much higher for the 90° cone angle (as expected) and that gravity gradient forces contribute nothing, therefore the thrusters must do it all.

Table 6.4: Example Torques and ΔV's (SR=-2.6, θ=90°, r_{disk}=5.7km, m_{disk}=600kg, Δt=10s, Alt=1.1 DU).

	Total Required	Provided by Gravity Gradient	Required by Thruster
Torque (kg-m^2/s^2)	60017.78	2.79e-4	
ΔV (m/s)	0.173	8.07e-13	
ΔV over 10K secs (m/s)	1732.42	8.07e-9	1732.42

6.3.4 Rigid Body Results as a Multi-Body System Estimate. Remember that the whole reason for doing this rigid body work is to conservatively estimate the magnitude of the thrust required on a multi-body system. Therefore, we need to select rigid body mass properties that emulate the multi-body system. Using the tether length of 10 km, the formation radius is calculated at 5.774 km. In addition, each satellite body is also assumed to have a mass of 200 kg. With these simple values, the axial and transverse moments of inertia are calculated for the multi-body system using equations from Chapter V. These MOI's are readily transferable to the rigid body model.

$$C_{sys} = 3m\,(r)^2 = 20,000kg \cdot km^2 \tag{6.17}$$

$$A_{sys} = m\,(r_{ss})^2 \left(\frac{3}{2}\right) = 10,000kg \cdot km^2 \tag{6.18}$$

Now referring back to our preferred operating condition for this control scheme (identified on the Spin Rate Plot in Figure 6.21), we choose conditions that are as close as possible to the stable L-P curve while maximizing cone angle and without entering the SR Range. Specifically, a spin rate ratio of -2.4 and a cone angle of 45° are used. These conditions are applied to the rigid body model and the simulation is run for an altitude of 1.1 DU. The results are presented in Table 6.5.

Table 6.5: Rigid Body Simulating System – Torques and ΔV's Required for "Perfect" Precession (SR=-2.4, θ=45°, r_{disk}=5.774km, m_{disk}=600kg, Δt=10s, Alt=1.1 DU).

	Total Required	Provided by Gravity Gradient	Required by Thruster
Torque (kg-m^2/s^2)	33403.50	17312.82	
ΔV (m/s)	0.096	0.049	
ΔV over 10K secs (m/s)	964.19	499.74	464.46

It is already apparent that we have a problem here. A ΔV of 464.46 m/s that is required to torque a rigid disk after only 10K seconds (and without the presence of perturbations) far exceeds the *yearly* ΔV budgets of most satellites [73]. If we consider a conservatively high (geosynchronous) orbit altitude, the ΔV cost after 10K seconds is reduced to 2.15 m/s (Table 6.6), but as will be discussed in the next Chapter, this cost is still an order of magnitude greater than thruster-only free-flyer budgets.

Table 6.6: Rigid Body Simulating System – Torques and ΔV's Required for "Perfect" Precession (SR=-2.4, θ=45°, r_{disk}=5.774km, m_{disk}=600kg, Δt=10s, Alt=6.6 DU).

	Total Required	Provided by Gravity Gradient	Required by Thruster
Torque (kg-m^2/s^2)	154.65	80.152	
ΔV (m/s)	4.46e-4	2.31e-4	
ΔV over 10K secs (m/s)	4.46	2.31	2.15

Furthermore, these ΔV budget assumes a rigid body with continuous thrust/-torque capability. In actuality, an equivalent multi-body system would not only be flexible and encounter perturbations, but the thrust could also not be applied continuously. Assuming the thrusters are located on the satellite bodies, a tethered system would have to wait to fire (or "pulse") its thrusters until each body is aligned normal to the $\hat{e}_\nu$-axis to ensure the torque is purely about the $\hat{e}_\nu$-axis. Both of these additional complications would translate into even more required thrust, therefore further investigation into this control concept is unnecessary... it might work for the system, but it will clearly be too costly since the simplified rigid body approximation is definitely too costly.

6.4 Control Method 4: Constant Tension Reels

The final control scheme considered for this system is another variable-length tether concept. This time, however, each individual tether's unstretched length (ρ_o) is modified to maintain a relatively constant positive tension throughout the simulation. Since each tether experiences varying dynamics effects due to the changing aspect of the gravity gradient forces on the original spinning formation, this control concept allows for each tether to individually respond to undesirable tension levels and hopefully keep all tethers taut at all times. The desired positive tension level is maintained by reeling-in or paying-out tether, based on current tension levels at each step in the simulation. By keeping the tethers in positive tension, slacking should be eliminated.

The nearest equilibrium condition to our desired motion is once again the natural, free-flying, strobo-planar, repeating ellipsoidal motion of each individual satellite that starts in the Likins-Pringle conditions. This is therefore the equilibrium condition about which this control method (variable length tethers) will be applied.

6.4.1 Model Modifications. The original 3-body model used a single, fixed value for the unstretched tether length (ρ_o) for all three tethers. In this model, each tether will have its own unstretched tether length (ρ_{io}) that varies over the course of the simulation. The process for determining those variations in ρ_{io} is shown in the pseudocode in Figure 6.25. The basic idea here is that when a tether is slack, reel it in, and when the tether is in too much tension, reel it out. The spring-damper from the original model is still used whenever the tether is in tension.

Another way to look at this is in Figure 6.26 which shows the control response based on current tether length relative to the current unstretched tether length. Notice that there is a dead-band based on the size of the tension threshold that is set.

The pseudocode in Figure 6.25 is applied to the equations of motion at each integration step for each of the three tethers. Appropriate modifications are made in the MATLAB® model and initial values are chosen for reel rates and tension threshold.

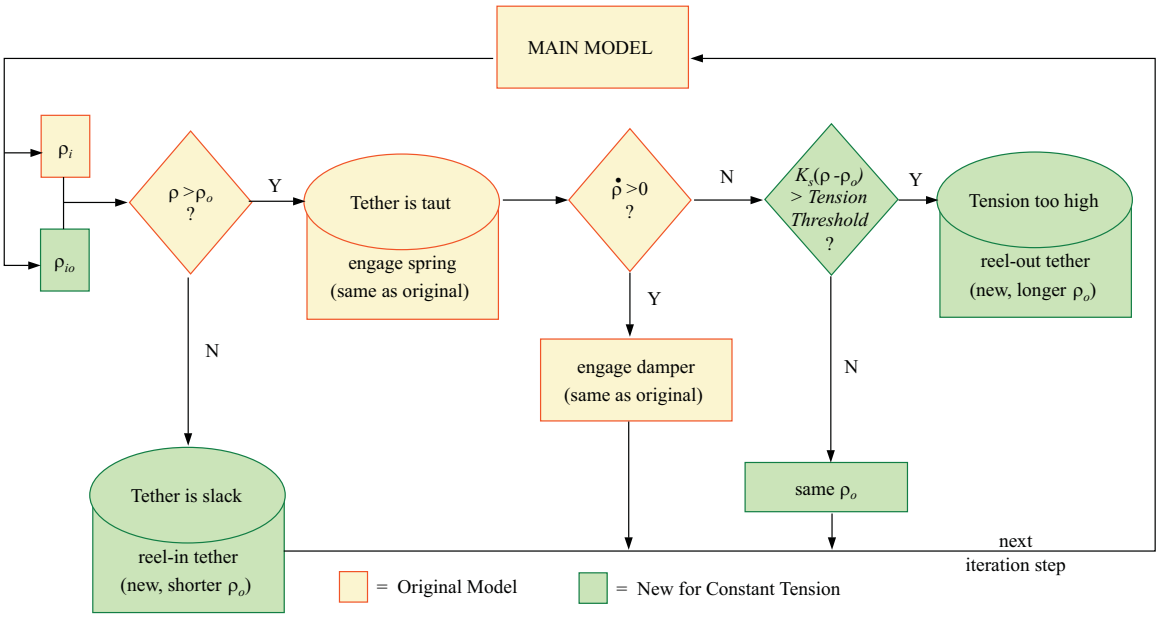


Figure 6.25: Constant Tension Pseudocode

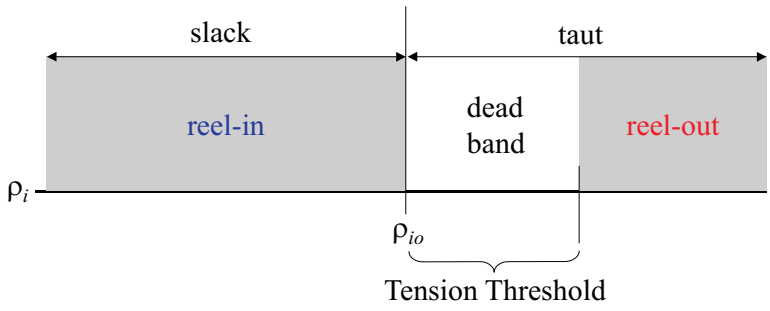


Figure 6.26: Tension Control Response

6.4.2 Initial Constant Tension Results. For the initial case, the tension threshold (T_{thd}) is chosen to be 0.2 which equates to a 10 m displacement from the current ρ_{io}. This value is large enough to encapsulate the "breathing" oscillations seen in the original simulations of Chapter V. The initial reel rates (rr_{in} and rr_{out}) are chosen to be 1 m/s with a simulation step size of 1 second. All other parameters are the same as the baseline Likins-Pringle case (β=40°). The response for this initial case is shown in Figures 6.27 and 6.28.

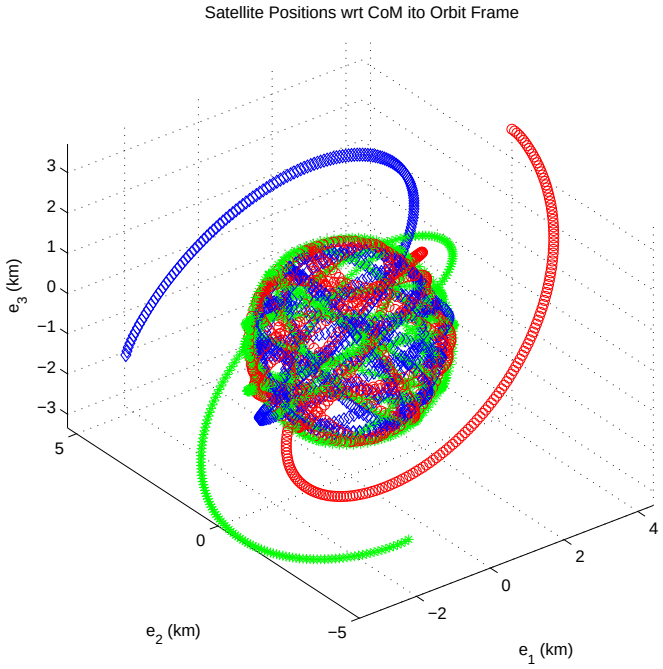


Figure 6.27: Body Positions Relative to System CoM (Orbit Frame, Constant Tension Tethers, L-P, β=40°, $rr = 1$, $T_{thd} = 0.2$, Δt=1, 10K secs)

We know from before that the spin rate for β=40° is insufficient to keep all three tethers in positive tension, so it is no surprise that the tethers tend to reel in initially. Notice however, that within 1/2 of an orbit, all three tethers are reeled in until they find a stabilized length around 3.5-3.9 km, essentially shrinking the formation. Unfortunately, because of conservation of specific angular momentum, this shrinking of the formation causes the spin rate to increase proportionally, which in turn makes the formation precess at a higher rate than was originally intended.

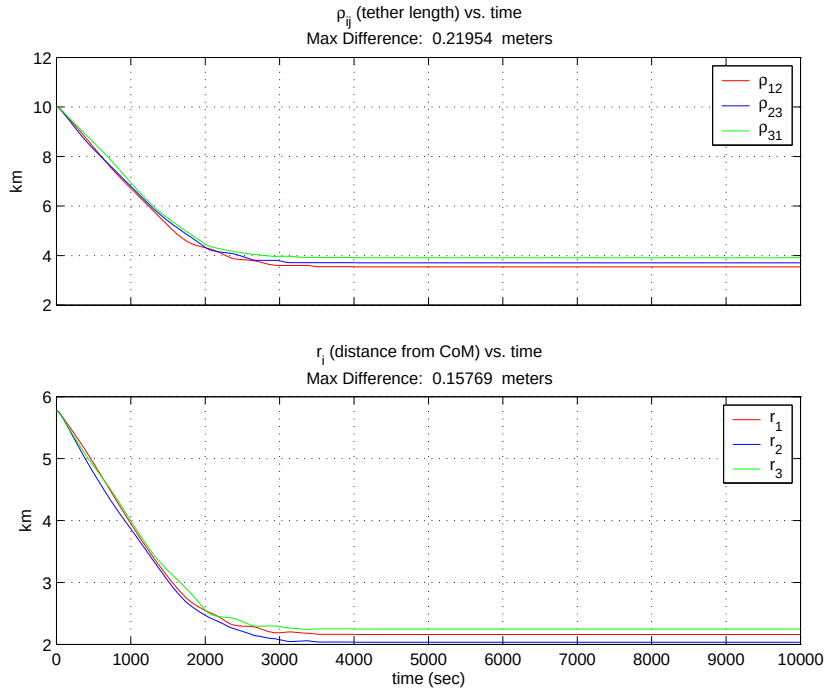


Figure 6.28: Tether Lengths and Radial Distance over Time (Constant Tension Tethers, L-P, β=40°, $rr = 1$, $T_{thd} = 0.2$, Δt=1)

The high precession of this smaller formation is evident as the "ball" at the center of Figure 6.27 which is in the orbit frame. The magenta circle in the center of the ball is the tip of the spin axis of the formation as it precesses around. Obviously, this is not maintaining the desired equilibrium condition which would have a stationary spin axis in the orbit frame.

Some quick hand calculations based on conservation of the specific angular momentum

$$\rho^2 \left(\frac{\dot{\psi}}{\dot{\nu}} \right) \Bigg|_{orig} = \rho^2 \left(\frac{\dot{\psi}}{\dot{\nu}} \right) \Bigg|_{new} \tag{6.19}$$

reveal that the new spin rate ratio for this shrunken formation is SR=-11.19, which is clearly outside the SR Range for β=40° shown on the Spin Rate Plot (see Figure 6.21 again), so it not a surprise that the tethers stabilize themselves at the lengths shown in Figure 6.28.

6.4.3 Changing the Constant Tension Parameters. A number of additional simulations are conducted with variations in the tension threshold, reel rates, and integration step size. Overall, the response is similar to initial constant tension case, but some of the examples are briefly discussed here.

When the simulation step size is shortened, the tethers stabilize more quickly at shorter lengths (Figure 6.29) but the overall result is basically the same (Figure 6.30). This small change in the rate of shortening (and the different stabilizing length) is expected since a different time step creates new delays in decision times and essentially makes a slightly different model.

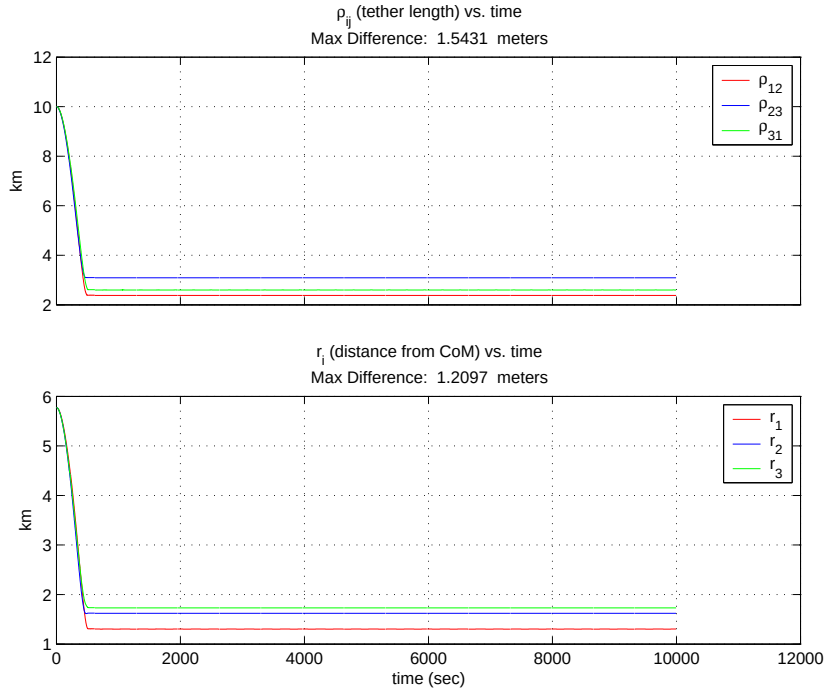


Figure 6.29: Tether Lengths and Radial Distance over Time (Constant Tension Tethers, L-P, β=40°, $rr = 1$, $T_{thd} = 0.2$, Δt=0.1)

Decreasing the reel rates too much causes the system to behave more like the original, uncontrolled, baseline Likins-Pringle case. The slacking and snapping interaction return because the reels are acting too slowly to make a real difference.

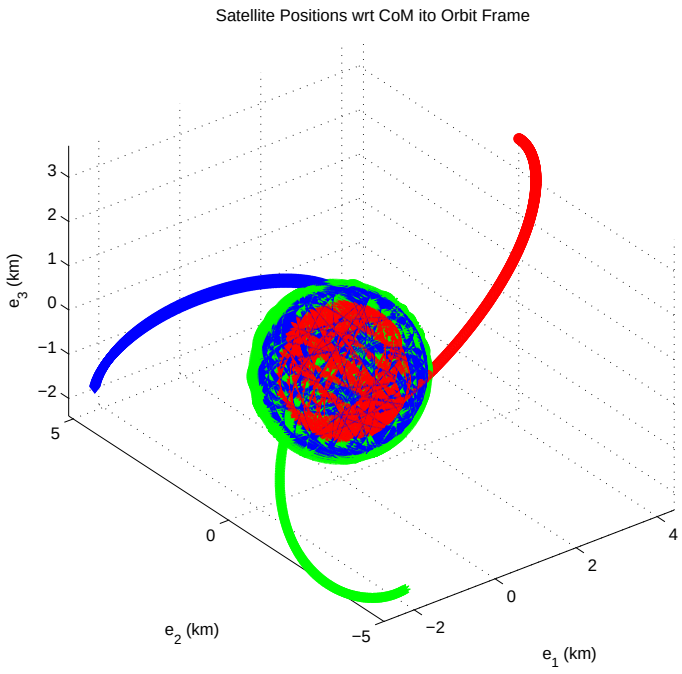


Figure 6.30: Body Positions Relative to System CoM (Orbit Frame, Constant Tension Tethers, L-P, β=40°, $rr = 1$, $T_{thd} = 0.2$, Δt=0.1, 10K secs)

Increasing the rr_{out} speed doesn't have much impact on the response since our scenario generates more slack time than taut time. Increasing the rr_{in} speed obviously makes the tethers stabilize even more quickly at even shorter lengths.

Increasing the tension threshold simply increases the dead-band, which essentially nullifies its purpose. Decreasing the tension threshold by an order of magnitude has only a small effect (slightly slower to stabilize at slightly shorter lengths), but decreasing the deadband by too much causes the formation to break down.

6.4.4 Bottom Line. Overall, the response using constant tension reels is insensitive to the values for tension threshold, reel rates, and time step: the formation collapses until a high enough spin rate is achieved to keep tethers taut, but the higher spin rate creates too high of a precession to be useful for our application. This undesirable response is observed even without perturbations added, therefore, there is no need to investigate perturbation effects with this control method.

6.5 Summary

This chapter covered the development and results of four different control schemes that were applied to the 3-body tethered system.

Control Method 1 (*Thrust to Mimic Spring Compression*) used thrusters to compliment tethers such that the combination would form a full, massless spring. Even under the effects of J_2 perturbations, this method held the desired equilibrium condition very well. In most scenarios, the nominal thruster budget was approximately 135 m/s or higher over a 10,000 second simulation. However, when "optimal" formation parameters were used (section 5.5.5), the total ΔV after 100K seconds was 6.14 m/s.

Control Method 2 (*Programmed Reels*) used variable-length tethers where tether reels were pre-programmed to follow a repeating pattern based on the natural motion of the individual satellites. Two Likins-Pringle-based patterns were explored under the effects of J_2 perturbations: the "Single Satellite Ellipse" pattern and the Circular Formation pattern. Regardless of the pattern, and even when replacing the tethers with variable-length springs, this control method did not work. Formation integrity was maintained satisfactorily, but the desired orientation of the formation was lost after one orbit.

Control Method 3 (*Thrust to Precess High Spin Rate*) allowed the system to have a high enough spin rate to ensure formation integrity was maintained, and used thrusters to supply the additional torque required to keep the system precessing at the desired rate (that is, maintain desired orientation). This concept was first applied to an equivalent rigid body to conservatively estimate the magnitude of the ΔV required. After only 10K seconds of continuous thrust, 85 m/s of ΔV was required to torque an equivalent rigid body without the presence of perturbations. Since the rigid body result was too costly and the system would not be able to improve on that value, the investigation of this control method for the system was terminated.

Control Method 4 (*Constant Tension Reels*) used variable-length tethers where each individual tether was allowed to reel-in or pay-out in order to maintain positive tension and eliminate slacking. Regardless of the tension threshold or reel rates selected, the result was basically the same even without perturbations: the formation collapsed to generate a high enough spin rate to keep the tethers taut, but at the cost of a precession rate that was too high for the desired application.

Overall, of the 4 control methods applied, two did not work due to formation orientation issues and two may work well enough, but with a high cost in ΔV. The evaluation of those costs is part of an overall assessment of the utility of tethered systems for this mission application, which is the subject of the next chapter.

VII. Assessing Utility

In this final task, we take all of the results from the previous chapters and discuss the utility of multi-body tethered systems for the purpose of space-based remote sensing. Particularly, we are addressing the fifth, final, and broadest objective of this work: *Assess the relative utility of using tethered systems for formation control on continuous earth-facing aperture clusters.*

7.1 Assumptions and Foundational Rigid Body Motion

In making this assessment, a couple assumptions are key. First, we assume that the portion of the satellite cluster that forms the virtual aperture is distributed in a "ring" or circular formation to most closely simulate a single large aperture, and therefore create the best observation plane for the mission. While it is understood that simpler formations such as a two-body dumbbell configuration could be used, they are less dynamically challenging and do not produce a true aperture shape, which is assumed to be desired. Second, given the mission of space-based remote sensing, it is further assumed that the aperture should continuously face the earth. Given these assumptions, the foundational rigid body motion that satisfies our criteria is the conical Likins-Pringle equilibria.

Knowing that we want to build upon stable rigid body motion for the desired system motion, and understanding that elastic tethered systems are by no means rigid bodies, we make preliminary assessments of system performance by first evaluating the behavior of semi-rigid bodies in the presence of energy dissipation.

From the results of Chapter IV, we know that energy dissipation has an adverse effect on semi-rigid bodies (and hence elastic tethered systems) that originate in a Likins-Pringle equilibrium. Specifically, given the studied energy dissipation effects, a prolate Likins-Pringle body fails to achieve long-term stable behavior, therefore so too would a prolate Likins-Pringle *formation* fail to achieve long-term stable behavior. Meanwhile, there is hope for the oblate case. In the long-term, an oblate Likins-Pringle body settles into a near-"limit cycle": simple circularized behavior that remains earth-

facing, and nearly repeats itself in the orbit frame. The size of this circularized behavior is about 4° in pitch (or "nodding") and only about 2° in yaw. While this isn't the perfect equilibrium condition, it is close enough to warrant further exploration of oblate (only) formations of tethered satellites.

7.2 Tethered-Only System Dynamics

The most direct way for this tethered system to demonstrate its utility for the space-based remote sensing mission would be to have a natural equilibrium condition such that the aperture's spin axis is fixed in the rotating orbit frame. Given the exhaustive work detailed in Chapter's V and VI, we can say with reasonable certainty that *the desired equilibrium condition is not maintainable for fixed-length (without control) or variable-length (controlled) tethered systems.*

The problem boils down to a constant battle between spin rate (which affects formation integrity) and precession rate (which affects formation orientation). Continuously earth-facing apertures require a spin rate that is too slow to maintain positive tether tension. Tether slacking and the snapping interaction between tethers cause the formation to lose its integrity and subsequently its orientation, and there is no apparent method to solve the slacking/snapping problem without increasing the spin rate. Conversely, tethered systems with higher spin rates keep the tethers taut and maintain the formation, but do not continuously face the earth because they precess at too high a rate.

7.3 Thruster Assistance

Since tethers by themselves cannot control the formation in the desired manner, consideration is given to tethers and thrusters acting in concert with the hope that the ΔV cost would be lower than thrusters doing formation control alone.

7.3.1 Thrust for Spring Compression. Using the control method where thrusters and tethers create the combined effect of a massless spring, the desired

equilibrium condition is maintained, but the total ΔV budget of the thrusters over 10K seconds is typically 135 m/s or more. Even in the case where the tether and formation parameters are "optimized" to create the closest motion to the desired equilibrium, the total ΔV budget is 6.14 m/s in 100K seconds. Forecasting this value out over a year, the total ΔV cost is approximately 1935 m/s.

To get a comparable number for thrusters-only, we look at Sabol et al. [54], who estimates the ΔV required for a free flying formation using thrusters alone to perform both stationkeeping and formation maintenance. Sabol estimates the cost per satellite for a circular formation with a 1 km radius to be 50.4 m/s/yr. This 50.4 m/s/yr breaks out in the following manner:

Table 7.1: Free Flying ΔV Requirements for a Circular Formation [54].

Maneuver	ΔV, m/s/yr
Nodal Spacing (formation keeping)	38 (per km of separation)
Perigee Maintenance (formation keeping)	10.9
Drag make-up (station keeping)	1.5
Total	50.4

Based on these results, for a formation comparable to ours, the 38 m/s/yr gets multiplied by 5.774 km (the average radius of our aperture), yielding a per satellite nodal spacing cost of 219.4 m/s/yr, and a total ΔV cost of 231.8 m/s/yr per satellite. Since our formation has three satellites, we triple the last value to get the total yearly ΔV required for a free flying formation that uses thrusters alone: 695.4 m/s.

Clearly, the tether/thruster combination costs almost three times what is required for thrusters alone! It is also important to appreciate that our "tethers/thrusters-as-springs" numbers are conservatively low while the thruster-only calculations are conservatively high. In actuality, the "springs" would not compress in a straight line since they would have mass and would therefore generate more complex requirements from the thrusters. Our model also only included J_2 perturbations while Sabol included earth oblateness, atmospheric drag, and tesseral resonance. The calculations

based on Sabol are also conservatively high because the assumed 10 km aperture is not absolutely necessary.

7.3.2 Thrust to Precess High Spin Rate. The other control method using a thruster/tether combination allowed the system to spin at a high enough rate such that formation integrity is automatically maintained with the tethers while thrusters supply the additional torque (normal to the aperture plane) required to keep the system in the desired orientation.

The estimate of the ΔV magnitude (based on that required to torque a rigid body disk at 1.1 DU altitude) is 464.46 m/s after only 10K seconds. This number translates into 268,056 m/s over a year and is without considering perturbations. As before, this number also far exceeds the comparable costs for the thrusters alone. Even for the geosynchronous case, the total ΔV is 6780 m/s/yr, which is an order of magnitude higher than the thruster-alone costs.

7.3.3 Bottom Line. Using thrusters to assist a tethered system to maintain the desired equilibrium can clearly work, however the cost in ΔV is simply too high when compared to the stationkeeping/formationkeeping costs associated with a free-flying, thruster-only formation.

7.4 Breathing Effects

Recall that even with full, massless springs replacing the tethers, we see low-amplitude (6 cm), 120°-phased, "breathing" oscillations in the aperture that are created by the changing aspect of the gravity gradient forces on the spinning formation. Since the mission application is space-based remote sensing, we briefly consider the impact of this "breathing" on the optics.

The importance of relative positions of the individual receivers to optical interferometry comes from the need for temporal coherence in the received signals. Normally, optical systems maintain this coherence by equalizing the optical pathlengths

between the individual receivers and some correlator. This requires the capability to first accurately *measure* the optical pathways, and then *equalize (control)* them to the order of $\frac{\lambda_o^2}{\Delta\lambda}$, where λ_o is the mean design wavelength and $\Delta\lambda$ is the passband for the system [46].

Therefore, the impact of the "breathing" oscillations would be more dependent on the ability to rapidly measure and control the optical pathways, than it would be on the size or nature of the physical oscillations. Since the study of measuring or controlling the optical pathways is beyond the scope of this research, it is assumed for this assessment that the appropriate capabilities exist, and that the breathing oscillations will not impact the utility, but must be corrected for.

7.5 Overall Assessment

An overall look at the utility of tethered systems is broken out across the indicator areas that were studied for this research and summarized in Figure 7.1. Red indicates undesirable utility, green means highly useful and yellow represents a marginal utility (notice there are no green regions).

	Continuously Earth-Facing Aperture	
	Oblate Structure	Prolate Structure
Rigid Body w/ Energy Dissipation	Very close to Limit Cycle	No stable, long-term behavior
Natural System Dynamics	No Equilibrium Condition (formation integrity vs orientation)	No Equilibrium Condition (no stable, long-term behavior)
System w/ Controls	Doesn't work or cost prohibitive	Presumed costs even higher than oblate given rigid body results

Figure 7.1: Utility Assessment Indicator Areas

Given the results of this research, a couple of general statements can now be made:

- *Tethers have great value for formation control on general aperture clusters as long as there are no restrictions on spin rate.* If we suspend the need to be continuously earth facing, the entire chart above would turn green. In fact, there-in lies an idea for future study, but this will be discussed in the last chapter. Unfortunately, one of our initial assumptions for this research is the requirement for the system to be *continuously* earth-facing, which bring us to the next statement.
- *Tethers, by themselves, cannot conduct formation control for* continuously *earth-facing aperture clusters.* No equilibrium condition, no compression capability, and insufficient spin rate means no utility for this mission without help from other control methods.
- *Even with additional controls (thrusters), tethers add little value for continuously earth-facing apertures.* Tether/thruster combinations on oblate systems are too costly compared to the free-flying, thruster-only formation, and the rigid body basis for prolate systems is more erratic than the oblate. One could still investigate the use of controls on prolate systems by skipping right from the rigid body work directly to controls, but we are reasonably certain there would be no equilibrium condition found for prolate systems.

This chapter presented the final phase of this research and discussed the last of five research objectives. A review of all research objectives is conducted in the next chapter along with recommendations and a review of the contributions.

VIII. Conclusions

This study examined the utility of tethered systems for the purpose of space-based remote sensing. A summary of the work that was conducted is presented below through a review of the research objectives, a discussion of recommendations for future research, and a highlight of the contributions to science from this work.

8.1 Review of Research Objectives

Objective 1: *Determine the effects of energy dissipation on semi-rigid bodies that are in/near Likins-Pringle dynamic equilibria.*

Foundational semi-rigid body dynamics based on conical Likins-Pringle equilibria were investigated and the effects of energy dissipation were found to be adverse for both oblate and prolate structures. The adverse effects have long-term implications for the prolate case since it fails to achieve long-term stable behavior. On the other hand, the destabilizing effect of energy dissipation on the oblate structure is more short-lived. In the long-term, an oblate semi-rigid body in a Likins-Pringle configuration settles into a near-"limit cycle" with simple circularized behavior that remains earth-facing, and nearly repeats itself in the orbit frame (see the next objective).

Objective 2: *Define and/or determine the existence of an equilibrium condition for a semi-rigid body with a continuous earth-facing component in the presence of energy dissipation.*

We defined a "perfect" equilibrium condition as a dynamic state where the nadir projection of the aperture remains unchanged with respect to the rotating orbit frame – that is, the spin axis would be completely fixed in the orbit frame. By this definition, no equilibrium condition was found. If we relax our constraint about a perfect equilibrium and accept (as an equilibrium condition) behavior that is somewhat fixed in the orbit frame with oscillations that are small, periodic, and simple, then we can consider the long term oblate L-P response to be an acceptable near-equilibrium condition for an oblate semi-rigid body.

Objective 3: *Define and/or determine the existence of an equilibrium condition for a flexible tethered satellite system with a continuous earth-facing component.*

After an exhaustive examination of tethered system dynamics, it is shown that an equilibrium condition for elastic, fixed-length, tethered formations does not exist. This argument also extrapolates to flexible systems (i.e. tethers with mass). Continuously earth-facing apertures require a spin rate that is too slow to maintain positive tether tension. Lack of tension causes the formation to destabilize, and there is no apparent method for correcting this without increasing the spin rate. Conversely, tethered systems with higher spin rates keep the tethers taut and maintain the formation, but do not continuously face the earth because they precess at too high a rate. Interestingly, it was discovered that equilibrium conditions *are* found when conical Likins-Pringle conditions are applied to a free-flying formation (without tethers). As it turns out, these are the same equilibrium conditions that are approximated by the well-known C-W linearization solutions.

Objective 4: *Apply control schemes to the tethered system to combat perturbations and maintain desired motion.*

Four different control methods were applied to tethered system: two involved simulating variable-length tether reels and two simulated the addition of thrusters. The desired equilibrium condition was not maintainable using the variable-length tethers, as the formation orientation would break down. When thrusters were used to emulate spring compression, the desired equilibrium condition was maintained, but the ΔV costs were prohibitive – conservatively estimated to be 3 times more than using thrusters alone on a free-flying formation. Likewise, if the thrusters were used to provide external torques to a high spin rate system, the ΔV was estimated to be another order of magnitude higher than the thruster-only free-flyer.

Objective 5: *Assess the relative utility of using tethered systems for formation control on continuous earth-facing aperture clusters.*

Tethers have great value for formation control on general aperture clusters as long as there are no restrictions on spin rate. Tethers, by themselves, cannot conduct formation control for *continuously* earth-facing aperture clusters. Even with additional controls, tethers add little value for continuously earth-facing apertures. Tether/thruster combinations on oblate systems are too costly compared to the free-flying, thruster-only formation, and the rigid body basis for prolate systems is more erratic than the oblate, so there is little hope that the control costs would improve.

8.2 Recommendations for Future Research

It was shown that the prolate semi-rigid bodies suffered more from the effects of energy dissipation than the oblate structures. As a result, the focus of the tethered systems portion of this research became the oblate structures. While an equilibrium condition for a prolate formation is not going to be found (based on oblate results), it might be useful to skip directly to a control application on a prolate system to determine if the costs are less than the free-flying, thruster-only formation.

Recall from our assessment on utility, that tethers have great value for formation control as long as there are no restrictions on spin rate. If we were to relax the condition that the aperture need to be continuously earth-facing, then we could spin the system up to a higher rate and tethers would do a fantastic job of maintaining the formation with almost no stationkeeping costs. The high spin rate would keep the formation's spin axis inertially fixed, but from this simple idea we offer the following concept of operations: create a constellation of a number of these inertially pointed formations as notionally shown in Figure 8.1. In effect, each formation stays fixed inertially, and as it orbits the earth the projection of its aperture toward nadir oscillates between a full circle and a line. Some target opportunities will occur when an aperture coverage is maximized, others when it is minimized. Although not required,

one could also re-phase the orientation of the inertial spin axis by applying simple reels and the conservation of angular momentum to change the precession rate.

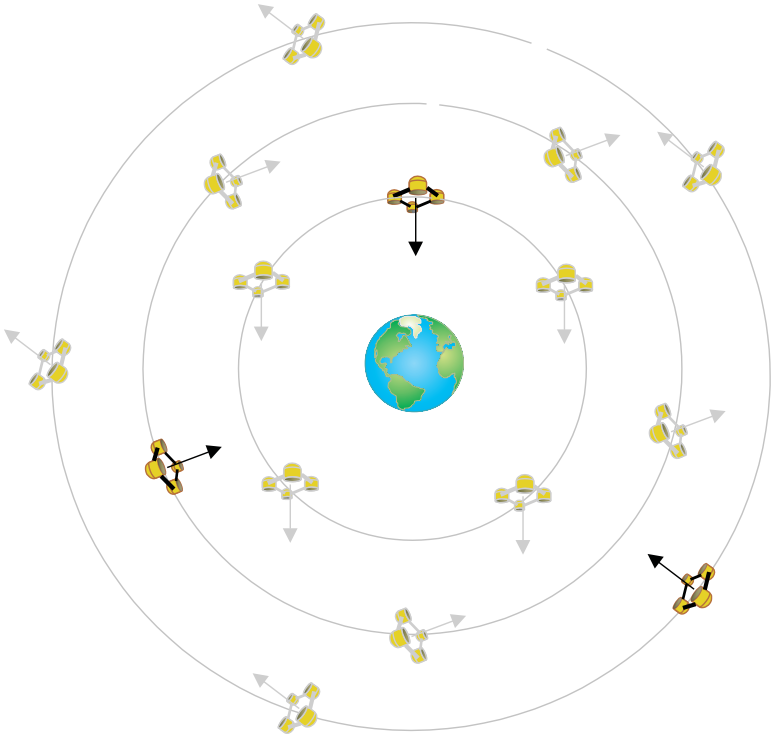


Figure 8.1: High Spin Rate Constellation Concept

While this concept requires more spacecraft and the spacecraft would require slewable optics, the cost to maintain the formations would be cheaper. It becomes a sort-of scheduling/systems engineering analysis and could be explored to determine the required number of formations in the constellation, necessary orbits, and inertial aperture orientations to satisfy specific targeting requirements.

8.3 Contributions

This research advanced the knowledge of semi-rigid body dynamics, satellite formation dynamics, and tethered systems. The following are the unique contributions of this research to those fields:

- **Determined the effects of energy dissipation on structures that are in/near the Likins-Pringle equilibria.** Energy dissipation effects are al-

ready generally known for rigid-bodies and somewhat investigated for tethered formations, but no previous work studied the effects of energy dissipation on the Likins-Pringle equilibria. In particular, this research shed light on the unique challenge to prolate configurations of tethered clusters in that energy dissipation will eventually zero-out the aperture's spin rate.

- **Discovered that conical Likins-Pringle rigid body conditions can be used to generate free-flying satellite formation equilibria.** When the Likins-Pringle geometrical approach to assigning initial conditions for a free-flying system is used, the results are equilibria that are the same as those approximated with the C-W linearization solutions. A new perspective was gained on a previously known relative motion equilibrium condition.
- **Numerically defined the steady-spin range of $SR = \frac{\dot{\psi}}{\dot{\nu}}$ for cone angles other than 0°.** Until now, the steady-spin range was only determined for the Thompson equilibrium (0° cone angle). This is what we have called the Kumar Range. In this research, we confirmed that the Kumar Range is only valid for 0°, then numerically determined a new "SR Range" for *all* other cone angles.
- **Provided an overall assessment of the utility of tethers for the purpose of formation control on *continuously* earth-facing aperture clusters.** Deep space interferometry studies have shown that tethers can be of great value, however efforts to demonstrate the utility of tethers for continuously nadir-pointing systems have been frustrated. This research, taken as a whole, serves as an explanation to program directors, researchers, and mission engineers on its limited utility.

Appendix A. Likins-Pringle Equilibria Development

This appendix covers the detailed development of the conical Likins-Pringle equilibrium conditions for the rigid body model discussed in Chapter IV. For convenience, the reference frames and Euler angles are shown again in Figure A.1.

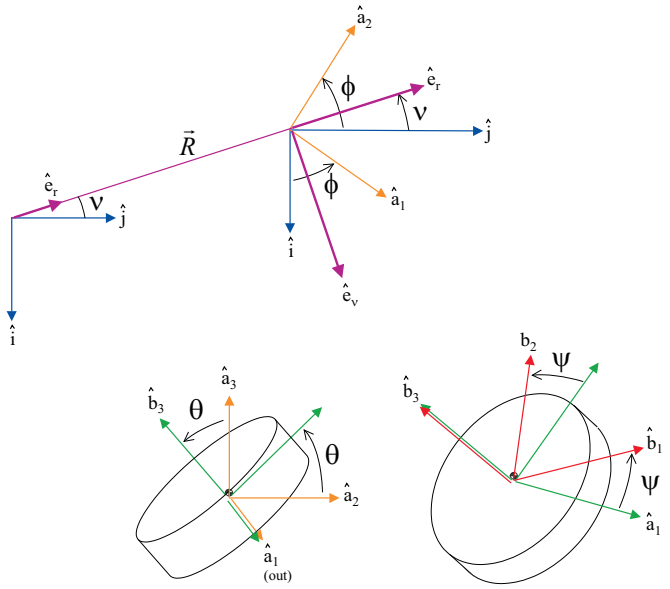


Figure A.1: Coordinate Reference Frames and Rotations

A.1 Equilibrium Condition Development

The rotational equations-of-motion for the rigid body follow from Euler's equation. They are developed in detail in Section 4.1.2 and are shown again here:

$$\begin{aligned} A\dot{\omega}_1 - (A-C)\omega_2\omega_3 &= 3\mu_\oplus R^{-5} YZ(C-A) \\ A\dot{\omega}_2 - (C-A)\omega_1\omega_3 &= 3\mu_\oplus R^{-5} XZ(A-C) \\ C\dot{\omega}_3 &= 0 \end{aligned} \tag{A.1}$$

where $\mu_\oplus = GM_\oplus$ is the gravitational constant for the Earth, G is the universal gravitational constant, and $M_\oplus$ is the mass of the Earth. X, Y, Z are the body frame

components of the orbit position vector, $\vec{R}$. The body frame components of the rigid body's angular velocity with respect to the inertial frame are given by

$$\begin{aligned}
\omega_1 &= \dot{\phi}\sin\psi\sin\theta + \dot{\theta}\cos\psi \\
\omega_2 &= \dot{\phi}\cos\psi\sin\theta - \dot{\theta}\sin\psi \\
\omega_3 &= \dot{\phi}\cos\theta + \dot{\psi}
\end{aligned} \tag{A.2}$$

By taking the derivative of the equations in A.2, we get

$$\begin{aligned}
\dot{\omega}_1 &= \ddot{\phi}\sin\psi\sin\theta + \dot{\phi}\dot{\psi}\cos\psi\sin\theta + \dot{\phi}\dot{\theta}\sin\psi\cos\theta + \ddot{\theta}\cos\psi - \dot{\theta}\dot{\psi}\sin\psi \\
\dot{\omega}_2 &= \ddot{\phi}\cos\psi\sin\theta - \dot{\phi}\dot{\psi}\sin\psi\sin\theta + \dot{\phi}\dot{\theta}\cos\psi\cos\theta - \ddot{\theta}\sin\psi - \dot{\theta}\dot{\psi}\cos\psi \\
\dot{\omega}_3 &= \ddot{\theta}\cos\theta - \dot{\phi}\dot{\theta}\sin\theta + \ddot{\psi}
\end{aligned} \tag{A.3}$$

From Equation 4.30 in Chapter IV, the body frame components of $\vec{R}$ are:

$$X = -R(\mathrm{s}\nu\mathrm{c}\psi\mathrm{c}\phi - \mathrm{s}\nu\mathrm{c}\theta\mathrm{s}\psi\mathrm{s}\phi - \mathrm{c}\nu\mathrm{c}\psi\mathrm{s}\phi - \mathrm{c}\nu\mathrm{c}\theta\mathrm{s}\psi\mathrm{c}\phi) \tag{A.4}$$

$$Y = R(\mathrm{s}\nu\mathrm{s}\psi\mathrm{c}\phi + \mathrm{s}\nu\mathrm{c}\theta\mathrm{c}\psi\mathrm{s}\phi - \mathrm{c}\nu\mathrm{s}\psi\mathrm{s}\phi + \mathrm{c}\nu\mathrm{c}\theta\mathrm{c}\psi\mathrm{c}\phi) \tag{A.5}$$

$$Z = -R(\mathrm{s}\nu\mathrm{s}\theta\mathrm{s}\phi + \mathrm{c}\nu\mathrm{s}\theta\mathrm{c}\phi) \tag{A.6}$$

where $s*$=$sin*$, $c*$=$cos*$, and R is the scalar distance from the center of the earth to the rigid body.

Now introduce the necessary assumptions that arise from the desired equilibrium condition, which is an axisymmetric body whose spin axis does not move with respect to the rotating orbit frame. For a circular orbit, this means the cone angle does not

change over time (θ=constant), and the rate of change in ϕ remains constant and is equal to the orbit rate ($\dot{\nu}$), ensuring the spin axis always "faces" the earth. Also, we can let the orbit angle ν equal the ϕ without loss of generality, so the first part of these equilibrium conditions are given by:

$$\begin{aligned} \theta &= \text{const} & \phi &= \nu \\ \dot{\theta} &= 0 & \dot{\phi} &= \dot{\nu} = \text{const} \\ \ddot{\theta} &= 0 & \ddot{\phi} &= \ddot{\nu} = 0 \end{aligned} \tag{A.7}$$

For ϕ=ν, the equations for X, Y, Z reduce significantly:

$$\begin{aligned} X &= -R(\mathrm{s}\nu\mathrm{c}\psi\mathrm{c}\nu - \mathrm{s}^2\nu\mathrm{c}\theta\mathrm{s}\psi - \mathrm{c}\nu\mathrm{c}\psi\mathrm{s}\nu - \mathrm{c}^2\nu\mathrm{c}\theta\mathrm{s}\psi) \\ X &= R(\mathrm{s}^2\nu\mathrm{c}\theta\mathrm{s}\psi + \mathrm{c}^2\nu\mathrm{c}\theta\mathrm{s}\psi) \\ X &= R(\mathrm{c}\theta\mathrm{s}\psi) \end{aligned} \tag{A.8}$$

$$\begin{aligned} Y &= R(\mathrm{s}\nu\mathrm{s}\psi\mathrm{c}\nu + \mathrm{s}^2\nu\mathrm{c}\theta\mathrm{c}\psi - \mathrm{c}\nu\mathrm{s}\psi\mathrm{s}\nu + \mathrm{c}^2\nu\mathrm{c}\theta\mathrm{c}\psi) \\ Y &= R(\mathrm{s}^2\nu\mathrm{c}\theta\mathrm{c}\psi + \mathrm{c}^2\nu\mathrm{c}\theta\mathrm{c}\psi) \\ Y &= R(\mathrm{c}\theta\mathrm{c}\psi) \end{aligned} \tag{A.9}$$

$$\begin{aligned} Z &= -R(\mathrm{s}^2\nu\mathrm{s}\theta + \mathrm{c}^2\nu\mathrm{s}\theta) \\ Z &= -R\mathrm{s}\theta \end{aligned} \tag{A.10}$$

Furthermore, for a circular orbit, the spin rate of the body ($\dot{\psi}$) will also be constant, and is equal to the spin-to-orbit rate ratio (SR=$\frac{\dot{\psi}}{\dot{\nu}}$) times $\dot{\nu}$. For notation convenience, SR is redefined simply as S for the rest of this Appendix. Therefore, the remainder of the equilibrium conditions are:

$$\begin{aligned} \dot{\psi} &= S\dot{\nu} = \text{const} \\ \ddot{\psi} &= 0 \\ \psi &= S\dot{\nu}t + \psi_o \end{aligned} \tag{A.11}$$

where t is time and ψ_o can be arbitrarily set to zero.

By substituting the conditions shown in A.7 and A.11 into the angular velocity and acceleration Equations A.2 and A.3, we get

$$\begin{aligned} \omega_1 &= \dot{\nu} \sin(S\dot{\nu}t) \sin\theta \\ \omega_2 &= \dot{\nu} \cos(S\dot{\nu}t) \sin\theta \\ \omega_3 &= \dot{\nu} \cos\theta + S\dot{\nu} \end{aligned} \tag{A.12}$$

and

$$\begin{aligned} \dot{\omega}_1 &= S\dot{\nu}^2 \cos(S\dot{\nu}t) \sin\theta \\ \dot{\omega}_2 &= -S\dot{\nu}^2 \sin(S\dot{\nu}t) \sin\theta \\ \dot{\omega}_3 &= 0 \end{aligned} \tag{A.13}$$

Substitute these new relationships (Equations A.7-A.13) into the original equations-of-motion. The third EOM (A.1-c) is trivial (0=0). Therefore, we begin with Equation A.1-a:

$$
\begin{aligned}
AS\dot{\nu}^2\mathrm{c}\left(S\dot{\nu}t\right)\mathrm{s}\theta + (C-A)\dot{\nu}\mathrm{c}\left(S\dot{\nu}t\right)\mathrm{s}\theta\left(\dot{\nu}\mathrm{c}\theta + S\dot{\nu}\right) &= \frac{3\mu_{\oplus}}{R^5}R^2\mathrm{c}\theta\mathrm{c}\left(S\dot{\nu}t\right)\mathrm{s}\theta(A-C) \\
AS\dot{\nu}^2 + (C-A)\dot{\nu}\left(\dot{\nu}\mathrm{c}\theta + S\dot{\nu}\right) &= \frac{3\mu_{\oplus}}{R^3}\mathrm{c}\theta(A-C) \\
AS\dot{\nu}^2 + (C-A)\dot{\nu}^2\mathrm{c}\theta + (C-A)\dot{\nu}^2 S &= \frac{3\mu_{\oplus}}{R^3}\mathrm{c}\theta(A-C) \\
CS\dot{\nu}^2 + (C-A)\dot{\nu}^2\mathrm{c}\theta &= \frac{3\mu_{\oplus}}{R^3}\mathrm{c}\theta(A-C) \\
\dot{\nu}^2\mathrm{c}\theta(C-A) + CS\dot{\nu}^2 + \frac{3\mu_{\oplus}}{R^3}\mathrm{c}\theta(C-A) &= 0 \\
\dot{\nu}^2\mathrm{c}\theta(C-A) + CS\dot{\nu}^2 + 3\dot{\nu}^2\mathrm{c}\theta(C-A) &= 0 \\
\dot{\nu}^2\left(1 + \frac{CS}{\mathrm{c}\theta(C-A)} + 3\right) &= 0
\end{aligned}
\tag{A.14}
$$

Solving A.14 means either $\dot{\nu}$=0, which is impossible for any orbit, or

$$
\frac{CS}{\mathrm{c}\theta(C-A)} + 4 = 0
$$

or

$$
S = \frac{-4\mathrm{c}\theta(C-A)}{C}
$$

Therefore, the first condition (from Equation A.1-a) that must be satisfied for the axisymmetric body to achieve the desired equilibrium condition is

$$
S = \frac{\dot{\psi}}{\dot{\nu}} = \frac{4\cos\theta(A-C)}{C} \tag{A.15}
$$

Looking at the second equation-of-motion (A.1-b) with all of the new substitutions yields the same result as Equation A.14:

$$
\begin{aligned}
-AS\dot{\nu}^2\mathrm{s}\left(S\dot{\nu}t\right)\mathrm{s}\theta - (C-A)\dot{\nu}\mathrm{s}\left(S\dot{\nu}t\right)\mathrm{s}\theta\left(\dot{\nu}\mathrm{c}\theta + S\dot{\nu}\right) &= \frac{3\mu_{\oplus}}{R^5}R^2\mathrm{c}\theta\mathrm{s}\left(S\dot{\nu}t\right)\mathrm{s}\theta(C-A) \\
-AS\dot{\nu}^2 - (C-A)\dot{\nu}\left(\dot{\nu}\mathrm{c}\theta + S\dot{\nu}\right) &= \frac{3\mu_{\oplus}}{R^3}\mathrm{c}\theta(C-A) \\
-AS\dot{\nu}^2 - (C-A)\dot{\nu}^2\mathrm{c}\theta - (C-A)\dot{\nu}^2 S &= \frac{3\mu_{\oplus}}{R^3}\mathrm{c}\theta(C-A) \\
AS\dot{\nu}^2 + (C-A)\dot{\nu}^2\mathrm{c}\theta + (C-A)\dot{\nu}^2 S &= \frac{3\mu_{\oplus}}{R^3}\mathrm{c}\theta(A-C) \\
CS\dot{\nu}^2 + (C-A)\dot{\nu}^2\mathrm{c}\theta &= \frac{3\mu_{\oplus}}{R^3}\mathrm{c}\theta(A-C) \\
\dot{\nu}^2\mathrm{c}\theta(C-A) + CS\dot{\nu}^2 + \frac{3\mu_{\oplus}}{R^3}\mathrm{c}\theta(C-A) &= 0 \\
\dot{\nu}^2\mathrm{c}\theta(C-A) + CS\dot{\nu}^2 + 3\dot{\nu}^2\mathrm{c}\theta(C-A) &= 0 \\
\dot{\nu}^2\left(1 + \frac{CS}{\mathrm{c}\theta(C-A)} + 3\right) &= 0
\end{aligned}
\tag{A.16}
$$

which has the same condition for equilibrium as previously shown. Therefore, the single condition that must be satisfied for the axi-symmetric body to achieve the desired equilibrium condition is Equation A.15:

$$
S = \frac{\dot{\psi}}{\dot{\nu}} = \frac{4\cos\theta(A-C)}{C} \tag{A.17}
$$

A.2 Stability Analysis

Linear stability analysis can be performed to determine the infinitesimal stability of the equilibrium condition shown in Equation A.15. To do this, one can follow the development of either Likins [30] or Hughes [20]. Likins uses different Euler angles and slightly different notation than what is used here, while Hughes uses a completely different notation and model. Following the Likins approach yields a biquadratic characteristic equation of the form [30]:

$$
\lambda^4 + 2b\lambda^2 + c = 0 \tag{A.18}
$$

with eigenvalues (roots):

$$\lambda^2 = \left[-b \pm \left(b^2 - c\right)^{\frac{1}{2}}\right]$$

where

$$b = \frac{7 + 3\frac{C}{A}\left[3\left(\frac{C}{A} - 1\right)\cos^2\theta - 2\right]}{2}$$

and

$$c = 3\left(1 - \frac{C}{A}\right)\left(4 - 3\frac{C}{A}\right)\sin^2\theta$$

Instabilities will occur if the roots have positive real parts, which happens if λ^2 is complex or if λ^2 is real and positive. There are three situations where this will occur as shown in Likins [30]. First, when c is negative, λ^2 will have a positive real value. Second, if $b^2 - c$ is negative then λ^2 will be complex. Third, if b is negative, λ^2 will be complex or have a real positive value depending on the value of c. Therefore, any one of these three conditions denotes instability:

$$\begin{aligned} &i) && c < 0 \\ &ii) && b^2 - c < 0 \\ &iii) && b < 0 \end{aligned} \tag{A.19}$$

That is, (i) or (ii) or (iii) will yield instability. Conversely, we can determine infinitesimal stability as the intersection of the opposites of all three conditions. In other words, the conditions where "(i) is not met" and "(ii) is not met" and "(iii) is not met" simultaneously will give the infinitesimal stability conditions for the equilibrium.

Letting $K = \frac{C}{A}$ for simplicity and starting with Equation A.19-i, we need

$$3\left(1 - K\right)\left(4 - 3K\right)\sin^2\theta < 0 \tag{A.20}$$

Since this research focuses on oblate, axisymmetric bodies $1 < K < 2$, therefore $(1-K)$ is strictly negative. Also, as long as θ is not 0 or π, $sin^2(\theta)$ is always positive. Therefore, the first condition for instability is:

$$K < \frac{4}{3} \tag{A.21}$$

For Equation A.19-*iii*, the following must be satisfied:

$$\frac{7+3K\left[3(K-1)\cos^2\theta-2\right]}{2} < 0$$

$$7 - 6K + 9K\left(K-1\right)\cos^2\theta < 0$$

$$\cos^2\theta < \frac{6K-7}{9K(K-1)}$$

$$|\cos\theta| < \sqrt{\frac{6K-7}{9K(K-1)}}$$

or

$$|\theta| > \arccos\left(\sqrt{\frac{6K-7}{9K\left(K-1\right)}}\right) \tag{A.22}$$

Finally, from Equation A.19-*ii*,

$$\frac{\left(7+3K\left[3\left(K-1\right)\cos^2\theta-2\right]\right)^2}{4} - 3\left(1-K\right)\left(4-3\left(K\right)\right)\left(1-\cos^2\theta\right) < 0$$

which can be re-written as

$$x\cos^4\theta + y\cos^2\theta + z < 0 \tag{A.23}$$

where

$$
\begin{aligned}
x &= \tfrac{(9K(K-1))^2}{4} \\
y &= \tfrac{(7-6K)9K(K-1)}{2} - 3(K-1)(4-3K) \\
z &= \tfrac{(7-6K)^2}{4} + 3(K-1)(4-3K)
\end{aligned}
\tag{A.24}
$$

Now, by re-writing Equation A.23 as

$$x\left(\cos^2\theta - \gamma\right)\left(\cos^2\theta - \delta\right) < 0$$

where

$$
\begin{aligned}
\delta &= \tfrac{-y \pm \sqrt{y^2 - 4xz}}{2x} \\
\gamma &= \tfrac{z}{x\delta}
\end{aligned}
$$

and knowing that x is always positive, we know that either

$$|\cos\theta| < \sqrt{\gamma} \quad \text{and} \quad |\cos\theta| > \sqrt{\delta}$$

or

$$|\cos\theta| > \sqrt{\gamma} \quad \text{and} \quad |\cos\theta| < \sqrt{\delta}$$

We can assume, without loss of generality that $\gamma \leq \delta$, therefore the condition from Equation A.19-*ii* that could create instability is:

$$|\theta| < \arccos\left(\sqrt{\gamma}\right) \quad \text{and} \quad |\theta| > \arccos\left(\sqrt{\delta}\right) \tag{A.25}$$

A plot of all three instability conditions (Equations A.21, A.22, and A.25) is shown in Figure A.2. For infinitesimal stability, we want the area in the lower right corner, where none of these conditions are met.

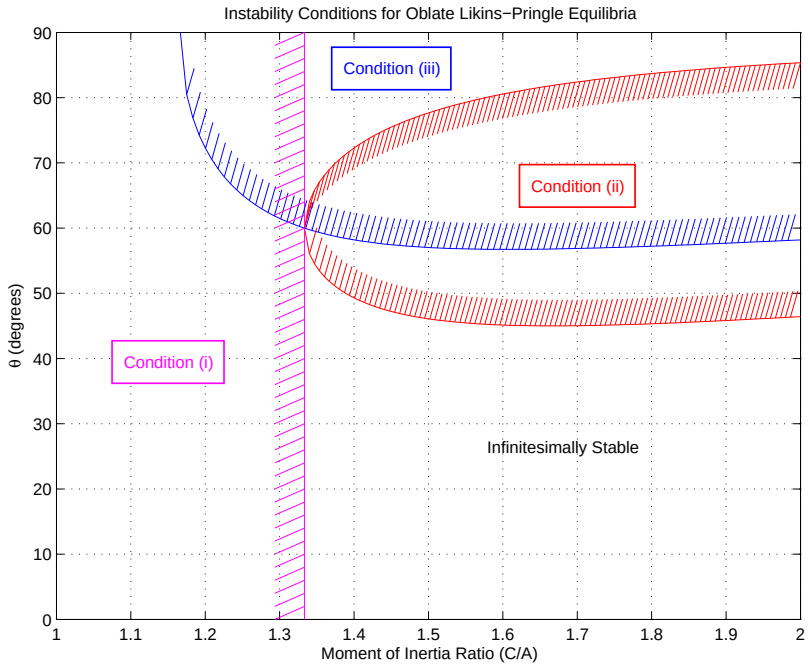


Figure A.2: Instability Conditions for Oblate Likins-Pringle Equilibria

For this analysis, we evaluate the stability for the specific moment-of-inertia ratio used exclusively in multi-body system simulations: $K = C/A = 2$. By default, we avoid the first instability condition ($K < 4/3$) regardless of cone angle. The second condition requires that $|\theta|$ be below 46.434° or above 85.376° to be stable. The third condition requires that $|\theta|$ be less than 58.19°. Therefore, looking at the intersection of all these requirements, we get infinitesimal stability when:

$$|\theta| < 46.434^\circ$$

Appendix B. Transverse Moment-of-Inertia Development

This appendix develops the transverse moment-of-inertia (MOI) equation for an axisymmetric, multi-body system with any number of point-mass bodies in a ring formation.

Consider the axi-symmetric formation with an arbitrary number of bodies (n) connected by massless tethers as shown in Figure B.1. The masses (m_j) are considered point masses and evenly distributed around the ring at a distance r from the center of mass.

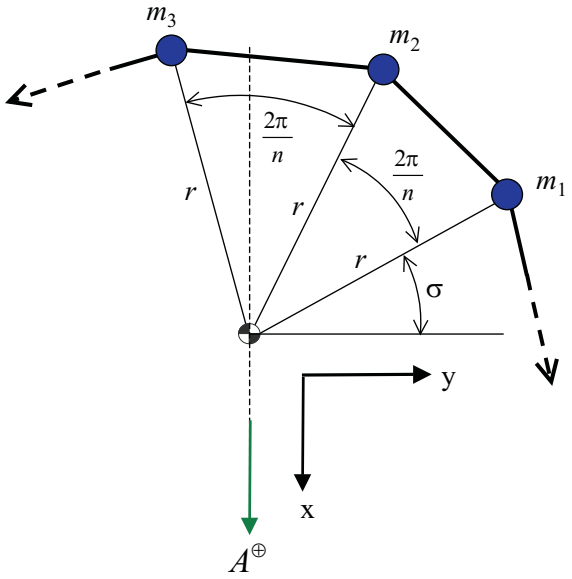


Figure B.1: Transverse Moment-of-Inertia of an Axisymmetric Formation from an Arbitrary Viewpoint

The transverse MOI of each body about the center of mass is given by

$$\begin{aligned}
A_1^{\oplus} &= m_1 \left\{ r \cos \sigma \right\}^2 \\
A_2^{\oplus} &= m_2 \left\{ r \cos \left(\sigma + \left(\tfrac{2\pi}{n} \right) \right) \right\}^2 \\
A_3^{\oplus} &= m_3 \left\{ r \cos \left(\sigma + \left(\tfrac{2\pi}{n} \right) 2 \right) \right\}^2 \\
A_4^{\oplus} &= m_4 \left\{ r \cos \left(\sigma + \left(\tfrac{2\pi}{n} \right) 3 \right) \right\}^2 \\
&\vdots \\
A_n^{\oplus} &= m_n \left\{ r \cos \left(\sigma + \left(\tfrac{2\pi}{n} \right) (n-1) \right) \right\}^2
\end{aligned} \tag{B.1}$$

The overall transverse MOI for the system is found by summing all of those individual MOI's from each body:

$$A_{sys}^{\oplus} = \sum_{j=1}^{n} m_j r^2 \cos^2\left(\sigma + (j-1)\left(\frac{2\pi}{n}\right)\right) \tag{B.2}$$

If we assume all of the masses are equal (m_j=m), then

$$A_{sys}^{\oplus} = k\sum_{j=1}^{n} \cos^2\left(\sigma + (j-1)\left(\tfrac{2\pi}{n}\right)\right) \quad ; \quad k = mr^2 \tag{B.3}$$

We want this transverse MOI to be constant regardless of the aspect angle. That is, we want to know that $A_{sys}^{\oplus}$ will *not* be a function of σ. Therefore, we now must determine for what values of n will Equation B.3 be constant. To begin, re-package Equation B.3 as

$$A_{sys}^{\oplus} = k\sum_{j=0}^{n-1} \cos^2\left(\sigma + j\left(\frac{2\pi}{n}\right)\right) \tag{B.4}$$

and use the trigonometric identity, $\cos^2\alpha = \frac{1}{2}(1+\cos 2\alpha)$, so that

$$A_{sys}^{\oplus} = k\sum_{j=0}^{n-1} \tfrac{1}{2}\left[1 + \cos\left(2\sigma + j\left(\tfrac{4\pi}{n}\right)\right)\right]$$

$$A_{sys}^{\oplus} = k\left\{\sum_{j=0}^{n-1} \tfrac{1}{2} + \tfrac{1}{2}\sum_{j=0}^{n-1} \cos\left(2\sigma + j\left(\tfrac{4\pi}{n}\right)\right)\right\}$$

$$A_{sys}^{\oplus} = k\left\{\tfrac{n}{2} + \tfrac{1}{2}\sum_{j=0}^{n-1} \cos\left(2\sigma + j\left(\tfrac{4\pi}{n}\right)\right)\right\}$$

Once again, using a trigonometric exponential relation ($\cos\alpha = \frac{e^{i\alpha}+e^{-i\alpha}}{2}$), we get

$$A_{sys}^{\oplus} = k\left\{\frac{n}{2} + \frac{1}{2}\sum_{j=0}^{n-1} \frac{e^{i\left(2\sigma+\frac{4\pi}{n}j\right)} + e^{-i\left(2\sigma+\frac{4\pi}{n}j\right)}}{2}\right\}$$

$$A_{sys}^{\oplus} = k\left\{\frac{n}{2} + \frac{1}{4}\sum_{j=0}^{n-1} e^{i2\sigma}e^{i\frac{4\pi}{n}j} + e^{-i2\sigma}e^{-i\frac{4\pi}{n}j}\right\}$$

The exponential terms that are not functions of j may be pulled out of the summations,

$$A_{sys}^{\oplus} = k\left\{\frac{n}{2} + \frac{1}{4}e^{i2\sigma}\sum_{j=0}^{n-1} e^{i\frac{4\pi}{n}j} + \frac{1}{4}e^{-i2\sigma}\sum_{j=0}^{n-1} e^{-i\frac{4\pi}{n}j}\right\}$$

Now, if we let $x = e^{\frac{4\pi}{n}i}$, then

$$A_{sys}^{\oplus} = k\left\{\frac{n}{2} + \frac{1}{4}e^{i2\sigma}\sum_{j=0}^{n-1} x^{j} + \frac{1}{4}e^{-i2\sigma}\sum_{j=0}^{n-1} x^{-j}\right\}$$

or

$$A_{sys}^{\oplus} = k\left\{\frac{n}{2} + \frac{1}{4}e^{i2\sigma}\sum_{j=0}^{n-1} x^{j} + \text{C.C.}\right\} \tag{B.5}$$

where "C.C." denotes the complex conjugate of the term preceding it, for convenience.

Since n represents the number of satellites in the formation, it must be a positive integer greater than one. If n=2, $x = e^{\frac{4\pi}{n}i}$=1 and the summation from Equation B.5 becomes

$$\begin{aligned}\sum_{j=0}^{1} x^{j} &= x^{0} + x^{1} \\ &= 1 + x \\ &= 1 + e^{2\pi i} \\ &= 2\end{aligned} \tag{B.6}$$

which reduces B.5 to

$$
\begin{aligned}
A_{sys}^{\oplus} &= k\left\{1+\frac{1}{4}e^{i2\sigma}\,(2)+\text{C.C.}\right\} \\
&= k\left\{1+\frac{1}{2}e^{i2\sigma}+\frac{1}{2}e^{-i2\sigma}\right\} \\
&= k\left\{1+\cos 2\sigma\right\} \\
&= 2k\cos^2\sigma
\end{aligned}
\tag{B.7}
$$

Therefore, for two bodies (n=2), the transverse MOI is

$$
A_{sys}^{\oplus} = 2mr^2\cos^2\sigma \tag{B.8}
$$

which is a function of σ. That is, it changes with your inertial reference and therefore is not constant.

For $n > 2$, we go back to Equation B.5. It can be shown, by induction, that the following relationship is true:

$$
\sum_{k=0}^{n} x^k = \frac{x^{n+1}-1}{x-1}
$$

Therefore,

$$
\sum_{j=0}^{n-1} x^j = \frac{x^{(n-1)+1}-1}{x-1} = \frac{x^n-1}{x-1} \tag{B.9}
$$

If we apply Equation B.9 to Equation B.5

$$
A_{sys}^{\oplus} = k\left\{\frac{n}{2}+\frac{1}{4}e^{i2\sigma}\left(\frac{x^n-1}{x-1}\right)+\text{C.C.}\right\}
$$

or

$$
A_{sys}^{\oplus} = k\left\{\frac{n}{2}+\frac{1}{4}e^{i2\sigma}\left(\frac{e^{4\pi i}-1}{e^{\frac{4\pi}{n}i}-1}\right)+\text{C.C.}\right\} \tag{B.10}
$$

Now consider the term inside the inner parenthesis:

$$\left(\frac{e^{4\pi i}-1}{e^{\frac{4\pi}{n}i}-1}\right) \tag{B.11}$$

This term always has a zero in the numerator since $e^{4\pi i}$=1 always. Therefore Equation B.10 simplifies to just

$$A_{sys}^{\oplus} = k\left\{\frac{n}{2}+0\right\} = \frac{mr^2n}{2} \tag{B.12}$$

which is constant for all σ, therefore the transverse MOI is independent of the reference chosen for $n > 2$.

Appendix C. Calculations for Period Matching

Chapter V discusses how a free-flying formation that begins in Likins-Pringle-based initial conditions experiences slight in-track drifting between bodies that start at different altitudes in the formation (Section 5.3.1). One can choose to eliminate this slight in-track drift between two orbits by using a technique called "period matching", where the initial velocity of one body is slightly modified such that its orbital period exactly matches the period of the other body. This appendix specifies the period matching technique that was used in this research (where indicated).

To begin, let's say there are two bodies with initial position and velocity vectors: $\vec{R}_1$, $\vec{V}_1$, $\vec{R}_2$, $\vec{V}_2$. Furthermore, let's say we want to adjust the orbital period of body 2 to match the period of body 1. What we really want to do is "zero out" the difference in the orbital periods:

$$\Delta \mathrm{P} = \mathrm{P}_2 - \mathrm{P}_1 = 0 \tag{C.1}$$

The formula for the period of a particular orbit is [3]

$$\begin{aligned} \mathrm{P}_i &= \frac{2\pi}{\dot{\nu}} \\ &= 2\pi\sqrt{\frac{a_i^3}{\mu_\oplus}} \\ &= 2\pi\sqrt{\frac{\left(\frac{\mu_\oplus}{-2E}\right)^3}{\mu_\oplus}} \\ &= 2\pi\mu_\oplus\left(-2E\right)^{-\frac{3}{2}} \\ &= 2\pi\mu_\oplus\left(-2\left\{\frac{\left|\vec{V}_i\right|^2}{2} - \frac{\mu_\oplus}{\left|\vec{R}_i\right|}\right\}\right)^{-\frac{3}{2}} \end{aligned} \tag{C.2}$$

where $\dot{\nu}$ is the mean motion, $\mu_\oplus = GM_\oplus$ is the gravitational constant for the Earth, a_i is the semi-major axis of the orbit, and E is the total energy per unit mass. For convenience, we define $\left|\vec{R}_i\right| = R_i$ and $\left|\vec{V}_i\right| = V_i$. Going back to Equation C.1, we want

$$\Delta \mathrm{P} = 2\pi\mu_{\oplus}\left(-2\left\{\frac{V_2^2}{2} - \frac{\mu_{\oplus}}{R_2}\right\}\right)^{-\frac{3}{2}} - 2\pi\mu_{\oplus}\left(-2\left\{\frac{V_1^2}{2} - \frac{\mu_{\oplus}}{R_1}\right\}\right)^{-\frac{3}{2}} = 0$$

$$2\pi\mu_{\oplus}\left(-2\right)^{-\frac{3}{2}}\left[\left\{\frac{V_2^2}{2} - \frac{\mu_{\oplus}}{R_2}\right\}^{-\frac{3}{2}} - \left\{\frac{V_1^2}{2} - \frac{\mu_{\oplus}}{R_1}\right\}^{-\frac{3}{2}}\right] = 0$$

$$\left\{\frac{V_2^2}{2} - \frac{\mu_{\oplus}}{R_2}\right\}^{-\frac{3}{2}} - \left\{\frac{V_1^2}{2} - \frac{\mu_{\oplus}}{R_1}\right\}^{-\frac{3}{2}} = 0 \tag{C.3}$$

Next solve C.3 for V_2.

$$\frac{V_2^2}{2} - \frac{\mu_{\oplus}}{R_2} = \left(\left\{\frac{V_1^2}{2} - \frac{\mu_{\oplus}}{R_1}\right\}^{-\frac{3}{2}}\right)^{-\frac{2}{3}}$$

$$\frac{V_2^2}{2} - \frac{\mu_{\oplus}}{R_2} = \left\{\frac{V_1^2}{2} - \frac{\mu_{\oplus}}{R_1}\right\}$$

$$\frac{V_2^2}{2} = \frac{V_1^2}{2} - \frac{\mu_{\oplus}}{R_1} + \frac{\mu_{\oplus}}{R_2}$$

$$V_{2_{new}} = \sqrt{V_1^2 - \frac{2\mu_{\oplus}}{R_1} + \frac{2\mu_{\oplus}}{R_2}} \tag{C.4}$$

To modify the original initial velocity of body 2, we use the new magnitude, $V_{2_{new}}$, but in the original direction:

$$\vec{V}_{2_{new}} = V_{2_{new}}\frac{\vec{V}_{2_{old}}}{V_{2_{old}}} \tag{C.5}$$

This new velocity for body 2 will yield an orbital period that matches the period of body 1. This technique can also be applied between one of the bodies and the system center-of-mass' velocity.

Appendix D. Period Difference Between Free-Flying Bodies in Likins-Pringle Equilibria

To confirm that Likins-Pringle-based initial conditions produce relative equilibria for free-flying systems, it is useful to compare the difference in the orbit periods and show that they are nearly the same. This appendix is an analytic demonstration of how close the orbital periods are for two such bodies. Specifically, for reasons explained in Section 5.3.1, we choose to compare bodies 1 and 2 of the 3-body system in the L-P free-flight scenario.

To perform this comparison analytically, we use many of the relations in Section 5.2.2 to determine the initial positions and velocities of the two bodies. The positions are taken from Equation 5.35. For body 1, we get

$$
{}^{\hat{i}}\vec{R}_1 = {}^{\hat{i}}\vec{R}_{\oplus} + C^{ib\hat{b}}\vec{r}_1 = \begin{bmatrix} X_{\oplus} \\ Y_{\oplus} \\ Z_{\oplus} \end{bmatrix} + R_3\left(-\nu-\alpha\right) R_2\left(\beta\right) \begin{bmatrix} \frac{\sqrt{3}}{3}\rho \\ 0 \\ 0 \end{bmatrix}
$$

$$
{}^{\hat{i}}\vec{R}_1 = \begin{bmatrix} X_{\oplus} + \frac{\sqrt{3}}{3}\rho\cos\beta\cos(-\nu-\alpha) \\ Y_{\oplus} - \frac{\sqrt{3}}{3}\rho\cos\beta\sin(-\nu-\alpha) \\ Z_{\oplus} + \frac{\sqrt{3}}{3}\rho\sin\beta \end{bmatrix} \tag{D.1}
$$

Likewise, for body 2

$$
{}^{\hat{i}}\vec{R}_2 = {}^{\hat{i}}\vec{R}_{\oplus} + C^{ib\hat{b}}\vec{r}_2 = \begin{bmatrix} X_{\oplus} + \frac{\rho}{2}\sin(-\nu-\alpha) - \frac{\sqrt{3}}{6}\rho\cos\beta\cos(-\nu-\alpha) \\ Y_{\oplus} + \frac{\rho}{2}\cos(-\nu-\alpha) + \frac{\sqrt{3}}{6}\rho\cos\beta\sin(-\nu-\alpha) \\ Z_{\oplus} - \frac{\sqrt{3}}{6}\rho\sin\beta \end{bmatrix} \tag{D.2}
$$

Recall that from the initial set-up (Equation 5.40) many of these terms drop out: $\alpha = 0$, $\nu = 0$, $Y_{\oplus} = 0$, and $Z_{\oplus} = 0$. Therefore the initial position vectors become

$$^{\hat{i}}\vec{R}_1 = \begin{bmatrix} X_\oplus + \frac{\sqrt{3}}{3}\rho\cos\beta \\ 0 \\ \frac{\sqrt{3}}{3}\rho\sin\beta \end{bmatrix} \tag{D.3}$$

$$^{\hat{i}}\vec{R}_2 = \begin{bmatrix} X_\oplus - \frac{\sqrt{3}}{6}\rho\cos\beta \\ \frac{\rho}{2} \\ -\frac{\sqrt{3}}{6}\rho\sin\beta \end{bmatrix} \tag{D.4}$$

To get the initial velocities, we need the angular momentum from Equation 5.41:

$$^{\hat{b}}\vec{\omega}^{bi} = \begin{bmatrix} 0 \\ 0 \\ \dot{\psi} \end{bmatrix} + C^{be}\begin{bmatrix} 0 \\ 0 \\ \dot{\nu} \end{bmatrix} = \begin{bmatrix} 0 \\ 0 \\ \dot{\psi} \end{bmatrix} + R_2(-\beta)\,R_3(\alpha)\begin{bmatrix} 0 \\ 0 \\ \dot{\nu} \end{bmatrix}$$

and since $\alpha = 0$

$$^{\hat{b}}\vec{\omega}^{bi} = \begin{bmatrix} \dot{\nu}\sin\beta \\ 0 \\ \dot{\nu}\cos\beta + \dot{\psi} \end{bmatrix} \tag{D.5}$$

From Appendix A, we know that for the Likins-Pringle set-up:

$$\dot{\psi} = \frac{\dot{\nu}4\cos\beta(A-C)}{C} \tag{D.6}$$

so the angular momentum can be re-written as

$$^{\hat{b}}\vec{\omega}^{bi} = \begin{bmatrix} \dot{\nu}\sin\beta \\ 0 \\ \dot{\nu}\cos\beta\frac{(4A-3C)}{C} \end{bmatrix} \tag{D.7}$$

With the angular momentum in hand, we calculate the initial velocities using Equations 5.36 and 5.37:

$$^{\hat{i}}\vec{V}_i = {}^{\hat{i}}\vec{V}_{\oplus} + {}^{\hat{i}}\vec{v}_i$$

$$^{\hat{i}}\vec{v}_i = {}^{\hat{i}}\frac{d}{dt}{}^{\hat{b}}\vec{r}_i = {}^{\hat{b}}\frac{d}{dt}{}^{\hat{b}}\vec{r}_i + {}^{\hat{b}}\vec{\omega}^{bi} \times {}^{\hat{b}}\vec{r}_i$$

where ${}^{\hat{b}}\frac{d}{dt}{}^{\hat{b}}\vec{r}_i$ is zero and

$${}^{\hat{b}}\vec{\omega}^{bi} \times {}^{\hat{b}}\vec{r}_1 = \begin{bmatrix} 0 \\ \frac{\sqrt{3}}{3}\rho\dot{\nu}\cos\beta\frac{(4A-3C)}{C} \\ 0 \end{bmatrix}$$

$${}^{\hat{b}}\vec{\omega}^{bi} \times {}^{\hat{b}}\vec{r}_2 = \begin{bmatrix} -\frac{\rho}{2}\dot{\nu}\cos\beta\frac{(4A-3C)}{C} \\ -\frac{\sqrt{3}}{6}\rho\dot{\nu}\cos\beta\frac{(4A-3C)}{C} \\ \frac{\rho}{2}\dot{\nu}\sin\beta \end{bmatrix}$$

What is left for the ${}^{\hat{i}}\vec{v}_i$ terms is still expressed in the body frame coordinates, therefore they must be rotated back into the inertial frame using $C^{ib} = R_2(\beta)$ (for convenience let $s*=sin*$, $c*=cos*$):

$${}^{\hat{i}}\vec{v}_1 = \begin{bmatrix} \mathrm{c}\beta & 0 & -\mathrm{s}\beta \\ 0 & 1 & 0 \\ \mathrm{s}\beta & 0 & \mathrm{c}\beta \end{bmatrix} \begin{bmatrix} 0 \\ \frac{\sqrt{3}}{3}\rho\dot{\nu}\mathrm{c}\beta\frac{(4A-3C)}{C} \\ 0 \end{bmatrix} = \begin{bmatrix} 0 \\ \frac{\sqrt{3}}{3}\rho\dot{\nu}\mathrm{c}\beta\frac{(4A-3C)}{C} \\ 0 \end{bmatrix}$$

$${}^{\hat{i}}\vec{v}_2 = \begin{bmatrix} \mathrm{c}\beta & 0 & -\mathrm{s}\beta \\ 0 & 1 & 0 \\ \mathrm{s}\beta & 0 & \mathrm{c}\beta \end{bmatrix} \begin{bmatrix} -\frac{\rho}{2}\dot{\nu}\mathrm{c}\beta\frac{(4A-3C)}{C} \\ -\frac{\sqrt{3}}{6}\rho\dot{\nu}\mathrm{c}\beta\frac{(4A-3C)}{C} \\ \frac{\rho}{2}\dot{\nu}\mathrm{s}\beta \end{bmatrix} = \begin{bmatrix} -\frac{\rho}{2}\dot{\nu}\mathrm{c}^2\beta\frac{(4A-3C)}{C} - \frac{\rho}{2}\dot{\nu}\mathrm{s}^2\beta \\ -\frac{\sqrt{3}}{6}\rho\dot{\nu}\mathrm{c}\beta\frac{(4A-3C)}{C} \\ -\frac{\rho}{2}\dot{\nu}\mathrm{s}\beta\mathrm{c}\beta\frac{(4A-3C)}{C} + \frac{\rho}{2}\dot{\nu}\mathrm{c}\beta\mathrm{s}\beta \end{bmatrix}$$

The initial velocities take the form

$$
{}^{\hat{i}}\vec{V}_1 = \begin{bmatrix} \dot{X}_\oplus \\ \dot{Y}_\oplus + \frac{\sqrt{3}}{3}\rho\dot{\nu}\cos\beta\frac{(4A-3C)}{C} \\ \dot{Z}_\oplus \end{bmatrix}
$$

$$
{}^{\hat{i}}\vec{V}_2 = \begin{bmatrix} \dot{X}_\oplus - \frac{\rho}{2}\dot{\nu}\mathrm{c}^2\beta\frac{(4A-3C)}{C} - \frac{\rho}{2}\dot{\nu}\mathrm{s}^2\beta \\ \dot{Y}_\oplus - \frac{\sqrt{3}}{6}\rho\dot{\nu}\mathrm{c}\beta\frac{(4A-3C)}{C} \\ \dot{Z}_\oplus - \frac{\rho}{2}\dot{\nu}\mathrm{s}\beta\mathrm{c}\beta\frac{(4A-3C)}{C} + \frac{\rho}{2}\dot{\nu}\mathrm{c}\beta\mathrm{s}\beta \end{bmatrix}
$$

but once again, given the initial set-up of a circular orbit at some altitude $X_\oplus$, the inertial velocities in all but the Y direction are zero ($\dot{X}_\oplus = 0$, $\dot{Z}_\oplus = 0$), while $\dot{Y}_\oplus$ becomes $\sqrt{\frac{\mu_\oplus}{X_\oplus}}$. Furthermore, we know from Equations 5.43 and 5.44 that the ratio of C:A is 2:1, so $\frac{(4A-3C)}{C} = -1$. Finally, we can redefine $\dot{\nu}$ from Equation 5.39 as $\frac{X_\oplus \dot{Y}_\oplus}{X_\oplus^2} = \frac{1}{X_\oplus}\sqrt{\frac{\mu_\oplus}{X_\oplus}}$. Therefore, the initial velocities of these two bodies become:

$$
{}^{\hat{i}}\vec{V}_1 = \begin{bmatrix} 0 \\ \sqrt{\frac{\mu_\oplus}{X_\oplus}} - \frac{\sqrt{3}\rho}{3X_\oplus}\sqrt{\frac{\mu_\oplus}{X_\oplus}}\cos\beta \\ 0 \end{bmatrix} \tag{D.8}
$$

$$
{}^{\hat{i}}\vec{V}_2 = \begin{bmatrix} \frac{\rho}{2X_\oplus}\sqrt{\frac{\mu_\oplus}{X_\oplus}}(2\mathrm{c}^2\beta - 1) \\ \sqrt{\frac{\mu_\oplus}{X_\oplus}} + \frac{\sqrt{3}\rho}{6X_\oplus}\sqrt{\frac{\mu_\oplus}{X_\oplus}}\mathrm{c}\beta \\ \frac{\rho}{X_\oplus}\sqrt{\frac{\mu_\oplus}{X_\oplus}}\mathrm{s}\beta\mathrm{c}\beta \end{bmatrix} \tag{D.9}
$$

With the initial positions and velocities in hand, we now look at the difference in the two bodies' orbital periods. Using the expression for period from Appendix C, we show that $\mathrm{P}_2 = \mathrm{P}_1$ by

$$
2\pi\mu_\oplus\left(-2\left\{\frac{V_1^2}{2} - \frac{\mu_\oplus}{R_1}\right\}\right)^{-\frac{3}{2}} = 2\pi\mu_\oplus\left(-2\left\{\frac{V_2^2}{2} - \frac{\mu_\oplus}{R_2}\right\}\right)^{-\frac{3}{2}} \tag{D.10}
$$

which is equivalent to equating the total energies (E_i):

$$E_1 = E_2$$

$$\frac{V_1^2}{2} - \frac{\mu_\oplus}{R_1} = \frac{V_2^2}{2} - \frac{\mu_\oplus}{R_2} \tag{D.11}$$

where R_i and V_i are the magnitudes of the position (Equations D.3-D.4) and velocity (Equations D.8-D.9) vectors. After making these substitutions, the left side of Equation D.11 (body 1's total energy) becomes

$$E_1 = \frac{\mu_\oplus}{2X_\oplus} - \frac{\sqrt{3}\mu_\oplus \rho \mathrm{c}\beta}{3X_\oplus^2} + \frac{\mu_\oplus \rho^2 \mathrm{c}^2 \beta}{6X_\oplus^3} - \frac{\mu_\oplus}{\sqrt{X_\oplus^2 + \frac{2\sqrt{3}\rho \mathrm{c}\beta X_\oplus}{3} + \frac{\rho^2}{3}}} \tag{D.12}$$

while the right side of Equation D.11 (body 2's total energy) becomes

$$E_2 = \frac{\mu_\oplus}{2X_\oplus} + \frac{\sqrt{3}\mu_\oplus \rho \mathrm{c}\beta}{6X_\oplus^2} + \frac{\mu_\oplus \rho^2 (2\mathrm{c}^2\beta - 1)^2}{8X_\oplus^3} + \frac{\mu_\oplus \rho^2 \mathrm{c}^2 \beta}{24X_\oplus^3}$$

$$+ \frac{\mu_\oplus \rho^2 \mathrm{c}^2 \beta \mathrm{s}^2 \beta}{2X_\oplus^3} - \frac{\mu_\oplus}{\sqrt{X_\oplus^2 - \frac{\sqrt{3}\rho \mathrm{c}\beta X_\oplus}{3} + \frac{\rho^2}{3}}} \tag{D.13}$$

The next step is to evaluate the difference in these two equations.

$$\Delta E = E_1 - E_2$$

This is done by comparing "like" terms. For terms on the order of $\frac{1}{X_\oplus}$, there is no difference between D.12 and D.13:

$$\Delta E_{\left(\frac{1}{X_\oplus}\right)} = \frac{\mu_\oplus}{2X_\oplus} - \frac{\mu_\oplus}{2X_\oplus} = 0 \tag{D.14}$$

For terms on the order of $\frac{\rho}{X_\oplus^2}$, the difference is:

$$\Delta E_{\left(\frac{\rho}{X_\oplus^2}\right)} = -\frac{\sqrt{3}\mu_\oplus \rho \mathrm{c}\beta}{3X_\oplus^2} - \frac{\sqrt{3}\mu_\oplus \rho \mathrm{c}\beta}{6X_\oplus^2} = \frac{-\sqrt{3}\mu_\oplus \rho \mathrm{c}\beta}{2X_\oplus^2} \tag{D.15}$$

For terms on the order of $\frac{\rho^2}{X_\oplus^3}$, the difference is:

$$\begin{aligned}
\Delta E_{\left(\frac{\rho^2}{X_\oplus^3}\right)} &= \frac{\mu_\oplus \rho^2 \mathrm{c}^2\beta}{6X_\oplus^3} - \frac{\mu_\oplus \rho^2 (2\mathrm{c}^2\beta - 1)^2}{8X_\oplus^3} - \frac{\mu_\oplus \rho^2 \mathrm{c}^2\beta}{24X_\oplus^3} - \frac{\mu_\oplus \rho^2 \mathrm{c}^2\beta \mathrm{s}^2\beta}{2X_\oplus^3} \\
&= \frac{\mu_\oplus \rho^2 \mathrm{c}^2\beta}{6X_\oplus^3} - \frac{\mu_\oplus \rho^2 \mathrm{c}^2\beta}{X_\oplus^3}\left(\frac{1}{2}\mathrm{c}^2\beta - \frac{1}{2} + \frac{1}{24} + \frac{1}{2}\mathrm{s}^2\beta\right) - \frac{\mu_\oplus \rho^2}{8X_\oplus^3} \\
&= \frac{\mu_\oplus \rho^2 \mathrm{c}^2\beta}{6X_\oplus^3} - \frac{1}{24}\frac{\mu_\oplus \rho^2 \mathrm{c}^2\beta}{X_\oplus^3} - \frac{\mu_\oplus \rho^2}{8X_\oplus^3} \\
&= \frac{1}{8}\frac{\mu_\oplus \rho^2 \mathrm{c}^2\beta}{X_\oplus^3} - \frac{\mu_\oplus \rho^2}{8X_\oplus^3}
\end{aligned} \tag{D.16}$$

Evaluating the difference between the last two terms of D.12 and D.13 is a little less straightforward:

$$\begin{aligned}
\Delta E_{\left(\frac{1}{\sqrt{\bullet}}\right)} &= -\frac{\mu_\oplus}{\sqrt{X_\oplus^2 + \frac{2\sqrt{3}\rho \mathrm{c}\beta X_\oplus}{3} + \frac{\rho^2}{3}}} + \frac{\mu_\oplus}{\sqrt{X_\oplus^2 - \frac{\sqrt{3}\rho \mathrm{c}\beta X_\oplus}{3} + \frac{\rho^2}{3}}} \\
&= -\mu_\oplus \left(X_\oplus^2 + \frac{2\sqrt{3}\rho \mathrm{c}\beta X_\oplus}{3} + \frac{\rho^2}{3}\right)^{\frac{1}{2}} + \mu_\oplus \left(X_\oplus^2 + \frac{2\sqrt{3}\rho \mathrm{c}\beta X_\oplus}{3} + \frac{\rho^2}{3} - \sqrt{3}\rho \mathrm{c}\beta X_\oplus\right)^{\frac{1}{2}}
\end{aligned} \tag{D.17}$$

For this, we need to expand these terms in powers of $\frac{\rho}{X_\oplus}$ up to order 3. In doing so, we re-write the first term of D.17 as

$$E_{1_{\left(\frac{1}{\sqrt{\bullet}}\right)}} = -\mu_\oplus \left(\frac{1}{X_\oplus} - \frac{\sqrt{3}\rho \mathrm{c}\beta}{3X_\oplus} + \frac{\rho^2}{2X_\oplus^2}\left(\frac{-1}{3X_\oplus} + \frac{\mathrm{c}^2\beta}{X_\oplus}\right) + O\left(\frac{\rho}{X_\oplus}\right)^3\right) \tag{D.18}$$

and the second term of D.17 as

$$E_{2_{\left(\frac{1}{\sqrt{\bullet}}\right)}} = -\mu_{\oplus}\left(\frac{1}{X_{\oplus}} - \frac{\sqrt{3}\rho c\beta}{6X_{\oplus}} + \frac{\rho^2}{2X_{\oplus}^2}\left(\frac{-1}{3X_{\oplus}} + \frac{c^2\beta}{4X_{\oplus}}\right) + O\left(\frac{\rho}{X_{\oplus}}\right)^3\right) \tag{D.19}$$

Note that $\rho << X_{\oplus}$, so the additional term that is on the order of $\left(\frac{\rho}{X_{\oplus}}\right)^3$ is a very small number. Therefore the difference between D.12 and D.13 for the $\frac{1}{\sqrt{\bullet}}$ terms is:

$$\Delta E_{\left(\frac{1}{\sqrt{\bullet}}\right)} = E_{1_{\left(\frac{1}{\sqrt{\bullet}}\right)}} - E_{2_{\left(\frac{1}{\sqrt{\bullet}}\right)}} = \frac{\sqrt{3}\mu_{\oplus}\rho c\beta}{2X_{\oplus}^2} - \frac{3\mu_{\oplus}\rho^2 c^2\beta}{8X_{\oplus}^3} + O\left(\frac{\rho}{X_{\oplus}}\right)^3 \tag{D.20}$$

Combining all of the ΔE's from all of the term-by-term comparisons, we get the total difference in energy ΔE_{tot} between the two bodies:

$$\Delta E_{tot} = \Delta E_{\left(\frac{1}{X_{\oplus}}\right)} + \Delta E_{\left(\frac{\rho}{X_{\oplus}^2}\right)} + \Delta E_{\left(\frac{\rho^2}{X_{\oplus}^3}\right)} + \Delta E_{\left(\frac{1}{\sqrt{\bullet}}\right)} + O\left(\frac{\rho}{X_{\oplus}}\right)^3$$

$$\Delta E_{tot} = -\frac{\sqrt{3}\mu_{\oplus}\rho c\beta}{2X_{\oplus}^2} + \frac{3\mu_{\oplus}\rho^2 c^2\beta}{24X_{\oplus}^3} - \frac{\mu_{\oplus}\rho^2}{8X_{\oplus}^3} + \frac{\sqrt{3}\mu_{\oplus}\rho c\beta}{2X_{\oplus}^2} - \frac{3\mu_{\oplus}\rho^2 c^2\beta}{8X_{\oplus}^3} + O\left(\frac{\rho}{X_{\oplus}}\right)^3$$

$$\Delta E_{tot} = \frac{-\mu_{\oplus}\rho^2 c^2\beta}{4X_{\oplus}^3} - \frac{\mu_{\oplus}\rho^2}{8X_{\oplus}^3} + O\left(\frac{\rho}{X_{\oplus}}\right)^3$$

$$\Delta E_{tot} = \frac{-\mu_{\oplus}\rho^2}{4X_{\oplus}^3}\left(\cos^2\beta + \frac{1}{2}\right) + O\left(\frac{\rho}{X_{\oplus}}\right)^3 \tag{D.21}$$

Notice that this difference in energy is going to be fairly small – on the order of 10^{-5} – for a low earth orbit ($X_{\oplus} = 1.1DU$) and apertures as large as $\rho_o = 10km$, regardless of the cone angle (β). In fact, as the altitude increases or the aperture decreases, the difference in energy gets even smaller. For our sample orbit of $1.1DU$,

the total energy of one of the orbits is on the order of 10^{+2}. This translates into a difference in orbital periods of milliseconds:

$$\Delta P \cong 2\pi\mu_{\oplus}\left((-2E)^{-3/2} - (-2(E+\Delta E))^{-3/2}\right) \approx 10^{-3}\text{secs}$$

Appendix E. Back-of-Envelope Calculations for Kumar Range

This appendix serves as a "back-of-the-envelope" calculation of the range of spin-to-orbit rate ratios (Kumar Range) required for a tethered system to maintain tether tension while in a 0° cone angle configuration.

Recall from Section 5.3.4 the initial configuration as originally shown in Figure 5.29 and shown again here in more detail in Figure E.1

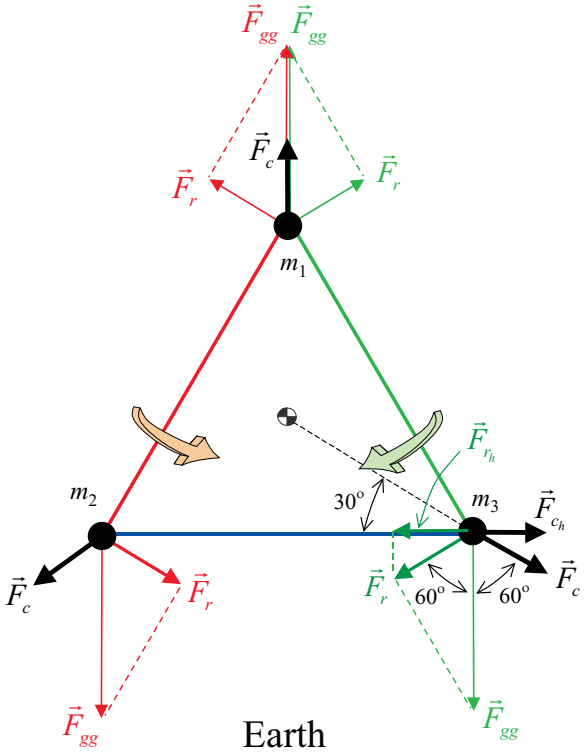


Figure E.1: Centrifugal vs Gravity Gradient Restoring Forces

As discussed in Chapter V, the blue tether is the first to go slack with insufficient spin rate, since it is the most horizontal. We are trying to determine the conditions under which the blue tether will not go slack. To combat this slacking at this moment in time, we need the horizontal component of the centrifugal force (F_{c_h}) to be greater than the horizontal component of the gravity gradient restoring force (F_{r_h}).

$$F_{c_h} > F_{r_h}$$

$$F_c \sin(60^\circ) > F_r \sin(60^\circ)$$

Note that since the angle of F_c and F_r are equal and opposite from the vertical, we can simply say that

$$F_c > F_r \tag{E.1}$$

The restoring force is calculated using an approximation for the gravity gradient force as presented by Cosmo and Lorenzini [12]

$$F_r = F_{gg} \sin(30^\circ) = 3Lm\dot{\nu}^2 \sin(30^\circ)$$

where $\dot{\nu}$ is the orbital angular velocity, m is the mass of one of the bodies, and $L = \frac{\rho}{2}$ is the distance to the tether's CoM which should be the "pivot point" of the gravity gradient restoring motion. It is important to recognize, however, that the two "vertical" tethers (red/green) are anchored together at the top, which creates the pivot point for the gravity gradient restoration and causes the restoring effect to be doubled at the bottom ends of those tethers. This can be interpreted as doubling the restoring force or a doubling of L such that $L = \rho$:

$$F_r = 3\rho m\dot{\nu}^2 \sin(30^\circ)$$

Now, getting the centrifugal force is straightforward:

$$F_c = mr\left(\dot{\psi} + \dot{\nu}\right)^2 = m\frac{\rho}{\sqrt{3}}\left(\dot{\psi} + \dot{\nu}\right)^2$$

where the total "spin" that causes centrifugal force is felt from both the spinning ($\dot{\psi}$) and the orbit rate ($\dot{\nu}$). Therefore, the condition that must be met for the blue tether to remain taut is found by substituting back into Equation E.1:

$$m\frac{\rho}{\sqrt{3}}\left(\dot{\psi}+\dot{\nu}\right)^2 > 3\rho m\dot{\nu}^2\sin(30^\circ) \tag{E.2}$$

Now solve Equation E.2 for the spin-to-orbit rate ratio ($\frac{\dot{\psi}}{\dot{\nu}}$):

$$\frac{\left(\dot{\psi}+\dot{\nu}\right)^2}{\dot{\nu}^2} > \frac{3\sqrt{3}}{2} = 2.598$$

$$\left|\frac{\dot{\psi}+\dot{\nu}}{\dot{\nu}}\right| > 1.61$$

$$\left|\frac{\dot{\psi}}{\dot{\nu}}+1\right| > 1.61$$

So, from this simple calculation, we estimate that the spin-to-orbit rate ratio must be:

$$\frac{\dot{\psi}}{\dot{\nu}} < -2.61 \quad \text{or} \quad 0.61 \; > \frac{\dot{\psi}}{\dot{\nu}} \tag{E.3}$$

which compares quite nicely with the detailed Kumar Range values of -2.58 and 0.58 [26]. Given that the equation for F_{gg} is an approximation for tethers that are close to nadir, this is a decent "back-of-the-envelope" estimation of the Kumar Range considering the relatively simple approach.

Appendix F. MATLAB Code

This appendix holds the main MATLAB® codes that were used in this research. There are two sections of this appendix, each dedicated to a different kind of simulation: the first section contains the semi-rigid body codes, which are simply extension of the rigid body codes. A script file and an EOM file, which houses the equations-of-motion for the main model, are the two files provided in the first section. The second section holds the multi-body system codes. The code "Tether3B" is the main code used for most of the multi-body simulations in this research. It is fairly self-contained and includes its own equations-of-motion.

F.1 Semi-Rigid Body Codes

Listing F.1: This is the script file for the semi-rigid body simulation. (appendixf/code/RBand3fullrotorscript.m)

```
%*****************************************************
% SEMI-RIGID BODY MODEL (3 rotors -- full development)
% Maj Kurt Vogel
% May 2005
%
% This script file sets constants and ICs for ODE45 to integrate
% the EOM for a rigid body using Eulers Equation for angular
% acceleration and Euler Angles for orientation.
%
% In addition, 3 rotors have been added as energy sinks.  They are
% free to spin about the body axes, but with damping.  New states
% are added for the relative spin rates of the rotors.
%
% The state is
%    {phi, theta, psi, w1, w2, w3, sigma1, sigma2, sigma3}'
%       (w in the body frame)
%       (sigma's are the spin velocities of the 3
%        rotors relative to the body frame)
%*****************************************************

clf
clear all
close all

global I I_Inv mu A C nu0 nudot R GG_on mu_d D J

%*****************************************************
% Define constants and initial conditions
```

```
% Orbit
R=9378145; % orbital radius (m)
mu=398600.4418E9; % grav const (m^3/s^2)
nu0=0; % Initial orbital angular position (rad)
nudot=sqrt(mu)/(R^(3/2)); % mean motion (rads/sec)

stepsize=10;
tmax=90000; % total end run time
parts=1; % break up total run into # integration runs
n=tmax/parts; % time part size
sampsize=1; % take every # samples to reduce data memory
tvec=[0:stepsize:2*pi/nudot*1];
% General Oblate SRB -- no L-P
% stepsize=.1; tmax=200; parts=1; n=tmax/parts; sampsize=1;
% General Prolate SRB -- no L-P
% stepsize=1; tmax=1000; parts=1; n=tmax/parts; sampsize=1;

% Moments of Inertia
A=10; % kg*m^2
C=50; % kg*m^2
D=1;
J=.0001;
I=[A 0 0;0 A 0;0 0 C];
I_Inv=inv(I);
if A>C
    body='Prolate'
elseif A==C
    body='Equal MOI Axes'
else
    body='Oblate'
end

% Initial Euler Angles and rates
% phi0=nu0+0;
% theta0=45*pi/180;
% psi0=0;
% phidot0=.2;
% thetadot0=0;
% psidot0=.5;
% %% For Likins-Pringle
phi0=nu0+0;
theta0=45*pi/180;
psi0=0;
phidot0=nudot;
thetadot0=0;
psidot0=(-nudot*cos(theta0)*4*(C-A)/C);

%*************************************************
% Other Settings

% Gravity Gradient Torques
GG_on=1;  % 1=on 0=off
```

```
GG='Gravity Off';
if GG_on == 1
    GG='Gravity On';
end

% Energy Sink Stuff
mu_d=.5;  % N-m-s   or   kg-m^2/s
sigma1_0=psidot0*0;
sigma2_0=psidot0*0;
sigma3_0=psidot0*0;

%*****************************************************
% Initialize State
K0=[sin(psi0)*sin(theta0) cos(psi0) 0;
    cos(psi0)*sin(theta0) -sin(psi0) 0;
    cos(theta0) 0 1];
w0=K0*[phidot0,thetadot0,psidot0]';
x0=[phi0,theta0,psi0,w0(1),w0(2),w0(3),...
        sigma1_0,sigma2_0,sigma3_0]';

%*****************************************************
% Run integrator

options = odeset('MaxStep',stepsize);

for i=1:parts % running integrator one part at a time
tvec=[(i-1)*n:stepsize:i*n];
[tp,Xp]=ode45(@rb_3fullrot_eom,tvec,x0,options);
x0=[Xp(length(tp),1),Xp(length(tp),2),Xp(length(tp),3),...
    Xp(length(tp),4),Xp(length(tp),5),Xp(length(tp),6),...
    Xp(length(tp),7),Xp(length(tp),8),Xp(length(tp),9)]';

%% uncomment this if you want to look at all parts...
% downsampled state vector for this part only
Xtemp=downsample(Xp,sampsize);
% downsampled time vector for this part only
td=downsample(tp,sampsize);
if i==1
    X=Xtemp;
    t=td;
else
    X=[X;Xtemp(2:(length(Xtemp(:,1))),:)];
    t=[t;td(2:(length(td)),:)];
end

%% uncomment these lines if just want to look at last 3 parts
% if i>=(parts-3)
%     if i==(parts-3)
%         X=Xp;
%         t=tp;
%     else
%         X=[X;Xp];
```

```
%          t=[t;tp];
%      end
% end
%%
end

%*******************************************************
% Calc H (ang momentum)

w=(X(:,4:6));
H_b=(I*w')'; % Can only
H_r=[D*X(:,7),D*X(:,8),D*X(:,9)]+((D+2*J)*w); % Rotors only
H=H_b+H_r; % Whole system

%*******************************************************
% Express w & H in inertial frame
% (rotate from b-frame to i-frame)

for i=1:length(t)
    R3psi=[cos(X(i,3)) sin(X(i,3)) 0;
           -sin(X(i,3)) cos(X(i,3)) 0;
           0 0 1];
    R1theta=[1 0 0;
             0 cos(X(i,2)) sin(X(i,2));
             0 -sin(X(i,2)) cos(X(i,2))];
    R3phi=[cos(X(i,1)) sin(X(i,1)) 0;
           -sin(X(i,1)) cos(X(i,1)) 0;
           0 0 1];
    C_ib=[R3psi*R1theta*R3phi]';
    w_i(i,1:3)=(C_ib*w(i,1:3)')';
    H_i(i,1:3)=(C_ib*H(i,1:3)')';
    b3_i(i,1:3)=(C_ib*[0,0,1]')';
end

%*******************************************************
% Calculate total system kinetic energy over time

for i=1:length(t)
    KE(i)=0.5*((w(i,1:3)*I*w(i,1:3)')+ ...;
         (2*J*(w(i,1)^2+w(i,2)^2+w(i,3)^2))+...;
         (D*((w(i,1)+X(i,7))^2+(w(i,2)+X(i,8))^2+...
         (w(i,3)+X(i,9))^2)));
end

%*******************************************************
% Express b3 in orbit frame
% [0 0 1] in b=[-sin(theta)*sin(nu-phi) -sin(theta)*cos(nu-phi)
% cos(theta)] in e

for i=1:length(t)
    nu(i)=(nudot*t(i))+nu0;
    b3_e(i,1:3)=[-sin(X(i,2))*sin(nu(i)-X(i,1))...
```

```
                -sin(X(i,2))*cos(nu(i)-X(i,1))...
                 cos(X(i,2))];
end

nod=(asin(max(b3_e(:,3)))-asin(min(b3_e(:,3))))*180/pi;
shake=(asin(max(b3_e(:,1)))+abs(asin(min(b3_e(:,1)))))*180/pi;
```

Listing F.2: This next routine holds the equations of motion for the ODE45 integrator on the semi-rigid body simulation.
(appendixf/code/rb3fullroteom.m)

```
function xdot=rb_3fullrot_eom(t,x)
global I I_Inv mu A C nu0 nudot R GG_on mu_d D J

%*****************************************************
% Maj Kurt Vogel
% May 2005
% This function propagates the EOM for a rigid body using
% Eulers Equation for angular acceleration and Euler Angles for
% orientation. In addition, a 3 orthonormal rotors have been
% added as an energy sink.
% The state is
% {phi, theta, psi, w1, w2, w3, sigma1, sigma2, sigma3}'
%       (w in the body frame)
%       (sigma's are the spin velocities of the 3
%          rotors relative to the body frame)
%*****************************************************

%*****************************************************
%  Compute applied torgues due to gravity gradient

% No torque for now...
M1=0;
M2=0;
M3=0;

if GG_on == 1
    % (using position of RB seen from inertial earth i-frame ...
       expressed in b-frame)
    nu=(nudot*t)+nu0;
    Xb=-R*((sin(nu)*cos(x(3))*cos(x(1)))-(sin(nu)*cos(x(2))*...
        sin(x(3))*sin(x(1)))-(cos(nu)*cos(x(3))*sin(x(1)))-...
        (cos(nu)*cos(x(2))*sin(x(3))*cos(x(1))));
    Yb=R*((sin(nu)*sin(x(3))*cos(x(1)))+(sin(nu)*cos(x(2))*...
        cos(x(3))*sin(x(1)))-(cos(nu)*sin(x(3))*sin(x(1)))+...
        (cos(nu)*cos(x(2))*cos(x(3))*cos(x(1))));
    Zb=-R*((sin(nu)*sin(x(2))*sin(x(1)))+(cos(nu)*sin(x(2))*...
        cos(x(1))));
    M1=3*mu*Yb*Zb*(C-A)/(R^5);
```

```
        M2=3*mu*Xb*Zb*(A-C)/(R^5);
        M3=0;
end

M=[M1 M2 M3]';

%*****************************************************
%  Equations of Motion for Euler Angles (Orientation)

K_Inv=[sin(x(3))/sin(x(2)) cos(x(3))/sin(x(2)) 0;
       cos(x(3)) -sin(x(3)) 0;
       -sin(x(3))*cos(x(2))/sin(x(2))...
           -cos(x(3))*cos(x(2))/sin(x(2)) 1];
Edot=K_Inv*[x(4) x(5) x(6)]';

%*****************************************************
%  Equations of Motion for Euler Equation (Angular Acceleration)

w1dot=(M1/(A+(2*J)))+(((A-C)*x(5)*x(6))+(D*x(6)*x(8))-...
    (D*x(5)*x(9))+(mu_d*x(7)))/(A+(2*J));
w2dot=(M2/(A+(2*J)))+(((C-A)*x(4)*x(6))-(D*x(6)*x(7))+...
    (D*x(4)*x(9))+(mu_d*x(8)))/(A+(2*J));
w3dot=(M3/(C+(2*J)))+((D*x(5)*x(7))-(D*x(4)*x(8))+...
    (mu_d*x(9)))/(C+(2*J));
sig1dot=-(w1dot)-(mu_d*x(7)/D);
sig2dot=-(w2dot)-(mu_d*x(8)/D);
sig3dot=-(w3dot)-(mu_d*x(9)/D);

%*****************************************************
% Total EOM

xdot=[Edot;w1dot;w2dot;w3dot;sig1dot;sig2dot;sig3dot];
```

F.2 Multi-Body System Codes

Listing F.3: This is the main model for a three-body system coupled by elastic, linear tethers.
(appendixf/code/Tether3B.m)

```
%*******************************************************
% Three-body System Model with Elastic, Linear Tethers
% LtCol Kurt Vogel
% Nov 2005 -Mar 2006
%
% The routine simulates three bodies connected by
% tethers in earth orbit.  There are options in the EOM to change
% the linear tethers into springs, thrusters, non-linear tethers,
% and variable-length tethers.  J2 Perturbations can be
% selectively turned on/off.  In addition, this model is easily
% modified to create more bodies and tethers.
%
% The state is {Rx1,Ry1,Rz1,Vx1,Vy1,Vz1,Rx2,Ry2,Rz2,
%               Vx2,Vy2,Vz2,Rx3,Ry3,Rz3,Vx3,Vy3,Vz3}'
%*******************************************************

% NOTE: To create the 4B HAS, 6B Ring, and 7B CHAS Models, this
% code was used as a basis.  Additional masses, states, tether
% vector lines, etc were added as required and saved as other
% files.

function dummy_output=Tether_3B;  % This is the 'script' function

    disp(['Start of program run ', datestr(now)]);
    clf; clear all; close all;
    format long;

    %*******************************************************
    % Define constants and settings

    global m1 m2 m3 mu_damp Re J2 K_spring rho_o mu_earth beta_ic...
        ...
         pick_f thresh num_firings programmed_rhos;
    m1 = 200;                    % kg
    m2 = 200;                    % kg
    m3 = 200;                    % kg
    mu_damp = .05;               % kg/s
    K_spring = 20;               % kg/s^2
    rho_o = 10.0;                % km (unstretched tether length)
    mu_earth = 398600.4415e0;    % km^3 / sec^2
    Re = 6378.13655;             % km
    J2 = 0.1082626925638815e-2; %
    tf=400  ;                    % sec
    stepsize = .1;               % sec
    samplesize = 1;              % number of steps between samples
    num_iterations=floor(tf/(samplesize*stepsize))+1;
```

```
pick_f = 'e';                % reference frame for plots
%                            e=orbit
%                            s=stroboscopic
%                            i=inertial
num_firings=0;               % if using thrusters
thresh=.0001;                % threshold for thruster firing
                             % to create spring compression

%*****************************************************
% Set initial conditions in Generalized Coords (assumes
% perfect equilateral triangle for initial conditions)

rho_ic = 10.5;                          % km
alpha_ic = 75 * pi/180.;                % deg -> rad
beta_ic = 0 * pi/180;                   % deg -> rad
rho_dot_ic = 0;                         % km/sec
alpha_dot_ic = 5 * pi/180               % deg/sec -> rad/sec
beta_dot_ic = 0 * pi/180;               % deg/sec -> rad/sec
R_c_ic = [1.1 0 0]*Re;                  % DU -> km
V_c_ic = [0 sqrt(mu_earth/norm(R_c_ic)) 0]; % km/s

% Diagnostic for looking at Thompson-like scenarios
%         H=cross(R_c_ic,V_c_ic);
%         nu_dot=norm(H)/((norm(R_c_ic))^2)
%         spin_ratio=alpha_dot_ic/nu_dot

% Convert from Generalized Coords to Newtonian State
State=Gen_Coord_2_State(rho_ic, alpha_ic, beta_ic,...
    rho_dot_ic, alpha_dot_ic, beta_dot_ic, R_c_ic, V_c_ic);

%*****************************************************
% Uncomment these next lines for L-P Initial Conditions
% (overrides the I.C.'s from above)

tf=10000;                   % sec
stepsize = 1;               % sec
samplesize = 1;             % number of steps between samples
num_iterations=floor(tf/(samplesize*stepsize))+1;

% Read in L-P ICs that were generated with GET3BLPICs.m
load 3B_LP_ICs.mat Initial_State rho_ic alpha_ic beta_ic...
                   R_c_ic V_c_ic spin_ratio
State=Initial_State;

%*****************************************************
% Read in pre-programmed tether lengths
% (basically loading a baseline run from an E.C.)
%
%     load 3B_data_case27_1sec_sample.mat All_VOI
%     programmed_rhos=All_VOI(:,19:21);

%*****************************************************
```

```
% Run integrator

t=0;
count=1;
sample=0;
All_States=zeros(num_iterations,19);
All_VOI=zeros(num_iterations,25);
All_States(count,:)=[State, t];
[R_c, V_c, r1_f, r2_f, r3_f, h_f, rho_12, rho_23, rho_31,...
    rho_12_dot, rho_23_dot, rho_31_dot]=State_2_VOI(State);
All_VOI(count,:)=[R_c, V_c, r1_f, r2_f, r3_f, h_f, rho_12,...
    rho_23, rho_31, rho_12_dot, rho_23_dot, rho_31_dot, t];

while t<tf
NewState=RK4(State,stepsize,t);
t=t+stepsize;
sample=sample+1;

if sample==samplesize  % Only look at sampled data
    count=count+1;
    sample=0;
    All_States(count,:)=[NewState, t];

    % Convert from State to Variables of Interest (VOI)
    [R_c, V_c, r1_f, r2_f, r3_f, h_f, rho_12, rho_23, rho_31...
       ,...
     rho_12_dot, rho_23_dot, rho_31_dot]=State_2_VOI(NewState)...
        ;
    All_VOI(count,:)=[R_c, V_c, r1_f, r2_f, r3_f, h_f, rho_12...
       ,...
     rho_23, rho_31, rho_12_dot, rho_23_dot, rho_31_dot, t];
end

State=NewState;
end % iteration loop

num_firings
total_delta_V=(num_firings*K_spring*thresh/m1)*1000*stepsize

%*****************************************************
% Save data for use outside of program (re-runs later)

save 3B_data.mat All_VOI m1 m2 m3 mu_damp K_spring rho_o tf...
   stepsize rho_ic alpha_ic beta_ic rho_dot_ic alpha_dot_ic...
   beta_dot_ic R_c_ic V_c_ic All_States samplesize pick_f

%*****************************************************
% Plots -- Not included here for brevity

disp(['End of program run ', datestr(now)]);
return;  % End of Script File
```

```
%#############################################################
% Sub-Functions
%#############################################################

% Converts Generalized Initial Coords to Newtonian State
function State=Gen_Coord_2_State(rho, alpha, beta, rho_dot,...
                                 alpha_dot, beta_dot, R_c, V_c);
    global m1 m2 m3 mu_damp Re J2 K_spring rho_o mu_earth...
        beta_ic pick_f thresh num_firings programmed_rhos;
    nu=atan2(R_c(2),R_c(1));
    C2=Rot_2(beta);
    C3=Rot_3(-(nu+alpha));
    C_ib=C3*C2;
    C_bi=inv(C_ib);
    C2=Rot_2(-beta);
    C3=Rot_3(alpha);
    C_be=C2*C3;
    r1_b=[(rho*sqrt(3)/3) 0 0]';
    r2_b=[-(rho*sqrt(3)/6) (rho/2) 0]';
    r3_b=[-(rho*sqrt(3)/6) -(rho/2) 0]';
    r1_i=C_ib*r1_b;
    r2_i=C_ib*r2_b;
    r3_i=C_ib*r3_b;
    R1_i=R_c'+r1_i;
    R2_i=R_c'+r2_i;
    R3_i=R_c'+r3_i;

    H=cross(R_c,V_c);
    nu_dot=norm(H)/((norm(R_c))^2);
    omega_bi_b=(C_bi*[0 0 nu_dot]')+(C_be*[0 0 alpha_dot]')+...
               [0 beta_dot 0]';
    v1_i=C_ib*([(rho_dot*sqrt(3)/3) 0 0]'+cross(omega_bi_b,r1_b));
    v2_i=C_ib*([-(rho_dot*sqrt(3)/6) (rho_dot/2) 0]'+...
         cross(omega_bi_b,r2_b));
    v3_i=C_ib*([-(rho_dot*sqrt(3)/6) -(rho_dot/2) 0]'+...
         cross(omega_bi_b,r3_b));
    V1_i=V_c'+v1_i;
    V2_i=V_c'+v2_i;
    V3_i=V_c'+v3_i;

    State(1:18)=[R1_i; V1_i; R2_i; V2_i; R3_i; V3_i]';
return;

% Propagator
function NewState=RK4(State,stepsize,t);
    State_dot_temp=EOM(State,t);
    k1=stepsize*State_dot_temp;

    State_temp=State+(0.5*k1);
    State_dot_temp=EOM(State_temp,t);
    k2=stepsize*State_dot_temp;
```

```
        State_temp=State+(0.5*k2);
200     State_dot_temp=EOM(State_temp,t);
        k3=stepsize*State_dot_temp;

        State_temp=State+k3;
        State_dot_temp=EOM(State_temp,t);
205     k4=stepsize*State_dot_temp;

        NewState=State+(k1+(2*k2)+(2*k3)+k4)/6;

    return;
210
    % Converts Newtonian States to Variables of Interest (VOI)
    function [R_c, V_c, r1_f, r2_f, r3_f, h_f, rho_12, rho_23, rho_31...
        ,...
            rho_12_dot, rho_23_dot, rho_31_dot]=State_2_VOI(State);
        global m1 m2 m3 mu_damp Re J2 K_spring rho_o mu_earth ...
215          beta_ic pick_f thresh num_firings programmed_rhos;
        % position and velocity of COM
        R_c=(State(1:3)*(m1/(m1+m2+m3)))+(State(7:9)*...
            (m2/(m1+m2+m3)))+(State(13:15)*(m3/(m1+m2+m3)));
        V_c=(State(4:6)*(m1/(m1+m2+m3)))+(State(10:12)*...
220         (m2/(m1+m2+m3)))+(State(16:18)*(m3/(m1+m2+m3)));
        % position (rel to COM) and velocity of each mass
        r1_i=State(1:3)-R_c;
        r2_i=State(7:9)-R_c;
        r3_i=State(13:15)-R_c;
225     v1_i_i=State(4:6)-V_c;
        v2_i_i=State(10:12)-V_c;
        v3_i_i=State(16:18)-V_c;
        % Define positions in orbit frame (e-frame)
        %           or stroboscopic frame (s-frame)
230     %               or inertial frame (i-frame)
        nu=atan2(R_c(2),R_c(1));
        C_ei=Rot_3(nu);
        r1_f=[C_ei*r1_i']';                 % default is orbit frame
        r2_f=[C_ei*r2_i']';
235     r3_f=[C_ei*r3_i']';
        if pick_f == 's'
            C_se=Rot_2(-beta_ic);
            r1_f=[C_se*r1_f']';
            r2_f=[C_se*r2_f']';
240         r3_f=[C_se*r3_f']';
        end
        if pick_f == 'i'
            r1_f=r1_i;
            r2_f=r2_i;
245         r3_f=r3_i;
        end
        % Calulate system "spin axis" (local ang mom) in orbit frame
        %                                       or stroboscopic frame
        %                                           or inertial frame
```

```
250     h1_i_i=m1*cross(r1_i,v1_i_i);
        h2_i_i=m2*cross(r2_i,v2_i_i);
        h3_i_i=m3*cross(r3_i,v3_i_i);
        h_i_i=[h1_i_i+h2_i_i+h3_i_i]';
        h_i_e=C_ei*h_i_i;
255     h_f=h_i_e';                         % default is orbit frame
        if pick_f == 's'
            h_f=[C_se*h_i_e]';
        end
        if pick_f == 'i'
260         h_f=h_i_i';
        end
        % Calculate tether lengths (rho's) change in
        % lengths (rho_dot's)
        r12=State(7:9)-State(1:3);
265     r23=State(13:15)-State(7:9);
        r31=State(1:3)-State(13:15);
        rho_12=norm(r12);
        rho_23=norm(r23);
        rho_31=norm(r31);
270     v21=State(10:12)-State(4:6);
        v13=State(4:6)-State(16:18);
        v32=State(16:18)-State(10:12);
        rho_12_dot=dot(r12,v21)/rho_12;
        rho_31_dot=dot(r31,v13)/rho_31;
275     rho_23_dot=dot(r23,v32)/rho_23;
    return;

    % Equations of Motion
    function X_dot=EOM(X,t);
280     global m1 m2 m3 mu_damp Re J2 K_spring rho_o mu_earth...
            beta_ic pick_f thresh num_firings programmed_rhos;
        X_dot(1:18)=zeros(1,18);
        % Velocities
        R1_dot=X(4:6);
285     R2_dot=X(10:12);
        R3_dot=X(16:18);
        % Calculate tether lengths (rho's) change in
        % lengths (rho_dot's)
        r12=X(7:9)-X(1:3);
290     r23=X(13:15)-X(7:9);
        r31=X(1:3)-X(13:15);
        rho_12=norm(r12);
        rho_23=norm(r23);
        rho_31=norm(r31);
295     v21=X(10:12)-X(4:6);
        v13=X(4:6)-X(16:18);
        v32=X(16:18)-X(10:12);
        rho_12_dot=dot(r12,v21)/rho_12;
        rho_31_dot=dot(r31,v13)/rho_31;
300     rho_23_dot=dot(r23,v32)/rho_23;
        % Accelerations
```

```
        V1_dot=[0 0 0];
        V2_dot=[0 0 0];
        V3_dot=[0 0 0];
305     % Gravity
        V1_dot=V1_dot-((mu_earth/((norm(X(1:3)))^3))*X(1:3));
        V2_dot=V2_dot-((mu_earth/((norm(X(7:9)))^3))*X(7:9));
        V3_dot=V3_dot-((mu_earth/((norm(X(13:15)))^3))*X(13:15));

310 % Select which forces you want to model by uncommenting below...

    %####################  Standard Tether for fixed length  ########
        if rho_12>=rho_o        % Spring
            V1_dot=V1_dot+(K_spring*(rho_12-rho_o)/(m1*rho_12))*r12;
315         V2_dot=V2_dot-(K_spring*(rho_12-rho_o)/(m2*rho_12))*r12;
            if rho_12_dot>0             % Damper
                V1_dot=V1_dot+(mu_damp*rho_12_dot/m1*rho_12)*r12;
                V2_dot=V2_dot-(mu_damp*rho_12_dot/m2*rho_12)*r12;
            end
320     end
        if rho_23>=rho_o        % Spring
            V2_dot=V2_dot+(K_spring*(rho_23-rho_o)/(m2*rho_23))*r23;
            V3_dot=V3_dot-(K_spring*(rho_23-rho_o)/(m3*rho_23))*r23;
            if rho_23_dot>0             % Damper
325             V2_dot=V2_dot+(mu_damp*rho_23_dot/m2*rho_23)*r23;
                V3_dot=V3_dot-(mu_damp*rho_23_dot/m3*rho_23)*r23;
            end
        end
        if rho_31>=rho_o        % Spring
330         V3_dot=V3_dot+(K_spring*(rho_31-rho_o)/(m3*rho_31))*r31;
            V1_dot=V1_dot-(K_spring*(rho_31-rho_o)/(m1*rho_31))*r31;
            if rho_31_dot>0             % Damper
                V3_dot=V3_dot+(mu_damp*rho_31_dot/m3*rho_31)*r31;
                V1_dot=V1_dot-(mu_damp*rho_31_dot/m1*rho_31)*r31;
335         end
        end
    %####################  Full Spring for fixed length  ############

            % Spring
340         V1_dot=V1_dot+(K_spring*(rho_12-rho_o)/(m1*rho_12))*r12;
            V2_dot=V2_dot-(K_spring*(rho_12-rho_o)/(m2*rho_12))*r12;
                % Damper
                V1_dot=V1_dot+(mu_damp*rho_12_dot/m1*rho_12)*r12;
                V2_dot=V2_dot-(mu_damp*rho_12_dot/m2*rho_12)*r12;
345         % Spring
            V2_dot=V2_dot+(K_spring*(rho_23-rho_o)/(m2*rho_23))*r23;
            V3_dot=V3_dot-(K_spring*(rho_23-rho_o)/(m3*rho_23))*r23;
                % Damper
                V2_dot=V2_dot+(mu_damp*rho_23_dot/m2*rho_23)*r23;
350             V3_dot=V3_dot-(mu_damp*rho_23_dot/m3*rho_23)*r23;
            % Spring
            V3_dot=V3_dot+(K_spring*(rho_31-rho_o)/(m3*rho_31))*r31;
            V1_dot=V1_dot-(K_spring*(rho_31-rho_o)/(m1*rho_31))*r31;
```

```
            % Damper
            V3_dot=V3_dot+(mu_damp*rho_31_dot/m3*rho_31)*r31;
            V1_dot=V1_dot-(mu_damp*rho_31_dot/m1*rho_31)*r31;

%####################  Tether for a programmed length  ############
% without deadband added

    if rho_12>=programmed_rhos(t+1,1)       % Spring
        V1_dot=V1_dot+(K_spring*(rho_12-programmed_rhos(t+1,1))...
           /...
            (m1*rho_12))*r12;
        V2_dot=V2_dot-(K_spring*(rho_12-programmed_rhos(t+1,1))...
           /...
            (m2*rho_12))*r12;
        if rho_12_dot>0           % Damper
            V1_dot=V1_dot+(mu_damp*rho_12_dot/m1*rho_12)*r12;
            V2_dot=V2_dot-(mu_damp*rho_12_dot/m2*rho_12)*r12;
        end
    end
    if rho_23>=programmed_rhos(t+1,2)       % Spring
        V2_dot=V2_dot+(K_spring*(rho_23-programmed_rhos(t+1,2))...
           /...
            (m2*rho_23))*r23;
        V3_dot=V3_dot-(K_spring*(rho_23-programmed_rhos(t+1,2))...
           /...
            (m3*rho_23))*r23;
        if rho_23_dot>0          % Damper
            V2_dot=V2_dot+(mu_damp*rho_23_dot/m2*rho_23)*r23;
            V3_dot=V3_dot-(mu_damp*rho_23_dot/m3*rho_23)*r23;
        end
    end
    if rho_31>=programmed_rhos(t+1,3)        % Spring
        V3_dot=V3_dot+(K_spring*(rho_31-programmed_rhos(t+1,3))...
           /...
            (m3*rho_31))*r31;
        V1_dot=V1_dot-(K_spring*(rho_31-programmed_rhos(t+1,3))...
           /...
            (m1*rho_31))*r31;
        if rho_31_dot>0           % Damper
            V3_dot=V3_dot+(mu_damp*rho_31_dot/m3*rho_31)*r31;
            V1_dot=V1_dot-(mu_damp*rho_31_dot/m1*rho_31)*r31;
        end
    end

%################  Full Spring for a programmed length  ##########
% with deadband added
     if (abs(rho_12-programmed_rhos(t+1,1)))>=.00001
        % Spring
        V1_dot=V1_dot+(K_spring*(rho_12-programmed_rhos(t+1,1))...
           /...
            (m1*rho_12))*r12;
```

```
            V2_dot=V2_dot-(K_spring*(rho_12-programmed_rhos(t+1,1))...
                /...
                 (m2*rho_12))*r12;
                 % Damper
                 V1_dot=V1_dot+(mu_damp*rho_12_dot/m1*rho_12)*r12;
                 V2_dot=V2_dot-(mu_damp*rho_12_dot/m2*rho_12)*r12;
        end
        if (abs(rho_23-programmed_rhos(t+1,2)))>=.00001
            % Spring
            V2_dot=V2_dot+(K_spring*(rho_23-programmed_rhos(t+1,2))...
                /...
                 (m2*rho_23))*r23;
            V3_dot=V3_dot-(K_spring*(rho_23-programmed_rhos(t+1,2))...
                /...
                 (m3*rho_23))*r23;
                 % Damper
                 V2_dot=V2_dot+(mu_damp*rho_23_dot/m2*rho_23)*r23;
                 V3_dot=V3_dot-(mu_damp*rho_23_dot/m3*rho_23)*r23;
        end
        if (abs(rho_31-programmed_rhos(t+1,3)))>=.00001
            % Spring
            V3_dot=V3_dot+(K_spring*(rho_31-programmed_rhos(t+1,3))...
                /...
                 (m3*rho_31))*r31;
            V1_dot=V1_dot-(K_spring*(rho_31-programmed_rhos(t+1,3))/(...
                m1*rho_31))*r31;
                 % Damper
                 V3_dot=V3_dot+(mu_damp*rho_31_dot/m3*rho_31)*r31;
                 V1_dot=V1_dot-(mu_damp*rho_31_dot/m1*rho_31)*r31;
        end


%################  Thrusters for Compression (fixed length) #####

       if rho_12>=rho_o       % Spring
            V1_dot=V1_dot+(K_spring*(rho_12-rho_o)/(m1*rho_12))*r12;
            V2_dot=V2_dot-(K_spring*(rho_12-rho_o)/(m2*rho_12))*r12;
            if rho_12_dot>0          % Damper
                 V1_dot=V1_dot+(mu_damp*rho_12_dot/m1*rho_12)*r12;
                 V2_dot=V2_dot-(mu_damp*rho_12_dot/m2*rho_12)*r12;
            end
       elseif rho_12<=(rho_o-1*thresh)       % Thruster
            V1_dot=V1_dot-(K_spring*(thresh)/(m1*rho_12))*r12;
            V2_dot=V2_dot+(K_spring*(thresh)/(m2*rho_12))*r12;
            num_firings=num_firings+2;
       end
       if rho_23>=rho_o  % Spring
            V2_dot=V2_dot+(K_spring*(rho_23-rho_o)/(m2*rho_23))*r23;
            V3_dot=V3_dot-(K_spring*(rho_23-rho_o)/(m3*rho_23))*r23;
            if rho_23_dot>0  % Damper
                 V2_dot=V2_dot+(mu_damp*rho_23_dot/m2*rho_23)*r23;
                 V3_dot=V3_dot-(mu_damp*rho_23_dot/m3*rho_23)*r23;
```

```
445         end
        elseif rho_23<=(rho_o-1*thresh)         % Thruster
            V2_dot=V2_dot-(K_spring*(thresh)/(m2*rho_23))*r23;
            V3_dot=V3_dot+(K_spring*(thresh)/(m3*rho_23))*r23;
            num_firings=num_firings+2;
450     end
        if rho_31>=rho_o  % Spring
            V3_dot=V3_dot+(K_spring*(rho_31-rho_o)/(m3*rho_31))*r31;
            V1_dot=V1_dot-(K_spring*(rho_31-rho_o)/(m1*rho_31))*r31;
            if rho_31_dot>0     % Damper
455             V3_dot=V3_dot+(mu_damp*rho_31_dot/m3*rho_31)*r31;
                V1_dot=V1_dot-(mu_damp*rho_31_dot/m1*rho_31)*r31;
            end
        elseif rho_31<=(rho_o-1*thresh)         % Thruster
            V3_dot=V3_dot-(K_spring*(thresh)/(m3*rho_31))*r31;
460         V1_dot=V1_dot+(K_spring*(thresh)/(m1*rho_31))*r31;
            num_firings=num_firings+2;
        end
    %#################################################################

465 % ###################  Non-Linear Springs  ###############
        if rho_12>=rho_o  % Spring
            V1_dot=V1_dot+(K_spring*((rho_12-rho_o)^2)/...
                (m1*rho_12))*r12;
            V2_dot=V2_dot-(K_spring*((rho_12-rho_o)^2)/...
470             (m2*rho_12))*r12;
            if rho_12_dot>0     % Damper
                V1_dot=V1_dot+(mu_damp*rho_12_dot/m1*rho_12)*r12;
                V2_dot=V2_dot-(mu_damp*rho_12_dot/m2*rho_12)*r12;
            end
475     end
        if rho_23>=rho_o  % Spring
            V2_dot=V2_dot+(K_spring*((rho_23-rho_o)^2)/...
                (m2*rho_23))*r23;
            V3_dot=V3_dot-(K_spring*((rho_23-rho_o)^2)/...
480             (m3*rho_23))*r23;
            if rho_23_dot>0     % Damper
                V2_dot=V2_dot+(mu_damp*rho_23_dot/m2*rho_23)*r23;
                V3_dot=V3_dot-(mu_damp*rho_23_dot/m3*rho_23)*r23;
            end
485     end
        if rho_31>=rho_o  % Spring
            V3_dot=V3_dot+(K_spring*((rho_31-rho_o)^2)/...
                (m3*rho_31))*r31;
            V1_dot=V1_dot-(K_spring*((rho_31-rho_o)^2)/...
490             (m1*rho_31))*r31;
            if rho_31_dot>0     % Damper
                V3_dot=V3_dot+(mu_damp*rho_31_dot/m3*rho_31)*r31;
                V1_dot=V1_dot-(mu_damp*rho_31_dot/m1*rho_31)*r31;
            end
495     end
    %#################################################################
```

```
%## Individual Variable Length Tethers for constant tension ###
% Note: the main code would need modification to accommodate
% this addition.  Specifically, independent variable rho values
% would need to be defined and carried globally.  This was done
% in a separate code, but the key portion of the model is shown
% here.
    if rho_12>=rho1_o  % Spring
        V1_dot=V1_dot+(K_spring*(rho_12-rho1_o)/(m1*rho_12))*r12;
        V2_dot=V2_dot-(K_spring*(rho_12-rho1_o)/(m2*rho_12))*r12;
        if rho_12_dot>0     % Damper
            V1_dot=V1_dot+(mu_damp*rho_12_dot/m1*rho_12)*r12;
            V2_dot=V2_dot-(mu_damp*rho_12_dot/m2*rho_12)*r12;
        end
        if (K_spring*(rho_12-rho1_o))>=high_tension;
            rho1_o=rho1_o+reelout;
        end
    elseif rho1_o>0
        rho1_o=rho1_o-reelin;
    end
    if rho_23>=rho2_o  % Spring
        V2_dot=V2_dot+(K_spring*(rho_23-rho2_o)/(m2*rho_23))*r23;
        V3_dot=V3_dot-(K_spring*(rho_23-rho2_o)/(m3*rho_23))*r23;
        if rho_23_dot>0     % Damper
            V2_dot=V2_dot+(mu_damp*rho_23_dot/m2*rho_23)*r23;
            V3_dot=V3_dot-(mu_damp*rho_23_dot/m3*rho_23)*r23;
        end
        if (K_spring*(rho_23-rho2_o))>=high_tension;
            rho2_o=rho2_o+reelout;
        end
    elseif rho2_o>0
        rho2_o=rho2_o-reelin;
    end
    if rho_31>=rho3_o  % Spring
        V3_dot=V3_dot+(K_spring*(rho_31-rho3_o)/(m3*rho_31))*r31;
        V1_dot=V1_dot-(K_spring*(rho_31-rho3_o)/(m1*rho_31))*r31;
        if rho_31_dot>0     % Damper
            V3_dot=V3_dot+(mu_damp*rho_31_dot/m3*rho_31)*r31;
            V1_dot=V1_dot-(mu_damp*rho_31_dot/m1*rho_31)*r31;
        end
        if (K_spring*(rho_31-rho3_o))>=high_tension;
            rho3_o=rho3_o+reelout;
        end
    elseif rho3_o>0
        rho3_o=rho3_o-reelin;
    end
%#################################################################

%#########################  J2 Perturbation  ###############

    V1_dot(1)=V1_dot(1)-(3*J2*mu_earth*(Re^2)*X(1)*(1-...
            (5*X(3)/(norm(X(1:3))^2)))/(2*((norm(X(1:3)))^5)));
```

```
        V1_dot(2)=V1_dot(2)-(3*J2*mu_earth*(Re^2)*X(2)*(1-...
550             (5*X(3)/(norm(X(1:3))^2)))/(2*((norm(X(1:3)))^5)));
        V1_dot(3)=V1_dot(3)-(3*J2*mu_earth*(Re^2)*X(3)*(1-...
                (5*X(3)/(norm(X(1:3))^2)))/(2*((norm(X(1:3)))^5)));
        V2_dot(1)=V2_dot(1)-(3*J2*mu_earth*(Re^2)*X(7)*(1-...
                (5*X(9)/(norm(X(7:9))^2)))/(2*((norm(X(7:9)))^5)));
555     V2_dot(2)=V2_dot(2)-(3*J2*mu_earth*(Re^2)*X(8)*(1-...
                (5*X(9)/(norm(X(7:9))^2)))/(2*((norm(X(7:9)))^5)));
        V2_dot(3)=V2_dot(3)-(3*J2*mu_earth*(Re^2)*X(9)*(1-...
                (5*X(9)/(norm(X(7:9))^2)))/(2*((norm(X(7:9)))^5)));
        V3_dot(1)=V3_dot(1)-(3*J2*mu_earth*(Re^2)*X(13)*(1-...
560        (5*X(15)/(norm(X(13:15))^2)))/(2*((norm(X(13:15)))^5)));
        V3_dot(2)=V3_dot(2)-(3*J2*mu_earth*(Re^2)*X(14)*(1-...
           (5*X(15)/(norm(X(13:15))^2)))/(2*((norm(X(13:15)))^5)));
        V3_dot(3)=V3_dot(3)-(3*J2*mu_earth*(Re^2)*X(15)*(1-...
           (5*X(15)/(norm(X(13:15))^2)))/(2*((norm(X(13:15)))^5)));
565 %
        X_dot(1:3)=R1_dot;
        X_dot(4:6)=V1_dot;
        X_dot(7:9)=R2_dot;
        X_dot(10:12)=V2_dot;
570     X_dot(13:15)=R3_dot;
        X_dot(16:18)=V3_dot;
    return;

    % Rotation about axis 1
575 function R1=Rot_1(ang);
        R1=[1 0 0;0 cos(ang) sin(ang);0 -sin(ang) cos(ang)];
    return;

    % Rotation about axis 2
580 function R2=Rot_2(ang);
        R2=[cos(ang) 0 -sin(ang);0 1 0;sin(ang) 0 cos(ang)];
    return;

    % Rotation about axis 3
585 function R3=Rot_3(ang);
        R3=[cos(ang) sin(ang) 0;-sin(ang) cos(ang) 0;0 0 1];
    return;
```

Listing F.4: This small routine generates three-body system initial conditions based on geometric calculations from conical Likins-Pringle rigid-body equilibria. (appendixf/code/Get3BLPICs.m)

```
    %*****************************************************
    % Tool for determining L-P IC's for a 3 body system
    % LtCol Kurt Vogel
    % Nov 2005
  5 %*****************************************************
```

```
disp(['Start of program run ', datestr(now)]);
clf; clear all; close all;
format long;

%*****************************************************
% Define constants

global m1 m2 m3 mu_damp K_spring rho_o mu_earth;
m1 = 200;                    % kg
m2 = 200;                    % kg
m3 = 200;                    % kg
mu_damp = .05;                % kg/s
K_spring = 20;               % kg/s^2
rho_o = 10.0;                % km (unstretched tether length)
mu_earth = 398600.4415e0;    % km^3 / sec^2

%*****************************************************
% Set initial conditions in Generalized Coords (assumes
% perfect equilateral triangle for initial conditions)

rho_ic = 10.0;                                % km
alpha_ic = 0 * pi/180.;                       % deg -> rad
beta_ic = 40 * pi/180;                         % deg -> rad
R_c_ic = [1.1 0 0]*6378.13655;                % DU -> km
V_c_ic = [0 sqrt(mu_earth/norm(R_c_ic)) 0]; % km/s
r_ic = rho_ic*sqrt(3)/3;

%*****************************************************
% Convert to Newtonian State Velocity

H=cross(R_c_ic,V_c_ic);
nu_dot=norm(H)/((norm(R_c_ic))^2)
nu_dot_e=[0 0 nu_dot]';
C_be=[cos(-beta_ic) 0 -sin(-beta_ic);0 1 0;sin(-beta_ic)...
        0 cos(-beta_ic)];
nu_dot_b=C_be*nu_dot_e;
nu=atan2(R_c_ic(2),R_c_ic(1));
C2=[cos(beta_ic) 0 -sin(beta_ic);0 1 0;sin(beta_ic)...
        0 cos(beta_ic)];
C3=[cos(-nu) sin(-nu) 0;-sin(-nu) cos(-nu) 0;0 0 1];
C_ib=C3*C2;

error=1;
while error>=.00000001
    C=(m1+m2+m3)*(r_ic^2);
    A=C/2;

    % Standard L-P
    psi_dot=(nu_dot*cos(beta_ic)*4*(A-C))/C;
    % Spin 'er up (faster than L-P)
    % psi_dot=4*nu_dot;
```

```
        total_spin=psi_dot+nu_dot_b(3);

       rho_new=K_spring*rho_o/(K_spring-(((total_spin)^2)*(m1/3)))

        r_new=rho_new*sqrt(3)/3;

        error=abs(r_ic-r_new);
        r_ic=r_new;
    end

    r1_b=[r_ic 0 0]';
    r2_b=[-r_ic/2 r_ic*sqrt(3)/2 0]';
    r3_b=[-r_ic/2 -r_ic*sqrt(3)/2 0]';

    omega_bi_b=[0 0 psi_dot]'+nu_dot_b

    % d/dt of r1_b in b-frame = 0
    v1_i=C_ib*(cross(omega_bi_b,r1_b));
    v2_i=C_ib*(cross(omega_bi_b,r2_b));
    v3_i=C_ib*(cross(omega_bi_b,r3_b));

    V_1= V_c_ic'+v1_i; norm(V_1)
    V_2= V_c_ic'+v2_i
    V_3= V_c_ic'+v3_i


    %*****************************************************
    % Convert to Newtonian State Position

    R_1=R_c_ic'+(C_ib*r1_b)
    R_2=R_c_ic'+(C_ib*r2_b)
    R_3=R_c_ic'+(C_ib*r3_b)

% Period matching
%     magV2new=sqrt((norm(V_c_ic)^2)-(2*mu_earth/norm(R_c_ic))+...
%               (2*mu_earth/norm(R_2)))
%     V_2=(magV2new/norm(V_2))*V_2
%     V_3=(magV2new/norm(V_3))*V_3
%
%     magV1new=sqrt((norm(V_c_ic)^2)-(2*mu_earth/norm(R_c_ic))+...
%                (2*mu_earth/norm(R_1)))
%     V_1=(magV1new/norm(V_1))*V_1; norm(V_1)

    %*****************************************************
    % Save initial state to disk so it can be retrieved by model

    Initial_State=[R_1;V_1;R_2;V_2;R_3;V_3]';

    spin_ratio=psi_dot/nu_dot

    save 3B_LP_ICs.mat Initial_State rho_ic alpha_ic...
```

```
110         beta_ic R_c_ic V_c_ic spin_ratio

        %*****************************************************
        % Calculate eccentricities of the individual orbits

115     ecc_1=norm((((norm(V_1)^2)-(mu_earth/(norm(R_1))))*R_1...
            -(dot(R_1,V_1)*V_1))./mu_earth)
        ecc_2=norm((((norm(V_2)^2)-(mu_earth/(norm(R_2))))*R_2...
            -(dot(R_2,V_2)*V_2))./mu_earth)
        ecc_3=norm((((norm(V_3)^2)-(mu_earth/(norm(R_3))))*R_3...
120         -(dot(R_3,V_3)*V_3))./mu_earth)
        ecc_c=norm((((norm(V_c_ic)^2)-(mu_earth/(norm(R_c_ic))))...
            *R_c_ic-(dot(R_c_ic,V_c_ic)*V_c_ic))./mu_earth)

        %*****************************************************
125     % Calculate Periods of the individual orbits

        E1=((norm(V_1)^2)/2)-(mu_earth/(norm(R_1)))
        E2=((norm(V_2)^2)/2)-(mu_earth/(norm(R_2)))
        E3=((norm(V_3)^2)/2)-(mu_earth/(norm(R_3)));
130     Ec=((norm(V_c_ic)^2)/2)-(mu_earth/(norm(R_c_ic)));
        n1=((-2*E1)^1.5)/mu_earth;
        n2=((-2*E2)^1.5)/mu_earth;
        n3=((-2*E3)^1.5)/mu_earth;
        nc=((-2*Ec)^1.5)/mu_earth;
135     Period_1=2*pi/n1 %sec
        Period_2=2*pi/n2
        Period_3=2*pi/n3
        Period_c=2*pi/nc
        delta_Period_21=Period_2-Period_1
140     delta_Period_1c=Period_1-Period_c
        delta_Period_2c=Period_2-Period_c
        delta_r=((((Period_2-Period_1)/(2*pi))^2)*mu_earth)^(1/3)
```

Bibliography

1. "STS-75 Payloads". NASA Web Page on STS-75, June 2006. Available at http://liftoff.msfc.nasa.gov/Shuttle/STS-75/.

2. Austin, F. "Nonlinear Dynamics of a Free-Rotating Flexibly Connected Double-Mass Space Station". *Journal of Spacecraft and Rockets*, 2, No. 6:901–906, 1965.

3. Bate, Roger R., Donald D. Mueller, and Jerry E. White. *Fundamentals of Astronautics*. Dover Publications, Inc., Mineola, NY, 1st edition, 1971.

4. Beletskii, V.V. and E.T. Navikova. "On the Relative Motion of Two Cable-Connected Bodies in Orbit". *Cosmic Research*, 7, No. 3:377–384, 1969.

5. Beletsky, V.V. and E. M. Levin. *Advances in the Astronautical Sciences, Vol 83, Dynamics of Space Tether Systems*. Univelt, Inc., San Diego, California, 1st edition, 1993.

6. Bombardelli, C., E. Lorenzini, and M. Quadrelli. "Pointing Dynamics of Tether-Controlled Formation Flying for Space Interferometry". *2001 AAS/AIAA Astrodynamics Specialist Conference*. Quebec City, Quebec, Jul 2001. Vol 109, Pt II, AAS 01-404.

7. Bristow, J. "Formation Flying Technology Development and Initiatives at the Goddard Space Flight Center". *15th CNES International Symposium on Spaceflight Dynamics*. Biarritz, France, June 2000.

8. Carter, Thomas E. "State Transition Matrices for Terminal Rendezvous Studies: Brief Survey and New Example". *Journal of Guidance, Control, and Dynamics*, 21, No. 1:148–155, 1998.

9. Chobotov, V.A. "Gravity-Gradient Excitation of a Rotating Cable-Counterweight Space Station in Orbit". *Journal of Applied Mechanics*, 30, No. 4:547–554, 1963.

10. Clohessy, W. and R. Wiltshire. "Terminal Guidance Systems for Satellite Rendezvous". *Journal of the Aerospace Sciences*, 27, No. 9:653–658, 1960.

11. Cobb, R., A. Das, and K. Denoyer. "TechSat21: Developing Low-Cost, Highly Functional Micro-Satellite Clusters for 21st Century Air Force Missions". *50th International Astronautical Congress*. Amsterdam, Oct 1999.

12. Cosmo, M.L. and E.C. Lorenzini. *Tethers in Space Handbook*. Prepared for NASA Marshall Space Flight Center, Grant NAG8-1160, 3rd edition, 1997.

13. Decou, A.B. "Attitude and Tether Vibration Control in Spinning Tethered Triangles for Orbiting Interferometry". *Journal of the Astronautical Sciences*, 41, No. 3:373–398, 1993.

14. Decou, A.B. "Orbital Dynamics of the Hanging Tether Interferometer". *Journal of Guidance, Control, and Dynamics*, 14:1309–1311, 2004.

15. Decou, Anthony B. "Gravity Gradient Disturbances on Rotating Tethered Systems in Circular Orbit". *3rd International Conference on Tethers in Space*. San Fransisco, California, May 1989.

16. Decou, Anthony B. "Tether Static Shape for Rotating Multimass, Multitether, Spacecraft for "Triangle" Michelson Interfoerometer". *Journal of Guidance, Control, and Dynamics*, 12, No. 2:273–275, 1989.

17. Djebli, A., L.EL Bakkali, and M. Pascal. "On Fast Retrieval Laws for Tethered Satellite Systems". *Acta Astronautica*, 50, No. 8:461–470, 2002.

18. Farley, Rodger E. and David A. Quinn. "Tethered Formation Configurations: Meeting the Scientific Objectives of Large Aperture and Interferometric Science". *AIAA Space 2001 - Conference and Exposition*. Albuquerque, New Mexico, August 2001. AIAA-2001-4770.

19. Hand, Louis N. and Janet D. Finch. *Analytucal Mechanics*. Cambridge University Press, New York, 1st edition, 1998.

20. Hughes, Peter C. *Spacecraft Attitude Dynamics*. Dover Publications, Inc., Mineola, NY, 1st edition, 2004.

21. Hughes, Peter C. and Jonathan C. Fung. "Liapunov Stability of Spinning Satellites with Long Flexible Appendages". *Celestial Mechanics*, 4:295–308, 1971.

22. Kalantzis, S., J. Modi, and S. Pradhan. "Dynamics and Control of Multibody Tethered Systems". *Acta Astronautica*, 42, No. 9:503–517, 1998.

23. Keshmiri, M. and A.K. Misra. "General Formulation for N-Body Tethered Satellite System Dynamics". *Journal of Guidance, Control, and Dynamics*, 19, No. 1:75–83, 1996.

24. Kim, Mischa and Christopher D. Hall. "Dynamics and Control of Tethered Satellite Systems for NASA's SPECS Mission". *2003 AAS/AIAA Astrodynamics Specialist Conference*. AAS 03-532.

25. Kim, Mischa and Christopher D. Hall. "Control of a Rotating Variable-Length Tethered System". *Journal of Guidance, Control, and Dynamics*, 27, No. 5:849–858, 2004.

26. Kumar, K.D. and T. Yasaka. "Rotating Formation Flying of Three Satellites Using Tethers". *Journal of Spacecraft and Rockets*, 41, No. 6:973–985, 2004.

27. Lang, D.L. and R.K. Nolting. "Operations with Tethered Space Vehicles". *Proceedings of the Gemini Summary Conference*. Feb 1967. NASA SP-138.

28. Leamy, Michael J., Ahmed K. Noor, and Tamer M. Wasfy. "Dynamic Simulation of a Tethered Satellite System Using Finite Elements and Fuzzy Sets". *Computer Methods in Applied Mechanics and Engineering*, 190, Issues 37-38:4847–4870, 2001.

29. Likins, Peter W. *Elements of Engineering Mechanics*. McGraw-Hill Book Company, New York, 1st edition, 1973.

30. Likins, P.W. "Stability of a Symmetrical Satellite in Attitudes Fixed in an Orbiting Reference Frame". *Journal of the Astronautical Sciences*, 12, No. 1:18–24, 1965.

31. Livneh, Rafael and Bong Wie. "The Effect of Energy Dissipation on a Rigid Body with Constant Torques". *AIAA/AAS Astrodynamics Conference*. San Diego, California, July 1996. AIAA 1996-3667.

32. Melton, Robert G. "Time-Explicit Representation of Relative Motion Between Elliptical Orbits". *Journal of Guidance, Control, and Dynamics*, 23, No. 4:604–610, 2000.

33. Misra, A.K., Z. Amier, and V.J. Modi. "Attitude Dynamics of Three-Body Tethered Systems". *25th Aerospace Sciences Meeting*. Reno, Nevada, Jan 1987. AIAA-87-0021.

34. Misra, A.K., J. Bellerose, and V.J. Modi. "Dynamics of a Tethered System Near the Earth-Moon Lagrangian Points". *2001 AAS/AIAA Astrodynamics Specialist Conference*. Quebec City, Quebec, Jul 2001. Vol 109, Pt I, AAS 01-328.

35. Misra, A.K. and V.J. Modi. "A Survey on the Dynamics and Control of Tethered Satellite Systems". *NASA/AIAA/PSN International Conference on Tethers in Space*. Arlington, Virginia, Sep 1986. Vol 62, AAS 86-246.

36. Misra, A.K. and V.J. Modi. "Three-Dimensional Dynamics and Control of Tether-Connected N-Body Systems". *28th Aerospace Sciences Meeting*. Reno, Nevada, Jan 1990. AIAA-90-0751.

37. Misra, Arun. "Equilibrium Configurations of Tethered Three-Body Systems and Their Stability". *AAS/AIAA Space Flight Mechanics Meeting*. San Diego, California, 2001. Vol 108, AAS 01-191.

38. Moccia, A., M. D'Errico, and S. Vetrella. "Space Station Based Tethered Interferometer for Natural Disaster Monitoring". *Journal of Spacecraft and Rockets*, 33, No. 5:700–706, 1996.

39. Moccia, A., S. Vetrella, and M. Grassi. "Space Station Based Tethered Interferometer for Natural Disaster Monitoring". *Journal of Guidance, Control, and Dynamics*, 16, No. 2:264–269, 1993.

40. Modi, V.J. and R.C. Brereton. "The Stability Analysis of Coupled Librational Motion of an Axi-symmetric Satellite in a Circular Orbit". *XVIIIth International Astronautical Congress Conference*. Belgrade, 1967. Vol 1, p.109-120.

41. Mori, O., K. Nakaya, N Maeda, and S. Matunaga. "Formation and Attitude Control of Tethered Satellite Cluster". *23rd International Symposium on Space Technology and Science*. Matsue, Japan, May 2002. Japan Society for Aeronautical and Space Sciences, 2002, p. 899-904.

42. Mori, Osamu and Saburo Matunaga. "Coordinated Control of Tethered Satellite Cluster Systems". *AIAA Guidance, Navigation, and Control Conference and Exhibit*. Montreal, Canada, August 2001. AIAA-2001-4392.

43. Nakaya, K., M. Iai, O. Mori, and S. Matunaga. "On Formation Deployment for Spinning Tethered Formation Flying and Experimental Demonstration". Official Website for the 18th International Symposium on Spaceflight Dynamics, Oct 2004. Available at http://www.issfd.dlr.de/papers/P1088.pdf.

44. Nakaya, K., M. Iai, K. Omagari, H. Yabe, and S. Matunaga. "Formation Deployment Control for Spinning Tethered Formation Flying - Simulations and Ground Experiments". *AIAA Guidance, Navigation, and Control Conference and Exhibit*. Providence, Rhode Island, August 2004. AIAA-2004-4896.

45. O'Reilly, Oliver M. and Meng How Tan. "Steady Motions of an Axisymmetric Satellite: An Atlas of Their Bifurcations". *International Journal of Non-Linear Mechanics*, 39:921–940, 2004.

46. Parker, Timothy. *Mean Performance Optimization of an Orbiting Distributed Aperture by Warped Aperture Image Plane Comparisons*. Master's thesis, Graduate School of Engineering, Air Force Institute of Technology (AETC), Wright-Patterson AFB OH, September 2002. AFIT/DS/ENY/02-3.

47. Pizarro-Chong, A. and A.K. Misra. "Dynamics of a Multi-Tethered Satellite Formation". *AIAA/AAS Astrodynamics Specialist Conference and Exhibit*. Providence, Rhode Island, Aug 2004. AIAA 2004-5308.

48. Pradhan, S., V.J. Modi, and A.K. Misra. "Tether-Platform Coupled Control". *Acta Astronautica*, 44, No. 5:243–256, 1999.

49. Pringle, R. "Exploration of Nonlinear Resonance in Damping an Elastic Dumb-Bell Sateliite". *AIAA Journal*, No. 7:1217–1222, 1968.

50. Quadrelli, Marco B. "Modeling and Dynamics Analysis of Tethered Formations for Space Interferometry". *11th AAS/AIAA Space Flight Mechanics Conference*. Santa Barbara, California, Feb 2001. AAS 01-231.

51. de Queiroz, M., V. Kapila, and Q. Yan. "Adaptive Nonlinear Control of Multiple Spacecraft Formation Flying". *Journal of Guidance, Control, and Dynamics*, 23, No. 3:385–390, 2000.

52. Quinn, David A. and David C. Folta. "A Tethered Formation Flying Concept for the SPECS Mission". *Proceedings of the 23rd Rocky Mountain Guidance and Control Conference*. San Diego, California, Jan 2000. Vol. 104, AAS 00-015.

53. Rumyantsev, V.V. "On Stability of Stationary Motions of the Gyrostat-Satellite". *XVIIIth International Astronautical Congress Conference*. Belgrade, 1967. Vol 1, p.103-108.

54. Sabol, C., R. Burns, and C.A. McLaughlin. "Satellite Formation Flying Design and Evolution". *AAS/AIAA Space Flight Mechanics Meeting*. Breckenridge, Colorado, Feb 1999. AAS 99-121.

55. Schaub, H. and K.T. Alfriend. "J2 Invariant Relative Orbits for Spacecraft Formations". *NASA GSFC Flight Mechanics and Estimation Conference*. May 1999.

56. Schaub, H., S.R. Vadali, and K.T. Alfriend. "Initial Conditions and Fuel-Optimal Control for Formation Flying of Satellites". *AIAA Guidance, Navigation, and Control Conference and Exhibit*. Portland, Oregon, August 1999. AIAA-99-4265.

57. Schaub, H., S.R. Vadali, J.L. Junkins, and K.T. Alfriend. "Satellite Formation Flying Control Using Mean Orbital Elements". *1999 AAS/AIAA Astrodynamics Conference*. Girdwood, Alaska, Aug 1999. Vol 103, Pt I, AAS 99-310.

58. Sedwick, R., D. Miller, and E. Kong. "Mitigation of Differential Perturbations in Clusters of Formation Flying Satellites". *Journal of the Astronautical Sciences*, 47, No. 4:309–331, 2000.

59. Serov, V.M. "Rotational Motion of a Dynamically Symmetric Rigid Body Under the Effect of a Nonlinear Moment". *Akademiia Nauk SSSR, Investiia, Mekhanika Tverdogo Tela*, 26–31, 1991.

60. Sidi, Marcel J. *Spacecraft Dynamics and Control*. Cambridge University Press, New York, NY, 1st edition, 1997.

61. Sparks, A. and H. Yeh. "Geometry and Control of Satellite Formations". *Proceedings of the American Control Conference*. Chicago, Illinios, June 2000.

62. Sparks, Andrew. "Satellite Formationkeeping Control in the Presence of Gravity Perturbations". *Proceedings of the American Control Conference*. Chicago, Illinois, June 2000.

63. Stepanov, S.Ia. "On the Steady Motions of a Gyrostat Satellite". *Journal of Applied Mathematics and Mechanics*, 33:121–126, 1969.

64. Thomson, William T. *Introduction to Space Dynamics*. Dover Publications, Inc., Mineola, NY, 1st edition, 1961.

65. Thomson, William T. "Spin Stabilization of Attitude Against Gravity Torique". *Journal of the Astronautical Sciences*, 9:31–33, 1962.

66. Tragesser, Steven G. "Formation Flying with Tethered Spacecraft". *AIAA/AAS Astrodynamics Specialist Conference*. Denver, Colorado, Aug 2000. AIAA 2000-4133.

67. Tragesser, Steven G. and Ayhan Tuncay. "Orbital Design of Earth-Oriented Tethered Satellite Formations". *AIAA/AAS Astrodynamics Specialist Conference and Exhibit*. Monterey, California, Aug 2002. AIAA 2002-4641.

68. Tsuchiya, K. and H. Saito. "Dynamics of a Spin-Stabilized Satellite Having Flexible Appendages". *AIAA Journal*, 12:490–495, 1974.

69. Tuncay, Ayhan. *Stability of a Tethered Satellite Formation about the Likins-Pringle Equlibria*. Master's thesis, Graduate School of Engineering, Air Force Institute of Technology (AETC), Wright-Patterson AFB OH, March 2002. AFIT/GSO/ENY/02-4.

70. Ulybyshev, Yuri. "Long-Term Formation Keeping of Satellie ConstellationUsing Linear-Quadratic Controller". *Journal of Guidance, Control, and Dynamics*, 21, No. 1:109–115, 1998.

71. Vallado, David A. *Fundamentals of Astrodynamics and Applications*. Microcosm Press, El Segundo, California, 2nd edition, 2001.

72. Wang, Li-Sheng, Kuang-Yow Lian, and Po-Tuan Chen. "Steady Motions of Gyrostat Satellites and Their Stability". *IEEE Transactions on Automatic Control*, 40 Issue 10:1732–1743, 1995.

73. Wertz, James R. and Wiley J. Larson. *Space Mission Analysis and Design*. Microcosm Press, El Segundo, California, 3rd edition, 1999.

74. Wie, Bong. *Space Vehicle Dynamics and Control*. AIAA, Inc., Reston, VA, 1st edition, 1998.

75. Wiesel, William E. *Spaceflight Dynamics*. McGraw-Hill Publishing, New York, 1st edition, 1989.

76. Wiesel, William E. "Relative Satellite Motion About an Oblate Planet". *Journal of Guidance, Control, and Dynamics*, 25, No. 4:776–785, 2002.

77. Williams, Paul. "Optimal Control of the Deployment/Retrieval of a Spinning Tethered Formation". *15th AAS/AIAA Space Flight Mechanics Conference*. Copper Mountain, Colorado, Jan 2005. AAS 05-207.

78. Williams, Trevor and Kenneth Moore. "Dynamics of Tethered Satellite Formations". *AAS/AIAA Space Flight Mechanics Meeting*. San Antonio, Texas, Jan 2002. AAS 02-198.

79. Zhu, Renzhang, Da Lei, Huabao Lin, and A.K. Misra. "Attitude Dynamics of Tethered Systems". *49th International Astronautical Congress*. Melbourne, Austrailia, Sept 1998. IAF-98-A5.03.

Vita

Lt Col Kurt Vogel was born in Anchorage, Alaska in 1967. Upon graduating from Clayton Valley High School in Concord, California in 1985, he received a presidential appointment to the U.S. Air Force Academy. In 1989, he graduated with a Bachelor of Science in Astronautical Engineering and received a regular commission in the USAF. His first assignment was to Kirtland Air Force Base, New Mexico, where he built and tested Weapons Laboratory technologies for experimental spaceflight. In 1990, he was selected for transfer into the Phillips Laboratory Optical Surveillance Division where he conducted orbital analyses for a presidentially directed, highly classified program. In 1993, he graduated from the Air Force Institute of Technology (AFIT) with a Master of Science in Astronautical Engineering before taking over as Chief of Space Test Operations at Onizuka Air Force Base where he provided real time satellite operations support to classified national priority systems. From 1996 to 1997, he attended the United States Air Force Test Pilot School at Edwards Air Force Base. Upon graduation, he was assigned to the Special Projects Test Squadron at a classified location where he led a selectively manned team conducting high priority presidentially directed flight tests. In 1999, he was re-assigned as the Assistant Operations Officer for the Classified Flight Test Squadron, where he conducted research and development of over 70 classified prototype aircraft and missiles. In 2001, he was transferred to the Pentagon where he developed United States foreign policy initiatives on airspace command and control cooperation worldwide and led technical evaluations of foreign air surveillance programs. From 2003 to 2006, he once again attended AFIT to earn his Doctorate in Astronautical Engineering. Following graduation, he was brought back to the Pentagon where is was assigned command of the Air Force Red Team, part of the Rapid Capabilities Office that reports directly to the Secretary of the Air Force.

Permanent address: 2950 Hobson Way
Air Force Institute of Technology
Wright-Patterson AFB, OH 45433

REPORT DOCUMENTATION PAGE

Form Approved
OMB No. 0704–0188

The public reporting burden for this collection of information is estimated to average 1 hour per response, including the time for reviewing instructions, searching existing data sources, gathering and maintaining the data needed, and completing and reviewing the collection of information. Send comments regarding this burden estimate or any other aspect of this collection of information, including suggestions for reducing this burden to Department of Defense, Washington Headquarters Services, Directorate for Information Operations and Reports (0704–0188), 1215 Jefferson Davis Highway, Suite 1204, Arlington, VA 22202–4302. Respondents should be aware that notwithstanding any other provision of law, no person shall be subject to any penalty for failing to comply with a collection of information if it does not display a currently valid OMB control number. **PLEASE DO NOT RETURN YOUR FORM TO THE ABOVE ADDRESS.**

1. REPORT DATE *(DD–MM–YYYY)*	2. REPORT TYPE	3. DATES COVERED *(From — To)*
14–09–2006	Doctoral Dissertation	Sept 2003 — Sep 2006

4. TITLE AND SUBTITLE

Dynamics and Control of Tethered Satellite Formations for the Purpose of Space-Based Remote Sensing

5a. CONTRACT NUMBER

5b. GRANT NUMBER

5c. PROGRAM ELEMENT NUMBER

6. AUTHOR(S)

Kurt A. Vogel, Lt Col, USAF

5d. PROJECT NUMBER

5e. TASK NUMBER

5f. WORK UNIT NUMBER

7. PERFORMING ORGANIZATION NAME(S) AND ADDRESS(ES)

Air Force Institute of Technology
Graduate School of Engineering and Management
2950 Hobson Way
WPAFB OH 45433-7765

8. PERFORMING ORGANIZATION REPORT NUMBER

AFIT/DS/ENY/06-04

9. SPONSORING / MONITORING AGENCY NAME(S) AND ADDRESS(ES)

N/A

10. SPONSOR/MONITOR'S ACRONYM(S)

11. SPONSOR/MONITOR'S REPORT NUMBER(S)

12. DISTRIBUTION / AVAILABILITY STATEMENT

Approval for public release; distribution is unlimited.

13. SUPPLEMENTARY NOTES

14. ABSTRACT

This dissertation assesses the utility of tethered satellite formations for the space-based remote sensing mission. Energy dissipation is found to have an adverse effect on foundational rigid body (Likins-Pringle) equilibria. It is shown that a continuously earth-facing equilibrium condition for a fixed-length tethered system does not exist since the spin rate required for the proper precession would not be high enough to maintain tether tension. The range of required spin rates for steady-spin motion is numerically defined here, but none of these conditions can meet the continuously earth-facing criteria. Of particular note is the discovery that applying certain rigid body conditions to a free-flying formation creates the desired equilibrium condition. Control methods applied to the tethered system fail to maintain formation orientation or are cost prohibitive. The overall assessment is that tethers have great value for general formations, however, by themselves tethers cannot conduct formation control for continuously earth-facing aperture clusters. Even with additional controls, the utility of tethers for this mission is limited.

15. SUBJECT TERMS

satellite formations, tethered satellites, Likins-Pringle equilibria, energy dissipation, axisymmetric rigid bodies, remote sensing

16. SECURITY CLASSIFICATION OF:			17. LIMITATION OF ABSTRACT	18. NUMBER OF PAGES	19a. NAME OF RESPONSIBLE PERSON
a. REPORT	b. ABSTRACT	c. THIS PAGE			Dr. Richard G. Cobb
U	U	U	UU	296	19b. TELEPHONE NUMBER *(include area code)* (937) 255–6565, ext 4559